In-situ transmission electron microscopy on high-temperature phase transitions of Ge-Sb-Te alloys

D i s s e r t a t i o n

zur Erlangung des akademischen Grades
doctor rerum naturalium (Dr. rer. nat.)
im Fach: Physik
Spezialisierung: Experimentalphysik

von

M.Sc. Katja Berlin (geb. Hagemann)

eingereicht an der

Mathematisch-Naturwissenschaftlichen Fakultät
der Humboldt-Universität zu Berlin

Präsidentin der Humboldt-Universität zu Berlin
Prof. Dr.-Ing. Dr. Sabine Kunst

Dekan der Mathematisch-Naturwissenschaftlichen Fakultät
Prof. Dr. Elmar Kulke

Gutachter/innen:
1. Prof. Dr. Henning Riechert
2. Prof. Dr. Gerhard Dehm
3. Dr. Marc Willinger

Tag der Einreichung: 14.11.2017
Tag der mündlichen Prüfung: 23.05.2018

Zusammenfassung

Das Hochtemperaturverhalten, insbesondere die strukturellen Übergänge erster Ordnung, beeinflusst viele verschiedene Prozesse angefangen von der Materialverarbeitung bis hin zur technologischen Anwendung. Das Verständnis der beteiligten mikroskopischen Mechanismen ist entscheidend um diese Prozesse gezielt zu beeinflussen. In-situ Transmissionselektronenmikroskopie (TEM) bietet die Möglichkeit, die atomaren Prozesse direkt und in Realzeit während der strukturellen Phasenänderung zu beobachten. In der vorliegenden Arbeit wurde in-situ TEM angewendet, um die Phasenübergänge einer Heterostruktur im Hochtemperaturbereich zu untersuchen. Die Heterostruktur besteht dabei aus einer Ge-Sb-Te (GST) Dünnschicht auf einem kristallinen Siliziumsubstrat. Aufgrund der Anwendungen von GST Verbindungen im Bereich der Phasenwechselmaterialien, bei der ein starkes lokales Aufheizen notwendig ist, ist die thermische Stabilität und das Hochtemperaturverhalten nicht nur wesentlich um Funktionsausfällen vorzubeugen, sondern auch für ein besseres Verständnis der Materialeigenschaften. Das Hauptaugenmerk dieser Arbeit liegt auf der Untersuchung der Reversibilität des Schmelz- und Kristallisationsprozesses, sowie des anisotropen Sublimationsverhaltens.

Eine notwendige Voraussetzung für die erfolgreiche Beobachtung der beiden Phasenübergänge, Schmelzen und Sublimieren, sind angemessene Rahmenbedingungen. Die Beobachtung einer Flüssigphase unter Vakuumbedingungen des Mikroskops macht eine Einkapselung der Probe notwendig. Der Sublimationsprozess hingegen setzt eine saubere Oberfläche voraus. Die Absicht, die Prozesse auf atomarer Skala verfolgen zu können, macht es zusätzlich erforderlich, die Probe entlang kristallografisch niedrig indizierter Zonenachsen ausrichten zu können. Die Verwendung verschiedener Probenherstellungsverfahren für die Erzeugung solcher Rahmenbedingungen wird im Rahmen dieser Arbeit herausgestellt. Außerdem, wird die Elektronenenergieverlustspektroskopie eingesetzt um die lokale, chemische Zusammensetzung vor und nach den Phasenübergängen zu bestimmen.

Der Schwerpunkt der Arbeit liegt auf der Untersuchung der Phasenübergänge fest-flüssig und fest-gasförmig. Der Ausgangspunkt für die Analyse des fest-flüssig Überganges ist eine geordneter $Ge_1Sb_2Te_4$ Dünnschicht mit trigonalen Kristallstruktur. Die Dynamik der fest-flüssig-Grenzfläche ist sowohl für den Schmelzvorgang als auch den Kristallisationsprozess dargestellt. Die fest-flüssig-Grenzfläche weist während des Schmelzens einen ausgedehnten Übergangsbereich auf, der durch die Unordnung der Vakanzen gekennzeichnet ist. Obwohl die Geschwindigkeiten der Grenzflächenbewegung sowohl für den Schmelzvorgang als auch für die Kristallisation im Nanometer-pro-Sekunde Bereich liegen, sind die zugrunde liegenden Prozesse deutlich verschieden. Beim Schmelzvorgang wird eine lineare Zeitabhängigkeit offenbart, währenddessen bei der Kristallisation eine nicht-lineare Zeitabhängigkeit mit einer Start-Stopp-Bewegung identifiziert werden kann. Der Einfluss der Substrat-Grenzfläche wird diskutiert und die Grenzflächen- und Oberflächenenergie des GST-Si Systems bestimmt. Diese sind nicht nur sehr hilfreich für technologische Anwendungen, sondern auch notwendig für die Interpretation der Ergebnisse der Sublimationsstudie.

Der Phasenübergang fest-gasförmig wird für beide Kristallstrukturen von GST (kubisch und trigonal) analysiert. Der Sublimationsprozess weist eine klare anisotrope Dynamik auf. Für die kubische Struktur führt die Sublimation zu der Bildung stabiler $\{111\}$ Facetten. Dies erfolgt, entsprechend des Terrassen-Stufen-Kinken Models, über die Bildung von Kinken auf stabilen Stufen und der anschließenden Desorption von diesen Kinkplätzen entlang der $\langle 110 \rangle$ Richtungen. Die bevorzugten Keimbildungsorte der Kinken wurden identifiziert und stimmen mit den Voraussagen des auf "gebrochenen Bindungen" basierenden Models (engl. "broken-bond" model) überein. Die anisotrope Bildung von Kinken, Stufen und folglich stabilen Terrassen während der Sublimation ist dabei unabhängig von der GST-Kristallstruktur. Nach der Entstehung der kubischen Phase bleibt diese bis zum Sublimationspunkt stabil. Es konnte keine Ordnung der Vakanzen bzw. kein Übergang in die trigonal Phase beobachtet werden. Dies wird der Diffusion von Silizium in GST zugeschrieben.

Im Kontext dieser Arbeit konnte gezeigt werden, dass sich die Methode in-situ TEM hervorragend eignet, um die Hochtemperatur-Phasenübergänge komplexer Heterostrukturen zu analysieren. Es konnten dabei eindeutige Einblicke in die physikalischen Prozesse auf atomarer Ebene, die an den fest-flüssig und fest-gasförmig Phasenübergängen beteiligt sind, gewonnen werden.

Abstract

High-temperature behavior, especially first-order structural transitions, influence many different processes ranging from material processing to device applications. The understanding of the involved microscopic mechanism is crucial for controlling these processes. In-situ transmission electron microscopy (TEM) provides the means for direct observation of atomic processes during structural phase transitions in real time. In the presented thesis, in-situ TEM is applied to investigate the solid-liquid and solid-vapor phase transitions of a heterostructure composed of a Ge-Sb-Te thin film on a crystalline Si substrate. Due to the application of Ge-Sb-Te alloys as phase change material where intense local heating is required, the thermal stability and high-temperature behavior are essential not only to prevent failure of the functionality, but also for better understanding of the material properties. The main goals of this study are to address the reversibility of the melting and solidification processes as well as the anisotropic sublimation behavior.

A necessary requirement for the successful observation of the two phase transitions, melting and sublimation, is an adequate sample environment. The observation of the liquid phase inside the vacuum conditions of the microscope necessitates an encapsulation of the film whereas the solid-vapor transition requires a clean surface. Additionally, the intention to study the processes at an atomic scale requires the orientation along low-index crystallographic directions. The creation of those environments using different sample preparation techniques is emphasized. Furthermore, the experimental boundary conditions such as the local chemical composition before and after the phase transitions is evaluated using electron energy-loss spectroscopy in the TEM.

The main part of the thesis is concerned with the investigation of the solid-liquid and solid-vapor phase transitions. The starting point of the solid-liquid transition study is an ordered trigonal structured $Ge_1Sb_2Te_4$ film. The solid-liquid interface dynamics during melting and crystallization are presented. The solid-liquid interface during melting displays an extended transition zone that is characterized by a vacancy disordered state. Although the velocities of the interface motion are in the nanometer per second scale for both, melting and crystallization, the underlying dynamic processes are considerably different. Melting reveals linear dependence on time, whereas crystallization exhibits a non-linear time-dependency featuring a superimposed start-stop motion. The influence of the interface is addressed and therefore the interfacial and surface energies in the GST and Si heterostructure are determined. They are not only extremely useful for technological applications but are also used for the discussion of the sublimation results.

The solid-vapor transition is analyzed for both crystal structures of Ge-Sb-Te, trigonal and cubic. The sublimation process exhibits an anisotropic dynamic. For the cubic structure, sublimation leads to the formation of stable $\{111\}$ facets via kink nucleation on stable steps and subsequent sublimation from those kink sites along $\langle 110 \rangle$ as predicated by the terrace-step-kink model. Preferred kink nucleation sites are identified and are in accordance with the broken-bond model approach. The anisotropic formation of kinks, steps and subsequently stable terraces during sublimation is shown to be independent of the GST crystal structure. The cubic phase once formed, remains stable even up to the sublimation point and no ordering phenomena or transition to the trigonal phase is observed which is attributed to Si diffusion into the GST grain.

In conclusion, the thesis shows the feasibility of in-situ TEM to analyze high-temperature phase transitions of complex heterostructures and thus provide insights into the physical mechanism involved in transitions from solids into their liquid and vapor phase.

Scientific contributions

Publications related to the thesis

Phase stability and anisotropic sublimation of cubic Ge-Sb-Te alloy observed by in-situ transmission electron microscopy
K. Berlin and A. Trampert
The Journal of Physical Chemistry C **122** (2018), 2968

Liquid-solid phase transition of Ge-Sb-Te alloy observed by in-situ transmission electron microscopy
K. Berlin and A. Trampert
Ultramicroscopy **178** (2017), 27

In Situ Transmission Electron Microscopy of High-Temperature Phase Transitions in Ge-Sb-Te Alloys
K. Berlin and A. Trampert
Advances in Imaging and Electron Physics **190** (2015), 760

Further publications

Synthesis of quasi-free-standing bilayer graphene nanoribbons on SiC surfaces
M.H. Oliveira Jr., J. M. J. Lopes, T. Schumann, M. Ramsteiner, K. Berlin, A. Trampert and H. Riechert
Nature Communications **6** (2015), 7632

Element substitution from substrates in Bi2Se3, Bi2Te3 and Sb2Te3 overlayers deposited by hot wall epitaxy
Y. Takagaki, U. Jahn, B. Jenichen, K. Berlin, X. Kong and K. Biermann
Semiconductor Science and Technology, **29** (2014), 095021

Conference contributions

[FEMMS2015, Lake Tahoe (2015) Poster presentation] - **Liquid-solid phase transition of Ge-Sb-Te alloy observed by in-situ transmission electron microscopy**
K. Berlin and A. Trampert

[IAM Nano, Hamburg (2015) Poster presentation] - **In-situ transmission electron microscopy studies of dynamic crystallization behavior in layered materials**
K. Berlin and A. Trampert

[Conference on In-Situ and Correlative Electron Microscopy, Saarbrücken (2014), Oral presentation] - **In-situ transmission electron microscopy of high-temperature phase transitions in Ge-Sb-Te alloys**
K. Berlin and A. Trampert

[DPG Conference, Dresden (2014) Oral presentation] - **Kristallisationsverhalten und Kompositionsbestimmung von GeSbTe auf Si(111) mittels in-situ TEM & EELS**
K. Berlin, X. Kong and A. Trampert

[German Conference of Women in Physics, Heidelberg (2013) Oral presentation] - **Kristallisationsverhalten und Kompositionsbestimmung von GeSbTe auf Si(111) mittels in-situ TEM und EELS**
K. Berlin and A. Trampert

[Dresden Fraunhofer Cluster Nanoanalysis (2013) Invited Talk] - **In-situ transmission electron microscopy of microstructure modifications in (GeTe)1-x(Sb2Te3)x**
K. Berlin and A. Trampert

Table of Contents

List of Figures

Abbreviations

ADF	Annular dark-field
BF	Bright-field
CCD	Charge-coupled device
DF	Dark-field
DP	Diffraction pattern
DSC	Differential scanning calorimetry
DTEM	Dynamic transmission electron microscopy
EELS	Electron energy-loss spectroscopy
EDX(S)	Energy dispersive X-ray spectroscopy
FEG	Field emission gun
FIB	Focused ion beams
FWHM	Full width at half maximum
GST	Ge-Sb-Te
HAADF	High-angle annular dark-field
HRTEM	High-resolution transmission electron microscopy
ICP	Inductively coupled plasma spectrometry
MEMS	Micro-electro-mechanical systems
MLS	Multiple-least-square
PEELS	Parallel-recording electron energy-loss spectroscopy
PIPS	Precision ion polishing system
RBS	Rutherford backscattering spectroscopy
RDF	Radial distribution function
SAD	Selected area diffraction
SEM SEI	Scanning electron microscopy - secondary electron image
STEM	Scanning transmission electron microscopy
TEM	Transmission electron microscopy
TSK	Terrace-step-kink
UTEM	Ultrafast transmission electron microscopy
VL	Vacancy layer
VOC	Vacancy-ordered cubic
ZLP	Zero-loss peak

1 Introduction

In-situ transmission electron microscopy (TEM) is a fast-growing and fascinating method in modern electron microscopy as evidenced by the increasing number of recent publications [1]. During *in-situ* microscopy, physical and chemical processes are observed while they occur inside the microscope. It thus provides the opportunity to sequentially track changes of the sample caused by environment, stress or temperature. The application of this technique ranges from material science to chemistry and biology and can be used to characterize the dynamic changes in size, shape, interface structure, electronic state and chemical composition of a sample. Recent developments are based on combining high spatial resolution of aberration-corrected imaging, analytical electron energy-loss spectroscopy and energy dispersive X-ray spectroscopy with various external stimuli like temperature, pressure, magnetic and electric fields, as well as liquid and gas environments. With the growing availability of suitable and specialized TEM specimen holders, in-situ TEM was applied to various processes in material science and solid state physics such as phase transformations, surface reactions, crystal growth of nanostructures and thin films, magnetic phenomena and deformation processes. The books from Butler and Hale [2] and, more recently from Ross [3] provide comprehensive reviews about the versatile applications of in-situ TEM.

Especially high-temperature behavior, such as first-order structural transitions, influence many different processes ranging from material processing to device applications. Melting and solidification are two fundamental high-temperature, first-order phase transitions. Even though the changes of many physical properties of materials during melting and solidification are well understood, a detailed description of the solid-liquid and the solid-vapor transition on the atomic scale is still under discussion [4–6]. For instance, crystallization rates predicted by simulations or theoretically calculated melting temperatures can be orders of magnitude different than the experimental results, illustrating the need for further experimental investigations to justify theoretical models [5–7]. The dynamics of first-order phase transitions are often described as nucleation and growth processes and there are still many open questions. During the solid-liquid phase transition, questions arise where the transformation starts (e.g. in the bulk or at surfaces and other perturbations of the crystalline structure like grain boundaries or defects) and which processes cause the structural breakdown (e.g. vibrational lattice instabilities or vacancy clustering have been discussed). In this thesis, in-situ, real time, high-resolution TEM is used to observe the solid-liquid and solid-vapor phase transitions of bulk materials in a film-substrate configuration. The investigated heterostructure, which is composed of a Ge-Sb-Te (GST) thin film on a crystalline Si substrate, allows addressing some of those open questions.

In particular, although the processes of melting and solidification are thermodynamically reversible that does not imply that the involved atomistic processes are identical. For instance, Li *et al.* recently described that the nucleation process of the liquid-solid phase transition of bismuth nanoparticles involves different progressions in ordering during melting

and solidification [6]. During melting, the change in crystalline order is a stepwise process involving vacancy formation and aggregation. While during solidification, the change associated with the formation of an ordered liquid is linearly. It is interesting to explore if a similar difference between melting and solidification occurs during the growth process. There are indications that this is the case in Ge-Sb-Te alloys. The melting process in GST is theoretically predicted as a two-dimensional phenomenon where GST melts by forming linear and tangled clusters in two directions while keeping order in the perpendicular direction [8]. The inverse process of crystal growth on the other hand is described according to classical nucleation theory without a restricted dimensionality. In-situ TEM is especially suited to address the question of reversibility for atomistic processes during growth due to the high spatial resolution. Therefore, it is applied in this thesis to directly observe the dynamical behavior of the solid-liquid interface during melting and solidification.

Furthermore, the solid-liquid interface structure and its influence during the growth process are not comprehensively understood. For example, effects like premelting leading to the formation of a transitional, liquid-like surface layer can influence the interface structure. This has been observed for initially solid-vapor and solid-solid interfaces ([4, 9–13] and ref. therein). In this thesis, in-situ HRTEM is used to study the structure of the solid-liquid interface and particularly to address the question of the existence of an intermediate state during the phase transition.

Besides the high-temperature phase transition into the liquid phase, the solid-vapor transition and its associated atomistic mechanism are likewise of fundamental significance. The direct observation of the sublimation processes on the atomic scale might also contribute to the understanding of the inverse process which is crystal growth. Especially, the process of epitaxy is essential for the growth of modern heterostructures and nanomaterials and insights into the underlying mechanism are crucial for controlling them. Sublimation is often treated as the inverse growth process and argued to involve stepwise progression based on the nearest-neighbor broken-bond model and the terrace-step-kink (TSK) model of surfaces [14, 15]. So far, most TEM studies only indirectly confirm the applicability of the TSK model for sublimation processes by observing changes in morphology or faceting at lower magnification [12, 16–18]. In-situ HRTEM provides the experimental means for the direct observation of sublimation at the atomic scale and in real time. Recently, a few studies investigating sublimation with atomic resolution were done for dispersed nanoparticles [19–22]. For instance, Hsin *et al.* as well as Buha *et al.* reported that sublimation occurred via energetically favorable stepwise migration [20, 21]. An open question is however, how a complex system such as the quasi-binary GST alloy, influences the sublimation process and whether this sublimation process can be viewed as the reverse growth process where the theoretically described TSK model is applicable.

Additionally, as Chen *et al.* recently pointed out, the substrate can significantly influence the high-temperature behavior during phase transitions. They demonstrated that the choice of the substrate changed the melting to a sublimation process for Cu nanoparticles [23]. The film-substrate configuration used in this work provides the opportunity to investigate the influence of the substrate on melting and sublimation processes in this system of a GST-Si heterostructure. Thereby, questions related to the thermal stability of the GST-Si heterostructure and to the determination of interfacial energies can be addressed.

Beside the interests in those fundamental questions about the solid-liquid and solid-vapor

phase transitions, there are technological aspects to consider as well. The cubic-to-amorphous transition which is technologically exploited in information storage applications is argued to involve local melting [24]. This is required to transform the cubic crystal structure into the amorphous structure during the subsequent quenching process. Additionally, volume shrinkage during re-crystallization can lead to void formation in encapsulated GST material after high temperature processes [25]. Thus, sublimation can occur at the crystal-void interface. Therefore, the investigations of high-temperature structural and chemical stability as well as the dynamics involved in phase transitions are also of technological interests for GST alloys.

Outline of thesis

After this introduction, chapter 2 starts with an overview of fundamentals of phase transitions. It consists of two parts. First, thermodynamic theory is used to classify phase transitions and to describe the driving force behind them. In the second part, kinetic theory is used to explain the rate of the solid-liquid and the solid-gas phase transitions.

Chapter 3 is dedicated to the working principles and application of transmission electron microscopy. First, the set-up of the microscope is illustrated. Then, imaging formation based on electron diffraction theory is introduced limited to those image modes used throughout this thesis. The last part of this chapter gives an overview of quantitative electron energy-loss spectroscopy. After introducing the fundamentals, the first experimental results of this work are shown, where the chemical composition of GST alloys used in subsequent experiments is determined.

Chapter 4 addresses the experimental challenges involved with in-situ TEM. First, the advantages and limitations of in-situ TEM are explained. Next, the experimental realization applied in this work is presented. Therein, the discussion is focused on the temporal resolution, the temperature control and finally the influence of the electron beam on the in-situ experiments. At last, the sample preparation needed for the investigation of the different phase transitions is discussed.

Chapter 5 is concerned with the material system Ge-Sb-Te which is used as a case study. It focuses on the material properties related to this work. After introducing the general ideas of phase change materials, the structures of the different GST phases are summarized. The information provided there is used to identify the different phases in the following experiments. Subsequently, the relevant thermodynamic data for GST is summarized. In order to provide context for the investigated phase transitions into vapor and liquid phase, experimental in-situ TEM results are used to describe the processes involved in the solid-to-solid phase transitions from amorphous to cubic and then to trigonal structure. Beyond previously known processes, experimental results are shown addressing the start-stop behavior observed during grain boundary migration.

The next two chapters present the main part of this thesis and dwell on the experimental results of the high-temperature phase transitions of GST. They start with the solid-liquid transition in chapter 6. First, some further aspects of melting are introduced which are used to interpret the observations. The encapsulation of the GST film is then discussed as necessity to ensure that the liquid phase can be observed inside the microscope. The solid-liquid interface dynamics during melting and crystallization are presented. Therein, the interface

structure for both processes is compared and the origin of the different observed temporal behavior is addressed. Subsequently, the microstructure that is developed after solidification is analyzed for various temperature profiles. The last section contains the investigation of surface energies in the GST-Si system. Therein, the interfacial energies between Si and GST are estimated based on contact angle measurements and the surface energies for different low-index {hkl} planes are estimated based on the Wulff-Kaishev construction.

Chapter 7 continues with the experimental results of the solid-to-gas phase transition. Here, the terrace-step-kink model and its implications for the sublimation process are introduced. The main part then focuses on the sublimation of the cubic phase. The structural and chemical stability of the cubic phase is addressed first. Then, the anisotropic sublimation dynamic is investigated beginning with the determination of the formed sample morphology. Based on that, the kink and step dynamics leading to stable facets are analyzed. Finally, the sublimation of the trigonal phase is discussed and compared to the cubic phase.

The last chapter summarizes all results presented in this thesis and draws conclusions. In addition, an outlook on future research projects is given.

2 Thermodynamics and kinetics of phase transitions

For the description of phase transitions both thermodynamic and kinetic theories are used. Thermodynamics states that a process or reaction can occur spontaneously if the free enthalpy is thereby lowered. It describes therefore whether or not a phase transition can occur. On the other hand,thermodynamics does not predict "how" or "when" an allowed process indeed takes place, and is therefore sometimes called "the science of the impossible" [26]. To answer the questions about the "how" and "when", kinetic theories need to be applied. In this chapter, first the thermodynamics involved in phase transitions is introduced and then the kinetics of how the phase transitions occur is discussed.

2.1 Thermodynamics

In the following sections, fundamental aspects of thermodynamics of phase transitions relevant to this work will be presented as a short introduction. It starts with the representation of different phases in phase diagram which is described based on Ref. [27]. After that, the driving force for and classification of phase transitions are discussed based on Ref. [28].

2.1.1 Phase diagram

Matter can exist in different states such as solid, liquid or gas. In addition, there are different modifications of the same state, e.g. different crystal structures in the solid state. The phase (state and modification) that a material is in depends on the applied pressure (p), its temperature (T) and composition (c). The existence of a phase is represented by an area in the p-T-c space, also known as a phase diagram.

Considering a one component material, the p-T-c space reduces to a p-T diagram. Figure 2.1(a) shows an exemplary phase diagram of a one-component system with a solid, liquid and gas phase. The lines separating two different phases are called phase boundaries. On those lines, both phases are in equilibrium - meaning that the difference of their free energies (ΔG) is zero. The number of phases, P, in thermodynamic equilibrium with each other follows Gibbs phase rule [27]

$$f = n - P + 2 \tag{2.1}$$

where n is the number of components that the system consists of and f is the number of degrees of freedom of intensive variables like temperature or pressure. According to this rule, in a one-component system (n=1) there is only one temperature at a given pressure (p^*) where

- the solid and liquid phase coexist (P=2), known as the melting temperature (T_m^*),
- the solid and gas phase coexist, known as the sublimation temperature (T_{sub}^*) and

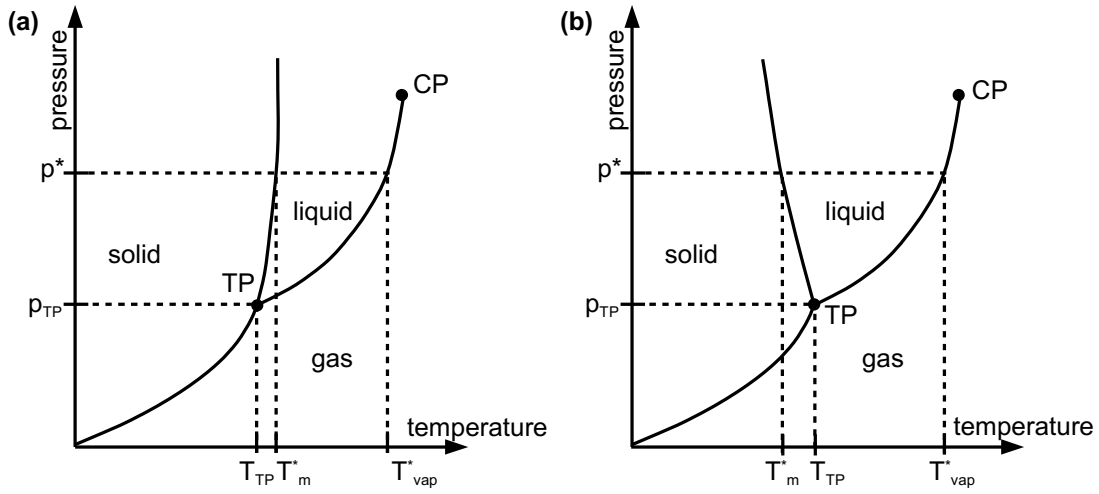

Figure 2.1 Exemplary phase diagrams (p-T-plot) of one-component systems for materials exhibiting a (a) positive (most materials) and (b) negative thermal expansion. At the triple point (TP), all three phases (solid, liquid and gas) coexist. Above the critical point (CP), the phase liquid-gas transition is no longer discontinuous. After Ref. [27].

- the liquid and gas phase coexist, known as the vaporization temperature (T^*_{vap})

In addition, there is only one point (pressure and temperature) where all three phases coexist, known as the triple point (TP).

In a multi-component system, there is an additional degree of freedom, namely the composition. In most experiments, the pressure is kept constant, and therefore the p-T-c space reduces to a c-T diagram for binary systems (n=2). Figure 2.2 displays the differences for the phase transition temperatures of a one-component and a two-component system at a given pressure. In a binary system, there is no defined melting temperature but a finite range where solid and liquid are in equilibrium. The temperature above which the system is completely liquid is called liquidus temperature and the temperature below which the system is completely solid is called the solidus temperature. Between those temperatures the system consists of a mixture of liquid and solid phases of different composition.

2.1.2 Phase transitions

Figure 2.3 summarizes the six possible phase transitions between solid, liquid and gas state. The transition from solid to liquid is called "melting" and the reverse process is known as "solidification" or more specific "crystallization" in case of crystalline materials. "Sublimation" is the transformation from solid to gas, and "deposition" from gas to solid. The transition from liquid to gas is called "vaporization", and the process from gas to liquid is known as "condensation". In this thesis, three of those phase transitions are investigated. Chapter 6 covers both transitions involving the solid and liquid phase and in chapter 7, the solid-to-gas transition is discussed.

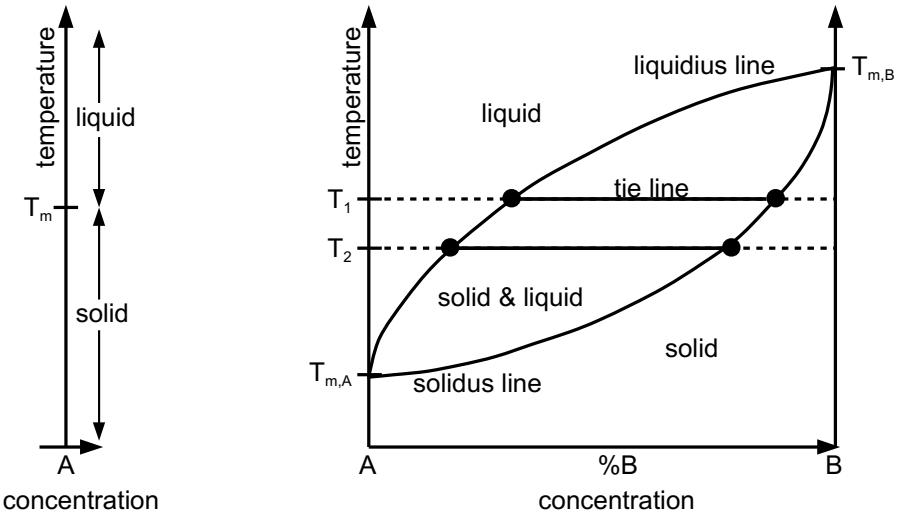

(a) one component system (A) **(b)** two component system (A&B)

Figure 2.2 Exemplary phase diagrams (c-T-plot) displaying the difference in solid-liquid transition temperatures at a given pressure for (a) one-component systems with only one melting temperature T_m and (b) two-component systems exhibiting a melting range limited by solidus and liquids lines. Both lines can either rise (shown) or fall (not shown) with increasing concentration. The tie line connects equilibrium concentrations, after Ref. [27].

Driving force

In equilibrium, a thermodynamic potential fully describes the macroscopic state of a system. The Gibbs free energy (eq. 2.2), $G(T, p, N)$, (also known as free enthalpy) with its total differential given by eq. (2.3) is the thermodynamic potential which is often used because of the accessibility of its natural variables in experiments (pressure, p, volume, V, and number of particles N).

$$G = U - TS + pV = H - TS \tag{2.2}$$

$$\mathrm{d}G = -S\mathrm{d}T + V\mathrm{d}p + \sum_{j=1}^{\alpha} \mu_j \mathrm{d}N_j \tag{2.3}$$

U is the internal energy, S the entropy, H the enthalpy, and μ the chemical potential of a system with α components.

The combination of the first and second law of thermodynamics states that a spontaneous transition in a closed system (dN=0) with a thermal reservoir (dT=0) and constant pressure (dp=0) can only happen, when the Gibbs free energy is thereby reduced [28]:

$$\Delta G < 0 \tag{2.4}$$

Therefore, in equilibrium the free Gibbs free energy is minimal.

Figure 2.4 shows a schematic illustration of the Gibbs free energy as a function of temperature for a solid and liquid phase. At T_m the solid and liquid phase are in thermodynamic

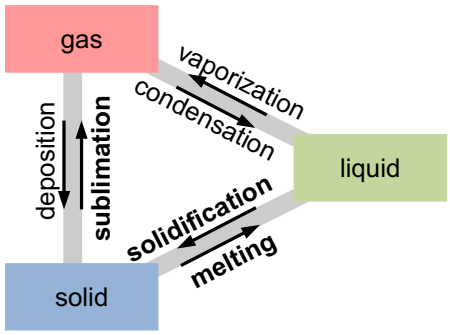

Figure 2.3 Overview of phase transitions between solid, liquid and gas. The transitions studied in this thesis are in bold.

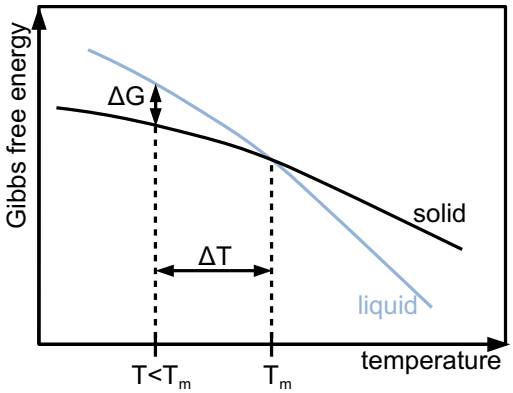

Figure 2.4 Schematic illustration of the Gibbs free energy as a function of temperature for a solid and liquid phase at a constant pressure. The Gibbs free energy is minimal in equilibrium. Therefore, at an undercooling of ΔT, the difference in Gibbs free energy between solid and liquid phase, ΔG, is the driving force for solidification.

equilibrium meaning that the Gibbs free energy of both phases is equal (ΔG=0). Below T_m, the solid phase has a smaller Gibbs free energy compared to the liquid phase and is therefore the thermodynamically stable phase. Above T_m, the liquid phase has a smaller Gibbs free energy and is there the stable phase. The difference in Gibbs free energy between both phases at a given temperature, ΔG, is then the thermodynamic driving force for either solidification or melting.

Clausius-Clapeyron relation

To assess the response of a material to a phase transitions with respect to the change in volume, the Clausius-Clapeyron relation can be derived. Using the Gibbs-Duhem relation (eq. 2.5) which states that the chemical potential can be interpreted as Gibbs free energy per particle [28],

$$G(T, p, N) = N\mu(T, p) \tag{2.5}$$

together with the total differential of the Gibbs free energy (eq. 2.3) leads to the Clausius-Clapeyron relation for closed systems (dN=0) along a phase boundary where (d$\mu_{\text{phase 1}}$ = d$\mu_{\text{phase 2}}$) [28]:

$$\frac{\mathrm{d}p}{\mathrm{d}T} = \frac{\Delta S}{\Delta V} \tag{2.6}$$

Therefore, the slope in the p-T diagram can be expressed as the ratio of the change in entropy (ΔS) and the change in volume (ΔV) during the phase transition. Most materials feature a positive p-T-slope ($\mathrm{d}p/\mathrm{d}T > 0$) along the solid-liquid phase boundary (cf. phase diagram in Fig. 2.1(a)). Taking into account that the entropy change is positive in the solid-to-liquid transition ($\Delta S > 0$) then leads to a volume increase upon melting ($\Delta V > 0$). In other words, most materials expand during melting and contract during solidification. Therefore, the density of the solid phase is larger than that of the liquid phase. Some materials on the other hand have a negative p-T slope ($\mathrm{d}p/\mathrm{d}T < 0$) for the phase transition between solid and liquid. That is true for example for silicon, germanium, antimony, tellurium [29] and most famously water. Now, the solid-to-liquid transition leads to a volume decrease upon melting ($\Delta V < 0$). Figure 2.1(b) shows a phase diagram of a one component system exhibiting such a negative thermal expansion. Kalkan *et al.* [30] found evidence implying that the material investigated in this thesis ($Ge_1Sb_2Te_4$) also has a negative p-T slope.

Classification of phase transitions

According to the Ehrenfest classification, for a phase transition of the n-th order the Gibbs free energy and its (n-1) derivatives are continuous and the n-th derivative exhibits a discontinuity [28]. Modern classification only differentiates between discontinuous and continuous phase transitions [28]. In a discontinuous phase transition, there is as discontinuity in the first derivatives of the Gibbs free energy:

$$S = -\left(\frac{\partial G}{\partial T}\right)_p \text{ and } V = -\left(\frac{\partial G}{\partial p}\right)_T \tag{2.7}$$

A discontinuous phase transition from phase 1 to 2 is therefore characterized by a latent heat of transformation due to the finite jump in entropy $\Delta S = S_2 - S_1$. The latent heat of transformation leads to the transition of phase 1 while leaving the temperature constant. The Clausius-Clapeyron relation (eq. 2.6) is only valid for a discontinuous phase transition, where the entropy and volume of the two phases along the phase boundary are different. All phase transitions between different states - as shown in Fig. 2.3 - are examples of discontinuous phase transitions. Continuous phase transitions exhibit continuity in the first derivatives of the Gibbs free energy and therefore there is no heat of transformation associated with it. The second order derivatives on the other hand are discontinuous during the transition. An example is the glass transition from a liquid phase to an amorphous phase where the change in volume and entropy is continuous as opposed to a jump in volume and entropy during the crystallization process [31]. The second order derivatives, in this case heat capacity and thermal expansion, do not change continuously classifying the glass transition as a continuous (or second-order) phase transformation.

2.2 Kinetics

Using thermodynamics, the driving force of a phase transformation is identified as the reduction of the Gibbs free energy. The next section is now dedicated to kinetics and addresses the question of "how fast" a phase transition occurs. First, the rate and mechanism of the liquid-to-solid transformation (crystallization) is described based on Ref. [32] and [33]. And then, sublimation is introduced following a description of a comprehensive review article [15].

2.2.1 Crystallization kinetics

The process of solidification from amorphous or liquid to the crystalline phase involves two steps: nucleation and crystal growth. First, crystallization is initiated by nucleation where crystalline clusters in the melt are formed by thermal fluctuations. In a second step and after reaching a critical size, the stable nucleus grows. A comprehensive review on crystal growth from melt including both theoretical and experimental aspects can be found in Ref. [32] and a more compact review in Ref. [33]. Here only a short summary based on both references is given, reproducing the main ideas.

Nucleation

In an initial liquid phase (melt), crystalline clusters (called nuclei) have to be formed. This process is called nucleation. It can happen either as pure intrinsic process within the melt phase itself, known as homogenous nucleation, or with the involvement of a foreign substance (e.g. impurities, substrate) lowering the surface energy, known as heterogeneous nucleation.

The formation of crystalline nuclei is due to thermal fluctuations in the melt. As a first approximation, the homogenous nucleation can be described as the formation of a spherical nucleus with the radius, r, within the melt matrix. Based on ideas of Gibbs, the required energy for the formation involves two major contributions:

$$\Delta G^{\text{homo}}_{\text{nucleus}}(r) = \underbrace{4\pi r^2 \sigma_{\text{sm-interface}}}_{\text{surface term}} - \underbrace{\frac{4}{3}\pi r^3 \Delta G_{\text{ms,V}}}_{\text{volume term}} \tag{2.8}$$

The first term is associated with the energy required for the formation of an interface between the crystalline nuclei and the melt matrix and is proportional to surface area and surface energy of the solid-melt interface, $\sigma_{\text{sm-interface}}$. The second term is the energy gained by reducing the Gibbs free energy of the system during the transformation from liquid to solid. The total energy gain is proportional to the transformed volume and difference in Gibbs free energy between melt and solid phase per volume unit, $\Delta G_{\text{ms,V}}$.

In order to develop stable nuclei, the formation process needs to be energetically favorable (minimizing $\Delta G_{\text{nucleus}}$). Therefore, the Gibbs free energy of the solid phase must be lower than that of the liquid phase. In other words, the temperature needs to be below the melting temperature, T_m, in order to transform the liquid into the solid phase. Because the volume term in eq. (2.8) increases faster with increasing r compared to the surface term, the growth of a nucleus is energetically more favorable than its decay after reaching a critical radius,

r_{critical}, found at the maximum of $\Delta G_{\text{nucleus}}$:

$$\frac{\partial \Delta G_{\text{nucleus}}(r)}{\partial r} = 0$$

$$\Longrightarrow r_{\text{crit}}^{\text{homo}} = \frac{2\sigma_{\text{interface}}}{\Delta G_{\text{ls,V}}} \tag{2.9}$$

$$\Longrightarrow \Delta G_{\text{crit}}^{\text{homo}} = \Delta G_{\text{nucleus}}^{\text{homo}}\left(r_{\text{crit}}^{\text{homo}}\right) = \frac{16}{3}\pi \frac{\sigma_{\text{interface}}^3}{\Delta G_{\text{ms,V}}^2} \tag{2.10}$$

The energy required to form a critical nucleus, $\Delta G_{\text{crit}}^{\text{homo}}$, is then given by eq. (2.10) and called the activation barrier for nucleation.

The model for homogenous nucleation can be extended to include the presence of a flat substrate acting as a heterogeneous nucleation site and is based on the ideas of Volmer and Weber ([33] and references therein). The substrate thereby reduces the energy required to form a critical nucleus by a factor $f(\theta)$ through lowering the surface area:

$$\Delta G_{\text{crit}}^{\text{hetero}} = f(\theta)\Delta G_{\text{crit}}^{\text{homo}} \tag{2.11}$$

The activation barrier for heterogeneous nucleation is reduced as long as the difference in interface energy between solid-substrate and melt-substrate is smaller than the interface energy of solid-melt. Its reduction depends therefore on the wetting angle, θ, between substrate and solid cluster.

Based on ideas of Volmer, Weber, Becker, Döring, Turnbull and Fischer ([33] and ref. therein), nucleation is assumed to occur by addition of one more atom to a critical nucleus. The nucleation rate depends therefore on the arrival rate, k, of the melt phase atoms to the nucleus. The arrival rate in a melt phase can be either "diffusion-limited" or "collision-limited". The first refers to local rearrangement across the liquid-solid interface by diffusive jumps (not to long-range diffusion due to different compositions) and depends therefore on the diffusivity of atoms in the melt parent phase. The later refers to atomic movements due to thermal vibrations and is dominated by collisions of atoms. Taking also into account that a critical nucleus has the same probability for growth as for decay, the nucleation rate needs to be modified by the Zeldovic factor, Γ_z. Finally, the rate of nucleation for diffusion-limited crystallization is given by eq. (2.12) [33]:

$$I_{\text{nucleation}} = \epsilon \cdot s_{cr} \cdot \underbrace{\frac{6D}{\lambda^2}}_{k} \cdot N_0 \cdot \underbrace{\frac{1}{i_{cr}} \cdot \left(\frac{\Delta G_{\text{crit}}}{3\pi k_B T}\right)^{\frac{1}{2}}}_{\Gamma_z} \cdot \exp\left(-\frac{\Delta G_{\text{crit}}}{k_B T}\right) \tag{2.12}$$

where ϵ is the number of atoms which are in contact with the substrate during heterogeneous nucleation. It is equal to one for homogenous nucleation because then all atoms in the melt can act as nucleation sites. D is the diffusivity, λ the mean distance between atoms and N_0 is number of atoms per volume unit in the melt phase. s_{cr} is the number of surface atoms and i_c the total number of atoms in the critical nucleus. Analyzing the temperature dependence of eq. (2.12) leads to:

- For $T = T_m$: $I_{\text{nucleation}} \to 0$ because $\Delta G_{\text{crit}} \to \infty$ since $\Delta G_{ms,V}(T_m) = 0$ (cf.

eq. (2.10))

- For $T = T_g$: $I_{\text{nucleation}} \to 0$. T_g is the glass transition temperature marking the transition from an undercooled liquid to a glassy state, therefore at $T = T_g$ the diffusivity is so small that the nucleation rate is also negligible small

Taking both aspects together the nucleation rate must exhibit a maximum value between the glass transition temperature, T_g, and the melting temperature, T_m.

Crystal growth

After the crystalline nucleus reaches a critical size and becomes stable, it grows. The rate of crystal growth is either controlled by long-range diffusion in the melt or processes at the crystal-melt interface, in which case it is called interface-controlled.

If the growth is controlled by long-range diffusion, the growth velocity is time-dependent and can be expressed as equation (2.13) [32]

$$u_{\text{diffusion-controlled}} = k \left(\frac{D}{t} \right)^{1/2} \tag{2.13}$$

where k is a constant involving concentration terms, D is the diffusion constant in the melt and t is time. This time-dependent growth velocity occurs in alloys where the composition of melt and crystal are not the same and a depletion around the growing crystal develops. The continual growth then requires diffusion of the required component into this depleted region leading to diffusion-controlled growth and a time-dependent growth velocity.

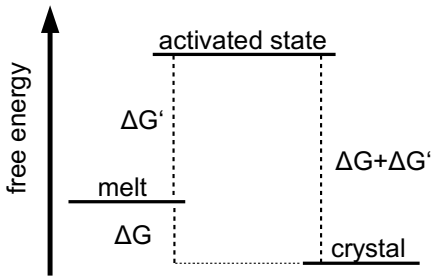

Figure 2.5 Free energy of states involved in the attachment and detachment processes at crystal-melt interface at temperature $T < T_m$, after [32].

When crystal and melt have the same composition, the growth is controlled by rearrangement processes at the crystal-melt interface. The growth rate then does not depend on the position of the interface and is time-independent. Figure 2.5 illustrates the energy states of atoms associated with the rearrangement processes: For temperatures below T_m, the crystalline state has a lower free energy than the melt state. The thermodynamic driving force for crystal growth is then given by the energy difference between both states (ΔG). For the attachment to the crystal surface, the atom in the melt needs to pass through an intermediate, activated state into the crystalline state and thereby needs to overcome an activation energy barrier ($\Delta G'$). The crystal growth velocity for interface-controlled growth is then given by the difference between attachment and detachment processes multiplied by the average

interatomic distance λ. If the rearrangement processes at the interface are limited by diffusive motion rather than thermal vibration, the growth is called diffusion-limited instead of collision-limited. Using rate equations with the associated energy differences for attachment and detachment processes the growth velocity is then given by equation (2.14) [33]

$$u_{\text{interface-controlled}} = \frac{f_s 6D}{\lambda}\left[1 - \exp\left(-\frac{\Delta G_{\text{ms}}}{k_b T}\right)\right] \tag{2.14}$$

where f_s is the fraction of sites where a new atom can be incorporated ($0 \leq f_s \leq 1$) and D is the diffusion constant. ΔG_{ms} is the difference in Gibbs free energy between melt and crystalline phase per atom. Looking at the temperature dependent behavior of the interface-controlled growth yields:

- At $T = T_m$ the difference in Gibbs free energy between melt and crystal is zero, $\Delta G_{\text{ms}} = 0$, and therefore the growth rate is zero: $u(T_m) = 0$
- For $T = T_g$: the diffusivity is so small that the growth rate is also negligibly small

Taking both aspects together the growth velocity must exhibit a maximum value between the glass transition temperature T_g and the melting temperature T_m.

In macroscopic studies, in order to determine the mechanism of the interface-controlled growth and therefore study in which manner atoms attach to the crystal, the reduced growth rate is used [32]:

$$u_{\text{reduced}} = \frac{u_{\text{interface-controlled}}}{[1 - \exp(-\Delta G_{\text{ms}}/k_b T)]} = \frac{f_s 6D}{\lambda} \tag{2.15}$$

When the atoms can attach at any site, the growth is called continuous growth and f_s is temperature independent and large. The reduced growth rate is therefore independent of the applied undercooling. When atoms attach primarily at specific sites (such as surface steps) the growth is called lateral growth. Then, the growth rate depends on the nucleation of such specific sites which is temperature dependent and the reduced growth rate increases with undercooling.

2.2.2 Sublimation kinetics

According to Somorjai [15, 34] sublimation studies can be divided in equilibrium investigations where thermodynamic data such as vapor pressure, enthalpy and Gibbs free energy are sought and non-equilibrium studies revealing more information about reaction paths and the mechanism of sublimation. Considering the sublimation and condensation process of a monoatomic solid A

$$\text{A(solid)} \underset{k'}{\overset{k}{\rightleftharpoons}} \text{A(vapor)}$$

the net rate of sublimation J can be expressed as

$$J = kA_s - k'A_v \tag{2.16}$$

where k and k' are the rate constants for sublimation and condensation, A_s is the concentration of atoms in surface sites from which sublimation proceeds and A_v is the vapor density. From equilibrium conditions where the net rate is zero, the maximal theoretical rate of

sublimation from a surface, J_{max}, at a given temperature can be found and is equal to the impingement flux of vapor atoms on the surface per unit time:

$$J_{max} = \frac{p_{eq}}{\sqrt{2\pi m k_b T}} \tag{2.17}$$

This relation is known as the Hertz-Knudsen equation. The vacuum sublimation rate, where $k' A_v = 0$, may have any value $J \leq J_{max}$ and depends on the sublimation mechanism. The deviation from the maximal rate is expressed as the sublimation coefficient $\alpha(T)$ (often also called vaporization or evaporation coefficient):

$$\alpha(T) = \frac{J_{sub}(T)}{J_{max}(T)} \tag{2.18}$$

Equation 2.17 describes the sublimation when all atoms are available for desorption and are all bound by the same amount of energy, the energy of sublimation ΔE_{sub}. As discussed by Somorjai [15], a deviation from those conditions and therefore information about the sublimation mechanism is hidden away in the sublimation coefficient $\alpha(T)$. Deviations could arise from heterogeneous surfaces with nonequivalent sites or when the atoms undergo rearrangement processes (association or dissociation) upon sublimation. In macroscopic studies, complementary experiments such as measuring the sublimation rate dependence on surface concentration of subliming species, on impurities or on illumination are useful to study sublimation mechanism at a macroscopic scale.

The atomistic processes which are discussed in literature to be involved in sublimation are described in chapter 7.1.

3 Transmission electron microscopy

Transmission electron microscopy (TEM) is a powerful and versatile technique for the investigation of materials. It combines highest spatial resolution and structural as well as compositional information about the specimen. In this thesis, TEM is therefore the main experimental technique to investigate the microstructure and its dynamical changes during high temperature phase transitions.

This chapter is dedicated to the working principle of this technique and its application. In section 3.1, it is discussed why electrons are used for imaging and how a transmission electron microscope (TEM) is set-up. Section 3.2 summarizes the imaging formation principles based on electron diffraction theory and mentions several imaging modes used in this thesis. Finally, section 3.3 gives a brief overview of quantitative electron energy-loss spectroscopy (EELS) analysis starting with the introduction into the fundamentals such as the origin of the inelastic scattering, the experimental set-up and its implementation. At the end, the methodology for quantification is explained and its application to GeSbTe alloys discussed.

3.1 Transmission electron microscope

3.1.1 Using electrons

According to the Rayleigh criterion [35] the wavelength, λ, of the radiation used to magnify a specimen limits the resolution which can be achieved and the smallest distance that can be resolved is inverse proportional to the source wavelength. Therefore, in order to study phenomena on the atomic scale, a small source wavelength is needed. According to de Broglie's relation, the wavelength of an electron is related to its momentum:

$$\lambda = \frac{h}{p} = \frac{h}{mv} = \frac{h}{\sqrt{2m_0E(1+E/2E_0)}} = \frac{h}{\sqrt{2m_0eU(1+eU/2m_0c^2)}} \tag{3.1}$$

where h is the Planck constant, p, m, v, $E = eU$ and E_0 are the momentum, mass, velocity, kinetic energy and rest energy of the electron, U is the accelerating voltage and e is the elementary charge. Because the velocity of the electron at accelerating voltages typically used in the TEM ($U \geq$100 kV) is above 50% of the speed of light, relativistic effects had to be taken into account. As can be seen from eq. (3.1), with increasing accelerating voltages the wavelength of the electrons decreases, e.g. for the accelerating voltages of 200 kV and 300 kV used in this work, the electron wavelength is 2.51 pm and 1.97 pm, respectively. According to the Rayleigh criterion, the resolution limit of a TEM should therefore be in the picometer regime. However, the resolution in the TEM is typically not limited by the wavelength of the electrons but by lens aberrations.

In addition to the high spatial resolution that can be reached, the imaging with electrons

also allows the analysis of additional information such as chemical composition due to several electron-specimen interaction processes which are briefly discussed in section 3.2.

3.1.2 Microscope set-up

Figure 3.1 shows a schematic illustration of a TEM set-up. The microscope essentially consists of four parts: An electron gun where the electrons used for imaging are produced and accelerated and three electromagnetic lens systems; the condenser lens system to illuminate the sample, the objective lens system where the sample is located and the electron-sample interaction occurs and the image observation system which magnifies the image onto a screen or other detection devices. In the following, all parts of the microscope will be briefly discussed based on the established textbooks [35, 36] where a more detailed description can be found.

Electron gun. There are basically two different types of electron guns: electron sources based on thermionic emission and those based on field emission. For this work two different microscopes are used: In the JEOL 3010 thermal emission is used whereas in the JEOL 2100F field emission is exploited to generate electrons. Thermionic emission is the extraction of electrons from a source material using heat to overcome the work function (ϕ) of electrons in this material. Typically, a LaB_6 crystal is used because of its low work function which requires heating to only 1700 K. Older sources used tungsten which has a high melting point and can therefore withstand the required temperatures for thermionic emission. Field emission is the extraction of electrons using a high electric field. The electric field is used to lower the work function barrier to allow electrons to tunnel out of the source material. Typically, fine tungsten needles are used because the strength of an electric field is increased at sharp points. Compared to the thermionic sources field emission guns produce a higher current density and a more coherent electron beam. In the JEOL 2100F, thermal field emission is used. There, the electron emission is assisted by applying thermal energy and therefore less strict vacuum conditions are necessary than for cold FEG (field emission guns) where a pristine surface is needed. Those sources are also called Schottky FEG. After the generation of electrons either through thermionic or field emission, the electrons are accelerated to velocities around 70% of the speed of light using high accelerating voltage (200 kV at the 2100F and 300 kV at the 3010).

Condenser lens system. The lenses that the electron beam passes prior to the specimen are called the condenser lens system and are used to form the electron beam. Essentially, it can be switched between two illumination modes by changing the focal length of the condenser lenses: Either the specimen is illuminated by a convergent or a parallel electron beam.

Objective lens system. The most important lens system in the TEM is the objective lens system. It focuses the diffracted beam after the sample forming various images. Thereby, a direct, magnified image is formed in the first image plane of the objective lens. Here, an aperture (called selected area diffraction (SAD) aperture) can be inserted in the optical path

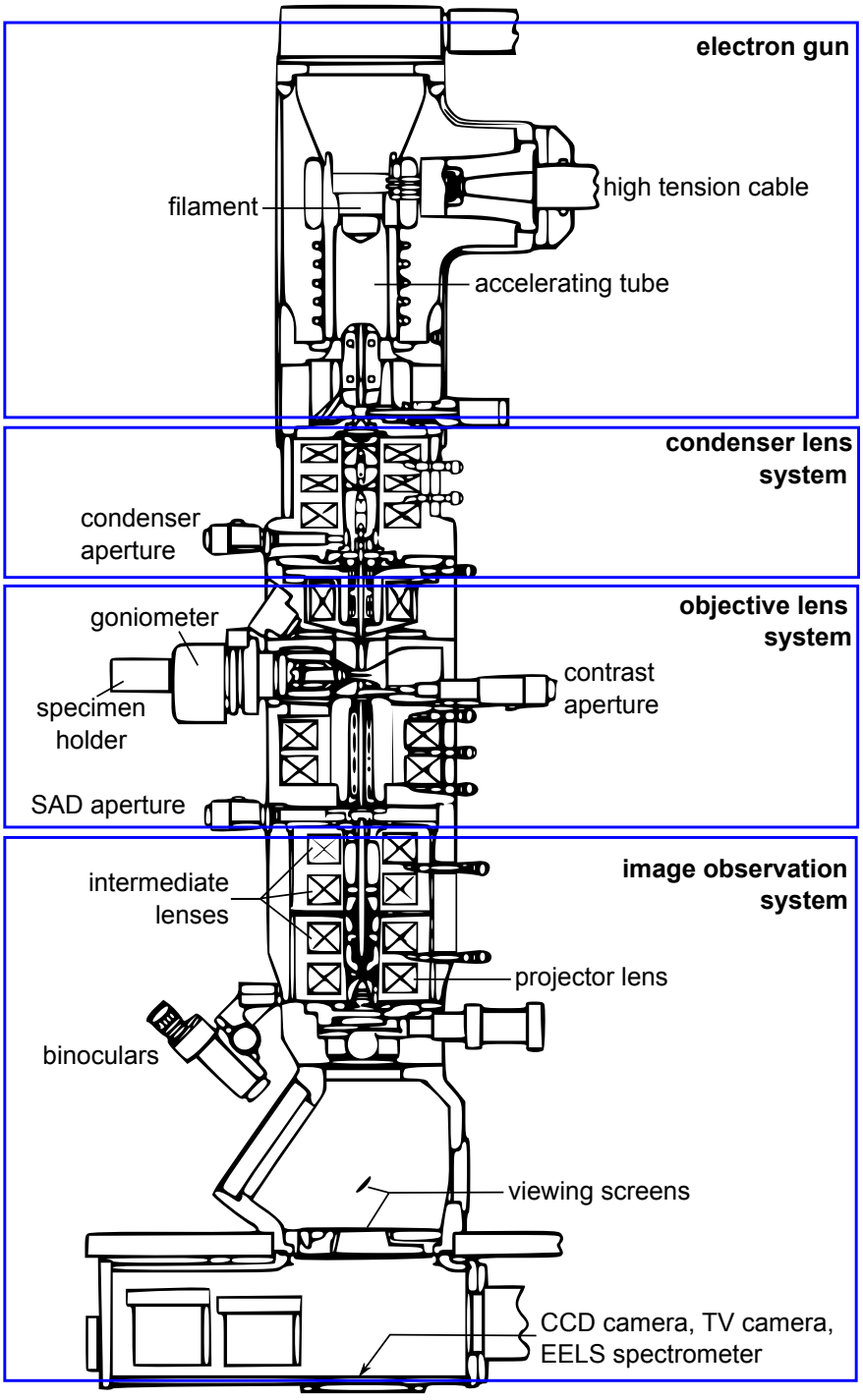

Figure 3.1 Schematic illustration of transmission electron microscope set-up.

to only let electrons from a certain sample region travel further and be analyzed. In the back focal plane the diffraction pattern is formed. Here, an aperture (called contrast aperture) can be inserted for selecting individual diffracted beams to form an image.

Image observation system. The next lens system which includes the projection and intermediate lens is used to further magnify the image formed by the objective lens. Together with a viewing screen or another detection device such as CCD camera they form the image observation system allowing to see and record the formed images. Particularly, changing the focal length of the intermediate lens is used to switch between direct and reciprocal space to view the diffraction pattern (diffraction mode) or the direct image (image mode) of the sample.

3.2 Image formation

When an electron travels through the specimen several interactions either by Coulomb force or energy excitation processes can take place. These interactions give rise to various signals which can be used to gain information about the sample. Figure 3.2 shows a schematic illustration of the various signals that arise in TEM. The interactions can be categorized into elastic and inelastic scattering as well as coherent and incoherent scattering. When the energy of the scattered electron is the same as the incident electron, the interaction is called elastic while a decrease in electron energy through an excitation process is called inelastic scattering. If the phase relationship between electrons is preserved after the scattering process, it is called coherent scattering whereas the loss of a phase relationship is called incoherent scattering. In TEM one can choose which electrons contribute to an image and therefore the information it contains. Elastically, coherently scattered electrons are used in diffraction pattern, bright- and dark-field microscopy as well as high-resolution (HR)TEM to study the structure of the specimen. Inelastically, incoherently scattered electrons are used for EELS to study the chemical composition of a specimen. Additionally, a whole range of signals arise from inelastic scattering due to the return of excited electrons in the specimen to the ground state such as characteristic X-rays (used in energy dispersive X-Ray spectroscopy (EDXS)), secondary electrons and cathodoluminescence.

3.2.1 Electron diffraction

The image formation in TEM can be explained on the basis of the theory of electron diffraction. In the following, a summary of the theory is given based on Ref. [35, 36].

For thin specimens and small scattering angles, scattering is approximated to involve single elastic scattering events (called the kinematical approximation). According to Huygens' principle, the scattering of an incident parallel wave front can be described as the sum of spherical waves from each scattering center. Interference between those spherical waves leads to an intensity modulation visible as the diffraction pattern of a crystalline structure. Using the Bragg condition (eq. (3.2)) or the equivalent Laue condition (eq. (3.3)) the position of diffraction spots in a diffraction pattern can be explained. (The deviation of the Bragg condition based on scattering geometry is shown in A.7.)

$$n\lambda = 2d_{hkl}sin\theta_B \tag{3.2}$$

$$\boldsymbol{g} = \Delta\boldsymbol{k} = \boldsymbol{k}_{\text{diff}} - \boldsymbol{k}_{\text{in}} \tag{3.3}$$

where λ is the wavelength of the electron wave ($|\boldsymbol{k}| = \frac{1}{\lambda}$), d_{hkl} is the distance between a

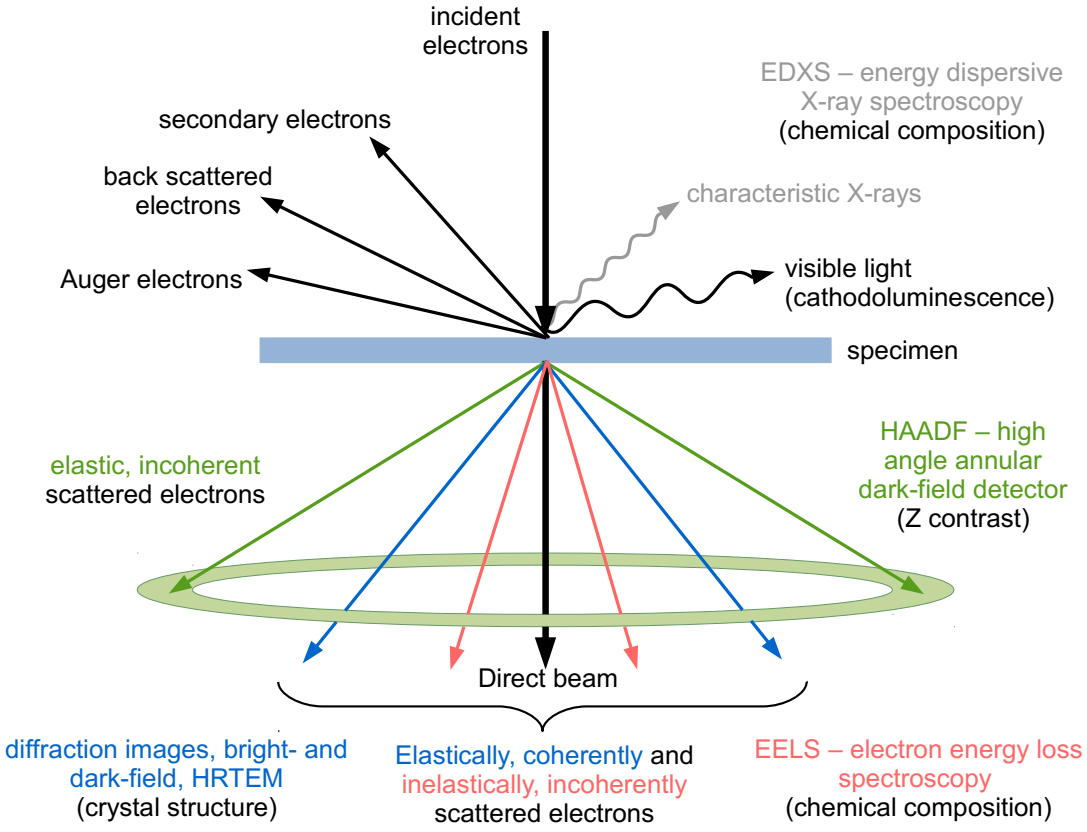

Figure 3.2 Schematic illustration of various signals that arise from the interactions between electrons and specimen, based on illustrations in Ref. [35].

set of lattice planes (hkl) and θ_B is the Bragg scattering angle. Thus, when the difference between the incident electron wave with wave vector $\boldsymbol{k}_{\text{in}}$ and diffracted wave with $\boldsymbol{k}_{\text{diff}}$ is equal to a reciprocal lattice vector, $\boldsymbol{g}$ (where $|\boldsymbol{g}| \equiv \frac{n}{d_{hkl}}$), there is constructive interference which leads to the formation of a diffraction spot. Therefore, each diffraction spot in a diffraction pattern corresponds to a set of parallel atomic planes.

The Bragg condition can be geometrical illustrated with the Ewald sphere construction. A two dimensional representation is shown in Fig. 3.3(a). The radius of the Ewald sphere is given by $|\boldsymbol{k}| = \frac{1}{\lambda}$. Since elastic scattering is considered, the incoming and outgoing wave have the same wavelength and therefore both incident and diffracted beam (all $\Delta\boldsymbol{k}$) end on the Ewald sphere. Whenever the Ewald sphere then intersects with a reciprocal lattice point the Bragg condition is fulfilled.

For the calculation of the amplitude of the diffracted electron wave in a given direction, three contributions need to be considered: First, the scattering from an individual atom. Secondly, the interaction of all scattered waves from each atom within a single unit cell and thirdly, the position of all unit cells within a crystalline structure. Taking all things together

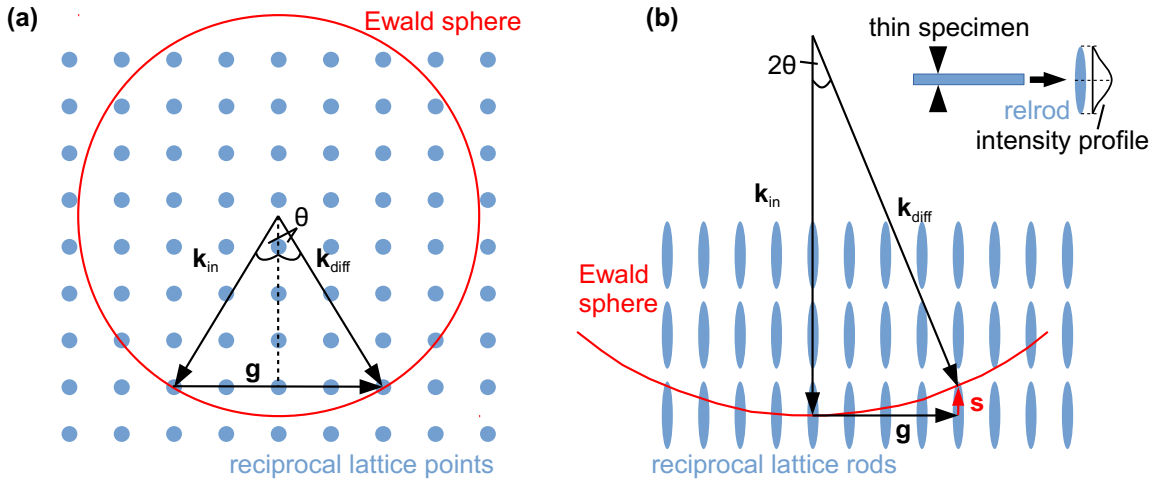

Figure 3.3 (a) Two-dimensional illustration of the Ewald sphere construction in reciprocal space for a bulk crystalline sample when the Bragg condition is exactly fulfilled. (b) Influence of crystal shape as formation of relrods due to thin TEM specimen. The Bragg condition is fulfilled with a non-zero excitation error, $\boldsymbol{s}$; based on illustrations in Ref. [35].

leads to eq. (3.4):

$$\Psi(\Delta\boldsymbol{k}) = \underbrace{\sum_{i=1}^{n} f_i(\Delta\boldsymbol{k}) e^{-2\pi \mathrm{i} \boldsymbol{r}_i \Delta\boldsymbol{k}}}_{F_{hkl}(\Delta\boldsymbol{k})} \underbrace{\sum_{j=1}^{N} e^{-2\pi \mathrm{i} \boldsymbol{r}_j \Delta\boldsymbol{k}}}_{G(\Delta\boldsymbol{k})} \tag{3.4}$$

The first term, $F_{hkl}(\Delta\boldsymbol{k})$, is called the structure factor and is the amplitude of the electron wave scattered from one unit cell in $\Delta\boldsymbol{k}$ direction. It depends on the atomic scattering amplitude, $f(\Delta\boldsymbol{k})_i$, of each atom in the unit cell and the atom positions, $\boldsymbol{r}_i$, within the unit cell. The second term in eq. (3.4), $G(\Delta\boldsymbol{k})$, is called the shape factor and takes into account the influence of the crystal shape. It depends on the location of each unit cell, $\boldsymbol{r}_j$.

The influence of the crystal structure on the diffraction pattern is given by the structure factor, $F_{hkl}(\Delta\boldsymbol{k})$. In the Bragg condition, the difference in wave vector is equal to a reciprocal lattice vector, $\Delta\boldsymbol{k} = \boldsymbol{g} = h\boldsymbol{g}_x + k\boldsymbol{g}_y + l\boldsymbol{g}_z$. For each crystal structure selection rules for diffraction spots from lattice planes, (hkl), can be derived. For example, the Si(200)-reflection produces $F = 0$ and is therefore not visible in the diffraction pattern and called kinematically forbidden.

Considering a TEM sample with a rectangular unit cell having sides a, b and c and N_x, N_y and N_z unit cells in x-, y- and z-direction respectively, the intensity of the scattered electron wave is then given by [35]

$$I = |\Psi|^2 = |F_{hkl}(\Delta\boldsymbol{k})|^2 \frac{\sin^2(\pi N_x \Delta k_x a)}{\sin^2(\pi \Delta k_x a)} \frac{\sin^2(\pi N_y \Delta k_y b)}{\sin^2(\pi \Delta k_y b)} \frac{\sin^2(\pi N_z \Delta k_z c)}{\sin^2(\pi \Delta k_z c)} \tag{3.5}$$

According to eq. (3.5), a thin specimen dimension parallel to the electron beam (small N in

that direction) leads to the formation of reciprocal lattice rods (relrods) rather than reciprocal lattice points. This extension of the reciprocal lattice points in one direction results in the fact that the Bragg condition does not need to be exactly fulfilled in order to lead to diffraction spots in the diffraction pattern. In this case, $\Delta\boldsymbol{k}$ can be expressed as $\Delta\boldsymbol{k} = \boldsymbol{g} + \boldsymbol{s}$ where $\boldsymbol{s}$ is called the excitation error. It is a measure how far away the intersection takes place from the exact Bragg conditions.

In a typical TEM diffraction pattern there are many diffraction spots visible at the same time. The Ewald construction helps to understand why in TEM so many diffraction spots are visible compared to e.g. a typical X-Ray diffraction experiment: First, the wavelength of high energy electrons used in TEM is much smaller than X-Ray radiation ($\lambda_{e^-} \cong 0.002$ nm $\ll$ $\lambda_{\text{X-ray}} \cong 0.1$ nm). The small electron wavelength translates into a radius of the Ewald sphere ($r_{\text{Ewald}} = \frac{1}{\lambda} \cong 500\,\text{nm}^{-1}$) that is much larger than the reciprocal lattice vectors ($g = \frac{1}{d} \cong 3\,\text{nm}^{-1}$). Therefore, the Ewald sphere curvature is small which facilitates the intersection between Ewald sphere and reciprocal lattice vectors and thus, fulfilling the Laue condition for many diffraction spots. And secondly, the formation of relrods due to the thin specimen dimension parallel to the electron beam required for TEM leads to the fact that the Ewald sphere does not have to intersect at an exact point and still fulfills the Bragg condition (cf. illustration in Fig. 3.3(b)).

3.2.2 Imaging modes

Figure 3.4 illustrates the imaging conditions for the various TEM imaging modes used in this thesis: selected area diffraction (SAD), bright-field, dark-field and high-resolution (HR)TEM imaging. All imaging modes are briefly discussed based on Ref. [35, 37].

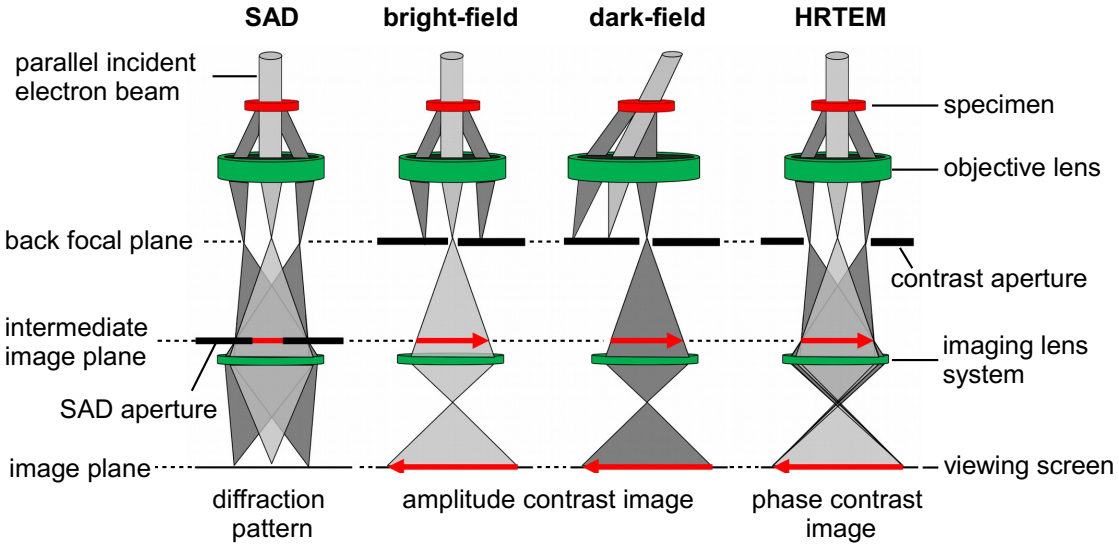

Figure 3.4 Schematic illustration of various TEM imaging modes: SAD diffraction, bright-field, dark-field and HRTEM; based on illustrations in Ref. [35].

Selected area diffraction

Selected-area electron diffraction (SAD) is a method used for investigating the reciprocal space and therefore provides information about the crystal structure of the specimen. The sample is illuminated by a parallel electron beam and a SAD aperture is inserted in the TEM image mode (cf. TEM images in Fig. 3.5) to select only those electrons from a certain sample area to contribute to the diffraction pattern. To display the diffraction pattern on the viewing screen, the intermediate lens is adjusted to display the back-focal plane of the objective lens (cf. schematics in Fig. 3.4).

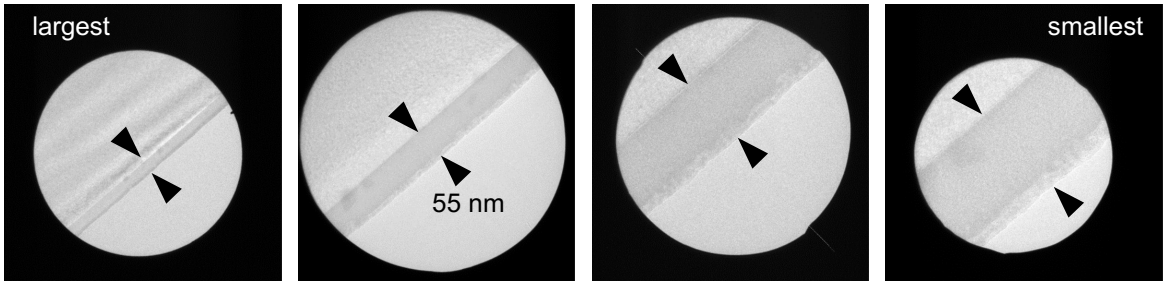

Figure 3.5 TEM image of an as-deposited GST thin film on a silicon substrate with inserted SAD apertures 1 to 4 in the JEOL 3010.

In the JEOL 3010 four different SAD apertures are available. They are all shown in the TEM images in Fig. 3.5 where the as-deposited amorphous GST thin film of known film thickness can be used as a reference to measure the size of all apertures. Table 3.1 summarizes the measured sizes of all four SAD apertures on the JEOL 3010 and 2100F.

Table 3.1 Summary of SAD aperture sizes in the JEOL 3010 and JEOL 2100F.

	aperture 1	aperture 2	aperture 3	aperture 4
JEOL 3010	910 nm	435 nm	195 nm	110 nm
JEOL 2100F	1040 nm	510 nm	235 nm	120 nm

For the measurements in this study, the smallest available aperture was used, which has a size of about 110 nm. The SAD pattern therefore contains information about the GST thin film (55 nm thick) and part of the substrate. Using the distance r_{hkl} between the diffraction spot and the center of the SAD pattern, the distance d_{hkl} between two parallel crystal planes {hkl} of the GST film are calculated by

$$d_{\mathrm{hkl}} = \frac{\lambda L}{r_{\mathrm{hkl}}} \tag{3.6}$$

where L is the camera length. The product λL is known as the camera constant and can be calibrated using known distances as a reference, e.g. the diffraction spots from the silicon substrate.

Bright- and dark-field image

Bright-field (BF) and dark-field (DF) TEM are complimentary techniques that are especially sensitive to deviations from the ideal crystal structure and are often used for defect analysis. As shown in Fig. 3.4 different parts of the diffraction pattern are chosen to contribute to the image formation using the contrast aperture located in the back focal plane of the objective lens. When only the direct beam is selected, the formed image is called a BF image whereas the selection of a diffracted beam leads to a DF image. Because there is only one beam selected for the imaging formation, there is no interference between different beams and therefore only amplitude contrast is observed. The amplitude contrast is caused by local changes in the diffraction conditions as well as in mass-thickness. Depending on the specific selected diffracted beam, certain features such as different defects types and even chemical information, can be made visible.

In this thesis, the technique is mainly used to differentiate between amorphous and crystalline parts of the sample during the investigation of phase transitions (e.g. crystallization and melting process). Due to different diffraction conditions, crystalline grains appear brighter or darker than the amorphous matrix in bright-field images. In addition, certain orientations of crystalline grains in polycrystalline films can be selected using DF-TEM, making it easier to observe the dynamics of a grain-boundary motion.

High-resolution TEM

High-resolution TEM (HRTEM) is a method used to image the crystal structure on an atomic scale. The schematic of the beam path for HRTEM in Fig. 3.4 illustrates that the inserted contrast aperture lets the direct beam and several diffracted beams pass. Those beams are superimposed resulting in an interference pattern on the viewing screen. The resulting image contrast is then called phase contrast and contains structural information about the specimen. Here, the HRTEM image formation process is briefly described based on Ref. [37].

In a thin sample, the modification of an incident electron wave done by the specimen can be approximated to only change the phase and leave the amplitude constant (thereby neglecting absorption effects). The specimen is thereby treated as a phase object and hence, the approximation is called a phase-object approximation resulting in the exit wave function

$$\Psi_{exit}(x,y) = \exp(\mathrm{i}\sigma V_p(x,y)) \tag{3.7}$$

with σ being the interaction constant and $V_p(x,y)$ the potential of the specimen projected in the direction the electron travel. A further approximation can be done for very thin specimens where the phase change is small. With this so called weak phase-object approximation eq. (3.7) can be written as

$$\Psi_{exit}(x,y) = 1 - \mathrm{i}\sigma V_p(x,y) \tag{3.8}$$

where only the linear term in the Taylor series is kept and higher order terms are neglected. A Fourier transformation of eq. (3.8) gives the scattered wave in the back focal plane of the objective lens.

$$\Psi_{\text{back-focal}}(\boldsymbol{k}_x, \boldsymbol{k}_y) = \Im\left\{1 - \mathrm{i}\sigma V_p(x,y)\right\} \tag{3.9}$$

After the modulation of the electron wave by the specimen, the electrons propagate further down through the microscope before the signal is visible on the viewing screen. Thereby, the electron wave is further modified by the microscope resulting in

$$\Psi'_{\text{back-focal}}(\boldsymbol{k}_x, \boldsymbol{k}_y) = \Im\left\{1 - \mathrm{i}\sigma V_p(x,y)\right\} A(\boldsymbol{k}_x, \boldsymbol{k}_y) \exp\left[i\chi(\boldsymbol{k}_x, \boldsymbol{k}_y)\right] \tag{3.10}$$

Thereby, $A(\boldsymbol{k})$ is the aperture function taking into account that an aperture lets all spatial frequencies, $\boldsymbol{k}$, smaller than a selected value pass and cuts off all $\boldsymbol{k}$ greater than the selected value. The additional phase shift of the objective lens can be expressed as the phase distortion function $\chi(\boldsymbol{k})$.

The wave function at the viewing screen is then given by the inverse Fourier transformation of eq. (3.10):

$$\Psi_{\text{screen}}(x,y) = \left\{1 - \mathrm{i}\sigma V_p(x,y)\right\} \otimes \Im^{-1}\left\{A(\boldsymbol{k}_x, \boldsymbol{k}_y) \exp\left[i\chi(\boldsymbol{k}_x, \boldsymbol{k}_y)\right]\right\} \tag{3.11}$$

Finally, the observable quantity at the viewing screen is the intensity distribution which is given by

$$\begin{aligned} I(x,y) &= \left|\Psi_{\text{screen}}(x,y)\right|^2 \\ &\approx 1 + 2\sigma V_p(x,y) \otimes \Im^{-1}\left\{A(\boldsymbol{k}_x, \boldsymbol{k}_y) \sin\left[\chi(\boldsymbol{k}_x, \boldsymbol{k}_y)\right]\right\} \end{aligned} \tag{3.12}$$

Therefore, the image contrast observed in HRTEM is proportional to the projected potential of the specimen (convoluted with the response function caused by the microscope).

When higher order aberrations are neglected, the additional phase shift caused by the objective lens is due to defocus, Δf, and spherical aberration, C_s:

$$\sin\left\{\chi(\boldsymbol{k})\right\} = \sin\left\{\pi\Delta f\lambda\left|\boldsymbol{k}\right|^2 + \frac{1}{2}\pi C_s\lambda^3\left|\boldsymbol{k}\right|^4\right\} \tag{3.13}$$

Thereby, spherical aberration is the focus spread caused by the lens field behaving differently for off-axis electrons (electrons further away from the optical axis are deflected stronger by the magnetic field of the lens). The phase contrast transfer function (PCTF) in eq. (3.13) is oscillatory meaning the transmission of spatial frequencies exhibits maxima, minima and zero transmissions. Those contrast inversions make image simulation necessary to interpret the HRTEM image. The point where PCTF reaches zero for the first time is called the point resolution. For spatial frequencies up to the point resolution no contrast inversion is observed and the image interpretation is more straight forward. The defocus where $\sin\left\{\chi(\boldsymbol{k})\right\}$ reaches the largest range of spatial frequencies before the point resolution is called Scherzer defocus:

$$\Delta f_{\text{Sch}} = -\sqrt{\frac{4}{3}C_s\lambda} \tag{3.14}$$

Using image simulation based on the multi-slice method done by JEMS software package [38], the influence of sample thickness and chosen defocus on the resulting HRTREM image contrast can be seen. Figure 3.6 shows a resulting thickness-defocus map of a cubic $Ge_1Sb_2Te_4$ crystal structure. As shown, depending on the thickness and the defocus the same

structure produces various contrast features, sometimes showing the atom position as bright contrast on a dark background (e.g. high defocus and high thickness values) and sometimes the other way around.

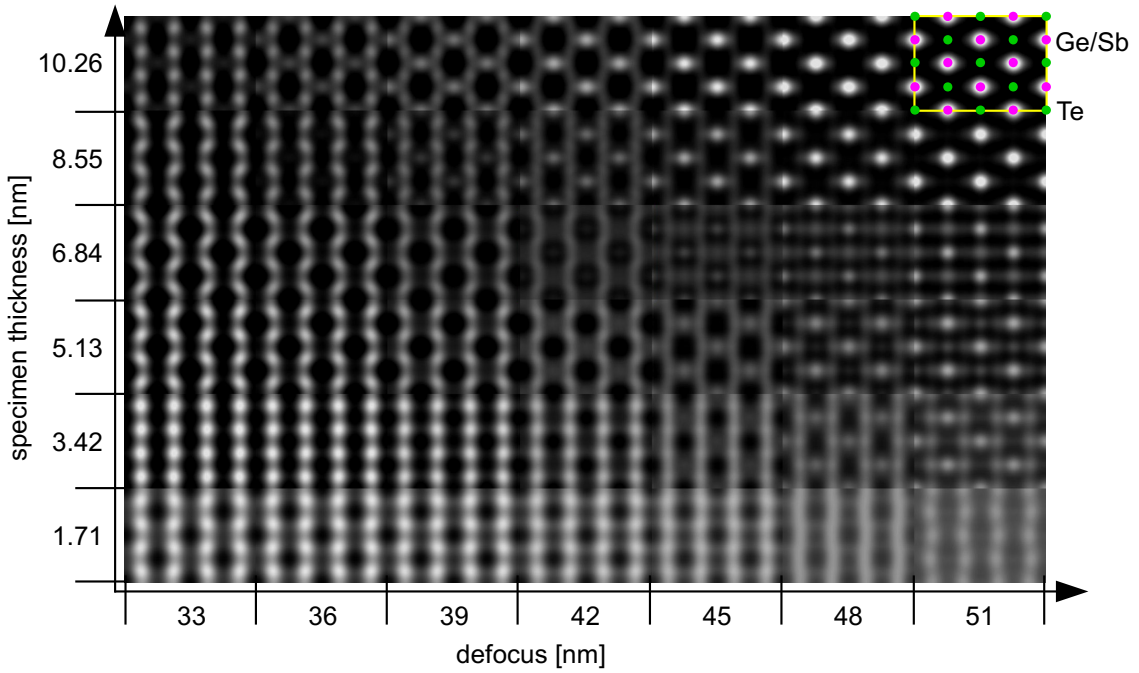

Figure 3.6 HRTEM image simulations done with JEMS [38] resulting in a thickness-defocus map of cubic $Ge_1Sb_2Te_4$ imaged in the $[110]$ zone axis. The corresponding atomic arrangement is displayed in the upper right corner. The microscopic parameter for JEOL 3010 are used ($E = 300\,\mathrm{kV}$, $C_s = 0.7\,\mathrm{mm}$ and $C_c = 1.2\,\mathrm{mm}$).

Bright-field and high-angle annular dark-field STEM

In contrast to TEM, in the scanning TEM (STEM) mode the electron beam is focused and scanned across the specimen. A schematic illustration of the STEM set-up is shown in Fig. 3.7. The beam scanning is thereby done by deflection coils using a periodic signal. For each beam position, a detector behind the specimen records the number of electrons that are scattered through a certain angular range. Therefore, STEM images are comprised of pixels that correspond to the accumulated intensity of scattered electrons originating from each position of the scanned specimen area. The size of the focused electron beam therefore limits the resolution of this technique.

Two detectors can be used for imaging and thereby different electrons can be selected to contribute to the image intensity: The bright-field (BF) detector is directly on the optical axis and therefore in the direct beam path. The annular dark-field (ADF) detector is ring shaped and positioned symmetrically around the optical axis and thus allowing the selection of diffracted electrons of different angular ranges. The collection angle depends on the dimension of the detector and the applied camera length. Since the dimensions are fixed, the detected angular range can be changed by varying the camera length. Choosing shorter

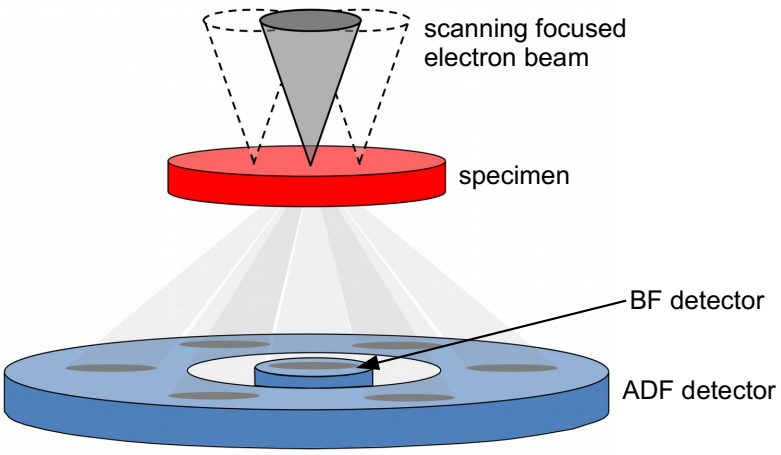

Figure 3.7 Schematic illustration of the STEM imaging mode featuring the bright-field (BF) and annular dark-field (ADF) detector.

camera lengths (by adjusting the imaging lens system) lead to the selection of electrons with higher scattering angles.

High-angle annular dark-field (HAADF-) STEM is a technique used for analysis of the crystal structure of a specimen on an atomic scale with additional local chemical information. At sufficiently high scattering angles the signal is incoherent due to thermal diffuse scattering being the main contribution [39]. This leads to intensities that can be described as being proportional to the thickness, t, and the average atomic number, Z, of the specimen at the investigated beam position [35, 40]:

$$I_{\mathrm{HAADF}} \propto Z^{\gamma} \tag{3.15}$$

The exponent γ in eq. (3.15) depends on the chosen detector collection angle, θ, (which determines the elastic and inelastic contribution) and ranges between 1.7 and 1.9 for typical HAADF conditions ($\theta \geq 50$ mrad) [35, 40]. Due to the fact that the intensity is proportional to the atomic number, this technique is also called Z-contrast imaging. Therefore, HAADF-STEM images are darker for areas with lighter atoms, i.e. atoms having a small atomic number compared to areas with heavier atoms having a large atomic number. In this thesis, only qualitative interpretations of images are made.

3.3 Quantitative EELS microanalysis

For in-situ experiments it is important to know the composition and its stability on a global and local scale during annealing. In order to quantify the chemical composition of the ternary system used in this work different methods have been used so far, e.g. proton induced x-ray emission (PIXE) [41], Rutherford backscattering (RBS) [41], inductively coupled plasma atomic emission spectrometry (ICP) [42] and X-ray photoelectron spectroscopy (XPS) [43]. The advantage of using EELS as a quantifying method is the spatial resolution on the nanometer scale in combination with the imaging possibilities in a TEM. This gives

the opportunity to analyze the composition before and after annealing in in-situ heating experiments. So far, only Song *et al.* [44] have reported EELS data on GeSbTe but focused on the electronic structure upon the phase transition rather than quantification of the chemical composition.

This section is dedicated to EELS measurements: First, the involved fundamentals are described. Then, the experimental realization and finally the methodology for quantification are discussed.

3.3.1 Fundamentals

Besides elastic scattering used for imaging as discussed in the previous section 3.2, the incident electrons can undergo inelastic scattering due to electron-shell interactions and contain therefore information about the sample such as the chemical composition. In this section, the fundamentals of EELS measurements are briefly introduced based on Ref. [35, 45]. First, a short description of the set-up is given and then a typical spectrum and the physical origin of the observed signals are discussed.

Set-up and important parameters

The energy-loss of the inelastically scattered electrons can be measured and displayed in an intensity vs. energy-loss plot, called an EEL spectrum. For that, a magnetic prism mounted below the TEM is used which acts as a spectrometer and focusing lens at the same time. The electrons are deflected through $\geq 90°$ by a magnetic field perpendicular to the electron beam. The deflection angle thereby depends on the velocity of the electrons (v). Electrons which have lost more energy (smaller value of v) are deflected further than those with less energy-loss (higher value of v) resulting in a dispersion plane at the end of the spectrometer. At the same time, electrons having lost the same amount of energy but traveling on- and off-axis are focused in the dispersion plane. After separating the electrons based on their energy-loss in the dispersion plane through the spectrometer, a detector located behind it measures the electron intensity for each energy. The detection can be done in serial acquisition where the intensity of one energy-loss is recorded at a time, parallel acquisition where the intensity of all energy-losses are recorded at the same time or energy-selected imaging where only electrons from a selected energy window contribute to an image or diffraction pattern. In this work, a parallel detection system ("Enfina" from Gatan) was used. Usually, the detector for parallel acquisition consists of a Ce-doped yttrium-aluminum garnet (YAG) scintillator and a CCD camera. The YAG scintillator thereby emits visible light when struck by electrons and the via fiber optics coupled CCD camera records the intensity of the emitted light.

There are two modes of operation: "Image mode" or "diffraction mode". In "image mode" there is an image on the TEM viewing screen and therefore a diffraction pattern (DP) in the back-focal plane of the projector lens which the post-column spectrometer uses as the object plane. This leads to an image in the front focal plane of the detector (where the entrance aperture sits). Because of the image at the entrance aperture plane, the angular distribution of the electrons is controlled by the objective aperture. This gives rise to a poor spatial resolution due to chromatic aberration. In the "diffraction mode" on the other hand, there is a DP on the viewing screen and therefore a DP at the entrance plane of the detector. The

DP at the entrance plane allows the control of the angular distribution of electrons by an entrance aperture of the spectrometer.

Important parameters to consider during EELS measurements include energy dispersion, energy resolution and collection angles. The dispersion is the distance in the spectrum (dx) between electrons which differ in energy by dE (i.e. energy range per channel in the spectrogram). It depends on the strength of the magnetic field of the spectrometer and controls the energy-loss range visible in the spectrum. The energy resolution of the spectrometer is defined as the full width at half maximum (FWHM) of the focused zero-loss peak. The energy spread of the incident electrons depends on the electron gun used and is smaller for a cold FEG (0.3 eV) when compared to a LaB_6 gun (1.7 eV). It is also influenced by the accelerating voltages used and the energy spread increases as the voltages increases. The collection angle, β, is the range of electron scattering angles allowed inside the spectrometer. It is therefore the most crucial parameter especially for quantification since the intensity distribution in the spectrum depends on the angular distribution of the scattered electrons. In "diffraction mode", the collection angle depends on the chosen size of the entrance aperture, d, and the camera length, L, and is given by equation 3.16 [35].

$$\beta = \frac{D}{D_A}\frac{d}{L} \tag{3.16}$$

where D_A is the distance between projector crossover and entrance aperture (for "Enfina" system: D_A=600 mm) and D is the distance between crossover and viewing screen and depends on the microscope (D ≈500 mm). A higher collection angle means a higher intensity in the spectrum but at the cost of energy resolution due to off-axis beam suffering aberrations. The characteristic angle, θ_E, for a certain energy-loss process, ΔE, is the most-probable scattering angle for this process and depends on the accelerating voltage. An estimation of θ_E is given by eq. (3.17) [35].

$$\theta_E \approx \frac{\Delta E}{m_0 v^2 \left(\sqrt{1-\frac{v^2}{c^2}}\right)} \tag{3.17}$$

where m_0 is the rest mass and v is the velocity of the incident electron. In the case of analyzing the EEL spectrum of Ge-containing samples (Ge-edge at 1217 eV [45]), as done in this thesis, the characteristic angle is $\theta_E \approx 6$ mrad for incident electrons with 300 keV. As a rule of thumb, the collection angle should be 2-3 times the characteristic scattering angle for the specific energy-loss process which is investigated to avoid losing intensity in the spectrum. For analyzing Ge-containing samples, the collection angle therefore should be greater than 12-18 mrad.

Typical EEL spectrum

A typical EEL spectrum can be divided into regions of different energy-losses, namely the zero-loss peak (around 0 eV), the low-loss region (5-50 eV) and the core-loss region (50-2000 eV). Each region contains electrons that underwent different interactions with the atoms of the specimen and therefore carry different information. Figure 3.8 shows a typical

EEL spectrum of a GeSbTe sample. The different energy regions are marked and discussed in more detail in the following.

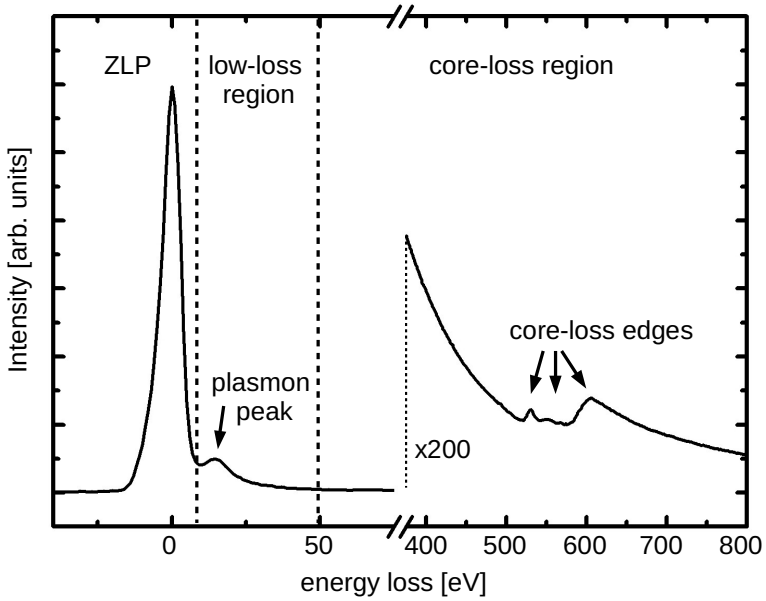

Figure 3.8 Typical EEL spectrum of GeSbTe specimen featuring the zero-loss peak (ZLP), the low-loss and core-loss region. Due to the low intensity of the core-loss region, this part of the spectrum is recorded using a 200 times longer exposure time.

Zero-loss peak. The zero-loss peak (ZLP) originates from electrons that did not undergo inelastic interaction with the specimen. They contain mostly electrons that are scattered elastically in a forward direction (electron-nucleus interaction) and to some extent electrons that did not interact with the specimen at all. The spread of the ZLP is caused by the fact that the incident electrons are not monochromatic. The width of the ZLP is therefore a measure of the energy resolution of the experimental system. Because of the finite energy resolution, the ZLP also contains electron with a small energy-loss originating from phonon excitations (~0.02 eV) causing the specimen to heat up.

In practice, the ZLP, taken without a specimen present in the beam path, is used to calibrate the experimental set-up by minimizing its width and scale the energy-loss based on the peak's position. In addition, the ZLP is used to calculate the local relative thickness, t, of the specimen in terms of the mean free path, λ, of inelastic scattering. Using Poisson statistics for independent events such as inelastic scattering, the comparison of the integrated intensity of the ZLP, I_0, to the total integrated intensity of the energy-loss spectrum, I_t yields for the local thickness [45]

$$\frac{t}{\lambda} = \ln\left(\frac{I_0}{I_t}\right) \tag{3.18}$$

This method is known as the Log-Ratio method. In practice, the limits of the integration to measure I_0 and I_t have to be chosen. The "compute thickness" procedure provided in the GATAN EELS software package models the right-hand side of the ZLP as a reflection of the

left-hand side in order to define the limits for the I_0 integration. In addition, it extrapolates the spectrum to higher energy-losses for the I_t integration. When λ is known, the local absolute thickness, t, of the specimen can be calculated using eq. (3.18). Egerton [45] uses scattering theory to derive eq. (3.19) to approximate λ as a function of the collection angle, β:

$$\lambda(\beta) \approx \frac{106F(E_0/E_m)}{\ln\left(2\beta E_0/E_m\right)} \tag{3.19}$$

with λ in nm, β in mrad, incident energy, E_0, in keV and mean energy-loss, E_m, in eV. The relativistic factor, F, is given by

$$F = \frac{1 + E_0/1022}{\left(1 + E_0/511\right)^2} \tag{3.20}$$

and the mean energy-loss can be approximated by eq. (3.21) [45]

$$E_m \approx 7.6 Z_{eff}^{0.36} \tag{3.21}$$

with the effective atomic number, Z_{eff}, which can be approximated by eq. (3.22) for compounds [45]

$$Z_{\text{eff}} = \frac{\sum_i f_i Z_i^{1.3}}{\sum_i f_i Z_i^{0.3}} \tag{3.22}$$

with f_i being the atomic fraction of each element with atomic number, Z_i. Note that eq. (3.19) used the dipole approximation and is valid only for $\beta << \sqrt{E/E_0}$ and that λ saturates at large collection angles. Applying eq. (3.19), (3.20), (3.21) and (3.22) to the compound $Ge_1Sb_2Te_4$ yields $\lambda_{GST}(10\text{mrad}) = 56$ nm with $Z_{\text{eff}} = 49.2$, $E_m = 30.9$ eV and $F(300\text{ keV}) = 0.514$.

Low-loss region. Besides the ZLP peak, the plasmon peak is the next prominent feature in the EEL spectrum. The low-loss region is defined to contain electrons with energy-losses up to 50 eV because the distinct feature of the core-loss regions, the ionization edges of inner-shell electrons, typically start at energy-losses above 50 eV. The small energy-loss in this region originates from incident electron interactions with weakly bound conductance or valence band electrons. The longitudinal oscillations that occur from these interactions are called plasmons. In addition, the incident electrons can excite single outer-shell electrons to undergo interband and intraband transitions. The low-loss region can therefore be used for phase identification of compounds with electronic differences and to gain information about the electronic structure such as the band gap.

Core-loss region. The region of large energy-loss (50-2000 eV) is called core-loss region and includes electrons that underwent an inner-shell ionization process leading to the formation of the major features in this region, the core-loss edges. Figure 3.9 shows a schematic illustration of the inner-shell ionization process. An incident electron interacts with an inner-shell electron of the atoms in the specimen. When sufficient energy is transferred, the inner-shell electron is excited into a higher energy state (transferred energy is larger than the Fermi

energy $\Delta E > E_F$) or even ionized (transferred energy is larger than the ionization threshold $\Delta E > E_{vac}$). Because of the conservation of the total energy, the incident electron loses the same amount of energy which is equal to or greater than the binding energy of the excited electron. During the de-excitation process, the hole left behind by the excitation process is filled with an outer-shell electron or an electron from a higher core-level leading to the generation of characteristic X-rays used in the complementary analysis technique called energy dispersive X-Ray spectroscopy (EDXS).

The binding energies are characteristic for a certain material and lead to the distinct positions of the core-loss edges which then can be used to identify the elements the specimen contains (qualitative chemical composition). In section 3.3.3 a methodology for the quantitative analysis of the composition is described. Furthermore, the analysis of fine structure yields additional information about the density of unoccupied states (using near edge fine structure (ELNES)) or the atomic-specific radial distribution of near neighbors (using extended fine structure (EXELFS)).

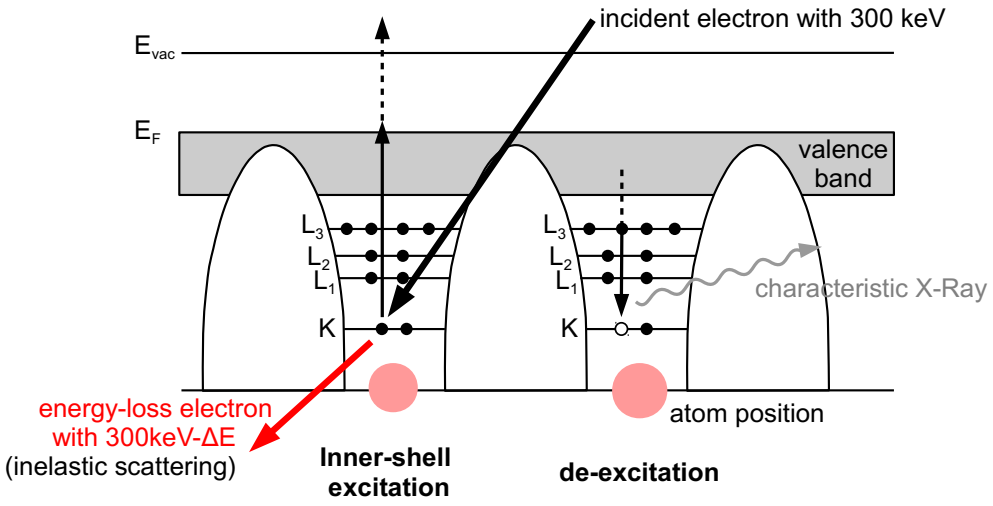

Figure 3.9 Generation of the core-loss EELS signal: Energy-level diagram of a specimen with K- and L-shell levels, valence band (continuum states), Fermi level (E_F) and vacuum level (E_{vac}). Illustration of inner-shell excitation process and subsequent de-excitation process with the generation of characteristic X-rays, based on Ref. [35, 45].

3.3.2 Experimental implementation

The EEL spectra shown in this work are recorded in the JEOL 3010 TEM operating at 300 kV with a thermal LaB_6 electron source and equipped with a post-column Gatan Enfina parallel EELS system. The energy resolution is about 1.7 eV determined by measuring the FWHM of the zero-loss peak recorded without a specimen. The spectra of GeSbTe samples are collected in diffraction mode applying a collection semi-angle of 25 mrad and using an energy dispersion of 1 eV/channel in order to simultaneously collect information of all three elements: antimony (Sb-M) edges ($\sim$ 528 eV), tellurium (Te-M) edges ($\sim$ 572 eV) and germanium (Ge-L) edges ($\sim$ 1217 eV) [45]. For a good balance of signal-to-noise ratio, spatial

resolution and minimizing beam drift and irradiation damage typical acquisition times for each core-loss spectrum were set to 20 sec using a spot size of about 20 nm in diameter. In addition, all spectra were corrected for gain variations within the spectrometer. Before the EELS analysis, the samples were cleaned with a GATAN Solarus Advanced Plasma Cleaning System (model 950) using the standard cleaning procedure for 2 min utilizing H_2 and O_2 gas to minimize carbon contamination built-up during electron beam exposure.

3.3.3 Methodology for quantification and its application to GeSbTe alloys

Figure 3.10(a) shows a typical core-loss EEL spectrum between 450 eV and 1550 eV obtained from crystalline GeSbTe thin film. It includes the characteristic energy edges of the elements contained in GeSbTe: In the energy range from 450 eV to 800 eV, it shows the overlapping oxygen (O-K) edges ($\sim$ 532 eV), the antimony (Sb-M) edges ($\sim$ 528 eV) and the tellurium (Te-M) edges ($\sim$ 572 eV) [45]. The signal from the germanium (Ge-L) edges ($\sim$ 1217 eV) [45] can be seen in the higher energy range from 1150 eV to 1550 eV. For better visibility, the signal in the higher energy range is multiplied by a factor of 5. The additional oxygen signal is also detectable on the Si substrate. Thus the oxygen signal seems to originate from oxidation on the surface of the TEM sample and is not considered in the quantification process to analyze the composition of the thin GeSbTe film.

For the quantification of the EELS data, four main steps are performed: (1) The background subtraction, (2) overlapped edge separation by applying multiple-least-square (MLS) fitting, (3) calculation of atomic ratios and then (4) atomic percentages using reference standards of known composition.

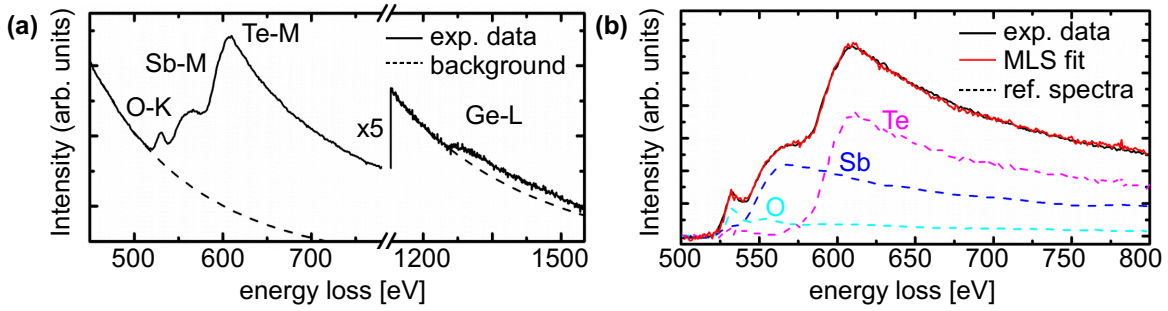

Figure 3.10 (a) Core-loss EEL spectrum taken from crystalline $Ge_1Sb_2Te_4$ including the characteristic ionization edges from antimony (Sb-M), tellurium (Te-M) and germanium (Ge-L) (the oxygen O-K edge originated from oxidation of the TEM sample). The signal in the high energy range (1150 eV-1550 eV) is multiplied by a factor of 5. The background signal is shown as a dotted line. (b) Overlapped core-loss EEL spectrum in the energy range of 500 eV and 800 eV of GST after background subtraction (black) with reference spectra of oxygen (cyan), antimony (blue) and tellurium (magenta) and the resulting MLS fit (red).

1. **Background subtraction:** In order to prepare the measured spectra for quantification analysis, the non-characteristic background signal (shown as dotted line in Fig. 3.10(a)) is subtracted from the experimental EELS data. The background signal contains electrons which underwent energy-loss processes with specimen electrons of lower binding energy. It can be modeled as having a power-law energy dependence

$A\Delta E^{-r}$ where the parameters A and r are measured by using least-square fitting of the EELS signal over an energy-loss range (ΔE) preceding the core-loss edge in question. The background signal is then extrapolated to isolate the intensity of the ionization edge.

2. **Extraction of individual contributions:** In the low energy range (500 to 800 eV) there is an overlap of the three elements oxygen, antimony and tellurium (cf. EELS spectrum in Fig. 3.10(a)). For quantification the isolated intensity contributions of each element are needed without the intensity contribution due to tails of preceding ionization edges. The overlapped experimental spectra can be separated in the three individual contributions using MLS fitting procedure to reference spectra [45]:

$$F(\Delta E) = A\Delta E^{-r} + c_O S_{O-Ref}(\Delta E) + c_{Sb} S_{Sb-Ref}(\Delta E) + c_{Te} S_{Te-Ref}(\Delta E) \quad (3.23)$$

where the first term in eq. (3.23) results from the background signal described in step (1), $S_{O,Sb,Te-Ref}(\Delta E)$ represent the core-loss spectra of oxygen, antimony and tellurium, respectively, and $c_{O,Sb,Te-Ref}$ are coefficients that minimize the difference between the measured EELS data, $F(\Delta E)$, and the sum of the individual core-loss spectra. The reference spectra for antimony and tellurium, $S_{Sb,Te-Ref}(\Delta E)$, are taken from GaSb and GeTe thin film TEM samples and the oxygen reference spectrum, $S_{O-Ref}(\Delta E)$, is obtained from the oxygen signal originating from the oxidized silicon substrate of the GeSbTe sample itself. Figure 3.10(b) shows a typical core-loss EEL spectrum (black, solid line) in the range of 500 to 800 eV after background subtraction. The individual reference spectra of oxygen (cyan, dotted line), antimony (blue, dotted line) and tellurium (magenta, dotted line) used in the fitting procedure and the resulting MLS fit (red, solid line) are displayed as well. The fit presents a good match to the experimental data in this energy range.

3. **Calculation of concentration ratios:** The integrated intensity of scattering from an inner-shell k of a selected element, which is characterized by a partial cross-section σ_k can be calculated by [45]:

$$I_k = N I_0 \sigma_k \quad (3.24)$$

where N are the atoms per unit area of the element and I_0 the ZLP intensity. The concentration ratio between two elements a and b can then be calculated using eq. (3.25) [45].

$$\frac{N_a}{N_b} = \frac{c_a}{c_b} \frac{I_{k,a}(\beta,\Delta)}{I_{l,b}(\beta,\Delta)} \underbrace{\frac{\sigma_{l,b}(\beta,\Delta)}{\sigma_{k,a}(\beta,\Delta)}}_{\sigma_{ba}} \text{ with } a,b \in \{Ge, Sb, Te\} \quad (3.25)$$

Thereby, $I_{a,b}$ are the integrals of the core-loss reference spectra, $S_{a,b}(\Delta E)$, over a convenient integration range Δ of the k and l core-loss edges for the elements a and b. For the recording of the spectra, scattered electrons up to the collection angle β are collected. $\sigma_{a,b}$ are partial cross-sections for the analyzed core-loss process and $c_{a,b}$

are coefficients resulting from the MLS fitting procedure [45]. The ratio of two partial cross-sections, σ_{TeGe} and σ_{TeSb}, can be determined in a full experimental approach using references of a known composition. In this case, $Ge_{0.46}Te_{0.54}$ and Sb_2Te_3 are used. The crystalline $Ge_{0.46}Te_{0.54}$ thin film is deposited on a cleaned crystalline Si(100) substrate in an ultra-high vacuum chamber by using effusion cells for the three elements[1]. The film composition is determined by x-ray fluorescence. A detailed description of the deposition process and compositional analysis is provided in Ref. [46]. For the Sb_2Te_3 reference, a FIB prepared lamella (cf. section 4.3.2) from Sb_2Te_3(99.999%) source material purchased from Alfa Aesar is used. Figure 3.11 shows the obtained and background subtracted EEL spectra of both references. Using eq. (3.25) the partial cross-sections, σ_{GeTe} and σ_{SbTe}, are calculated. The results are summarized in table 3.2 and used in the determination of GeSbTe films of unknown composition. Note that eq. (3.25) presumes a small angular spread of the incident beam compared to the collection angle, β, otherwise correction are needed. This prerequisite is fulfilled when using parallel illumination even for spot sizes of 20 nm.

4. **Calculation of atomic percent:** In order to calculate the atomic percentages of a GeSbTe film of unknown composition, it is assumed that the thin film consists only of Ge, Sb and Te (Ge%+Sb%+Te%=100%). The atomic percentage for each element can then be written as:

$$Ge\% = \frac{N_{Ge}}{N_{Ge} + N_{Sb} + N_{Te}} \tag{3.26}$$

Then, knowing the two composition ratios (N_{Ge}/N_{Te}) and (N_{Sb}/N_{Te}) which are calculated with eq. (3.25), the atomic percent of all three elements can be determined using eq. (3.27).

$$\begin{aligned} Ge\% &= \frac{N_{Ge}}{N_{Ge} + N_{Sb} + N_{Te}} = \frac{1}{1 + \frac{(N_{Sb}/N_{Te})}{(N_{Ge}/N_{Te})} + (N_{Ge}/N_{Te})^{-1}} \\ Sb\% &= \frac{N_{Sb}}{N_{Ge} + N_{Sb} + N_{Te}} = \frac{1}{1 + \frac{(N_{Ge}/N_{Te})}{(N_{Sb}/N_{Te})} + (N_{Sb}/N_{Te})^{-1}} \\ Te\% &= \frac{N_{Te}}{N_{Ge} + N_{Sb} + N_{Te}} = \frac{1}{1 + (N_{Ge}/N_{Te}) + (N_{Sb}/N_{Te})} \end{aligned} \tag{3.27}$$

Estimation of uncertainty. The described quantification procedure and its accuracy were verified with an amorphous GeSbTe thin film of known composition. The GeSbTe standard is grown by rf sputtering from two targets (GeTe and Sb_2Te_3) on a Si(111) wafer with a natural, amorphous oxidation layer (SiO_2) and a few nanometer thick silicon nitride (Si_3N_4) capping layer and its composition is Ge(22%):Sb(22%):Te(56%) [47][2]. Using the above

[1] The investigated $Ge_{0.46}Te_{0.54}$ thin film is grown and its composition is analyzed by Dr. Karthick Perumal (PDI) [46].

[2] The investigated $Ge_2Sb_2Te_5$ thin film is grown and its composition is analyzed by the group of Dr. Paul Fons (AIST) [47].

Table 3.2 Ratio of cross-sections σ_{TeGe} and σ_{TeSb} determined by references $Ge_{0.46}Te_{0.54}$ and Sb_2Te_3. EEL spectra are collected with β=25 mrad and the energy-loss range of the core-loss edge integrals $I_{k,a}$ are at the Ge-edge: Δ=1250–1350 eV, Sb-edge: Δ=550–700 eV and Te-edge: Δ=600–700 eV. The value of both σ is the arithmetic average determined from several recorded spectra.

	$Ge_{0.46}Te_{0.54}$	Sb_2Te_3
σ_{TeGe}	13 ± 1	—
σ_{TeSb}	—	0.68 ± 0.07

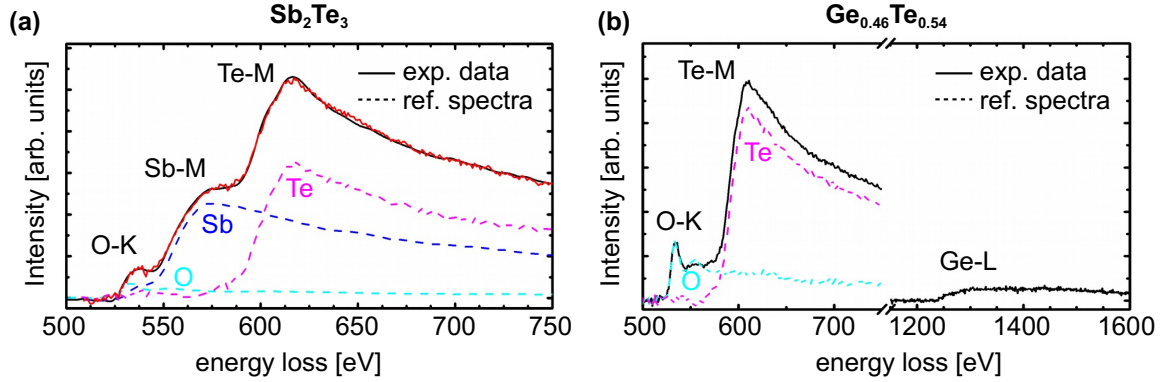

Figure 3.11 Core-loss EEL spectra of the two references **a** $Ge_{0.46}Te_{0.54}$ and **b** Sb_2Te_3 used for determination of the partial cross-sections σ_{TeGe} and σ_{TeSb} after background subtraction and after deconvolution (for **b**).

described EELS quantification process and calculating the arithmetic average over several recorded EEL spectra results in a composition of Ge($22\pm2\%$):Sb($21\pm2\%$):Te($57\pm2\%$). (An example of an EELS spectrum obtained from the $Ge_2Sb_2Te_5$ standard is shown in Fig. 3.12.) Therefore, the uncertainty of the quantification method is estimated with 5%. For the sake of completeness, the third partial cross-section ratio σ_{SbGe} can be calculated assuming a $Ge_2Sb_2Te_5$ composition and results in $\sigma_{SbGe} = 19 \pm 3$.

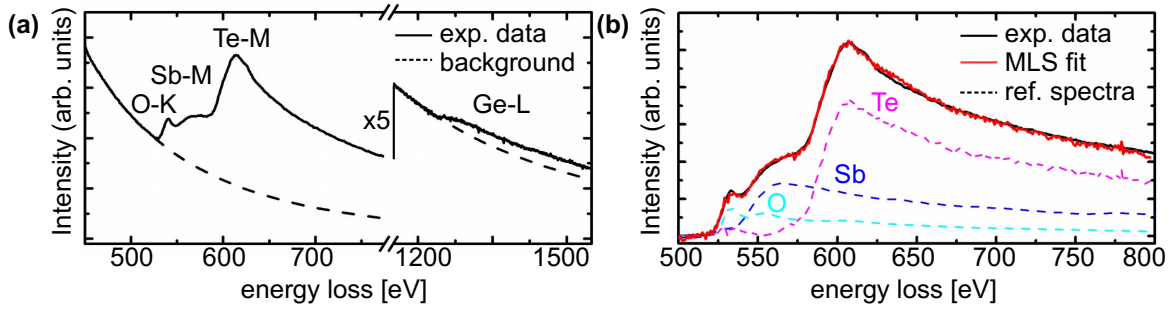

Figure 3.12 (a) Core-loss EEL spectrum taken from $Ge_2Sb_2Te_5$ standard. (b) Overlapped core-loss EEL spectrum in the energy range of 500 eV and 800 eV of GST after background subtraction (black) with the three reference spectra of O, Sb and Te and resulting MLS fit.

4 In-situ transmission electron microscopy

In-situ TEM is the method used in this thesis to investigate several dynamic processes. This chapter is dedicated to this exciting experimental technique and is an expansion of the static TEM methods described in the previous chapter. First, in-situ TEM is introduced with its advantages, limitations and a broad overview which dynamic processes can be investigated. Then, the experimental realization used in this thesis is discussed and finally the required sample preparation techniques are described.

4.1 Introduction

In the previous chapter, TEM was introduced as a powerful analytical method to characterize the structure and chemical composition of solids at the atomic scale. All the discussed imaging techniques are used to capture the status quo of a specimen. In-situ TEM on the other hand uses the different imaging techniques to analyze the response of a material to a stimulus. The response process is thereby observed inside the microscope while it occurs. The process can be deliberately triggered in a controlled and measurable way with the use of special TEM holders. Various external stimuli are possible like heat [1, 16, 18, 25, 44, 48–54], stress [55–57], electrical current [58–60], light [61, 62], the exposure to liquid or gas phases [63–71] or a combination of these depending on the specific specimen holder. The response of a material can then be studied either as a function of the strength of the external stimulus or as a function of time during a constant stimulus. It therefore adds an additional dimension to the TEM analysis. There are several good reviews about the merits and limitations of in-situ TEM. Here a short introduction is given based on Ref. [1–3, 72].

4.1.1 Why in-situ TEM?

While it is possible to study the response of a material using "ex-situ" (outside the microscope) applied stimulation by analyzing a sample before and after the process happens, "in-situ" provides the opportunity to study the process while it occurs. Therefore, not only the result of a response can be investigated but also intermediate steps leading to the result. Thus, removing the need to infer how a process leads the observed outcome. Moreover, there is no need to assume that the outcome of a process is the same state one observes in the TEM after the ex-situ stimulation was applied and stopped. In fact, in can also be observed if the state of the specimen changes after the stimulus ceases. Furthermore, studying processes in-situ is time saving as there is no need to prepare several samples at different states of treatment. In addition to seeing structural, morphological and chemical changes at the same time, thermodynamic and kinetic data such as activation energies or rates can be measured and compared to traditional bulk techniques [12, 73, 74]. The ability to directly

observe and characterize all the steps during a response opens up the possibility to gain a detailed understanding of the process and properties such as stability and reactivity.

4.1.2 Limitations

In order to use TEM, very thin specimen (thin foils) are required for electrons to be able to transmit through the sample (see section 4.3). The thin foil geometry can alter the response of the sample to an external stimulus for example by lowering the activation energy due to a domination of surface properties compared to bulk properties. Therefore, it needs to be confirmed that the response is representative of the bulk. This can be done by either comparing the results of ex-situ and in-situ studies or by comparing thicker and thinner parts of the TEM specimen. Nonetheless, with nanostructures becoming smaller and smaller the "thin specimen" TEM requirement is no longer a drawback since the dimension of the objects of interest is in the same order of magnitude as required by TEM investigation. Furthermore, the experimental realization is challenging. To apply a stimulus, a dedicated TEM specimen holder is required. TEM is a sensitive method and introducing an external stimulus is demanding. For instance, the application of heat leads to sample drift making it difficult to observe a process. Even though heating holders with low sample drift are now commercially available, they shift the challenges from the observation to the sample preparation side. Depending on the experimental set-up, the boundary conditions such as local temperature and pressure are difficult to accurately measure and control. Finally, one needs to take into consideration the influence of the high-energy electrons on the observed process for example by comparing specimen areas with different electron beam exposure.

4.1.3 What kind of dynamics can be studied using in-situ TEM?

In order to study a process using in-situ TEM, the changes during the process must be visible in TEM such as (1) morphological changes [16, 50, 65, 75], (2) structural changes like defect movement, grain boundary movement, crystalline-amorphous transitions or transformation between different crystalline structures [18, 25, 49, 51–53, 73, 76] and (3) chemical changes like the change in chemical composition [44, 54, 72, 77]. Additionally, the length scale of the change must be observable in TEM and therefore must be in the order of nano- to micrometers. Moreover, the timescale of the response is crucial and the rate of change needs to be suitable for TEM observations. Figure 4.1 offers an overview of the time and length scale of dynamic processes relevant in biology, chemistry and material science. The achievable temporal resolution in in-situ TEM depends on the experimental set-up. Conventional in-situ TEM which is used in this thesis and utilizes dedicated specimen holders and fast CCD cameras can cover up to atomic scale spatial resolution and second to millisecond temporal resolution. With a lot of effort and a dedicated TEM set-up the time limit can even be pushed further for the observation of certain processes: Dynamic (D)TEM is a pump-probe set-up using several cathode pulses to study phenomena triggered by a laser pulse at the nanometer length and nanosecond time scale [61, 62]. Ultrafast (U)TEM is also a pump-probe set-up aimed to study reversible processes such as electronic, plasmonic or photonic excitations by a stroboscopic imaging mode combining several thousand individual cycles to obverse a process with atomic spatial and femtosecond temporal resolution [79, 80].

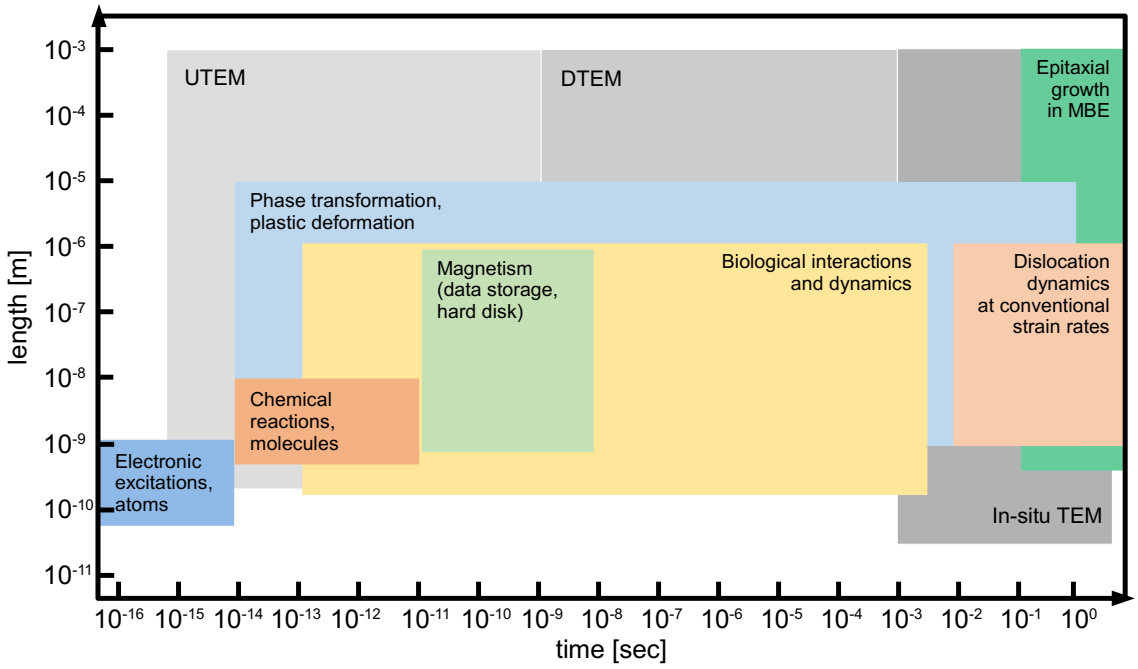

Figure 4.1 Overview of time and lengths scales for different dynamic processes and which scales are covered by conventional in-situ TEM, ultrafast (U)TEM and dynamic (D)TEM, based on Ref. [78].

Summing up, in order to observe a process with in-situ TEM the following conditions need to be matched: The process needs to be deliberately triggered by controlling a suitable stimulus (experiment set-up, e.g. dedicated specimen holder) and appropriate imaging conditions need to be found providing a contrast between process steps. Ross [3] gives a very detailed overview over several in-situ TEM studies classifying them into investigations of

1. **Phase transformations** (amorphization, crystallization, melting, grain growth, transition between different crystal structures and transformations in nanomaterials and size-dependent effects)
2. **Surface reactions and crystal growth** (surface structure modifications, catalysis, oxidation, growth of nanostructures and thin films)
3. **Magnetic, ferroelectric and superconducting phenomena** (magnetic domain motion, dynamics of vortices in superconductors)
4. **Elastic and plastic deformation** (deformation, relaxation and mechanical properties through indentation)
5. **Electrical properties** (device analysis, electrical measurements on individual nanostructures)
6. **Liquid phase processes** (liquid cells, electrochemical deposition)
7. **Ion and e-beam induced reactions**.

4.2 Experimental realization

In this thesis, high-temperature phase transitions of Ge-Sb-Te phase change materials are investigated. This section therefore describes the experimental set-up used and includes

the discussion of the temporal resolution, the temperature control and the influence of the electron beam.

The phase transformations are triggered by heating the TEM samples using dedicated TEM heating specimen holder. The involved dynamical processes are then recorded using a CCD camera.

4.2.1 Temporal resolution: Cameras

For the in-situ investigations, two different set-ups were used. The in-situ TEM data shown in chapter 6 were collected in a JEOL 3010 TEM equipped with a TV-rate camera (Gatan, model 692) for recording high-resolution images at 25 frames per second (fps). The in-situ data shown in chapter 7 were collected in a JEOL 2100F where a UltraScan 4000 (Gatan, model 895) CCD camera is used with a temporal resolution of 1.15 sec.

TV-rate camera. The sensor of the TV-rate camera is 6.6 mm (height) $\times$ 8.8 mm (width) and has (581 $\times$ 756) pixel. For comparison, the additional slow-scan CCD (Gatan, model 794) which is also mounted on the JEOL 3010 has a sensor with (24.6 $\times$ 24.6) mm^2 and (1024 $\times$ 1024) pixel. The exposure time of the slow-scan camera is chosen depending on the imaging mode. For HRTEM usually 0.2 sec are chosen to balance drift artifacts and signal-to-noise ratio. Figure 4.2 shows a comparison of image quality from the slow-scan camera (exposure time: 0.2 sec) and TV-rate camera (exposure time: 0.04 sec). The slow-scan camera shows a larger image section and the image quality is superior due to the 5 times longer exposure time and the better dynamic of the sensor. However, the TV-rate camera allows to record in-situ video data with a temporal resolution of 0.04 sec.
The TV-rate camera provides only an analog video signal. In order to record the in-situ videos and be able to analyze them using image processing software (Digital Micrograph software from GATAN and freeware ImageJ [81]), the analog signal is digitized using a frame grabber (CronosPlus) and software library (Matrox Imaging Library, MIL) from Matrox. The software automatically recognizes the provided frame rate of 25 fps and each frame is saved as grayscale tif file where information about magnification and time are overlaid.

UltraScan. The sensor of the UltraScan 4000 is (61.2 $\times$ 61.2) mm^2 with (4080 $\times$ 4080) pixel. The frame rate is 0.2 fps at full resolution (5 sec between images) up to 2 fps at (400 $\times$ 400) pixel. The in-situ videos are recorded using the continuous mode for a (1k $\times$ 1k) image in Digital Micrograph ("Live View") and the screen capture software Camtasia Studio provides a temporal resolution of 1.15 sec (0.87 fps). Since the screen capturing is not synced with the frame rate provided by the "Live View" option, the recorded images are subsequently processed to filter out identical frames using a Matlab script.

4.2.2 Temperature control: Sample holders

The in-situ heating measurements are done using two kinds of dedicated TEM heating holders. At the JEOL 3010 (chapter 6), the measurements are carried out with a conventional

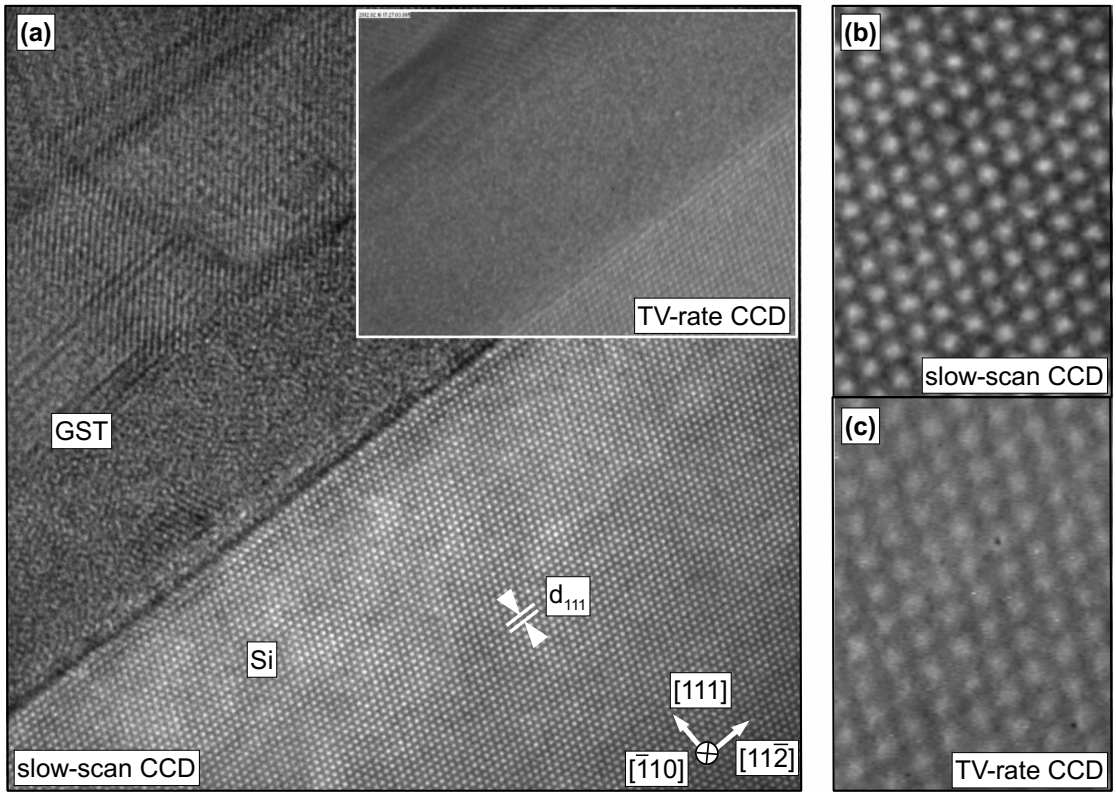

Figure 4.2 Comparison of image quality recorded with TV-rate and slow-scan CCD camera at JEOL 3010: (a) HRTEM image recorded with the slow-scan CCD. The inset shows the same sample area recorded with the TV-rate camera exhibiting a smaller field of view. The magnified area of the silicon substrate imaged in the zone axis $[\bar{1}10]$ shows the better signal-to-noise ratio of the (b) slow-scan CCD (exposure time: 0.2 sec) compared to the (c) TV-rate camera (exposure time: 0.04 sec).

bulk heating holder from JEOL. The measurements at the JEOL 2100F (chapter 7) are performed with a micro-electro-mechanical systems (MEMS)-based double-tilt sample holder from DENSsolutions.

Conventional bulk heating holder

The conventional bulk heating holder used in this work is the JEOL double-tilt specimen heating holder (model EM-31050) in combination with a JEOL controller unit (model EM-SHU2).

Set-up. Figure 4.3(a) shows a photograph of the holder tip and the schematics of the specimen mounting mechanism. The specimen is a conventionally prepared 3 mm disk which is thinned in the center to electron transparency. The specimen disk is fixed with a spring mechanism. The clamp is pinched with tweezers and released after placing it onto the specimen and thereby fixating the specimen in the tilt cradle. Because the clamp mechanism cannot be adjusted, the specimen does have room to slightly move in the cradle facilitating sample drift. After mounting the specimen the holder is inserted into the microscope. A sample stage is used to precisely control the specimen movement in x-, y- and z-direction.

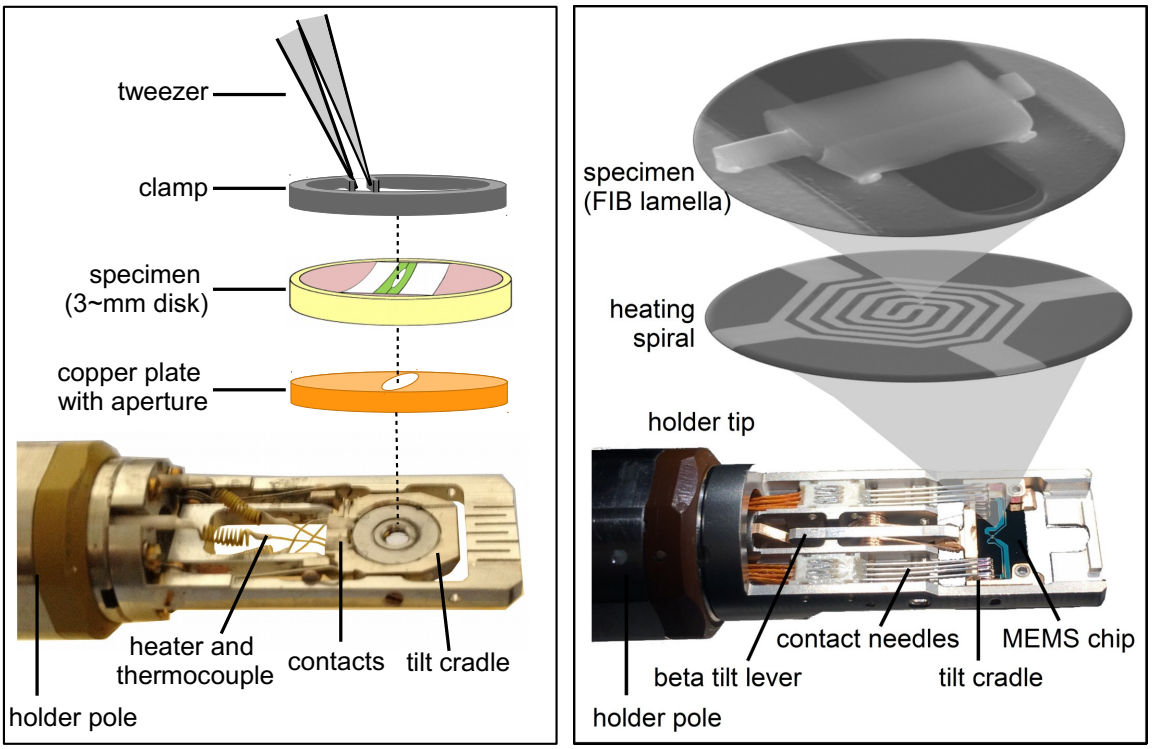

(a) Bulk heating holder **(b)** MEMS-based heating holder

Figure 4.3 (a) Conventional bulk heating holder with clamp specimen mounting system (JEOL EM-31050) and (b) MEMS-based heating holder with chip mounting system from DENSsolutions (model D9+).

The tilt cradle allows the specimen to be tilted around two axes: along the holder pole (α-tilt) and perpendicular to it (β-tilt).

Temperature control. In Fig. 4.3(a) two wire pairs are visible. One pair is connected to an electric furnace for heating the specimen via joule heating and the other pair is connected to a thermocouple for temperature measurements. The maximum heating current is 0.9 A and the maximum attainable temperature inside the microscope is approximately 800°C. In order to control the temperature of the specimen the controller unit is used where the actual measured temperature is displayed and heating current and target temperature can be adjusted. The heating rate can be controlled by adjusting the heating current, where a high heating current leads to a large heating rate. The heating rate needs to be small enough to minimize the sample drift and thermal stress caused by a temperature gradient. In addition, a high heating current leads to overshooting the target temperature. The controller unit uses a feedback loop to compare the set target temperature with the measured temperatures and reduces the heating current if necessary. For temperature measurements, a type R thermocouple is used. A type R thermocouple contains one platinum conductor and one platinum-rhodium alloy conductor with 13%-Rhodium (Pt-Pt·13% Rh). The controller does not display temperature values but rather a thermoelectric voltage U, the corresponding temperature, T, can be calculated with eq. (4.1) and the conversion from a measured U to T with

eq. (4.2) [82]:

$$T\,[^\circ\mathrm{C}] = \begin{cases} \sum_{i=1}^{10} \left(b_i \cdot U^i\,[\mu\mathrm{V}]\right), & \text{when } -226\,\mu\mathrm{V} < U < 1923\,\mu\mathrm{V} \\ \sum_{i=0}^{9} \left(c_i \cdot U^i\,[\mu\mathrm{V}]\right), & \text{when } 1923\,\mu\mathrm{V} < U < 13\,228\,\mu\mathrm{V} \end{cases} \tag{4.1}$$

$$U\,[\mu\mathrm{V}] = \sum_{i=1}^{9} \left(a_i \cdot T^i\,[^\circ\mathrm{C}]\right) \tag{4.2}$$

where the coefficients a_i, b_i and c_i for a type R thermocouple are listed in the appendix (table A.5). The stated temperatures in this thesis refer to the temperature values measured by the thermocouple and displayed by the controller unit (reading accuracy: $\pm$ 2°C). Note that the thermocouple measures the temperature at the tilt cradle and therefore at the border of the specimen. The local temperature where the sample is observed then depends on the thermal contact between cradle and specimen and also between the different parts of a cross-sectional sample such as brass ring, glue, substrate and thin film. When measuring quantities like activation energies, the local temperature inside the microscope environment is crucial and a careful calibration is necessary. Sinclair *et al.* and others [73, 83] described a method where a dual specimen is prepared to measure the local temperature. There, one side of the specimen is a control sample. It shows a known temperature dependent behavior and is therefore used to calibrate the temperature at the observation region of the sample. The known temperature behavior should be in the same temperature range as the process that being investigated. Sinclair *et al.* [73] used the regrowth of silicon (that was amorphized by ion implantation) for calibration of temperatures above 500°C. This allows a high accuracy due to the high activation energy of the regrowth process. Other possibilities for calibration in the medium temperature range are the disappearance of superlattice diffraction spots in graphite-halogens (graphite-Br_2 at 100$\pm$1°C and graphite-ICl at 41$\pm$1°C) [84] or the melting of pure metals like indium (157°C), tin (232°C), lead (327°C) and zinc (420°C) [2].

Thermal drift. The observed lateral sample drift in the order of nm/sec during in-situ heating is due to the thermal expansion of material. The drift is enlarged further by the holder geometry where the contacts of the furnace are only on one side. The thermal drift increases with an increasing heating rate and temperature. In order to balance reasonable experiment duration with minimal thermal drift, the samples are heated in several intermediate temperature steps with fast heating rates (20 K/min) until well below the indented target temperature (0.85 T_{target}). They are kept at these temperature steps until the thermal drift slowed done enough to perform the intended measurements (in the order of tens of minutes [2]). , e.g. longer wait times for atomic resolution HRTEM. Afterwards, a slow heating rate (1 K/min or less) is used to reach the target temperature. Additionally, a copper plate with a thin aperture is utilized as support of the cross-sectional TEM sample (cf. Fig. 4.3(a)). This leads to a faster decrease of the temperature gradient due to the higher thermal conductivity of copper compared to the glue and silicon, which are used as fill material in conventionally prepared TEM samples. That helps to reduce the time needed to achieve reasonable thermal drift rates.

MEMS-based heating holder

The MEMS-based double-tilt sample holder from DENSsolutions (model D9+) and the heating controller which is connected to a PC is used to perform low-drift in-situ heating measurements.

Set-up. MEMS-based TEM holders use chips of different designs to apply an external stimulus like heating or biasing in different geometries. The chips thereby replace the conventional 3 mm specimen disks and are fixed with two hex screws in the tilt cradle. Figure 4.3(b) shows a photograph of the holder tip and SEM images illustrating the specimen mounting mechanism. For heating, a 20 µm wide and 150 nm thick platinum or tungsten heating spiral is used. The spiral material determines the maximum temperature that can be reached and is 800°C for the platinum and 1200°C for the tungsten spiral. The heating spiral is located in a pit in the center of the chip and is embedded in a 400 nm thick SiN sandwich. Within the SiN membrane, there are (5x20) µm^2 holes where a TEM specimen can be placed and investigated without the obstruction of the thin membrane. The placement of the specimen in a lamella geometry is done with a dual FIB/SEM microscope (cf. section 4.3.2). As with the bulk heating holder the sample stage is used to control the movement of the specimen inside the microscope.

Temperature control. The holder can be connected to a laptop with the use of the temperature control box and the temperature of the DENSsolutions systems can then be controlled with the Digiheater software. The system regulates the temperature by monitoring the resistance of the platinum wire using a 4-point probe measurement [19]. Two contacts of the spiral are used to apply a voltage for heating, while the two remaining contacts are used to measure the resistance. The resistance, $R(T)$, is temperature dependent and can be used as a resistance thermometer to measure the average temperature of the small spiral by applying the Callendar-Van Dusen equation:

$$R(T) = aT^2 + bT + c \tag{4.3}$$

The coefficient a is assumed to be zero in the temperature operating range of the chips, i.e. the resistance dependents linearly on the temperature. The coefficient b is pre-calibrated by the manufacturer. The coefficient c is then used to calibrate each chip inside the microscope at room temperature. Because of the four-point measurement, the resistance of the heating spiral is independent of the resistance between contacts and spiral. The software compares the target temperature with the temperature determined by the resistance measurement every 3 sec and adjusts the applied voltage if necessary. In addition, the user is able to predefine the temperature profile specifying the target temperature and time when that temperature should be reached. Because of the small volume which needs to be heated compared to the bulk heating holders, the temperature settling time is short. The manufacturer quotes a settling time in the order of seconds and a temperature stability of less than 1K at 1.200°C. In addition, the small volume allows for much faster heating and cooling rates allowing experiments with various heat treatments. Figure 4.4 shows the target temperature profile and the actual measured temperature during a quenching experiment. The sample is set to be

heated from room temperature to 700°C in 2 sec (heating rate 350 K/sec) and back to room temperature in 1 sec (cooling rate 700 K/sec). The measured heating rate is 300 K/sec and the target temperature of 700°C is not reached because of the immediate cooling down procedure with a measured rate of 540 K/sec. The maximum temperature displayed in Fig. 4.4 is 655°C. Because of the limited temporal resolution during the temperature measurement of 0.133 sec, the maximum temperature reached and the maximum temperature displayed are different. Assuming the heating rate stays constant and taking half the time period of the temporal resolution, the maximum temperature reached can be estimated to be 677°C and differs therefore about 3% from the target temperature. After cooling down again, the measured temperature differs less than 1% of the target temperature after a settling time of about 2 sec.

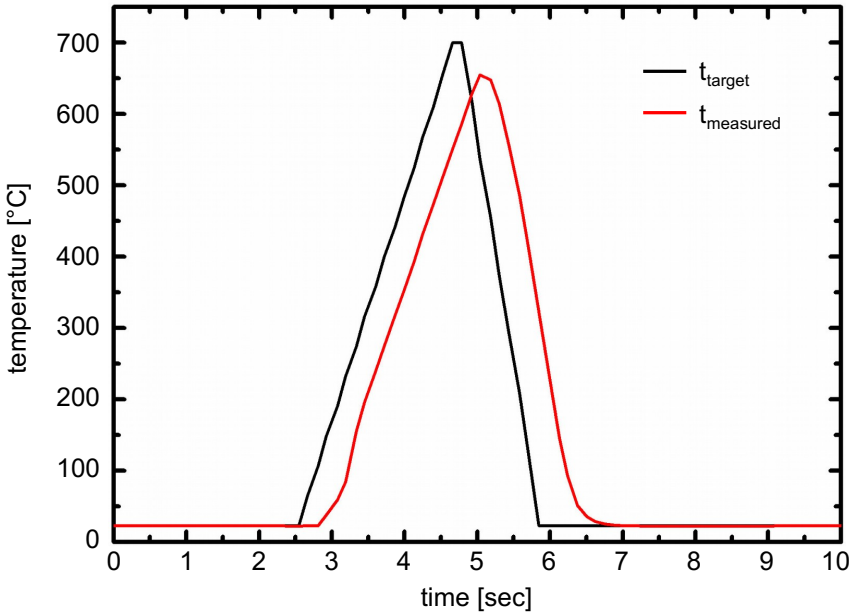

Figure 4.4 Temperature-vs-time plot of MEMS-based heating holder during quenching experiment displaying the target temperature (black) and the actual measured temperature (red).

Thermal drift. Because of the small volume which needs to be heated, the short temperature settling time and the high temperature stability of the MEMS-based holder, the thermal drift is significantly improved compared to the bulk heating holder. Figure 4.5 illustrates the drift in x- and y- direction over a duration of six minutes several minutes after reaching 640°C. In the graph of Fig. 4.5(a) the (x,y) position of a tracked sample area is plotted and in Fig. 4.5(b) the temporal development of the drift in both x- and y-direction is shown. The drift rate is less than 3 nm/min in either direction. In addition to the lateral drift in x- and y-direction, the sample moves in z-direction and therefore out of focus due to a bulging of the SiN membrane. The movement in z-direction is 8–10 µm when the sample is heated from room temperature to 400°C according to the stage reading. This movement is reproducible, and when the sample is cooled to room temperature again, the same z-position as before heating is regained. Thus, after a quenching experiment like the one shown in Fig. 6.19 the

holder returns to the same sample position within 5 nm (laterally).

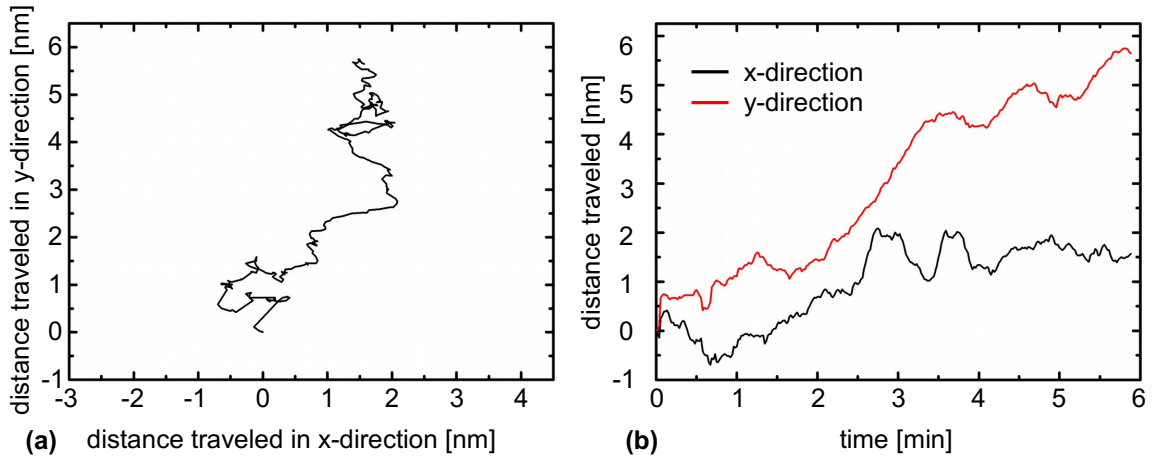

Figure 4.5 (a) The graph shows the (x,y) position of the same sample area (which is tracked over time) illustrating the overall lateral sample drift using the MEMS-based heating holder. (b) Graph shows the temporal development of the distance a certain sample position traveled in x- (black) and y-direction (red) over the course of six minutes.

To sum up, the accuracy of the temperature as well as the control of heating and cooling rate are less precise in case of the bulk heating holder compared to the MEMS-based heating holder. However, the presented dynamic in-situ studies are mostly performed at a fixed temperature and, therefore, they are less affected by drift or fluctuation of the targeted temperature as by the specimen induced local temperature variations. In addition, the conventional preparation technique is perfected and leads to reliable high-quality TEM specimen which are suited for HRTEM studies and are without Ga^+ ions contamination.

4.2.3 Influence of e-beam

The main effects of the electron beam on inorganic specimens during electron microscopic experiments are hydrocarbon contamination, displacement damage, sputtering damage and heating. In the following, the influence of the different effects on in-situ studies, especially for GeSbTe specimen, is discussed. Detailed information about e-beam damages can be found in Ref. [85] and [86].

Hydrocarbon contamination. The electron beam can polymerize hydrocarbon molecules on the surfaces of TEM specimen which leads to local mass gain [85]. The increase in local specimen thickness leads to poorer visibility and alters the surface of the specimen. The source of hydrocarbon molecules can be the imperfect vacuum inside the TEM and nowadays more importantly the specimen itself through sample preparation or storage and transfer. To minimize the hydrocarbon source on the specimen, the samples are treated in the GATAN plasma cleaner exposing it to energetic ions prior to TEM investigations. In

addition, heating the sample inside the microscope leads to the desorption of the hydrocarbons from the sample surface resulting in hydrocarbon contamination to be a minor problem during in-situ studies.

Displacement damage and sputtering. Due to the conservation of energy and momentum, there is a change in energy of the incident electron when it is deflected through an angle θ [85]. This energy change depends on the scattering angle and is small for small scattering angles used in TEM justifying the approximation of no energy change for elastically scattered electrons in the previous chapter. For back scattered electrons however, the energy transfer can amount to several eV [85]. When the energy transfer is higher than a displacement energy of the material which in turn depends on atomic bonding energies [86], displacement damage can lead to the degradation of crystallinity. For instance, Fig. 4.6 shows the amorphization of the Si-GST interface region at 400°C caused by recording the Si-GST interface region at a high magnification (contracted e-beam) in the JEOL 3010 at 300 kV. To estimate the sputtering rates Lotnyk *et al.* [87] used a highly focused scanning electron beam in a C_s-corrected FEG TEM with a high incident current density (108 e/A^{2}s) to move Ge and Sb atoms in the neighboring GeSb layers creating lines of vacancies. When the high-angle scattering happens at an atom on the surface of a specimen, the displacement can lead to the removal of said atom, a process known as sputtering [85]. According to an estimation of Lotnyk *et al.* [87], the sputtering rates for Ge and Sb atoms are 0.0003 monolayers per second and 0.0002 monolayers per second respectively for the incident current density of 108 e/A^{2}s using a Cs-corrected 200 kV TEM.

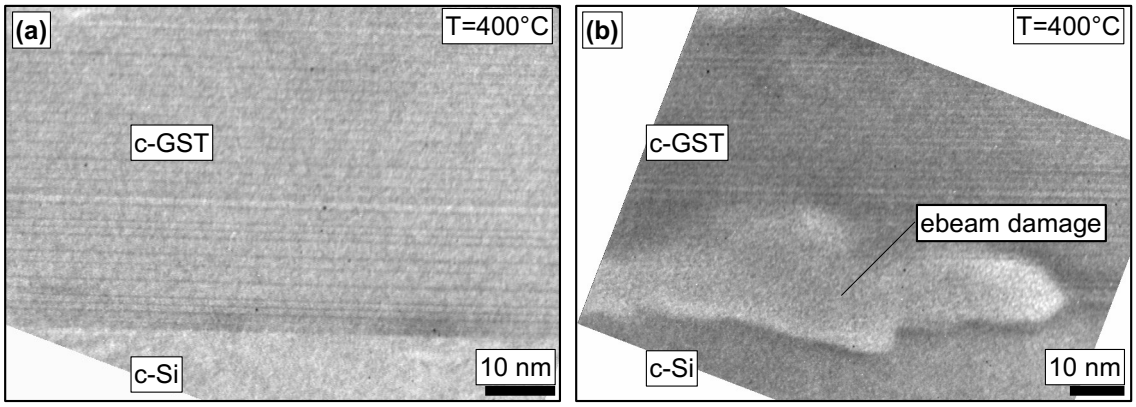

Figure 4.6 Amorphization due to electron beam radiation: crystalline GeSbTe (GST) thin film on crystalline Si substrate at 400°C (a) before and (b) after high magnification recording of the GST-Si interface region at 300 kV.

Heating. During inelastic scattering the transferred energy between incident electrons and atomic electrons (seen as energy-loss in EELS) leads to heating up the specimen. The rise in local temperature depends on the material which is investigated (thermal conductivity, average energy-loss per collision) and the imaging conditions (beam current and beam diameter). This local temperature change adds to the uncertainty of the temperature measurements discussed previously. For materials related to the material investigated in this thesis, only a

small rise in temperature is reported in literature using a comparable experimental set-up. Jencic et al. [88] calculated the maximum temperature to be no more than 7 K for Ge thin film, Yim et al. [12] estimated the temperature rise to amount to 15 K in GeTe thin films and Buha et al. [21] did not observe a temperature rise at all in BiTe nanocrystals. Using the MEMS-based holder in the JEOL 2100F, the crystallization of amorphous $Ge_1Sb_2Te_4$ is observed at 132°C at HRTEM imaging conditions. It is reported to occur at 131°C [89] and is therefore well within the temperature uncertainty arising from the average temperature measurements of the holder.

Minimize influence. To minimize the effect of e-beam damages, a high beam voltage should be used in order to minimize the inelastic scattering cross-section (reduce beam heating) but it should be kept below the displacement and sputtering threshold (reduce displacement and sputtering damages). In addition, the electron dose (current density times recording time) should be as low as feasible. In order to check for e-beam influences on the observed processes, a comparison between in-situ and ex-situ heated samples can be made or between sample areas that were exposed to the electron beam and those that were not. Such a comparison between in-situ and ex-situ heated was done for $Ge_1Sb_2Te_4$ proving that the same microstructure is formed [90].

4.3 Sample preparation

Although transmission electron microscopy has many advantages there is one major drawback: The sample preparation is destructive and time-consuming. Since transmission of electrons is used to study the sample, it must be electron transparent and therefore be thinned down to the nanometer regime. The required thickness for electron transparency depends on the chosen investigation method, material properties (atomic number Z) and accelerating voltage of the electrons (leading to the potential of electrons, V). The latter influences the cross section for elastic scattering of electrons σ_{elastic} having the charge e through an angle θ by atoms with atomic number Z [35]:

$$\sigma_{\text{elastic}} = \pi \left(\frac{Ze}{V\theta} \right)^2 \tag{4.4}$$

The equation 4.4 shows the behavior of electrons in the TEM: Electrons scatter less with increasing accelerating voltage and high angles, and are scattered less by lighter atoms (small Z). The choice of investigation method is also crucial in determining the necessary sample thickness. For example, simulations to interpret HRTEM images require the weak-phase approximation to apply which assumes very thin samples of a couple nanometer thickness [35].

In addition the sample holder limits the possible sample geometry. For instance, for the bulk heating holder the sample must fit in the 3 mm cradle. At the same time, the specimen needs to be stable enough to be loaded, transported and unloaded again. And even though the thickness of the samples needs to be reduced significantly in order to investigate it via TEM, the structure and chemistry should not be changed. Therefore preparation artifacts

need to be kept at a minimum and considered carefully when interpreting the experimental results. Thorough and reproducible sample preparation is key to successful experiments.

In this study the samples are prepared in cross-sectional geometry where the individual layers of the sample do not overlap and the interface between thin film and substrate are visible. Thus providing the opportunity to investigate the influence of the crystalline substrate on the high-temperature phase transitions.

In order to achieve different sample surface environments which are necessary to observe the melting (chapter 6) as well as the sublimation process (chapter 7) inside the microscope, two different preparation techniques are used: The conventional preparation for cross-sectional TEM samples and the micro-sampling technique with focused ion beams. In the following both are discussed in more detail.

4.3.1 Conventional TEM preparation

The cross-sectional TEM samples used in the bulk heating holder are prepared by applying the standard procedure of mechanical grinding, dimpling and argon ion beam milling [91, 92]. Figure 4.7 shows a schematic illustration of the necessary preparation steps. Sample stripes along the [110] direction are cut with a diamond wire saw from Well into 2 mm wide pieces (step 1). They are glued face-to-face together using a two-component epoxy (Gatan G1) (step 2), embedded in a brass cylinder with Ø 3 mm together with two silicon pieces for stabilization and enhanced thermal conductivity (step 3) and cut in slices of 500 µm thickness with the wire saw (step 4) before they are mechanically ground to 100 µm (step 5) and dimpled to the final central thickness of 5–10 µm (step 6). Finally, the samples have been thinned by argon ion beam milling with an energy of 3 keV under an incident angle of 3° using the Gatan precision ion polishing system (model 691) until a small perforation occurred (step 7). The region around the perforation is suitable for TEM investigations (cf. (8) in Fig. 4.7).

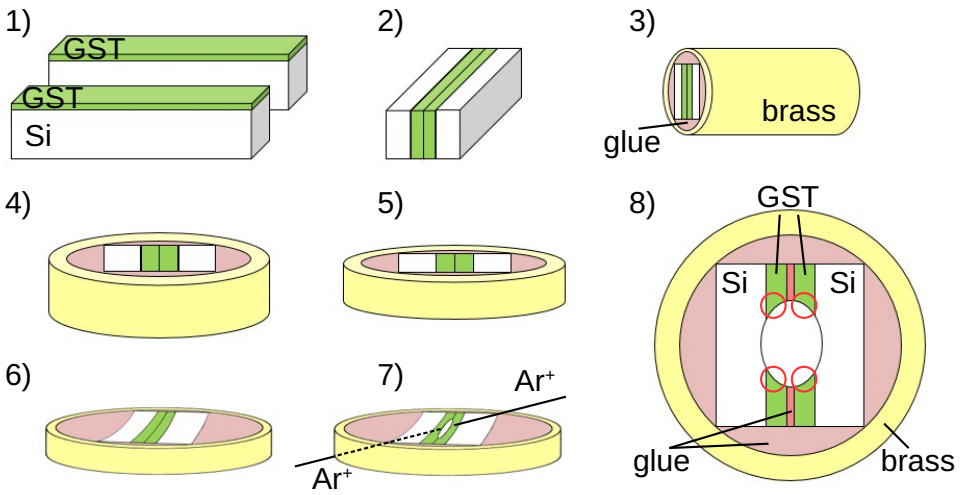

Figure 4.7 Schematic illustration of conventional cross-sectional TEM preparation: 1) cutting, 2) gluing face-to-face, 3) gluing in a brass tube, 4) cutting into disks, 5) grinding and polishing, 6) dimpling, 7) Ar^+ ion milling and 8) final TEM sample with area of interest marked in red.

Preparation of GeSbTe thin films. In order to preserve the initial amorphous state of the GeSbTe thin films, special care has to be taken regarding the temperatures the samples are exposed to during preparation. The crystallization temperature is about 130°C and therefore the temperatures reached during preparation should be considerably lower:

- The wax used in several steps for fixation is normally used at 140°C but starts softening around 90°C. The lower temperature has the disadvantage of a higher viscosity of the wax requiring a more careful thickness calibration.
- The epoxy can be cured at lower temperatures by prolonging the curing time.
- During ion milling the samples are cooled with liquid nitrogen to prevent unnecessary heating.

4.3.2 Micro-sampling technique with focused ion beams

For MEMS-based sample holders, the use of another preparation technique is required. The cross-sectional TEM samples are prepared in a lamella geometry and placed directly on the micro-hotplate (spiral) of the Nano-Chips (MEMS device). This preparation is done with a JEOL IB4501 dual beam system that combines a focused ion beam (FIB) and a scanning electron microscope (SEM). A good overview and introduction to the technique is given in [93]. First, the specimen is cut out of a wafer and transferred to a copper grid, where it is etched plane-parallel. After that, it is placed on the micro-hotplate where the final thinning to electron transparency is done. Figure 4.8 shows FIB and SEM secondary electron images (SEI) which illustrate several preparation steps. In the following the individual steps are explained in more detail.

Carbon coating. Before placing the sample inside the vacuum chamber of the FIB, a thin carbon film is deposited onto the wafer utilizing a carbon coater. This step is necessary in order to protect the GeSbTe thin film from direct Ga^+ ion exposure. The carbon coater from Quorum Technologies (model CC7650) evaporates carbon onto the specimen by heating a carbon fiber inside a vacuum chamber. The final film thickness can be varied by the distance of the sample from the fiber and the duration of the evaporation process. One has to keep in mind that by shortening the distance more carbon will be deposited but the heat generated close to the fiber could lead to unwanted crystallization of the amorphous thin film. In order to preserve the initial state of the sample, the largest possible distance is chosen. In addition, the evaporation periods are interrupted by pauses to give the system time to cool off.

Lift-out and transfer to copper grip. The carbon coated sample is placed inside the FIB where a lamella is cut out of the wafer and transferred to a copper grid using the standard FIB micro-sampling technique [94]. First, the area of interest is protected by ion beam assisted carbon deposition (Fig. 4.8a). Afterward, trenches are cut into the material around the protective layer to gain accesses to the lamella (Fig. 4.8b). Then, the bottom of the lamella is separated from the wafer by FIB milling and only a small bridge holding the lamella in place is left over. In addition, small regions left and right of the lamella with half the lamella thickness were left over (Fig. 4.8c). Those small "arms" are used as tools for easier positioning of the micro-manipulator, especially because there are several transportation steps

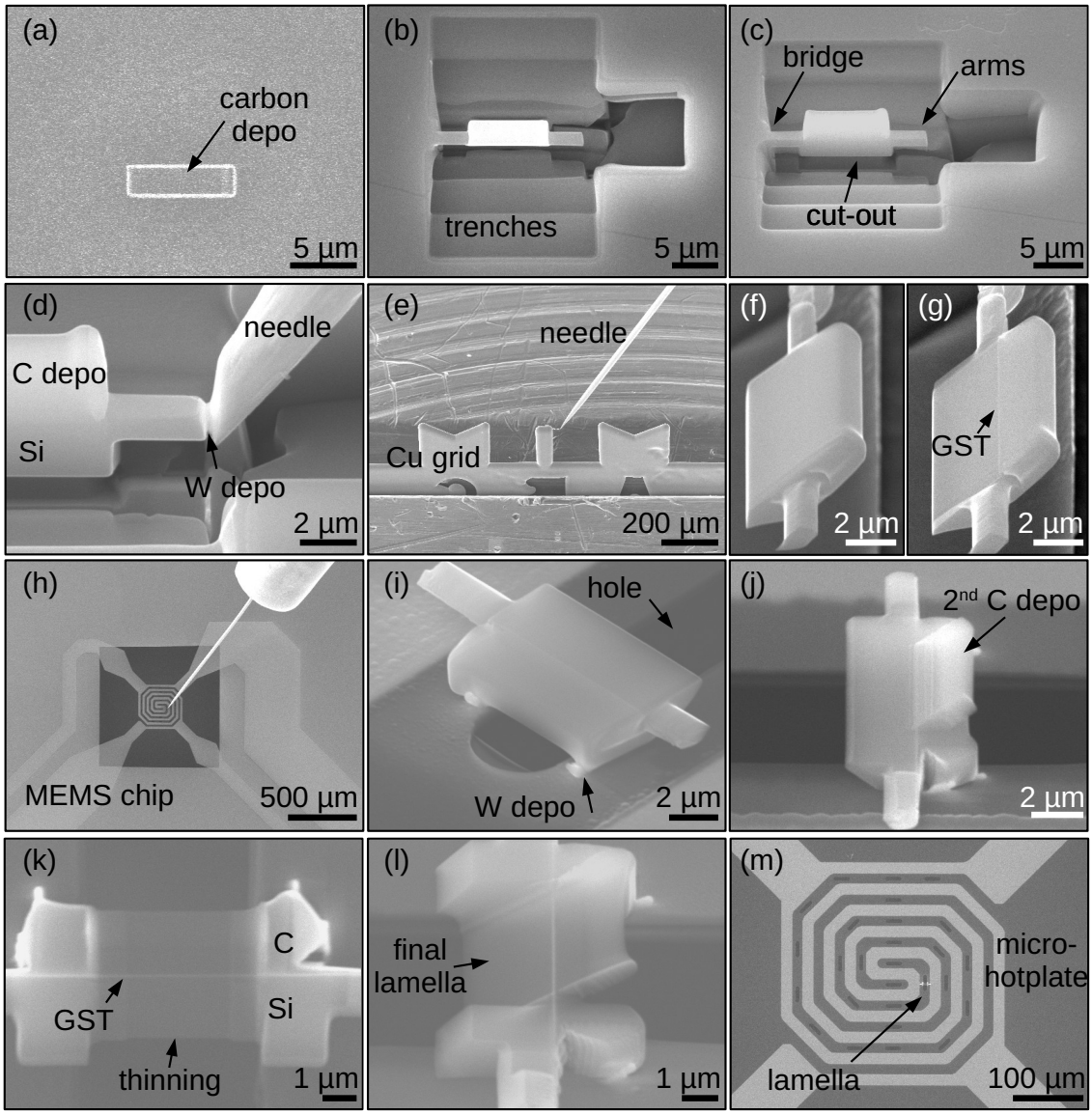

Figure 4.8 (a) FIB and (b)-(m) SEM secondary electron images of several preparation steps illustrating the micro-sampling technique via focused ion beams and transport to MEMS micro-hotplate.

necessary. The transport inside the FIB vacuum chamber is done by a micro-manipulator from Kleindiek Nanotechnik GmbH. The sharp tungsten needle from the manipulator is attached to one side of the lamella by ion beam assisted tungsten deposition (Fig. 4.8d). The lamella is then cut loose from the bulk by cutting the remaining bridge to the wafer and moved with the manipulator to a half-moon copper grid (Fig. 4.8e). There, the lamella is transferred from the sharp needle to the grid via tungsten deposition and subsequently FIB milling of the region connecting the needle to the lamella. To preserve the chosen crystallographic direction, the lamella needs to be rotated in a controlled way by 90° before placing it onto the Nano-Chip. Since the stage rotation is limited to 52°, the intermediate step of transferring the lamella to a copper grid is done. This allows rotating the lamella twice by 45° to achieve the full 90° rotation. In addition, the free-standing lamella on the grid can be

made plan-parallel by FIB milling (Fig. 4.8(f,g)) and this way the lamella can be placed flat onto the chip.

Transfer to chip and electron transparency. The lamella is then transferred onto the DENSsolutions chip using the micromanipulator (Fig. 4.8h). On the chip, it is placed over a hole within the micro-hotplate (Fig. 4.8i). The lamella is then glued to the chip by tungsten deposition to hold the lamella in place while cutting it loose from the needle. In order to protect the chip, the final thinning of the lamella to electron transparency is not done in a small grazing angle geometry. Therefore, a second carbon layer under 38° is placed on the lamella (Fig. 4.8j) and used to protect the sample while thinning the lamella via FIB milling (Fig. 4.8k). To minimize the thickness of the damage layer, ion beam accelerating voltages down to 5 kV are used. The final lamella is shown in Fig. 4.8(l). Even though all holes within the micro-hotplate can be used, the manufacturer states that a homogenous temperature distribution is best achieved in the central part of the chip where the lamella is therefore placed (Fig. 4.8m).

Ga contamination. During the FIB preparation, Ga^+ ions are deposited on or incorporated into the sample mainly in the protective carbon layer. During in-situ heating gallium becomes mobile ($T_M^{Ga} = 29.8°C$ [95]) and clusters into Ga droplets as shown in the BF-and HAADF-STEM images in Fig. 4.9(a,b,c) posing a risk of interfering with the process under study. Heating the sample further, several Ga droplets grow together and form bigger Ga droplets as shown in the BF-STEM images in Fig. 4.9(d). Despite the Ga contamination itself, those Ga droplets present an additional experimental challenge for in-situ heating experiments: Fig. 4.9(e) shows a TEM image of a Si-GeSbTe interface region where the Ga droplet obscure the view. An effective way to suppress the interference by Ga droplets is the application of a sufficient thickness of the protective carbon layer, in which case the Ga droplet will be formed away from the region of interest.

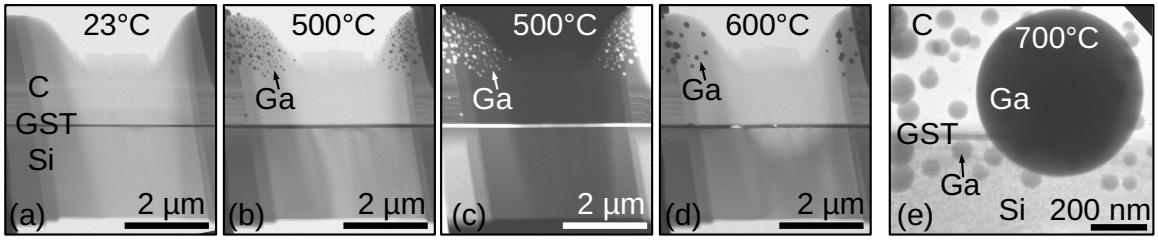

Figure 4.9 (a), (b), (d) BF-STEM and (c) HAADF-STEM images of the same lamella at different temperatures showing the formation and growth of Ga droplets in the carbon protection layer, (e) TEM image of GST-Si interface region in a different lamella with Ga droplets obscuring the view.

4.3.3 Summary

For processes where a slow temperature ramp-up is suitable and there is time for intermediate steps to minimize the sample drift, the conventional bulk heating holder can be used. This allows the conventional sample preparation technique to be applied and thus ensuring

high qualitative TEM specimen suited for high resolution without the Ga^+ ions contamination. Other experiments where a fast temperature response is necessary (such as quench treatments) or where a high resolution needs to be achieved fast after reaching the target temperature, the MEMS-based heating holder is used. It allows faster heating and cooling rates and provides lower sample drift. However, focused ion beams need to be used during sample preparation leading to Ga^+ ions contamination. This needs to be considered during the in-situ experiments since Ga becomes mobile at temperatures slightly above room temperature. An effective way to suppress the interference of forming Ga droplets during in-situ observation is a sufficiently thick protective carbon layer that allows the Ga droplet to form away from the region of interest.

5 Material system Ge-Sb-Te

This chapter is dedicated to the phase change material system Ge-Sb-Te used in this thesis as case study for the observation of high-temperature phase transitions. A comprehensive overview of this intriguing material class can be found in Ref. [31, 96, 97]. Here, a summary is presented focusing on material properties related to this work. First, the general idea of phase change materials is introduced in section 5.1. Then, the structures for the different relevant phases of the Ge-Sb-Te system are summarized in section 5.2. Section 5.3 focuses on relevant thermodynamic data of GST.

Finally, in-situ TEM observations of solid-to-solid phase transitions of Ge-Sb-Te studied in the framework of this thesis are discussed in section 5.4.

5.1 Introduction to phase change materials

The term phase change materials (PCMs) summarizes materials which combine two intriguing properties. They exhibit a fast and reversible phase transition between two solid states and both states differ distinctly in their physical properties such as electrical resistivity and optical reflectivity. The combination of those two properties makes them quite useful for information storage application. And indeed, they have been successfully used in optical information storage applications such as DVDs and Blu-rays for many years already [24, 47, 98].

The working principal of rewritable data storage application is illustrated in Fig. 5.1 and has been described e.g. in Ref. [24, 98]. In optical data storage the difference in reflectivity between amorphous and crystalline phase is exploited [24, 47, 98], whereas in applications of electrical data storage (such as random access memory) the difference in resistivity is used [24, 99–101]. Depending on the application either a laser or current pulse is used to store information by locally amorphizing ("write") or recrystallizing ("delete") the phase change material. For the writing process, a high and short pulse is used to locally amorphize the initial crystalline phase change material by raising the local temperature above the melting temperature and subsequently quenching the melt. This process is the power limiting process as the melting temperature of the material needs to be reached. For the deleting process, the amorphized region is crystallized again. Therefore a low and long pulse is needed to raise the temperature locally above the crystallization temperature long enough to crystallize the entire region. This step is the data-rate limiting process as the crystallization is the slowest process. Switching speeds around 50 ns have been reported [102–104] making it still slower than the 10 ns needed in DRAM storage solutions [105]. The latest developments are interfacial phase-change memory concepts where a superlattice structure is used to achieve faster crystallization speeds [106]. The melt-quench process during the write cycle on the other hand is much faster, otherwise recrystallization happens during a slow cool-down. Quenching rates for amorphization must therefore be in the order of 10^{10} K/s [62, 107]. Finally,

a short and low pulse can then be used to differentiate whether a region is amorphous or crystalline by detecting the difference in reflectivity or resistivity. The amorphous phase has a low reflectivity and a high resistivity whereas the crystalline phase has a high reflectivity and a low resistivity. Once the information is written the corresponding state (amorphous, crystalline) is kept without further power consumption making a non-volatile memory possible.

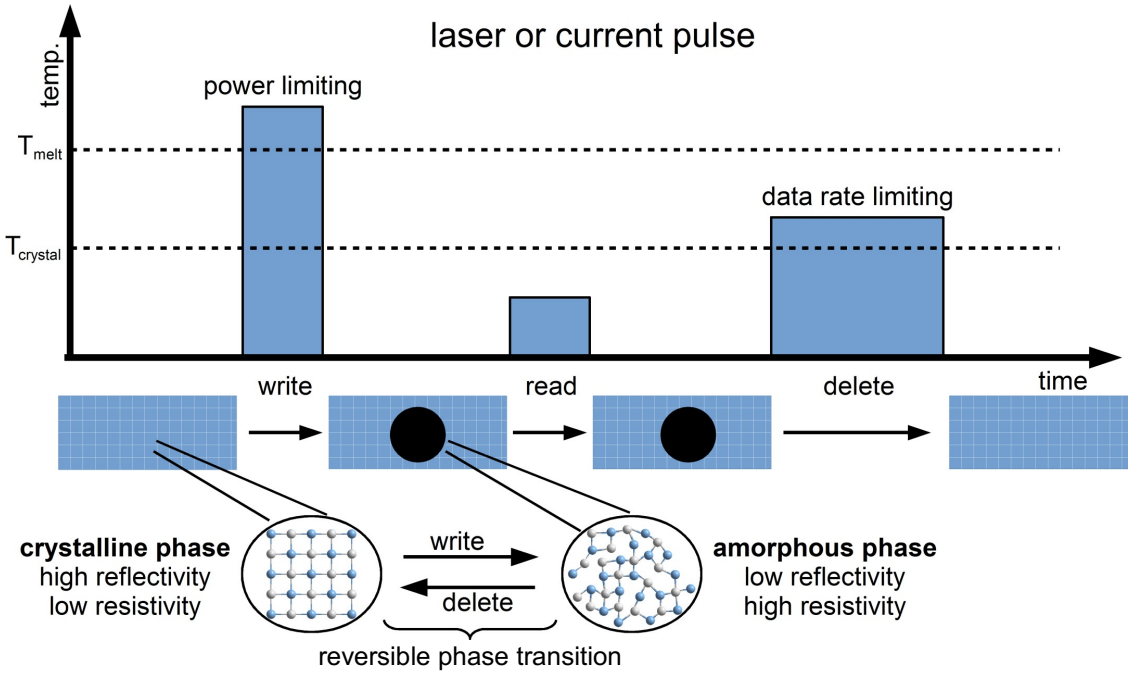

Figure 5.1 Schematic illustration of the information storage application of phase change materials.

For applications in the storage technology, the main criteria for a suitable material are therefore fast phase transitions (high data-rate), thermal stability of amorphous state (endurance), large contrast in a physical property between the two states (readability), chemical stability (durability for many cycles) and a low melting point (low power consumption) [24, 96]. Some of those requirements are contradictory and a good balance for the specific application has to be found. For instance, the ideal material has a low melting temperature, T_m, to achieve low power consumption. At the same time, a high thermal stability of the amorphous state and therefore a high crystallization temperature, T_c, is needed for endurance of the device. But both temperatures are not independent of each other. As a rule of thumb T_c lies between $\frac{1}{3}T_m$ and $\frac{2}{3}T_m$ [96].

In the late 1980s, Yamada *et al.* showed that GeTe-Sb_2Te_3 (GST) alloys were suited to fulfill the requirements for storage applications [89, 96]. They exhibit a large contrast of two orders of magnitude in resistivity [108] and reflectivity [96]. They can be crystallized very fast (around 50 ns [102, 103]) and at the same time retain the amorphous phase for several years [96]. Finally, the phase transition is highly reproducible and a large number of cycles can be reached due to their single-phase behavior [96, 109]. GST is therefore a typical and well known representative of phase change materials and used in this work as case study to

investigate high-temperature phase transitions.

5.2 Structure

The GeTe-Sb_2Te_3 (GST) alloys belong to the chalcogenides which are materials containing at least one of the Group VI elements, in this case Te [31]. Compositions along the GeTe-Sb_2Te_3 pseudo-binary tie line can be described as a compound of the two binary systems GeTe and Sb_2Te_3. GST has two crystalline states under ambient pressure conditions: At low temperatures, it exhibits a cubic phase and transforms into a trigonal phase at high-temperatures (which is often referred to as the hexagonal phase) [25, 89, 109–112].

5.2.1 Cubic phase

The low-temperature cubic phase is the technologically relevant phase as laser-irradiation of an amorphous GST film leads to its formation [89]. The cubic phase is described as a NaCl-like structure belonging to the cubic space group $Fm\bar{3}m$ [89, 113]. The structure can be viewed as two face-centered cubic (fcc) sublattices which are displaced relative to each other by $\left(\frac{1}{2}, \frac{1}{2}, \frac{1}{2}\right)$. In Figure 5.2(a), the NaCl-like structure of GST is displayed. The tellurium (Te) atoms occupy one sublattice (4(a) sites) and germanium (Ge) and antimony (Sb) atoms the other sublattice (4(b) site) [109, 113, 114]. A local distortion of the cubic phase resulting in shorter and longer Ge-Te and Sb-Te bond lengths was experimentally shown using extended X-ray absorption fine-structure spectroscopy [47] and theoretically calculated using density functional theory [115, 116]. Thereby, the Ge and Sb atoms deviate from the ideal NaCl position which is attributed to the differences in the covalent radii of the elements leading to an "overall buckled structure" [47]. The intrinsic vacancies of the structure are located on the Ge/Sb sublattice and their concentration depends on the chemical composition [109]. The lattice parameter, a_{cub}, also depends slightly on the composition and is listed in table 5.1.

composition	phase	space group	a [nm]	c [nm]	Ref.
GST225	cubic	$Fm\bar{3}m$	0.6027*	–	[117–120]
GST124	cubic	$Fm\bar{3}m$	0.60440*	–	[90, 110, 118]
GST147	cubic	$Fm\bar{3}m$	0.60876*	–	[118]
GST225	trigonal	$P\bar{3}m1$	0.42247	1.72391	[119, 121–124]
GST124	trigonal	$R\bar{3}m$	0.42721	4.1686	[90, 110, 122, 125, 126]
GST147	trigonal	$P\bar{3}m1$	0.425	2.3852	[121, 126]

Table 5.1 Lattice parameters for both cubic and trigonal crystalline GST structures, where GST225 refers to $Ge_2Sb_2Te_5$, GST124 to $Ge_1Sb_2Te_4$ and GST147 to $Ge_1Sb_4Te_7$.
*depends on the applied annealing temperature during crystallization with higher temperature leading to smaller lattice parameters, e.g. reported values for cubic GST225 range from 0.5964 nm to 0.6027 nm [117–120]

Although the crystal structure, space group and lattice constants of GST are well established, the specific atomic arrangement within the cubic unit cells is not comprehensively

solved. In particular, ordering phenomena in the Ge-Sb sublattice are still under discussion: Whether Ge, Sb and vacancies are randomly distributed [110, 113, 114], vacancies only or all three constituents at the same time are highly ordered and form single-species layers on (111) planes [120, 127, 128]. Using HAADF-STEM a vacancy semi-ordered cubic GST has been observed [129]. The degree of ordering can be changed by thermal annealing [130, 131] and electronic beam radiation [87]. Recently, Zhang *et al.* [111, 132] using HAADF-STEM observed that there are two cubic crystalline states: one with random distributions of vacancies and one with highly-ordered vacancies on (111) planes and that there is a transition between the two cubic states through thermal annealing [111, 132].

Figure 5.2(b) shows the structure of the disordered and the vacancy-ordered cubic (VOC) phase. For easy comparison, the atomic arrangement on the (110) plane is displayed. The difference lies in the highly ordered vacancy layers (VL) of the VOC state where vacancies accumulate and the corresponding (111) planes are fully depleted of Ge and Sb atoms.

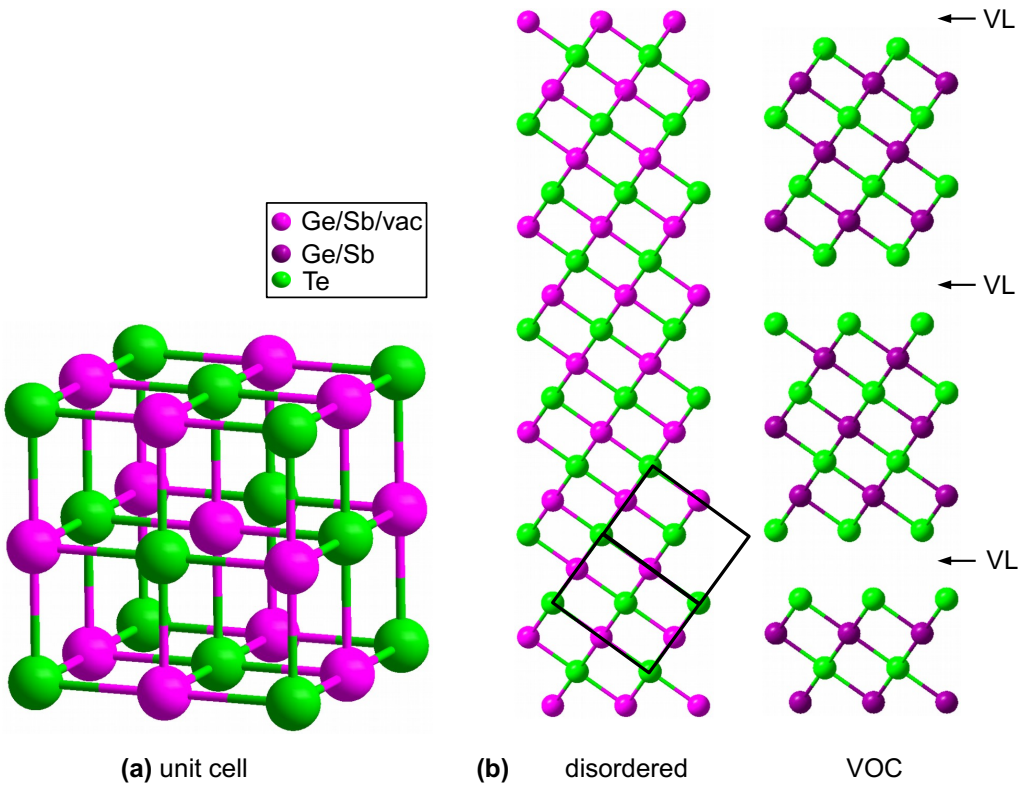

Figure 5.2 Schematic illustration of the cubic structure of GST. (a) shows a unit cell of the disordered state with Ge, Sb and vacancies randomly distributed on one sublattice. In (b), the disordered and vacancy-ordered cubic (VOC) states are compared and therefore the atomic arrangement on a (110) plane is displayed. The black box depicts the cubic unit cell. The difference between the states lies in the highly ordered vacancy layers (VL) in the VOC state where the vacancies accumulate and the corresponding (111) planes are fully depleted of Ge and Sb atoms.

5.2.2 Vacancies

Depending on the precise composition $(GeTe)_{1-x}(Sb_2Te_3)_x$, the percentage of vacancies changes according to the relation (5.1) [123]:

$$N_{\text{vac}} = \frac{x}{1+2x} \tag{5.1}$$

Therefore, with increasing Sb_2Te_3 content (larger x) in the GST composition, the number of intrinsic vacancies, N_{vac}, in the Ge/Sb sublattice increases. For three well-known compositions, the vacancy content is listed in table 5.2, e.g. $Ge_2Sb_2Te_5$ (GST225, x=1/3) has 20% vacancies.

The vacancies are of structural relevance and important for stability and the phase transition properties [42, 90, 133]. The occurrence of vacancies can be rationalized with the bonding nature of GST [47, 97, 116]: Bonding happens via the p-orbitals [134] which is ideal if the p-band is half filled with three p-electrons per lattice site on average. As Ge, Sb and Te have 2, 3 and 4 p-electrons, the ideal of three p-electrons per atom is fulfilled for GST for one Te and one Ge atom or three Te atoms together with two Sb atoms and one vacancy. That vacancies are indeed an intrinsic part of the structure is experimentally verified: By increasing the Ge [135] and Sb [113] content, the excess Ge and Sb atoms do not fill the vacancies in the Ge/Sb sublattice but accumulate at the grain boundaries or lead to phase separation.

composition	x	N_{vac}	n	m	N_{layers}
$Ge_2Sb_2Te_5$ (GST225)	1/3	20%	2	1	9
$Ge_1Sb_2Te_4$ (GST124)	1/2	25%	1	1	21
$Ge_1Sb_4Te_7$ (GST147)	2/3	28.6%	1	2	12

Table 5.2 Summary of crystal structure parameters for different compositions of GST: Number of vacancies (N_{vac}) in Ge/Sb sublattice and number of layers (N_{layers}) perpendicular to basal planes per unit cell in trigonal structure.

5.2.3 Trigonal phase

The high-temperature phase exhibits a trigonal crystal structure. The precise space group depends on the composition, e.g. GST225 belongs to the $P\bar{3}m1$ and GST124 to the $R\bar{3}m$ space group [121, 125, 136]. The atomic stacking sequence along the c-direction perpendicular to the basal planes (0001) is reported as being either fully ordered (Te-Ge-Te-Sb-Te-vac-Te-Sb-Te-Ge-) [122, 127] or with Sb and Ge atoms randomly occupying the same layer [110–112]. Siegrist *et al.* proposed that the degree of ordering depends on the annealing time [97].

Figure 5.3 displays the fully ordered structure to easily compare the three of the best known GST compositions, GST225, 124 and 147. The structure can be described as being composed of (GeTe) and (Sb_2Te_3) building blocks stacked on top of each other. The atomic arrangement is based on close-packed Te atoms with Ge and Sb in octahedral interstitial sites separated by van der Waals–bonded hexagonally stacked Te layers [97]. Cubic close-packed GeTe units are inserted into the centers of Sb_2Te_3 blocks and the number of blocks

depends on the specific composition, e.g. in GST124 there is one GeTe block in every Sb_2Te_3 unit [97]. On the other hand, the semi-ordered structure has mixed Ge and Sb layers [110, 111]. In the case of GST124 for example, there are Sb-rich layers with $Ge_{25}Sb_{75}$ (layers of red atoms in Fig. 5.3) and equally occupied layers with $Ge_{50}Sb_{50}$ (layers of blue atoms) in unison with the overall composition.

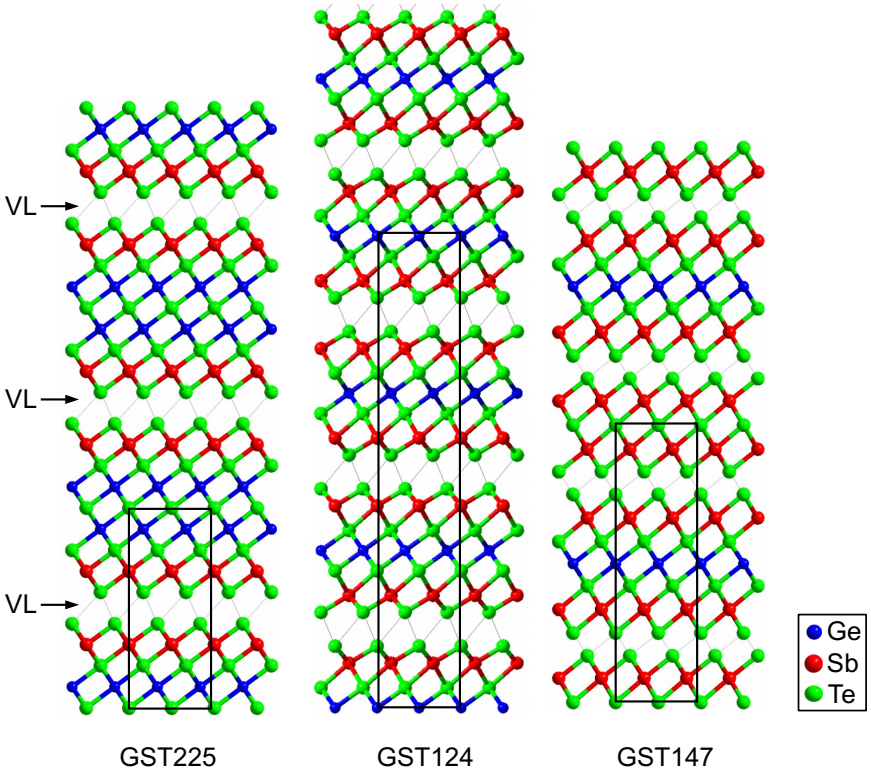

Figure 5.3 Schematic illustrations of the fully ordered, trigonal structure of GST225, 124 and 147 with Ge (blue), Sb (red) and Te (green) atoms. The black boxes show the trigonal unit cell and the black arrows mark the vacancy layers (VL), also known as van-der-Waals gaps between two Te layers.

The number of layers, N_{layers}, within one unit cell of the $(GeTe)_n(Sb_2Te_3)_m$ system can be easily determined using eq. (5.2) [96]:

$$N_{\text{layers}} = Z \cdot (2n + 5m) \text{ with } Z = \begin{cases} 1, \text{ for } (2n + 5m) \text{ divisible by 3} \\ 3, \text{ for } (2n + 5m) \text{ not divisible by 3} \end{cases} \tag{5.2}$$

Different compositions therefore have a distinct number of layers within one unit cell which are listed in table 5.2, e.g. GST124 (n=1, m=1) has 21 layers in one unit cell. The lattice parameter, c_{tri}, therefore depends strongly on the composition and is listed for some compositions in table 5.1 together with the second lattice parameter, a_{tri}.

Independent of the degree of ordering of the Ge and Sb atoms, the ordering of vacancy layers (VL) in the trigonal structure, also known as van der Waals gaps, between two neighboring Te layers, is present in both proposed stacking sequences [137]. The ordered se-

quence of VL is verified experimentally as well as theoretically with a measured distance of 1.39 nm in case of GST124 [112, 122, 123]. This VL ordering is used as a fingerprint for the existence of the trigonal crystal phase during the in-situ TEM studies of the liquid-solid phase transition.

Similarity between cubic and trigonal phase. The structures of both crystalline phases, cubic and trigonal, are similar. They can both be viewed as Ge/Sb and Te layers stacked along the $[111]_{\text{cub}}$ and $[0001]_{\text{tri}}$ direction, respectively, but they differ in the stacking sequence of the Te layers. The cubic structure has ABC-stacking whereas the stacking sequence of the trigonal structure depends on the composition (e.g. 124: ABABCACA and 225: ABCBCA). In addition, the distribution of vacancies is different. The vacancies in the cubic structure randomly occupy the Ge/Sb fcc sublattice whereas the vacancies in the trigonal structure are accumulated in vacancy layers between two adjacent Te layers. Calculating the total energy using *ab initio* calculations, Sun *et al.* showed that the energy difference is only 0.3% between the cubic phase and the trigonal, where the trigonal exhibits the lowest total energy [127].

5.2.4 Amorphous state

An amorphous state only exhibits short-range order and loses the long-range order which is characteristic for crystalline materials [138]. It can be described as an intermediate state between the perfectly ordered crystal and a dilute gas where atoms are randomly distributed with an average number of atoms per unit volume [31]. This can be illustrated using the radial distribution function (RDF), where the number of atoms is plotted as a function of distance from a given atom [138, 139] as shown in Fig. 5.4. In crystalline structures, the period atomic arrangements leads to distinct distances of each atom from a given atom and therefore the RDF is a series of delta functions [31]. In a dilute gas, atoms are uniformly distributed giving a parabolic RDF [138]. Information about the amorphous structure is therefore given by the deviation from this parabolic form [138]. The first broad peak corresponds to the nearest-neighbor distance and the disorder expressed in the variation of bond length and bond angles leads to a broadening of the peaks [31, 138]. With increasing distance the broadening increases and finally the disordered gas state is approached [31].

The amorphous structure of GST is still not comprehensively solved as it is difficult to obtain large quantities of melt-quenched GST and the number of suitable experimental techniques is limited [31]. So far, it was determined that the Ge-Te and Sb-Te bond length in the amorphous state are shorter than in the crystallized state and amount to 2.60-2.62 Å for Ge–Te and 2.82-2.84 Å for Sb–Te (compared to 2.83 Å and 2.94 Å in the cubic phase) ([31, 47, 140] and ref. therein). The bond lengths are therefore close to the sum of covalent radii of the constituent atoms ($r_{\text{Ge}} = 1.22$ Å, $r_{\text{Sb}} = 1.39$ Å, $r_{\text{Te}} = 1.36$ Å [141]) implying a covalent bonding nature [142] which is further underpinned by the fact that the coordination of the constituent atoms follow the "8-N" rule, i.e. Ge, Sb and Te are mainly four-, three and two-fold coordinated [31]. The same result is obtained for molten GST and based on the implied covalent bonding nature a semiconducting behavior was suggested [142]. This could be confirmed by electric resistivity measurements [143]. In addition, in laser-amorphized GST no Ge–Ge and Ge–Sb bonds were observed, whereas in as-deposited amorphous GST

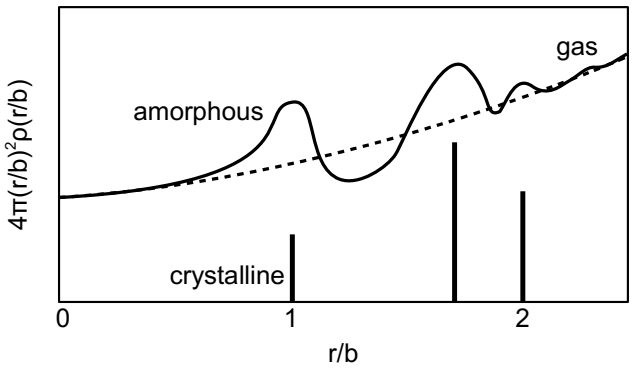

Figure 5.4 Schematic illustration of the radial distribution function (RDF) of amorphous and crystalline material. The number of atoms at a given distance from the atom (4π(r/b)$^2\rho$(r/b)) is plotted as a function of distance (r) from that given atom per bond length (b), after [31].

those "wrong" bonds are present ([31] and ref. therein). The term "wrong" is thereby attributed to the fact that Ge–Ge and Ge–Sb bonds are not present in the crystal. The bond lengths are 2.48 Å for Ge–Te and 2.69 Å for Sb–Te which are again close to the sum of the covalent radii [140].

The crystallization times for melt-quenched amorphous state are shorter than for the as-deposited amorphous state [144]. This fact and the observed differences in the structure of the two amorphous states lead to the suggestion that there is polymorphism of the amorphous states depending on the preparation pathway [31, 133, 144, 145]. There is a low-density amorphous (LDA) state which is found for as-deposited films [133] and a high-density amorphous (HDA) state observed after high-pressure amorphization of the crystalline structure [133]. In addition, studies found strong structural similarities between the melt, laser-amorphized and high-pressure amorphized phases in the short and intermediate range [30, 133, 146].

5.3 Thermodynamic data

5.3.1 Phase diagram of GeSbTe

The phase diagram for the GST alloy was first reported by Abrikosov and Danilova-Dobryakova [147] and then confirmed by Legendre *et al.* [148]. It is reprinted in Fig. 5.5 and shows that there are three compounds (GST225, 124 and 147) with incongruent melting. The incongruent melting for GST124 at 616°C transforms it into a liquid and GST225 which in turn melts at 630°C leaving behind a liquid and β-GeTe solid. According to Shelimova *et al.* [136], later studies found that only GST225 melts incongruently while GeSbTe124 and GeSbTe147 melt congruently at 615°C and 607°C, respectively.

5.3.2 Transition temperatures for solid-to-solid phase transitions

The quasi-binary alloy GST undergoes two solid-to-solid phase transitions. The first transition is from the amorphous to the cubic phase and the second from the cubic to the trigonal

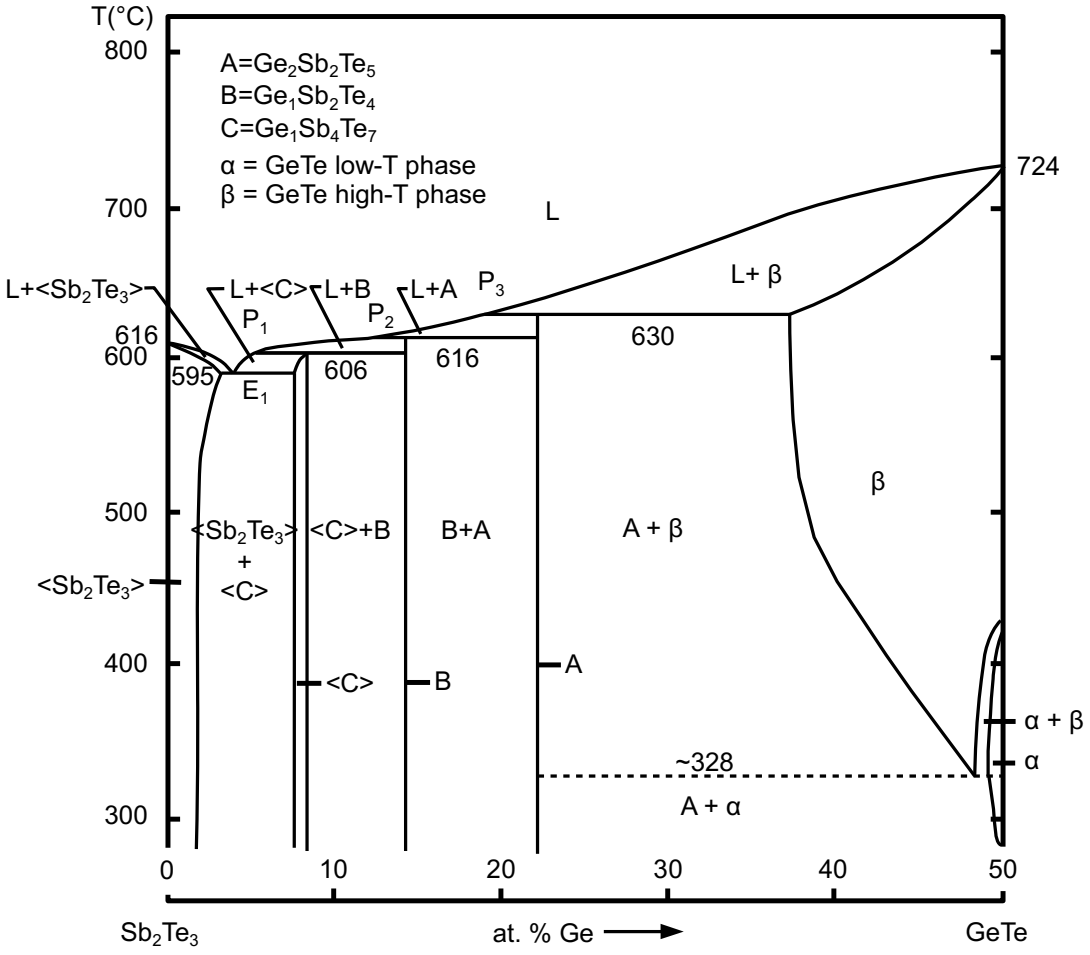

Figure 5.5 Phase diagram of Ge-Sb-Te alloy, reprinted with permission from Ref. [148].

phase. Both solid-to-solid phase transitions are accompanied by an abrupt change in atomic volume which indicates a first-order phase transition [30, 90, 110, 114, 149, 150].

The first transition from amorphous-to-cubic occurs at low temperature (T_{c1}~150°C) and the second from cubic-to-trigonal at higher temperature (T_{c2} ~300°C). In particular, the quasi-binary GST124 alloy undergoes the first transition at approximately 140°C and the second at a higher temperature around 220-300°C [89, 90, 118, 123, 149, 151]. For reference, melting takes place at 615°C under normal conditions [30, 89, 136, 152]. For different GST compositions the transition temperatures, T_{c1} and T_{c2}, and melting temperatures, T_m, are listed in the appendix in table A.4 and table A.3, respectively. The composition influences the transition temperatures: More (Sb_2Te_3) content leads to lower crystallization temperatures [89, 90, 96, 118, 153] which in turn lead to shorter laser heating times needed in device applications [96]. Furthermore, changes of the transition temperature are observed for doping with various elements. Mostly an increase in T_c is observed, e.g. for Si [117, 154–156], N [44, 157, 158], SiO_2 [159], Cu [160, 161], Al [161], In [162] and Ti [163, 164], but for some elements a decrease is reported, e.g. Sn and Bi [162]. The melting temperature on the other hand mostly decreases through doping [117, 159, 160].

5.3.3 Crystallization from amorphous phase

The process of crystallization involves two steps: nucleation and crystal growth as discussed in chapter 2.2.1. For metals, the driving force, ΔG_{ac}, for the amorphous-to-crystalline transition, can be approximated using the latent heat of fusion (ΔH_m) and the applied undercooling ΔT [165]:

$$\Delta G_{\text{ac}} \approx \frac{\Delta H_m \Delta T}{T_m} \tag{5.3}$$

For glass-forming systems, such as GST [166], ΔG_{ac} rises less rapidly with T [165]. Equation (5.3) can be adjusted to give eq. (5.4) [165]:

$$\Delta G_{\text{ac}}^{\text{glass-form}} \approx \frac{\Delta H_m \Delta T}{T_m} \left(\frac{2T}{T_m + T} \right) \tag{5.4}$$

For the latent heat of fusion of GST225 two different values are reported in literature: $\Delta H_m = 12.13 \frac{\text{kJ}}{\text{mol}}$ [165] and $\Delta H_m = 14.7 \pm 0.7 \frac{\text{kJ}}{\text{mol}}$ [167].

The crystal growth is controlled by rearrangement processes at the amorphous-crystal interface and does not depend on the position of the interface if the crystal and amorphous phase have the same composition. It is then time-independent and given by the difference between attachment and detachment processes multiplied by the average interatomic distance λ. For diffusion-limited kinetics, the crystal growth rate is given by eq. (2.14). Using the Stokes-Einstein relation relating diffusivity D and viscosity η, the growth rate can also be written as [33]:

$$u_{\text{interface-controlled}} = \underbrace{\frac{f_s 2 k_B T}{\eta \pi \lambda^2}}_{u_{kin}} \left[1 - \exp\left(-\frac{\Delta G_{\text{ac}}}{k_b T} \right) \right] \tag{5.5}$$

Orava *et al.* [165] used ultrafast calorimetry to analyze the crystal growth rate of amorphous GST225 for temperatures up to 0.72 T_m in order to determine the temperature-dependent growth rate and the growth rate maximum which is important in applications. They found a non-Arrhenius temperature dependence of η and therefore of u_{kin} (eq.(5.6)):

$$\log(u_{kin}) = A - \frac{B}{T - T_0 + \left[(T - T_0)^2 + 4CT \right]^{1/2}} \tag{5.6}$$

and determined the parameters to be $B = (121 \pm 2)\,\text{K}$, $C = (1.71 \pm 0.02)\,\text{K}$ and $T_0 = (427 \pm 1)\,\text{K}$. Using a theoretically determined viscosity at T_m for scaling [168, 169], the latent heat of fusion of $\Delta H_m = 12.13 \frac{\text{kJ}}{\text{mol}}$ and eq. (5.4), (5.5) and (5.6) they determined the growth rate from amorphous GST over a wide range of temperatures from the glass transition temperature ($T_g = 384\,\text{K}$) up to the melting temperature ($T_m = 900\,\text{K}$) which is displayed in Fig. 5.6. As expected the growth rate exhibits a maximum between T_g and T_m. It is in the order of m/s. Recently, other experiments also found similar high growth velocities: Zalden *et al.* [170] and Eising *et al.* [171] measured growth velocities in the order of m/s for comparable phase change materials (AgInSbTe and GeSb) using optical reflectance during optical excitation. Santala *et al.* [172] used ultrafast dynamic TEM for the laser-induced

crystallization of amorphous Ge which also happened in the order of m/s.

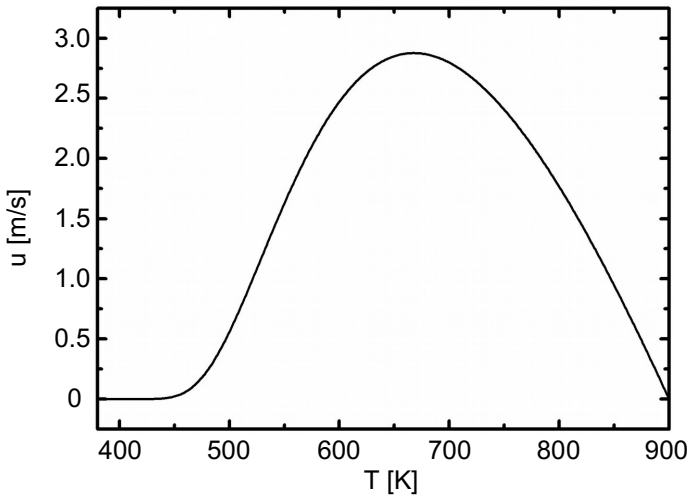

Figure 5.6 Crystal growth rate in supercooled liquid GST225 from the glass transition temperature ($T_g = 384\,\mathrm{K}$) up to the melting temperature ($T_m = 900\,\mathrm{K}$) [165].

Note that the experiments evaluating the growth velocity of phase change materials at high temperatures reported in literature so far used laser-excitation [170, 172] or are extrapolated from 0.72 T_m to T_m based on a theoretically determined viscosity value [165]. The experiments presented in this work study the thermal response of GST and therefore heating instead of laser-excitation is used as external stimulus. Nonetheless, the observation of the liquid-solid transition in chapter 6 are done close to the melting temperature in order to resolve the transition dynamics at high spatial resolution using the limited time-resolution of 25 fps in the experimental set-up.

5.4 In-situ TEM observation of solid-to-solid phase transitions

Even though GST has been successfully used in devices [24, 47, 58, 99, 102], the phase transitions, especially the involved structural changes, are not yet fully understood [47, 173]. The fast and reversible amorphous-to-cubic transition of GST is thereby the most frequently discussed in literature [25, 47, 111, 159, 173–178] due to its technological application.

In the following, the details known and discussed about both phase transitions are described using the results of an in-situ experiment for illustration. The TEM image series in Fig. 5.7 shows the transitions at low and high temperature of an initial amorphous GST film. Figure 5.7(a) displays the as-deposited amorphous GST thin film with a thickness of 55 nm on the crystalline Si substrate. For the work in this thesis, the Ge-Sb-Te (GST) thin films were deposited on a cleaned Si(111) substrate in an ultra-high vacuum chamber by using effusion cells for the three elements[1]. A detailed description of the deposition process is provided in Ref. [179, 180]. The as-deposited amorphous film exhibits a chemical composition that corresponds to $Ge_1Sb_2Te_4$ (GST124) which is ascertained by EELS measurements (cf. Fig. 5.8).

[1]The investigated GST thin films were grown by Dr. Alexandro Giussani (PDI).

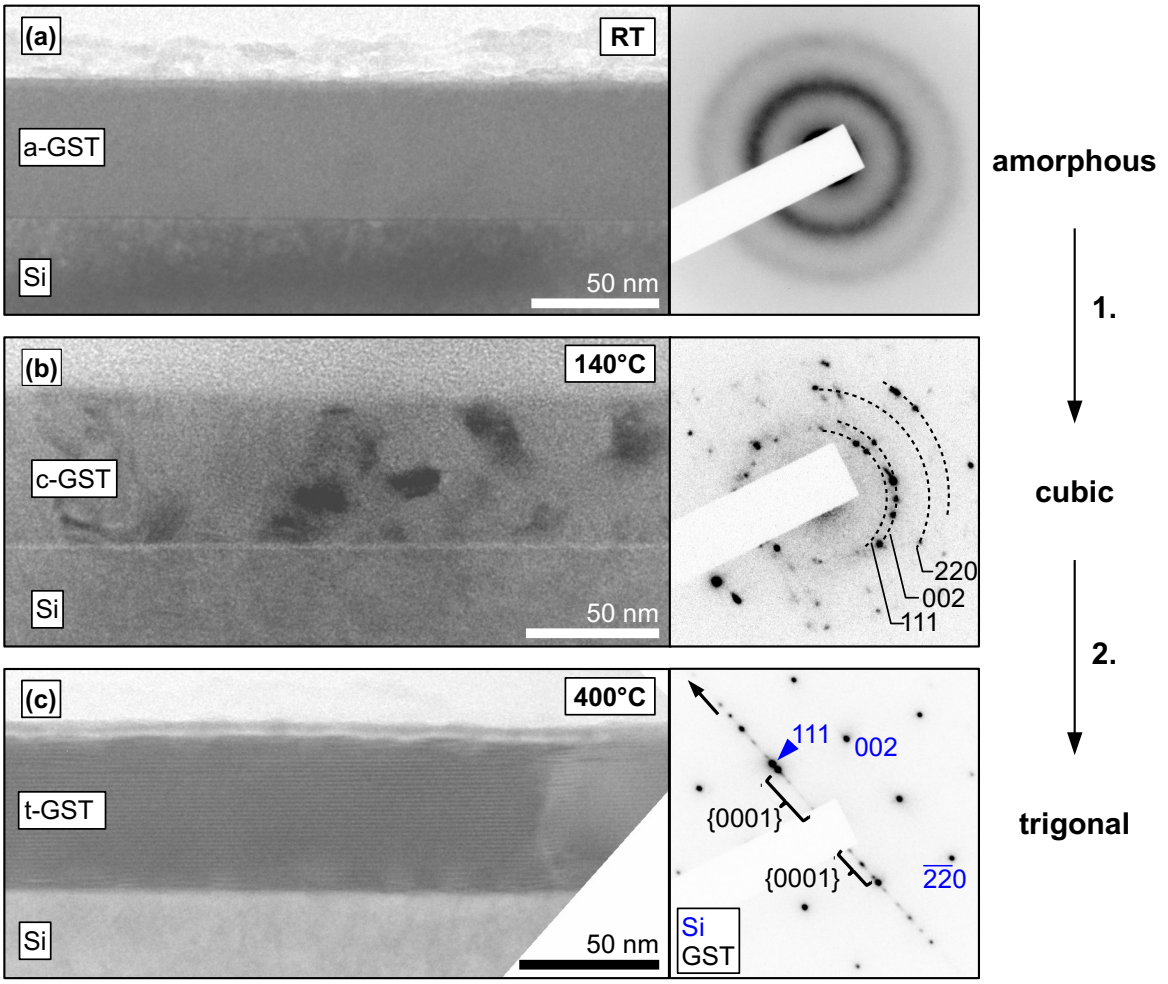

Figure 5.7 Low magnification TEM images showing the solid-to-solid phase transitions of GST thin film: (a) BF-TEM and SAD of the as-deposited amorphous phase at room temperature, (b) BF-TEM and SAD of the cubic crystalline phase after the first solid-to-solid transition at 140°C and (c) TEM and SAD image of trigonal crystalline phase after the second transition at 400°C. The SAD images are taken from the GST film at the corresponding temperature. The last SAD image shows additionally the diffraction spots of the silicon substrate (blue) and the arrow marks the direction of surface normal.

5.4.1 Low-temperature transformation: amorphous-to-cubic transition

The in-situ TEM measurements are done at the JEOL 3010. Using the JEOL heating holder for the conventional prepared sample, the GST film is heated from room temperature to above the first transition temperature at 140°C with 15°C/min. After annealing for several minutes, the whole amorphous film is crystallized.

Microstructure of cubic phase

The BF-TEM image in Fig. 5.7(b) shows the microstructure after the amorphous-to-cubic transition of the as-deposited amorphous GST film . The crystalline grains are 10-20 nm in size and randomly oriented. The SAD pattern shown in Fig. 5.7(b) is used to differentiate between the trigonal and the cubic phase. In this case, the cubic structure is identified by

the ratios of the spot spacings. The polycrystalline nature is confirmed by the observed ring pattern. To determine the lattice parameter of the GST grains, the indexed ring pattern is used to measure the d-values for (111), (200) and (220) and from those the average lattice parameter of GST a_{GST} is calculated using eq. (5.7) [181].

$$a_{\mathrm{GST}} = d_{\mathrm{hkl}}\sqrt{h^2 + k^2 + l^2} \tag{5.7}$$

The determined lattice parameter $\mathrm{a_{GST}} = (6.1 \pm 0.1)\,\mathrm{nm}$ is in agreement with the reported lattice parameter of 0.60440 nm for bulk cubic structured GST124 within the accuracy of the measurement [90, 110, 118].

The composition along the film is determined using the EELS quantification method described in section 3.3.3. Figure 5.8 shows the composition of the initial amorphous state at room temperature (first half) in comparison to the composition of the crystalline state after annealing at 140°C (second half). For each phase, three sample positions along the film are measured which are 100 nm apart. The EEL spectra are recorded using a 20 nm spot. Both the amorphous and the crystalline film exhibit a homogenous composition along the film. In addition, there is no observable difference between the composition of the amorphous and crystalline phase. Therefore, the composition is stable upon crystallization within the accuracy of the method.

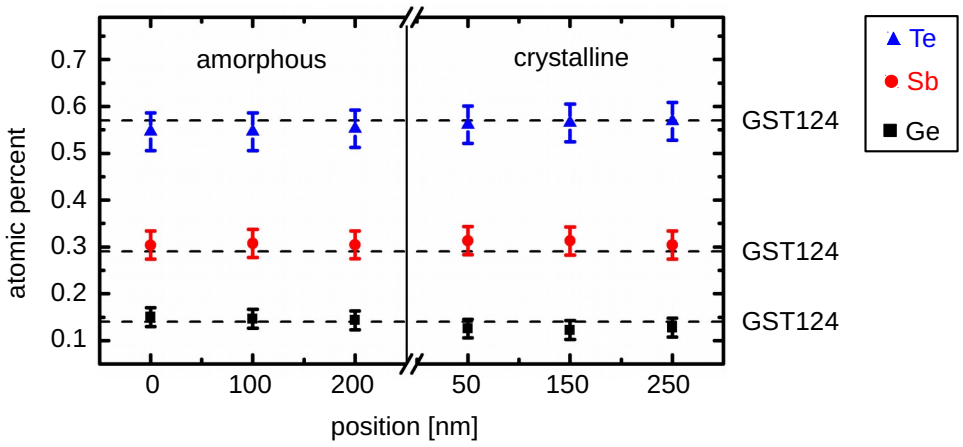

Figure 5.8 Atomic percent of Ge, Sb and Te content of the GST film obtained from core-loss EEL spectra taken at different positions along the film before and after crystallization.

Nucleation and grain growth

Figure 5.9 shows the onset of the amorphous-to-cubic transition which is observed 3 minutes after reaching 120°C. The BF-TEM image reveals isolated small crystallites within the amorphous GST phase. The nucleation of GST is homogenous and occurs within the GST film. Recently, Noe *et al.* [177] thoroughly investigated the crystallization behavior of GST thin films as function of the oxide structure at the film surface. They observed homogenous nucleation in adequately protected GST films and found that the previously reported heterogeneous nucleation on the GST surface [25, 175, 176, 182] is due to surface alterations.

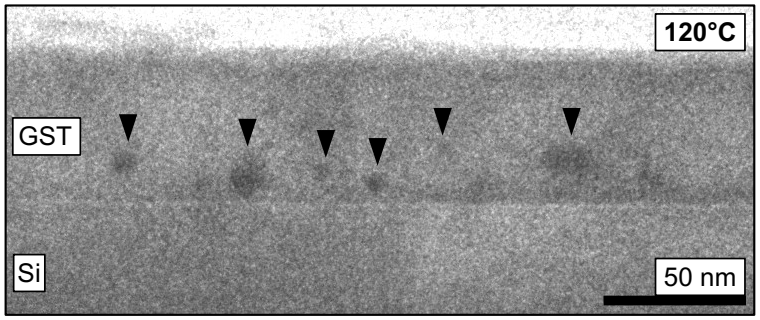

Figure 5.9 BF-TEM showing the onset of the amorphous-to-cubic phase transition at 120°C, where cubic grains (marked with arrows) nucleate within the GST film.

After nucleation the formed crystallites grow. Figure 5.10 shows the growth of a cubic grain in the amorphous GST film. The HRTEM image series in Fig. 5.10(a) is recorded at 132°C using the DENSsolutions heating holder with a FIB-prepared sample. The measurement is done in the JEOL 2100F. The length of the cubic grain is measured as a function of time and plotted in Fig. 5.10(b). As shown, the crystal growth rate is constant leading to a straight line in the length-vs-time plot. Using least-squares linear regression, a constant growth velocity of (0.70 ± 0.02) nm/s is determined.

Figure 5.11 compares the measured growth velocity around the first transition temperature with growth velocities for different GST compositions reported earlier. In the literature, several experimental techniques were used, e.g. atomic force microscopy measurements exploiting the density change during crystallization [167, 183], in-situ TEM [176, 184] and differential scanning calorimetry [165]. The determined growth velocity of (0.70 ± 0.02) nm/s in this thesis using in-situ TEM has the same order of magnitude as the speed determined by Kalb *et al.* for GST124 using atomic force microscopy [167]. Measuring the crystal growth velocity as a function of temperature allows the determination of the activation energy for growth. Assuming an Arrhenius temperature dependence, activation energies for growth in the range of 1.6-2.4 eV are reported [74, 167, 176, 183, 184]. Note that Orava *et al.* and others observed a non-Arrhenius temperature dependence for the crystallization of GST225 [165] and GeSb [171] meaning that the growth rate at higher temperature is lower than expected from Arrhenius behavior.

The crystallization of GST is often described as nucleation-dominated [62, 98, 104, 185, 186]. Thereby, during laser-irradiation an amorphous region which is surrounded by a crystalline matrix forms nuclei inside the amorphous region which grow subsequently until they impinge on one another. The nucleation rate is therefore higher than the growth rate leading to polycrystalline films with small grain sizes [25, 174]. This behavior is opposed to other phase change materials such as AIST [104, 185, 186] or SbTe [98, 185, 187] which exhibit growth-dominated crystallization. There, the amorphous mark crystallizes by growth from the surrounding crystalline matrix (and not from formed nuclei), meaning the growth rate is higher than the nucleation rate. Note that the observed crystallization behavior can be changed. Since both the nucleation rate and the growth rate are temperature dependent, the crystallization behavior depends on the applied temperature [25, 98]. And indeed, using the DENSsolutions holder slightly above where the onset of the first transition is observed,

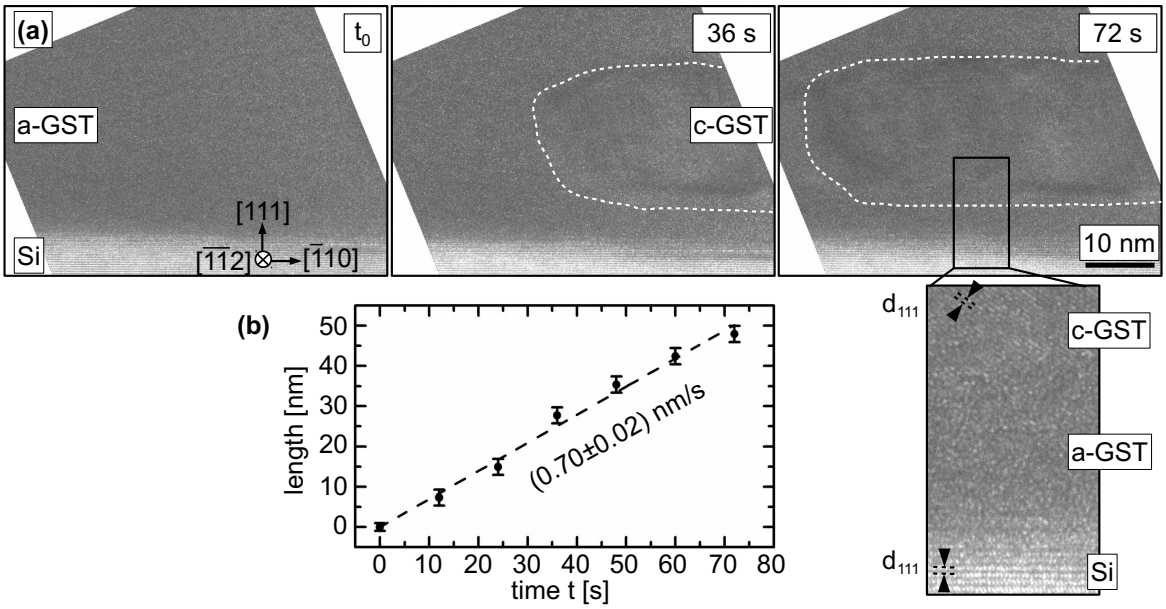

Figure 5.10 HRTEM image series showing the crystallization of as-deposited GST thin film at 132°C.

grain growth over several tens of seconds occurs without the nucleation of further grains (cf. Fig. 5.10). Furthermore, the addition of different materials to GST [104, 159, 188] can also influence the nucleation and growth rates. Thereby, the effect on the nucleation rate is much stronger than on the growth rate [188].

Kalb *et al.* [167, 183] studied the temperature dependence of the nucleation rate, I, and growth velocity, u. Both, I and u increase with increasing temperature implying that the crystallization kinetics are diffusion-limited (eq. (2.14)), as for collision-limited kinetics both quantities are expected to decrease. In addition, the above measured growth velocity is time-independent as was observed by others as well [167, 176, 183, 184] indicating an interface-controlled growth instead of a growth controlled by long-range diffusion [32].

In summary, amorphous-to-cubic transition close to the first transition temperature, T_{c1}, occurs via homogenous nucleation and subsequent crystal growth with a constant velocity leading to the formation of a polycrystalline cubic GST film with random oriented grains.

5.4.2 High-temperature transformation: cubic-to-trigonal transition

Further heating of the cubic-structured, polycrystalline GST film above the second transition temperature leads to the cubic-to-trigonal phase transition (cf. Fig. 5.7(c)). The in-situ observation of this second transition is done at the JEOL 3010. The annealing of the GST thin film at 400°C - well above T_{c2} - is done using the JEOL heating holder after ramping up to the target temperature with 50°C/min. For further structural analysis of the final trigonal phase the JEOL 2100F STEM is used.

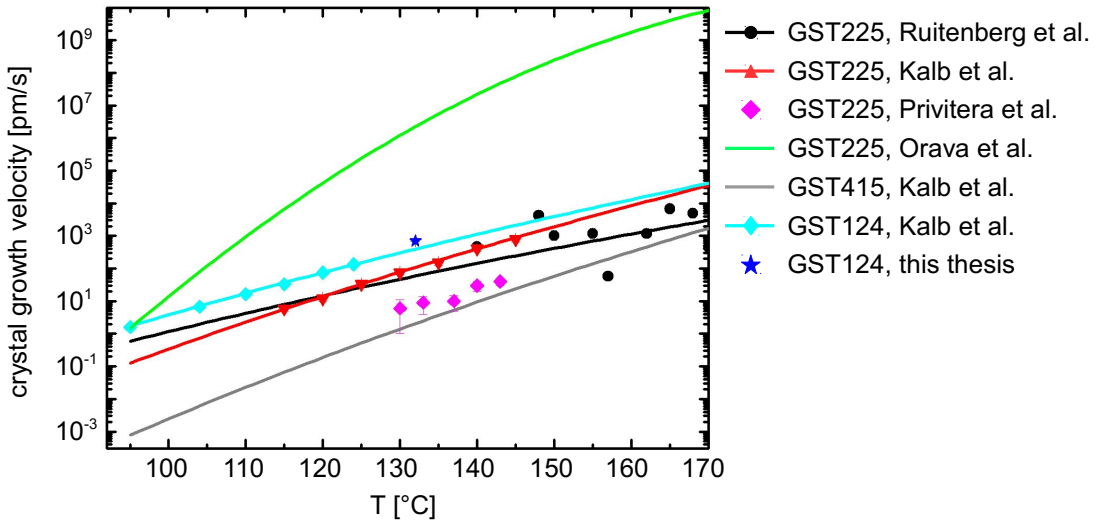

Figure 5.11 Comparison of reported crystal growth velocity around the first transition temperature, T_{c1} for GST225 [165, 176, 183, 184], GST415 [183] and GST124 [167]. The determined growth speed from the in-situ TEM measurement in this thesis agrees well with the reported speed for GST124 [167].

Superlattice structure of trigonal GST124

Figure 5.12 shows the final trigonal structure after 1 hour of annealing at 400°C. The GST thin film is texturized and consists of grains that are 200-300 nm in size and exhibit a preferred orientation where GST basal planes are aligned parallel to the substrate. Figure 5.12(a) displays a cross-sectional phase-contrast TEM image of the GST film-substrate heterostructure taken along the Si $[\bar{1}10]$ zone axis. A superlattice structure of the GST grain is visible as bright and dark lines. The superlattice fringes are aligned parallel to the substrate surface which is in accordance with the SAD pattern (see inset in Fig. 5.12(a)). There, the GST basal plane {0001} reflections are in-line with the Si(111) reflections. In some cases, the GST grains are even epitaxially aligned to the Si substrate with the definite orientation relationship: (111)Si $\parallel$ (0001)GST and $[11\bar{2}]$Si $\parallel$ $[1\bar{1}00]$GST (cf. Fig. 5.12(b)). Additionally, bright-field (BF) and high angle annular dark-field (HAADF) STEM images, shown in Fig. 5.12(c) and (d), reveal the vacancy layers (VL) that cause the superlattice structure as bright and dark lines, respectively (marked by black arrows) as discussed by Rotunno *et al.* [112]. The measured distance between VLs is (1.40 ± 0.05) nm and is in good agreement with the expected distance in trigonal GST124 (1.39 nm[112]). According to the Z-contrast imaging conditions of the HAADF-STEM, the Te (Z=52) layers produce a brighter contrast compared to the mixed layers containing Ge (Z=32) and Sb (Z=51). Within one block between two VLs, there are four layers with brighter contrast visible. These brighter layers correspond to the Te layers as seen by the comparison with the semi-ordered structure model of GST124 displayed in Fig. 5.12(e). This vacancy ordering is used in the later analysis as a fingerprint for the existence of the trigonal crystal phase during in-situ TEM studies of the liquid-solid phase transition.

The mechanism leading to the formation of the preferred orientation with aligned basal planes is unclear. In similar experiments, using GST225 thin film on an amorphous SiO_2

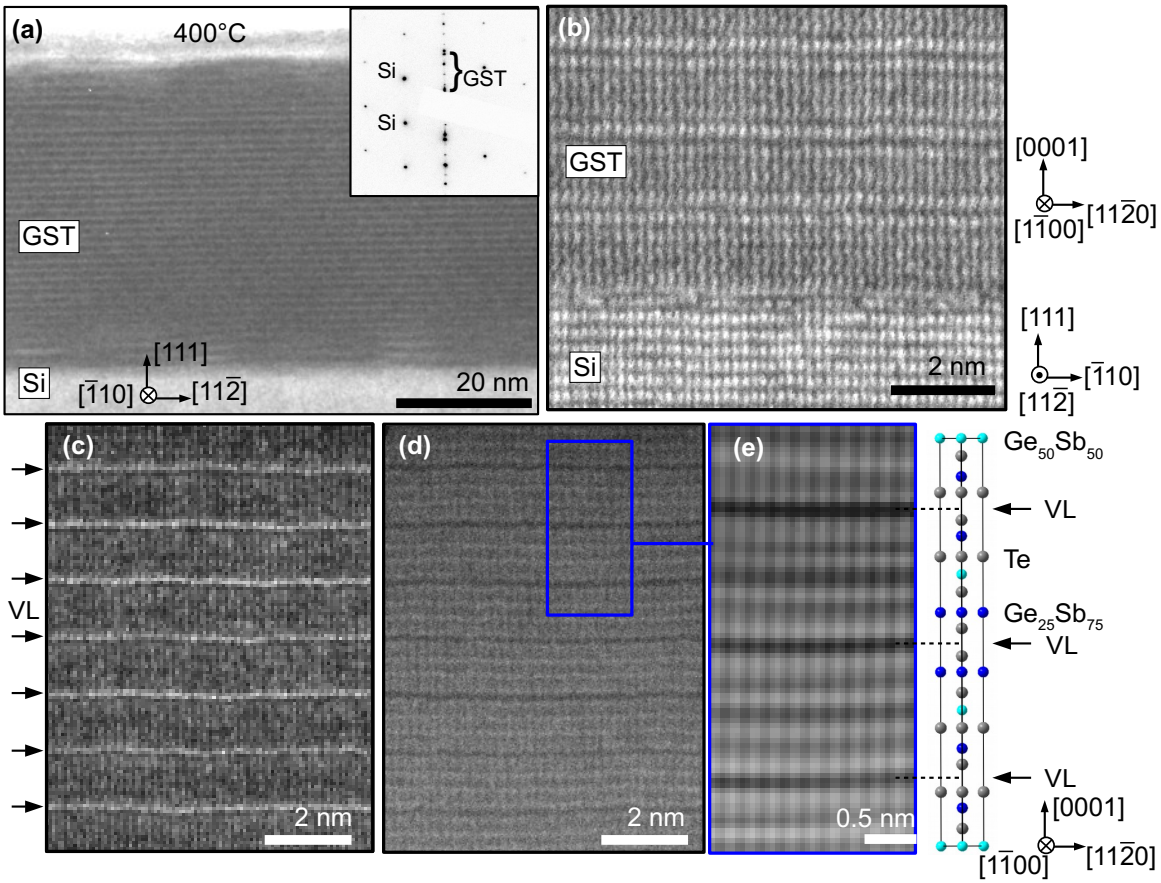

Figure 5.12 (a) TEM image of GST124 at 400°C, inset: corresponding SAD pattern (b) high resolution BF-STEM image of GST-Si interface region (Si [11$\bar{2}$] zone axis) taken at room temperature after annealing to 400°C, (c) overview BF-STEM image, (d) HAADF-STEM image of same region and (e) magnified and Fourier-filtered HAADF-STEM including a structure model of the GST124 unit cell based on the semi-ordered model of mixed GeSb layers [110] in [1$\bar{1}$00] zone axis.

substrate no alignment of the basal planes could be observed [189] indicating an influence of the crystalline Si substrate. On the other hand, grain growth of trigonal GST, where (0001) planes are parallel to the substrate surface, was also observed by others for non-crystalline substrates [25]. Kooi *et al.* [25] discussed this orientation in terms of lowering the surface energy by a preference of Sb atoms to be at the surface. They argue, that the basal planes in the fully ordered trigonal phase are occupied by atoms of one element only which then leads to the preferred formation of (0001) planes with a Sb termination.

Grain growth

The GST grains preferentially grow parallel to the (0001) planes. This behavior has also been observed by others [190]. During the in-situ annealing of an initial thin polycrystalline GST124 film at 400°C the motion of grain boundaries was observed. Dark-field imaging conditions are used to achieve an accurate determination of the grain boundary position. Figure 5.13 shows a sequence of dark-field snapshots taken from a video, where the bright grain is characterized by the before-mentioned preferential orientation to the substrate: GST basal

planes are parallel to Si(111) planes. The neighboring dark grain has a random unidentified orientation to the Si substrate. During the grain boundary motion the preferentially oriented grain grows. This growth is measured by the distance (d) between the actual boundary position and an unchanging obstacle at the interface versus time. The corresponding graph in Fig. 5.13 reveals a step-like character instead of a continuously increasing progression. This start-stop motion could be caused by the cubic-to-trigonal phase transition accompanying the grain boundary motion with the formation of the complex layered structure. In addition, the phenomena could involve an energy barrier which has to be overcome to form a crystalline interface between the aligned trigonal-structured GST grain and the Si(111) substrate. Because of the large lattice mismatch, dislocations for a full lattice relaxation will be generated at the interface [191]. The mismatch, f, between GST-$(11\bar{2}0)$ and Si-$(\bar{2}20)$ planes is calculated as $f = 11.3\%$ using eq. (5.8).

$$f = \frac{d_{hkil}^{GST} - d_{hkl}^{Si}}{d_{hkl}^{Si}} \tag{5.8}$$

As an approximation, for a fully relaxed GST structure one interfacial defect every nine Si-$(\bar{2}20)$ lattice planes is needed, that is every 1.7 nm. This is in the same order of magnitude as the start-stop motion, where grain boundary motion ceases after 2-4 nm of growth indicating the formation of defects as possible origin for the observed start-stop motion.

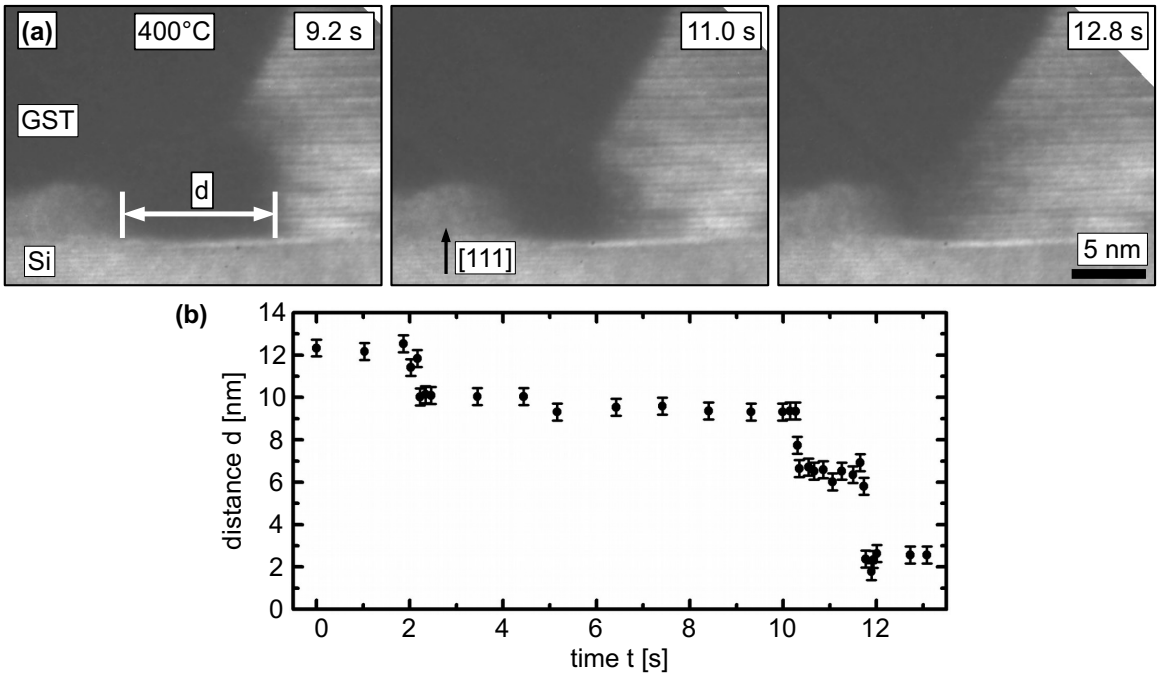

Figure 5.13 (a) DF-TEM images taken from a video sequence showing the recrystallization of GST thin film at 400°C: The grain with the preferred orientation of basal planes parallel to Si (111) planes grows laterally. (b) Graph showing distance-vs-time plot of the grain growth featuring a stepwise growth process.

Atomistic processes

The transformation into the trigonal phase depends on the vacancy concentration of the compound [192, 193]. Compounds with a low vacancy concentration, such as GeTe (0% vacancies) or $Ge_8Sb_2Te_11$ (9% vacancies), do not crystallize into vacancy-ordered structures [193]. Several authors proposed the important role of vacancies in the phase transition [97, 110, 111, 127, 129, 132, 192, 193]. Recently, Zhang *et al.* [111, 132] suggested that prior to the cubic-to-trigonal transition the cubic phase is transformed into a highly vacancy-ordered cubic (VOC) phase by annealing at temperatures between T_{c1} and T_{c2} [111, 129]. In this VOC phase, the previously randomly distributed vacancies are accumulated into (111) planes forming VL which are sandwiched by two Te-filled (111) layers (cf. Fig. 5.2(b)). Sun *et al.* [127] calculated that the highly vacancy-ordered structure has a lower total energy compared to the randomly distributed cubic phase meaning that the transformation into the VOC phase is energetically favorable. When a critical value of vacancies ordering is achieved [132], the transformation into the trigonal phase then happens via shifting of blocks that are separated by VLs and the subsequent collapse of the VLs [110, 127, 132]. The trigonal phase of different GST compositions therefore consists of a layered structure with building blocks of distinct numbers of layers separated by two van der Waals–bonded Te layers. The vacancy diffusion process is thereby predicted to take place by Ge and Sb migration and not by Te migration due to a calculated energy-loss caused by unfavorable Te-Te antibonds [110, 111].

6 Structural dynamics around the melting point

This chapter is dedicated to the GST molten state and the dynamics around the melting point. The set-up allows investigating the melting and solidification on a millisecond time scale and a nanometer length scale close to the melting temperature for a multi-component alloy with a complex layered crystal structure.
Section 6.1 introduces some fundamental aspects of melting. The in-situ observation of the liquid phase at 600°C is made possible due to an encapsulation of the TEM sample which will be discussed in section 6.2. Section 6.3 first addresses the experimental details for this study and then the focus is directed to the analysis of the dynamic motion of the liquid-solid and liquid-vacuum interfaces during melting and solidification. In section 6.4 then, the results of the microstructural analysis of GST after solidification are shown. Section 6.5 addresses the study of interfacial and surface energies based on contact angle measurements and Wulff-Kaishev construction. Finally, section 6.6 summarizes the results of this chapter. Parts of the presented results have been published in Ref. [194].

6.1 Processes involved in melting

The transition from a solid to a liquid phase is called melting. The reverse process of the transition from liquid to solid is called solidification and it involves nucleation and crystal growth. The temperature where the solid-to-liquid transformation takes place is called the melting temperature, T_m, and depends on the material and the applied pressure. T_m is therefore often reported at standard pressure (1 atm) unless otherwise specified. Together, melting temperature and corresponding pressure are called the melting point.

Upon melting the crystalline state breaks down which is accompanied by a volume change [27]: In materials crystallizing in close-packed structures, the packing density decreases during the structural breakdown and the volume thereby increases. The materials then have a positive thermal expansion and exhibit a positive slope in the p-T diagram (cf. Fig. 2.1(a)). When a crystal exhibits a more open structure, the structural collapse can cause a higher packing density in the melt and thus a decrease in volume upon melting causing a negative thermal expansion (cf. Fig. 2.1(b)). The resulting structure of the melt is not entirely random. The melt still has a pronounced short- and medium-range similar to the crystal structure but loses the long-range order. It is therefore comparable to the amorphous state [27]. Indeed, structural analysis of GST melt showed structural similarity between the melt and the high-density amorphous state obtained after laser-quenching or during pressure amorphization [133, 142, 146]. The concept of structural breakdown and a randomized arrangement caused by thermal motion is therefore an oversimplification [27]. The state of melt is rather dominated by the dynamical formation and decomposition of ordered dense atomic arrangements caused by the interaction of interatomic forces and thermal fluctuations [27].

According to Frenken *et al.* [4] even though the changes of many physical properties of materials during melting is well understood, a detailed description of the solid-to-liquid transition on the atomic scale is still under discussion. Theories try to understand how and why solids melt and what determines the involved temperature [5]. Two well-known approaches are the Lindemann criterion [195] and the Born criterion [196]. Both approaches discuss melting as an instability of the crystal lattice [7]. Lindemann's vibrational theory of melting proposed the idea that the amplitude of atom vibrations around their equilibrium position increases with increasing temperature until their displacement reaches a critical value causing the crystal to melt [4, 5, 7]. Born's mechanical melting theory proposed that the shear modulus of the crystal drops to zero upon melting causing the crystal to lose its rigidity to withstand shear which is a characteristic of the melt [5, 7]. Using molecular-dynamics simulation Jin *et al.* [197] showed that both criteria predict the same temperature when applied to the bulk without a surface [5]. The temperatures derived from both approaches lie above the experimentally determined melting temperatures [7]. This difference in temperature is discussed in terms of the experimentally observed preferential start of melting at the surface [5, 198] whereas the theoretical melting temperatures are derived for bulk atoms. The influence of a surface on the melting process in real systems is further evidenced by effects like the melting-point depression of small systems and premelting.

Melting-point depression. The observed decrease of the melting temperature in systems of decreasing size is explained by the increase of the surface-to-volume ratio so that the surface effects can no longer be neglected [9, 99, 198–201, 201–210]. In accordance with that, the melting-point depression is larger for systems of lower dimensionality and there is an influence of the surroundings (e.g. a matrix) through the interfacial energy.

Premelting. The formation of a transitional, liquid-like layer at solid interfaces below the bulk melting temperature is called premelting [10, 11, 13]. It occurs when the interfacial energy, $\gamma_{s\alpha}$, between a solid and a second phase α (solid, liquid, gas) is larger than the sum of the interfacial energies for solid-premelt (γ_{sp}) and α-premelt ($\gamma_{\alpha p}$) [13] (cf. Fig. 6.1):

$$\gamma_{s\alpha} > \gamma_{sp} + \gamma_{\alpha p} \tag{6.1}$$

Since the interfacial energies are temperature dependent, at small undercoolings it can be thermodynamically favorable to form a transitional premelting layer to lower the total surface energy [13]. Premelting thereby precedes the surface melting process which in turn

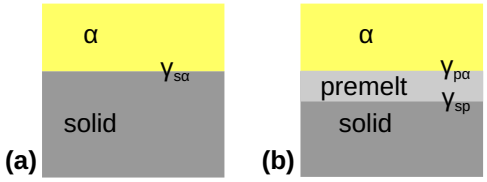

Figure 6.1 Schematic illustration of premelting. Solid and a second α-phase (solid, liquid, gas) are shown (a) with and (b) without a common interface.

forms a liquid surface layer burying the transitional premelting layer under it [4]. When the

temperature is further increased towards T_m the transition layer and melt front progress into the bulk [4]. The premelting layer is described as either defected crystalline or as a partially ordered liquid film [4] and its structural disordering increases from the ordered solid phase to the disordered surface [4, 11]. Experimental measurements of the premelting layer thickness show varying results, e.g. the thickness of the premelting layer of ice in the vapor/ice system close to its melting temperature varies up to two orders of magnitude (1.2-94 nm [10, 11] and references therein). For lead, a thickness of up to 2.6 nm close to the bulk melting temperature is measured [4].

6.2 The liquid state in the TEM

The observation of the liquid state inside the TEM is experimentally challenging due its incompatibility with the vacuum conditions necessary for electron microscopy [64]. Most studies use either dedicated liquid cell holders (hermetically sealed enclosures) or environmental TEM (ETEM; using differential pumping) when investigating materials within a liquid environment [63, 64, 67, 68, 70]. Although, there are some examples for investigations of encapsulated [198, 211, 212] and low-vapor-pressure liquids [66, 213] without the need for either a liquid cell or an ETEM.

This section is dedicated to the description of the experimental conditions that allow the investigations of the solid-liquid phase transition for GST thin films and how the melt state of GST can be identified.

6.2.1 Encapsulation

The direct observation of the liquid-solid transition inside the TEM is achieved thanks to a full encapsulation of the GST thin film.

There is no information available about the low pressure and high temperature behavior of GST like the pressure-dependent sublimation temperature. Considering the low base pressure of the microscope (10^{-5} Pa) and the applied high temperature which lies close to the bulk melting point of GST124 (T_M=615°C [89, 136, 152]), in-situ TEM heating of GST is expected to lead to sublimation. Indeed, sublimation is observed for samples which are prepared by FIB and subsequently annealed in the TEM up to a temperature of 600°C. Figure 6.2(a) shows a bright-field TEM image of a GST film after sublimation. In consequence of the sublimation, the initial continuous GST film decomposes, voids develop, and, finally, the film consists of faceted grains and holes. The sublimation process is discussed separately in the next chapter 7. On the other hand, if the GST film is completely encapsulated by coating the TEM lamella with carbon prior to the heat treatment, melting instead of sublimation is observed in the TEM. As an example, Fig. 6.2(b) displays a bright-field image taken at 600°C revealing a molten GST film. The existence of discontinuities or ruptures in the encapsulation enables the liquid GST to spray out and leave part of the capillary empty as shown in Fig. 6.2(b).

It is remarkable that encapsulation is even achieved in case of conventionally prepared TEM samples possibly due to the oxidation of the naturally introduced sputter damage layers on top and bottom of the thin film during storage. Local melting of Ge-Sb-Te inside a

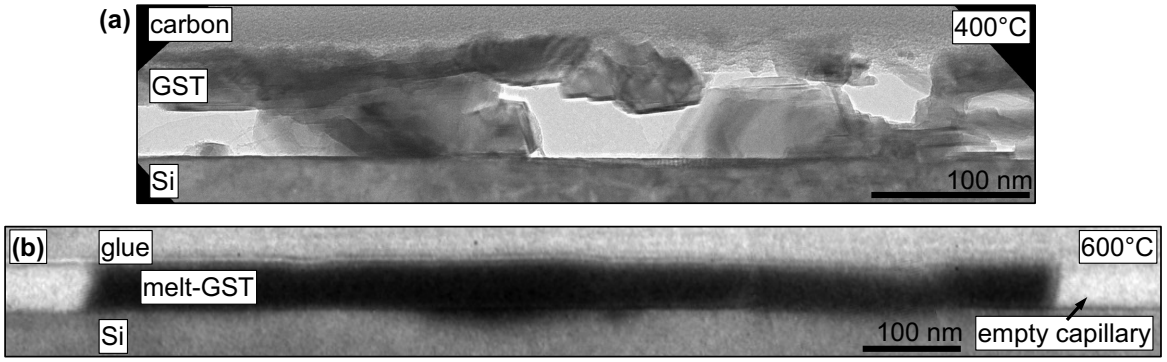

Figure 6.2 (a) Bright-field TEM image of a grainy GST film after sublimation at 600°C, recorded after cooling down to 400°C. (b) Molten GST inside a capillary at 600°C illustrated by a bright-field TEM image stitched together from several micrographs.

TEM is also mentioned by others using a similar conventional preparation technique [44]. Figure 6.3 shows a schematic drawing of a capillary with and without the GST thin film in a cross-sectional view. EELS analysis comparing both areas is used to investigate the origin of the encapsulation in conventionally prepared samples.

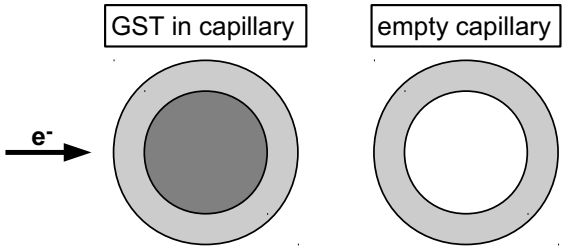

Figure 6.3 Cross-sectional schematic illustration of a capillary with and without GST film.

Figure 6.4 summarizes the results of EELS analysis of an empty capillary. The measurements are done after melting occurred and the sample is cooled down to room temperature again. Figure 6.4(a) shows a TEM image of the investigated sample region where a crystalline GST grain is next to an area without GST (empty capillary). The areas where the EEL spectra are taken are marked in red (GST) and black (capillary). The relative thickness of both areas can be calculated in multiples of the mean-free path using the zero-loss peak and the "compute thickness-procedure" in the Gatan EELS software which is based on the Log-Ratio method (eq. (3.18)). This results in a local thickness of 0.4 $\lambda_{\text{capillary}}$ for the empty capillary region and 0.8 $\lambda_{\text{GST+capillary}}$ for the neighboring region with a GST grain present. As expected (cf. illustration in Fig. 6.3), the thickness of the empty capillary is smaller compared to the GST filled capillary assuming that the mean free path lengths are comparable. Figure 6.4(b) shows two EEL spectra with the corresponding modeled background signal. Both spectra of the empty capillary (black) and the neighboring GST grain (red) are taken under the same conditions using a 20 nm spot size. The edges related to oxygen (O-K), antimony (Sb-M) and tellurium (Te-M) are displayed in the first part of the spectrum in the energy-loss range of 500-800 eV. At higher energy-losses (1100-1500 eV) the edges

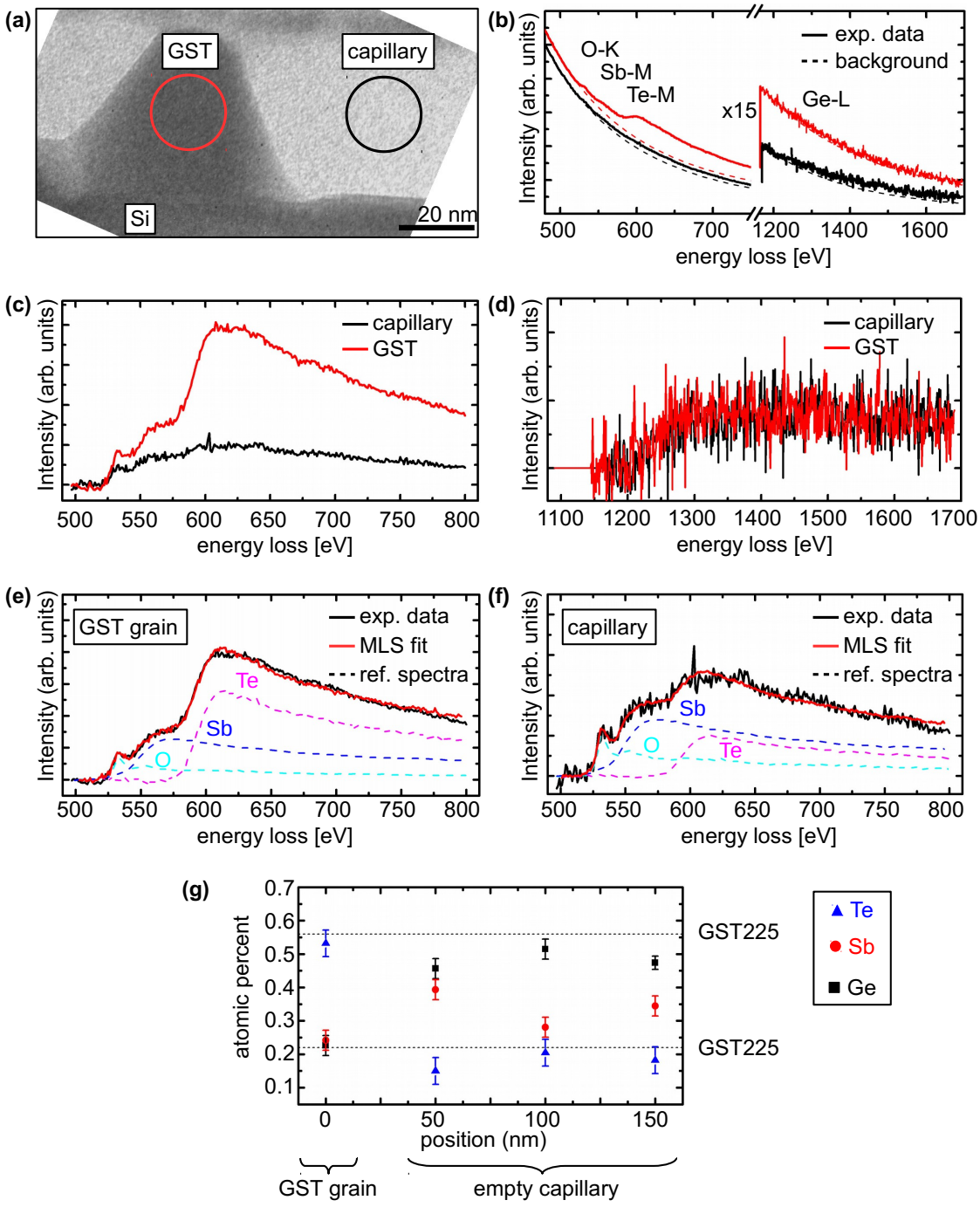

Figure 6.4 EELS analysis of empty capillary after melting: (a) TEM image of remaining GST grain in empty capillary. The regions of interest where the EEL spectra are taken from are marked. (b) EEL spectra of GST (red) and neighboring capillary (black) with modeled background signal. For easier comparison the GST spectrum is shifted upwards with a small offset. The background subtracted EEL spectra contains the signal from (c) the O-K, Sb-M and Te-M edges and (d) the Ge-L signal from the GST grain (red) and the capillary (black). The MLS fit of the background subtracted EEL spectrum and corresponding reference spectra of O, Sb and Te are shown for (e) GST grain and (f) capillary. (g) Graph of chemical composition of the GST grain (GST225) after melting and the neighboring capillary at three different positions.

related to germanium (Ge-L) are visible. The background-subtracted signals in both energy ranges can be found in 6.4(c) and (d). The direct comparison of the background-subtracted signal in Fig. 6.4(c) shows that more intensity for the Sb- and Te-edge in the GST filled area is measured. According to eq. (3.25) that already indicates that less Sb- and Te-atoms are present since the partial cross-section and zero-loss peak intensity are equal.

In order to assess the change quantitatively, the atomic percent for Ge, Sb and Te are calculated assuming that the three elements make up 100% in total. The quantification procedure using MLS fitting is described in detail in chapter 3.3. The result of the fitting is shown in Fig. 6.4(e) and (f) for the GST grain and the capillary respectively. As shown, both MLS fits (red) are in good agreement with corresponding experimental data (black). Figure 6.4(g) compares the result of the quantification for the GST grain and three different positions of the capillary. It shows that the composition of the GST is Ge(23±2)%:Sb(24±3)%:Te(53±4)% which is close to GST225. The composition of the empty capillary amounts to an average of Ge(48±4)%:Sb(34±3)%:Te(18±2)% assuming it consist entirely of Ge-Sb-Te. That means that the Ge/Sb, Ge/Te and Sb/Te ratios are higher than in the neighboring GST225 grain and also higher than in the initial GST124 composition of the film (Ge14%:Sb29%:Te57%). Initially after the sample preparation, the surface of the GST124 film had the same composition as the film itself (Ge14%:Sb29%:Te57%). Then, the composition of the surface layer changed either already during oxidation before the in-situ investigation or during the high-temperature treatment. Thereby, the material loss is preferential for Te over Sb which in turn is greater than Ge assuming that the capillary is indeed empty and no preferential adding of material occurred. And indeed, the change of composition during oxidation as well as high temperature treatment favors the loss of Te followed by Sb over Ge.

1. **Oxidation.** Zhang *et al.* [214] found that all elements of GST can be found in an oxidized state at the surface after air exposure and that the oxidation is highest for Ge (GeO_2), followed by Sb (Sb_2O_5) and then Te (TeO_3). They explained the difference with the decreasing heat of formation for the different oxides.

2. **Thermal stability.** The Ge oxide has a higher melting temperature ($T_m^{GeO_2}$=1115°C [210]) compared to the other oxides ($T_m^{Sb_2O_5}$=380°C , $T_m^{TeO_3}$=430°C , $T_m^{TeO_2}$=733°C [210]) and is thermodynamically more stable during the applied high temperature.

Therefore, GeO_2 is preferentially formed during air exposure leading to a higher Ge content in the surface layer forming the encapsulation. Additionally, if other oxides have formed, they will melt during the high temperature treatment of around 600°C necessary to observe the melting of GST. The encapsulation therefore primarily consists of GeO_x which has also been observed for melting of GeTe nanowires [210]. The Sb and Te measured in EELS are most likely caused by residual Ge-Sb-Te material indicating that the capillary is not entirely empty.

Figure 6.5 displays a schematic illustration of the proposed wedge-shaped sample geometry of a conventional prepared TEM sample featuring encapsulation. The GST film is thereby surrounded by thermally stable materials with melting temperatures that are higher than GST: The Si substrate, oxidized Ge on both sides of the film and the glue used during sample preparation. Together those materials act as encapsulation which enables temperature-pressure conditions where melting instead of sublimation can be observed.

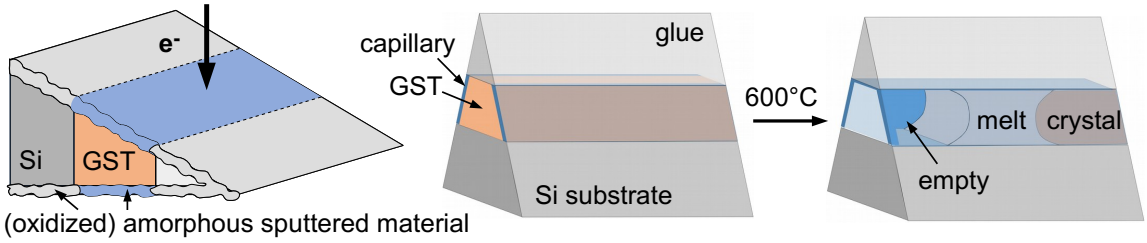

Figure 6.5 The model shows the proposed sample geometry for a conventional prepared TEM sample with the GST thin film and a surrounding capillary facilitating melting of the GST thin film at 600°C.

6.2.2 Identification of melt phase

The melt state is identified through several indicators: (1) vanishing of contrast features, (2) movement of melt and (3) recrystallization after cooling down.

After reaching the target temperature of 600°C, all contrast features of the crystalline grains, such as (super-)lattice fringes, vanish in some areas leaving a homogenous, featureless contrast behind. Additionally, as the GST film changes from crystalline to liquid the crystalline electron diffraction pattern disappears.

As previously described, some parts of the capillary are empty. As a result, an oscillatory motion of the melt is observed as short fragments of the molten film are able to flow back and forth inside the capillary. One example of melt movement inside the capillary is displayed in Fig. 6.6. It shows two bright-field TEM images which are recorded 38 sec apart from one another at the same sample position defined by a surface step which is marked by white arrows. The direction of the melt movement is shown with a black arrow. The melt-vapor interfaces are visible and their shape resembles a meniscus shape as is characteristic for a wetting liquid being located in a capillary. Another example of the oscillatory melt motion is illustrated in Fig. 6.7. It shows an HRTEM image series of (crystal-vacuum-melt)-front movement. The white arrow marks the same position in all images and the black arrow indicates the direction of the melt flow. The melt first flows from left to right (first three images) and then back again from right to left (last two images).

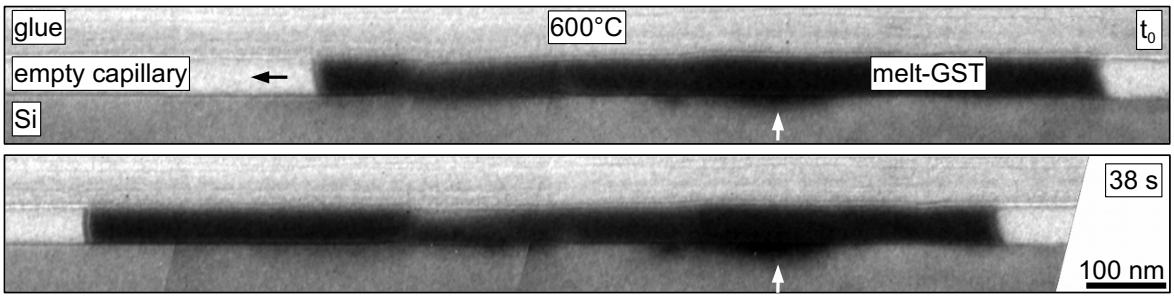

Figure 6.6 Movement of molten GST inside capillary at 600°C illustrated by two bright-field TEM images stitched together by several micrographs. The two images are taken 38 s apart.

Finally, after cooling the sample down, the liquid parts recrystallize again.

The observation of the homogenous contrast, the disappearing diffraction pattern, the meniscus shaped interfaces and the dynamic behavior (flowing and recrystallizing) confirm

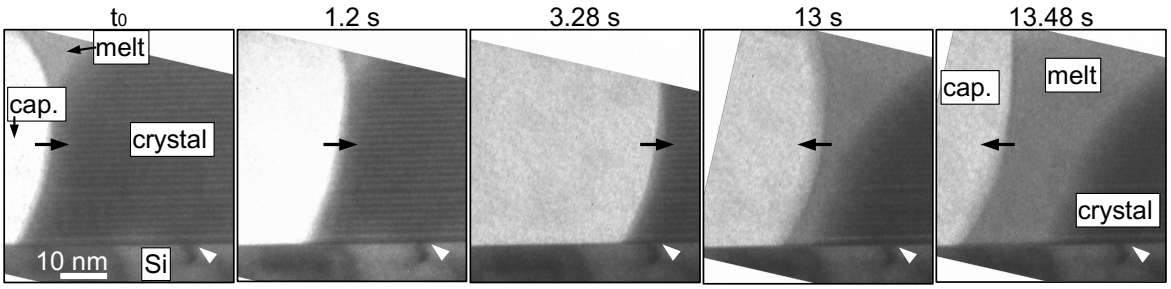

Figure 6.7 TEM images series of (crystal-vacuum-melt)-front movement showing the back and forth flowing of the melt inside the empty capillary (cap) at 600°C.

that the observed phase transition is indeed melting and not sublimation.

In conclusion, encapsulation of the GST film allows designed in-situ TEM experiments in order to probe the liquid-solid phase transition and the dynamic processes including melting and crystallization. Even so, the large atom fluctuations inside the liquid phase impede a high resolution observation and appropriate imaging conditions need to be found.

6.3 Dynamic interface observation of solid-liquid phase transition

In this section the experimental details of setting up the initial state are discussed first, then the initial state is characterized and finally the microstructure and dynamics around the melting temperature of GST are discussed involving both melting and re-crystallization from the melt of the GST film.

6.3.1 Initial melt state

Setting up. Figure 6.8 displays a schematic illustration of the heating procedure. In order to study the high temperature solid-liquid phase transition, a polycrystalline cubic GST film is heated with 50-70°C per minute up to nominally 600°C using the JEOL heating holder inside the JEOL 3010 TEM. Before reaching the target temperature, the sample is kept at 400°C and 500°C for several tens of minutes to stabilize the sample stage by minimizing the thermal drift due to the temperature gradients. In the course of the heating procedure the initial polycrystalline film changes into the trigonal phase around 400°C exhibiting a texturized structure such that the GST basal planes are orientated parallel to the Si(111) surface as described in the previous chapter in section 5.4.2. Finally, melting is observed at 600°C. That means that there is a slight decrease of 2% in the melting temperature of the thin GST film compared to bulk material at atmospheric pressure ($T_{m,bulk}$=615°C [89, 136, 152]). This decrease is comparable to the decrease of 3% reported for 10 nm thin GeTe films [99].

Figure 6.9 shows a bright-field TEM image displaying an overview snapshot of the initial sample state recorded a few minutes after reaching the target temperature of 600°C. The sample is oriented along the Si $[1\bar{1}0]$ zone axis to enable an edge-on view of the interface. A contrast aperture is introduced to differentiate between crystalline and non-crystalline areas.

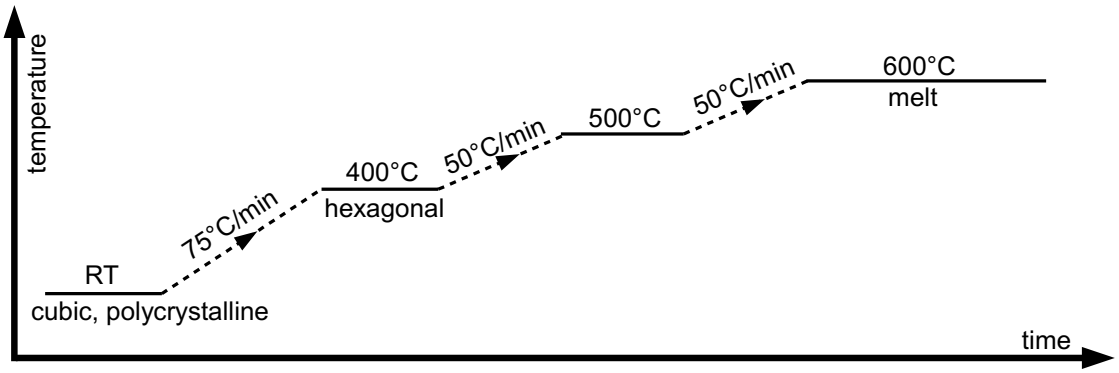

Figure 6.8 Schematic illustration of experimental procedure for in-situ heating of GST thin film from RT to 600°C.

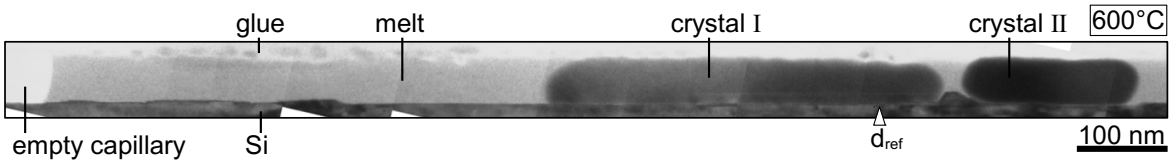

Figure 6.9 An overview of the initial melt state of the GST thin film in-situ annealed to 600°C before dynamics discussed in this section occurred. The image is stitched together combining several TEM images taken from a video sequence.

Several TEM images are stitched together to give a larger field of view: Two GST crystals, GST melt and an empty capillary region can be clearly distinguished by their corresponding contrasts. The molten GST on the left hand side of the image shows a bright and homogenous contrast, whereas the two crystalline grains on the right hand side exhibit a darker contrast with observable superlattice fringes. The contrast between crystal (dark) and melt (bright) is caused by the different diffraction behavior since liquid and crystal have a similar composition (no material contrast) and the sample thickness is also similar (no thickness contrast).

The molten GST is found on both sides of the crystals and partly or completely surrounds them inside the capillary creating a melt reservoir. Melting generally starts at the end of the film, e.g. at the TEM sample edge, or at grain boundaries along the film (e.g. between crystal I and II). The existence of discontinuities or ruptures in the encapsulation enables the liquid GST to spray out and leave part of the capillary empty. Therefore, heat transfer and temperature profile of our sample are complex and not accurately controllable. As the temperature lies within the phase transition region, some slightly different local thermal conditions result in the observation of both processes - melting and recrystallization. In addition, the molten GST describes an oscillatory motion that is independent of the melting and crystallization behavior of the crystals as shown exemplary in Fig. 6.6 and 6.7.

6.3.2 Overall dynamics

The presence of both the liquid and solid phase at 600°C provides the opportunity to study the dynamics of the melting and solidification process in this ternary system with good tem-

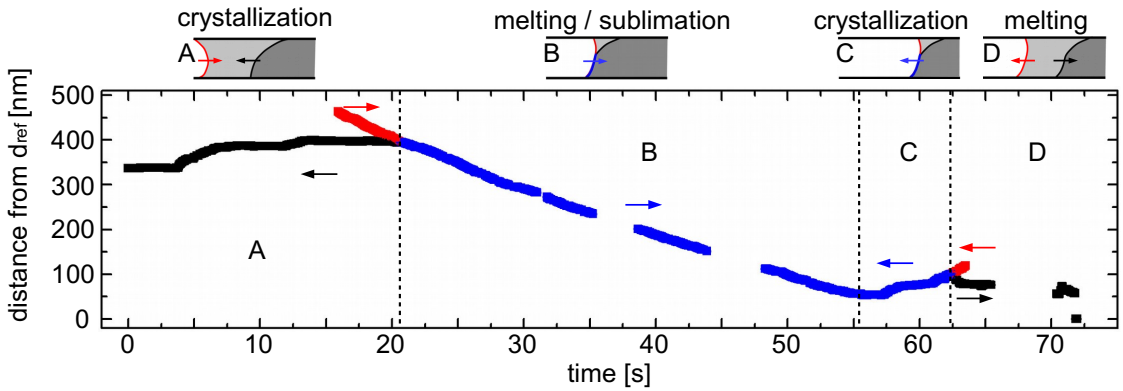

Figure 6.10 Graph displaying interface motion of all three interfaces as a function of time at 600°C: crystal-melt (black), vacuum-melt (red) and crystal-vacuum-melt (blue) interface as well as corresponding schematics showing principal behavior of all interfaces in the four different sectors A to D.

poral as well as spatial resolution. The distinct contrast between crystalline and molten GST enables the tracking of the liquid-solid (black) and vacuum-melt (red) interface motion. An overview of all dynamical events following the initial melt state (cf. Fig. 6.9) is given by the graph in Fig. 6.10. There, the time dependencies of the distance of each interface from a reference point, d_{ref}, is displayed. The reference point is defined by a step in the substrate surface and marked by an arrow in Fig. 6.9. Note that the measurements are interrupted several times when the observed interface leaves the field of view. The graph is divided in four different sectors A to D. They are characterized by the relative positions of both interfaces to each other and by the fact that melting or recrystallization is in progress at that time (as illustrated by the schematic diagrams above the graph in Fig. 6.10). Sector A is given by a longer period of recrystallization, i.e. the distance of the crystal-melt interface from d_{ref} increases. At some point, the vacuum-melt interface starts to move toward the crystal until both interfaces coincide. Sector B is defined by the motion of the common crystal-melt-vacuum interface (blue) describing the shrinkage of crystal I. Since a thin liquid layer in front of the crystal cannot be excluded, it is impossible to precisely differentiate between melting and sublimation at this stage. In region C, the supposedly collective melt/sublimation process ends and the GST crystal I recrystallizes again using material provided by the melt reservoir surrounding the crystal. In sector D, the interfaces separate again, molten GST flows back into the empty capillary - in Fig. 6.9 from right to left - and the GST crystal I starts to melt again until it vanishes completely.

In order to analyze the liquid-solid interface motion quantitatively, its velocities during crystallization and melting are calculated by the slope of the corresponding curve shape in sector A and D. Assuming a linear slope in a first coarse approximation, velocities between 7 and 22 nm/s are estimated which are not essentially different for the melting or crystallization case. Observation of melting of Ge nanowires using in-situ TEM also reported melting velocities of 3-20 nm/s close to the melting temperature [215]. The comparison of the growth velocity for GST at high temperatures from literature (cf. Fig. 5.6) and our experiment is inept. As discussed in section 5.3.3, other studies analyze the growth velocity using laser-excitation [170, 172] or extrapolate based on a theoretically determined viscosity value [165]. Additionally, the growth velocity is critically dependent on the local temperature at

the growth front which cannot be accurately controlled or measured in this set-up. Since we observe both crystallization and melting at the same time, the difference in free energy must be close to zero and therefore the observed processes are thermodynamically limited and slowed down to a point where the temporal resolution of the camera is enough to study the dynamic behavior at a nanometer scale. So far, the rate-controlling processes (e.g. diffusion- or interface-controlled) are still unclear. Therefore the dynamic behavior of the liquid-solid interface is explicitly studied in conjunction with structural information.

6.3.3 Interface dynamics during melting

Figure 6.11 shows the result of the final stage of melting, where the remaining GST grain can be described as a small crystal surrounded by its liquid phase. A sequence of TEM snapshots is reproduced in Fig. 6.11(a) illustrating the dynamics during melting by lateral movement of the liquid-solid interface. The lateral shrinkage of the particle diameter is obvious while the particle height remains constant. The graph in Fig. 6.11(b) shows the diameter as a function of time. The grain melts with a constant velocity in the range between 0.4 sec and 1.4 sec resulting in a value of 10 nm/s. Note that the grain actually shrinks with 20 nm/s because it melts from both sides of the crystal at the same time. Eventually, after reaching a diameter of about 50 nm - a value that corresponds to the film thickness - the crystal underwent a sudden crystalline to liquid phase change. During this abrupt change, no movement of the liquid-solid interface is detectable and the crystal therefore seems to vanish within one frame. The vanishing crystal leaves behind a shadow contrast of the former shape at 1.44 sec (cf. Fig. 6.11(b)). This shadow effect is due to the fact that melting occurred faster than our temporal resolution of 0.04 sec which leads to an overlap of the former crystal shape and the melt within one image frame. This observation suggests a strong increase of the melting velocity and can be understood in reference to a strong decrease in melting temperature for lower dimensional systems. It is reported that nanowires of $Ge_2Sb_2Te_5$ with a diameter of 80 nm exhibit a melting temperature that is only 60% of the bulk value [209]. Accordingly, the melting velocity in the present case could increase drastically when the melting temperature of the small crystal is reduced at a fixed surrounding temperature and thus increasing the thermodynamic driving force.

Transition zone

Figure 6.12 presents a magnified image of the same small crystal where its crystalline state is directly proven by the superlattice fringes which are clearly visible in the magnified inset. The superlattice fringes are induced by vacancy ordering and have a measured spacing of (1.40 ± 0.05) nm which corresponds well to the ordered trigonal phase of GST124 discussed in section 5.4.2. Notably, the width of the liquid-solid interface appears broad forming a transition zone of about 5 nm (marked by black arrows) between crystal and melt. The transition zone is characterized by a contrast that is similar to the crystalline phase, where, however, the superlattice fringes are lost. The transitional layer is observed all around the semi-spherical particle. A sharp transition at the melt-crystal interface is scarcely to be expected. Nonetheless, the loss of superlattice fringes at the crystal surface indicates that the melting process involves the local disordering of the vacancy order in the trigonal GST124.

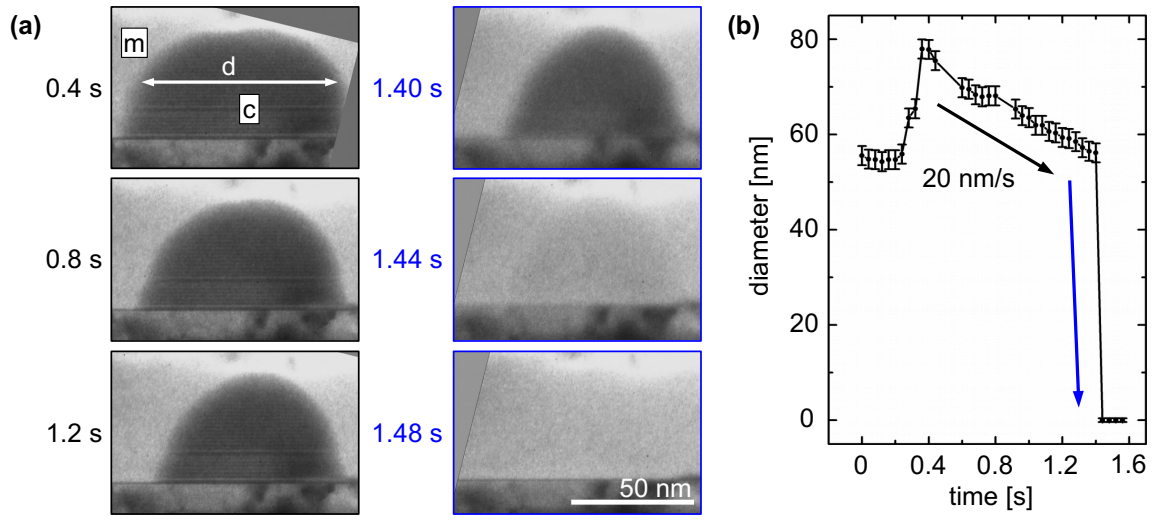

Figure 6.11 (a) TEM image series taken at 600°C showing the melting of a small GST crystal, c, surrounded by GST melt, m. (b) Graph of crystal diameter, d, versus time. The reduction of the diameter increases significantly after reaching a size of approximately 50 nm.

This disorder phenomenon at the solid-liquid interface can be linked to the mentioned interfacial premelting of a surface which results in a defective transitional surface layer.

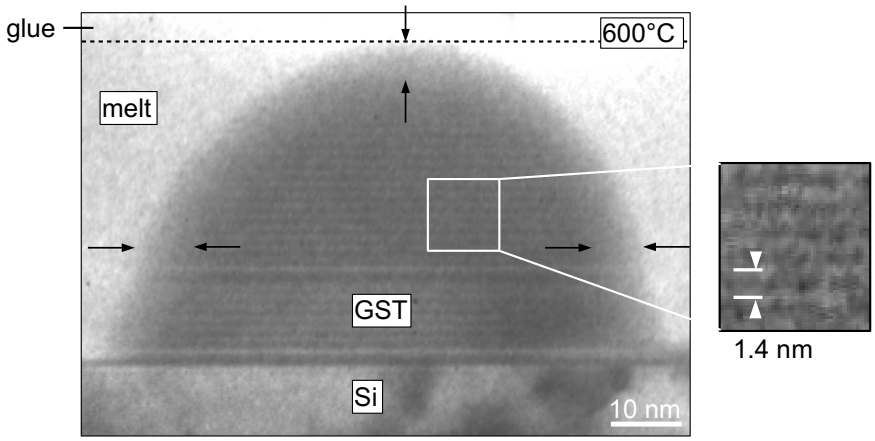

Figure 6.12 TEM image taken from the melting series recorded at 600°C (cf. Fig. 6.11) showing a close-up view of the same GST crystal visualizing the superlattice structure and the broad and diffuse interface (marked by black arrows).

The possibility that the described transitional zone is a projection artifact needs to be addressed. When considering the remaining GST crystal in three dimensions, the loss of fringes near the edge could be caused by the crystal having a hemispherical shape and near the edges only part of the through-thickness of the specimen is solid. The scattering in the liquid then may cause the loss of fringe contrast in the solid. During the entire melting sequence, the particle size changes by 30% and therefore the width of the transition zone should change as well if the transition zone is indeed a projection artifact. The width of the surface layer over the course of the melting sequence is measured and displayed in

Fig. 6.13. The thickness is thereby measured at three different positions: on the top, left and right side of the crystal (marked by black arrows in Fig. 6.12). For all three positions the layer thickness is the same and stays constant. Although the through-thickness changes, the observed transition zone width stays constant discouraging the idea of a projection artifact.

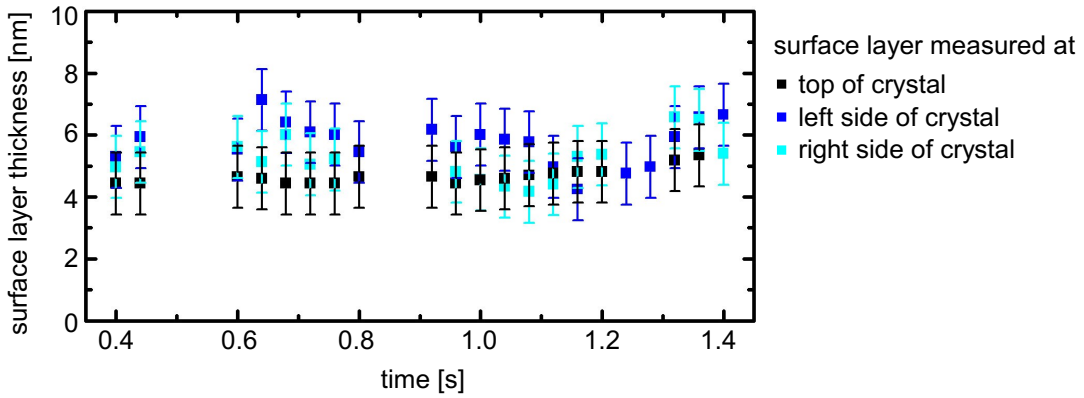

Figure 6.13 Graph showing the temporal development of the transition zone thickness measured at three different sites of the crystal shown in Fig. 6.11. The thickness remains constant during the whole melting process.

Melting dimensionality

Melting is observed only parallel to the Si-GST interface. Melting starting at the top of the GST film and moving towards the Si-GST interface is not observed. The melting direction is therefore perpendicular to the GST basal planes. This observation could be linked to the theoretically predicted two-dimensional melting of highly ordered cubic GST225 [8]. Sun *et al.* [8] reported that GST225 melts by forming linear and tangled clusters in two directions while keeping order in the perpendicular direction. Using *ab initio* molecular dynamics, the authors showed that at high temperatures, atoms behave like liquid in the {111} planes while parallel to the [111] direction, they are essentially vibrating around their initial configurations. A similar observation of a plane-like structure was done in a simulation 80 K above the melting temperature by others [173]. Based on those findings, Kolobov *et al.* [31] suggested that "the layering of the liquid phase is reminiscent of a [...] crystal when upon melting weak van-der-Waals interactions break while the stronger covalent backbone persists." In this work, melting of trigonal GST is studied, which also consists of layered basal planes which are parallel to the (111) planes of cubic GST and are separated by van-der-Waals gaps. Though the observed melting directionality is not conclusive proof for the two-dimensional melting behavior of GST, it provides an interesting starting point for further investigations.

6.3.4 Interface dynamics during crystallization from the melt

The reverse process, which is crystal growth from melt, is shown in Fig. 6.14. Figure 6.14(a) reveals a series of video-recorded images displaying the temporal development of the crystal grain front within the melt matrix. All nine TEM images are taken from the same position which is defined by a substrate surface step (indicated by the white arrow). Figure 6.14(b)

shows a magnified image of one frame of the growth sequence. The trigonal crystalline phase is again identified by superlattice fringes parallel to the Si surface with a spacing of (1.40 ± 0.05) nm as is done in Figure 6.12. The fringe contrast is detectable until close to the solid-liquid interface which appears nevertheless diffuse and not abrupt, which might be understood in relation to a projected view of a curved interface. In contrast to the melting process, there is no extended transition zone found during crystal growth. Consequently, the crystal growth does not involve an attachment of a transitional unordered crystalline phase and differs in this aspect from the melting process making both processes not exactly inverse.

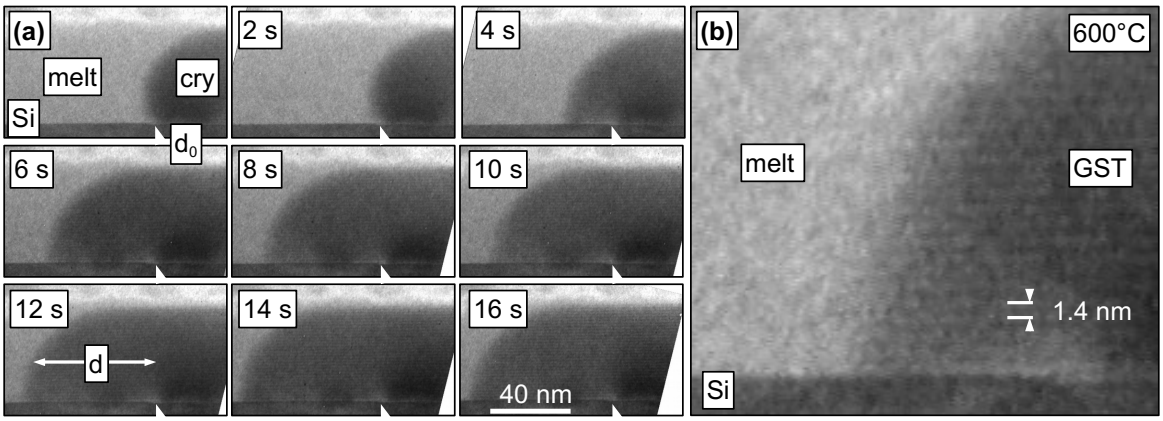

Figure 6.14 (a) TEM image series taken at 600°C showing the growth of a crystalline (cry) grain within the melt matrix and (b) close-up view of the GST crystalline structure and crystal-melt interface.

Non-linear growth

The step in the surface serves as reference point, d_0, for measuring the distance, d, the crystal-melt front has traveled. Both, d_0 and d, are marked and labeled in Fig. 6.14(a). The temporal development of the crystal-melt front position is summarized in Fig. 6.15 as a d-vs.-t plot over a time range of 20 sec. The interface movements can be divided into four growth parts (I-IV) each followed by stationary periods of no growth.

The growth parts (I)-(IV) are magnified and displayed in individual graphs in the bottom row of Fig. 6.15. As discussed in section 2.2.1, a growth process which is controlled by rearrangement processes at the liquid-melt interface has a time-independent growth rate (eq. (2.14)). The growth distance therefore depends linearly on the time, because the growth rate is the first derivative of the growth distance with respect to time. A long-range diffusion-controlled growth mechanism however shows a time-dependent growth rate (eq. (2.13)) with a square-root time-dependence of the interface motion. In order to quantify the time-dependence of the observed growth dynamics, the interface motion is fitted using $d = at^b$ with a non-linear curve fitting procedure using the Origin software. The parameter b is equal to unity when the growth distance has a linear time dependence and the growth rate is time-independent. The parameter is equal to 0.5 when long-range diffusion is involved. The resulting fit parameters (a and b) for each growth part are displayed in table 6.1 and the corresponding fits are plotted in each of the four magnified graphs in Fig. 6.15 as red solid lines. As an objective measure for the quality of the fits the adjusted R-square value

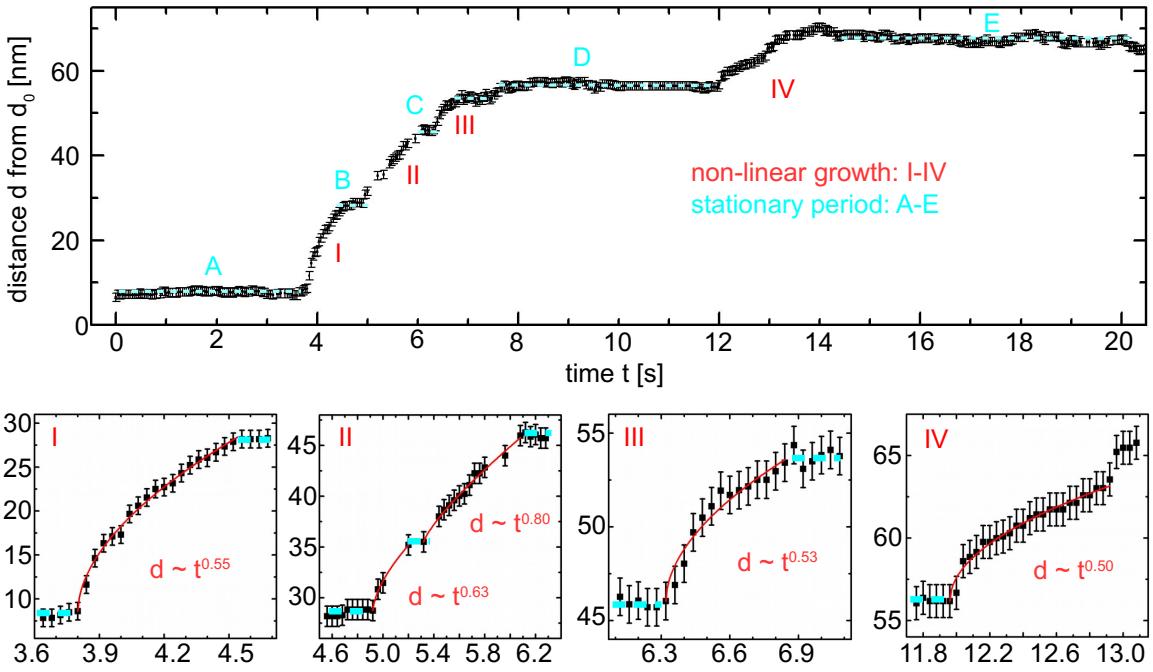

Figure 6.15 Graphs showing the position of the crystal-melt front as a function of time. The growth exhibits periods of stasis and rapid movement. The four growth periods (labeled I-IV) are displayed in a close-up view below the graph showing the transition between stationary and growth period in more detail. The growth periods are fitted with $d = at^b$ and the results for b are displayed in each graph.

for each fitting procedure is listed in table 6.1 as well: The closer the fit is to the data points, the closer R-square will be to unity. The growth parts I, III and IV show a square-root time-dependence (b=0.5) of the interface motion indicating that the crystal growth involves long-range diffusion. The parameter b for the second growth part (IIa and IIb) is between both growth modes. The origin of the deviation is unclear and might be caused by fluctuations in the unknown compositional gradient of the melt or by local temperature changes leading to a faster growth.

growth part	a	b	adjusted R-square
I	23.4±0.3	0.55±0.02	0.99084
IIa	14±2	0.63±0.06	0.98529
IIb	12.8±0.4	0.80±0.03	0.98073
III	10.7±0.8	0.54±0.06	0.91705
IV	7.1±0.1	0.50±0.02	0.97095

Table 6.1 Summary of the fitting parameter a and b for all observed growth parts using $d = at^b$ in the fitting procedure. As a measure for the goodness of the fit the adjusted R-square value for each fitting procedure is listed as well: The closer the fit is to the data points, the closer R-square will be to unity.

The square-root time-dependence of the crystal growth indicates the involvement of long-range diffusion. The local composition of the grain before melting and after crystallization

corresponds to GST124 which is concluded from the observed superlattice structure. The composition of the melt however could not be measured and could differ from the crystal. This would lead to the necessity of long-range diffusion for crystal growth. The inhomogeneity in the melt composition can be caused by the oscillatory melt movement and the preferential loss of material during spraying out of the capillary. There are indicators that the melt composition indeed differs from the composition of the GST124 crystal. Further experiments discussed in the next section 6.4 show that after solidification GST grains with a superlattice structure corresponding to GST225 are found (cf. Fig. 6.17(b)). Furthermore, EELS analyzes on crystallized melt droplets confirm the compositional inhomogeneities, e.g. the GST grain with 225 composition shown in Fig. 6.4.

Start-stop motion

In addition to the described growth periods, periods of no growth are observed as well. Measurements of the duration of each stationary period (displayed as plateau areas (A-E) in Fig. 6.15) range from 0.12 sec up to 7 sec. Figure 6.16 illustrates the change in the contact angle during the onset of each growth period (I-IV). While the non-linear time dependence of the growth parts can be explained by long-range diffusion, the superimposed start-stop motion indicates an influence of the Si substrate. For each period two magnified TEM images are shown displaying the triple point between crystalline and liquid GST and the Si substrate before and after the start of growth. The dotted line shows the estimated tangent line from the contact point along the crystal-liquid interface which is used to define the contact angle γ. Most of the time, the contact angle is close to 90°. Only before the onset of growth in part (I) and (III) the contact angle seems to be well above 90°. In part (I) a surface step is clearly visible which is known to affect the dynamic contact angle [216]. Nonetheless, in each case the contact angle decreases at the onset of growth indicating that the surface has an effect on the growth of the aligned GST structure. A similar behavior is observed during grain boundary migration for recrystallization and texture formation at around 400°C described in section (5.4.2). There the start-stop phenomenon is discussed to involve an energy barrier which has to be overcome for the formation of the crystalline interface between the aligned GST grain and the Si (111) substrate because of the introduction of lattice mismatch leaving interfacial defects.

Influence of capillary

The motion of the vacuum-melt interface is apparently affected by the capillary action as it is seen by the meniscus-like interface shape (cf. TEM images in Fig. 6.6 and Fig. 6.7), which itself is a result of the interaction between wall adhesion and melt surface tension. Even though the melt motion within the capillary is influenced by the melt-capillary interface, there is no indication that the encapsulation has an effect on the dynamics of crystallization or melting. The crystals are embedded within the melt and do not share an interface with the capillary itself as indicated by the independent melt flow dynamics (oscillatory motion) and the fact that the behavior of the liquid-solid interface does not depend on whether a complete film or a small and free-standing island is considered.

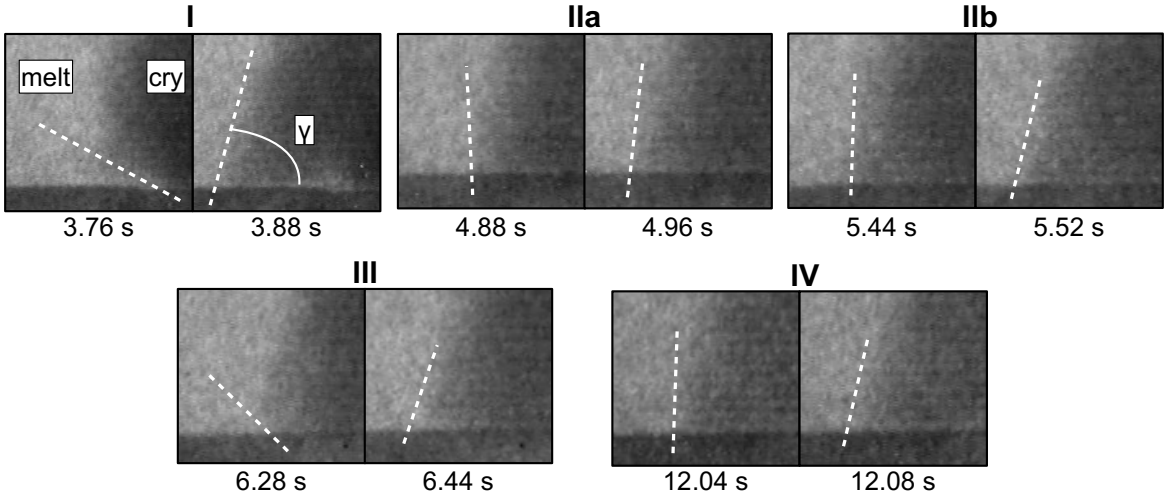

Figure 6.16 For each growth period (I-IV) two magnified TEM images display the Si-GST (crystalline [cry] and melt) triple point before and after the start of the growth period illustrating the decrease in contact angle γ during the onset of growth.

6.4 Crystal phases after fast solidification

In this section, the crystal structure of GST after solidification is investigated. Surprisingly, both crystalline phases - cubic and trigonal - are found. In order to detect whether or not the solidification conditions have an influence on the resulting crystal structure, three different cases are compared. First, after melting a GST film for several minutes at 600°C the melt is cooled down to 400°C. Secondly, a melt droplet is kept at 600°C during solidification and finally, an amorphous GST film is heated to 700°C and quenched to room temperature within seconds.

6.4.1 Solidification of molten GST after cooling down to 400°C

A thin GST film is molten at 600°C for several minutes using the same heating procedure as shown in Fig. 6.8. After cooling the liquid phase down to 400°C within one minute (~200°C/min), GST crystallizes in the thermodynamic stable trigonal phase. Surprisingly, a part of the GST film also crystallizes in the cubic phase. Exemplary HRTEM and the corresponding SAD images for both phases are shown in Fig. 6.17, where an aperture with a diameter of 195 nm for the SAD images is used. Figure 6.17(a) shows the cubic phase which can be identified from the SAD image. Both, HRTEM and SAD images, are taken along the Si $[1\bar{1}0]$ zone axis. The cubic grain is epitaxially aligned to the Si substrate with the orientation relationship (111)Si $\parallel$ (111)GST and $[1\bar{1}0]$Si $\parallel$ $[1\bar{1}0]$GST. Figure 6.17(b) shows the HRTEM and SAD image of the trigonal phase taken along the Si $[\bar{1}\bar{1}2]$ zone axis. The trigonal grains also exhibit an aligned orientation and are texturized with GST basal planes parallel to the Si (111) planes. Some trigonal grains are even aligned in a way that both Si and GST can be imaged along a zone axis at the same time as shown in Fig. 6.17(b). Note that the lattice spacing for GST in this example corresponds to the trigonal GST225 phase.

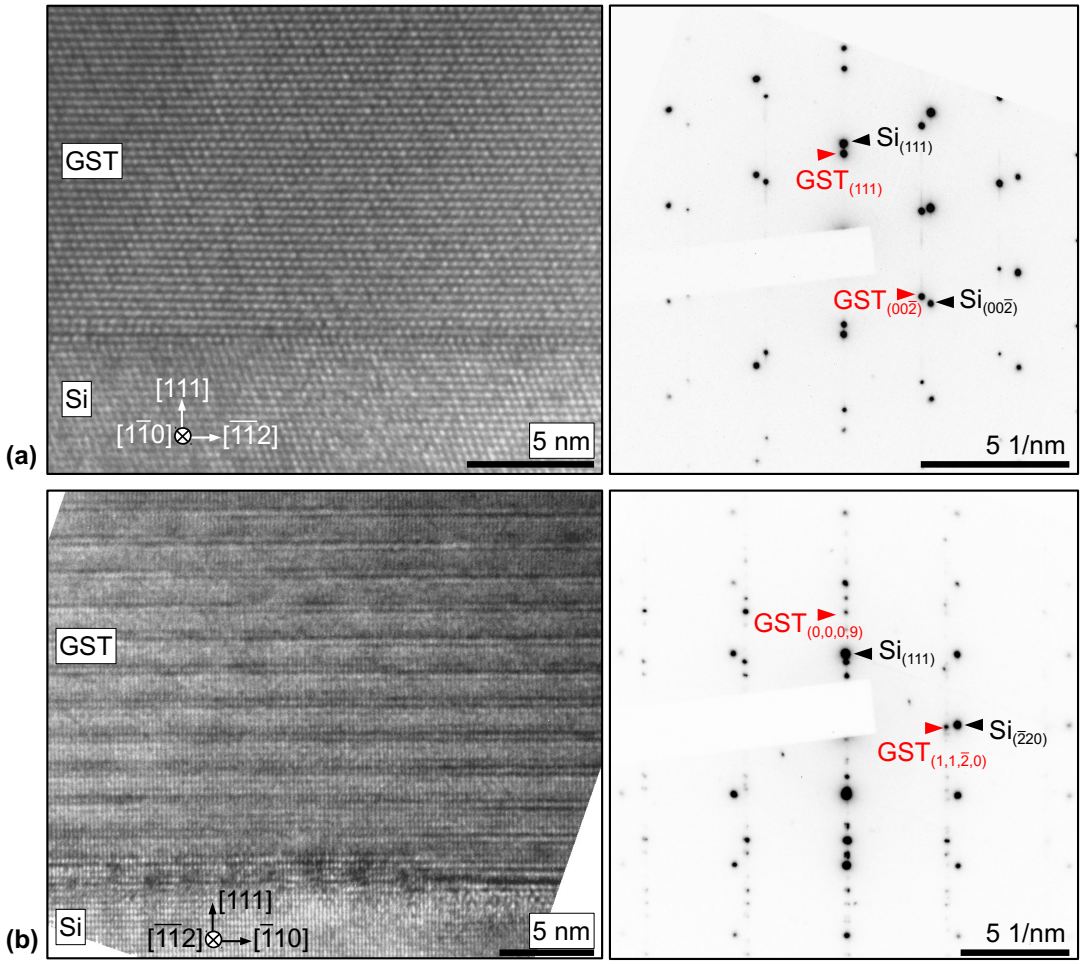

Figure 6.17 HRTEM and SAD images of the crystalline structure after solidification of GST melt during cooling down to 400°C, (a) cubic GST phase imaged in Si $[1\bar{1}0]$ zone axis and (b) trigonal GST225 phase imaged in Si $[\bar{1}\bar{1}2]$ zone axis.

6.4.2 Solidification of melt droplet at 600°C

When liquid GST sprays out of the capillary through discontinuities of the encapsulation, small liquid GST droplets are left behind. Figure 6.18(a) displays an example of a melt droplet within the empty capillary and its solidification. The TEM image series is taken from a video sequence several minutes after reaching 600°C using a similar heating procedure as before (cf. Fig. 6.8). The crystallization of the core is fast and occurs within one image frame (<0.04 sec). It is followed by some movement of the remaining liquid until the whole grain is crystalline after ~1 sec. Over the course of the next several minutes, the crystal shape changes slightly due to diffusion processes leading for example to the vanishing of transversely running facets (marked with a black arrow in Fig. 6.18(a)).

Figure 6.18(b) displays HRTEM images of the left and right side of the crystal taken at 600°C along the Si $[1\bar{1}0]$ zone axis and the corresponding FFT image of the GST region. They show that the whole grain crystallizes in the cubic phase which is aligned to the Si substrate with the same orientation relationship as previously mentioned: (111)Si ∥ (111)GST

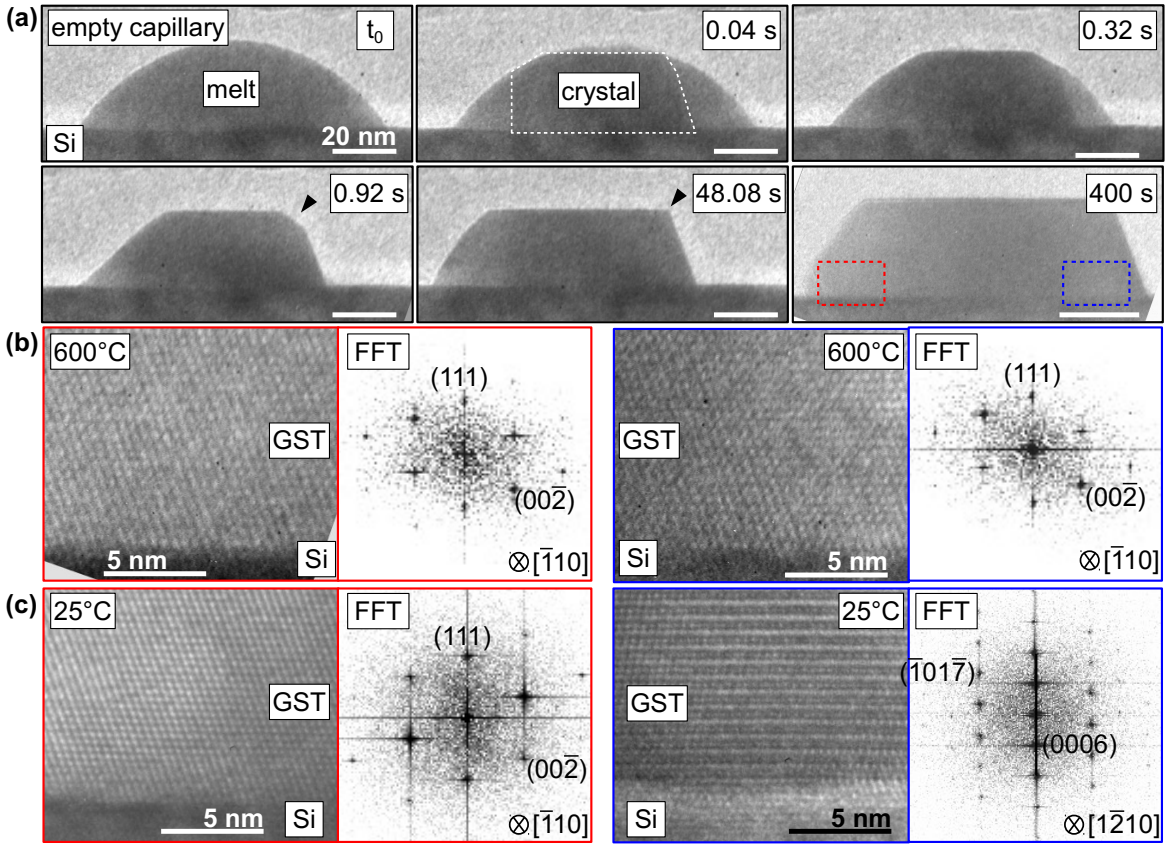

Figure 6.18 (a) TEM image series of the solidification of a GST melt droplet at T=600°C; HRTEM and FFT images showing the crystalline structure of the left (red) and right (blue) side of grain (b) at T=600°C and (c) at room temperature.

and $[1\bar{1}0]$Si ∥ $[1\bar{1}0]$GST.

Figure 6.18(c) displays again the left and right side of the same GST crystal after cooling down to room temperature using a cooling rate of 100°C/min. For each side of the crystal, a HRTEM image and a FFT of the GST region is displayed. The left side stays in the cubic phase with the same orientation relationship to the substrate as before. The right hand side however changed into the thermodynamic stable trigonal phase. The trigonal phase is also epitaxially aligned to the Si substrate: (111)Si ∥ (0001)GST and $[11\bar{2}]$Si ∥ $[1\bar{1}00]$GST and the lattice spacing corresponds to the GST124 trigonal phase.

6.4.3 Crystal phase after quenching

For the last experiment, the MEMS-based heating holder is used to achieve higher heating and cooling rates. The as-deposited amorphous GST film is prepared as two FIB lamellas of 200 nm thickness and mounted on the MEMS-based heating holder as described in section 4.3.2. Figure 6.19 shows the schematic illustrations of the applied heating procedure: In one experiment (cf. Fig. 6.19(a)), the amorphous GST film is heated from room temperature to 680°C with a rate of 113°C/s and then rapidly cooled down to room temperature with 250°C/s. In a second experiment (cf. Fig. 6.19(b)), the amorphous GST film is heated using

similar heating and cooling rates from room temperature to 690°C and back.

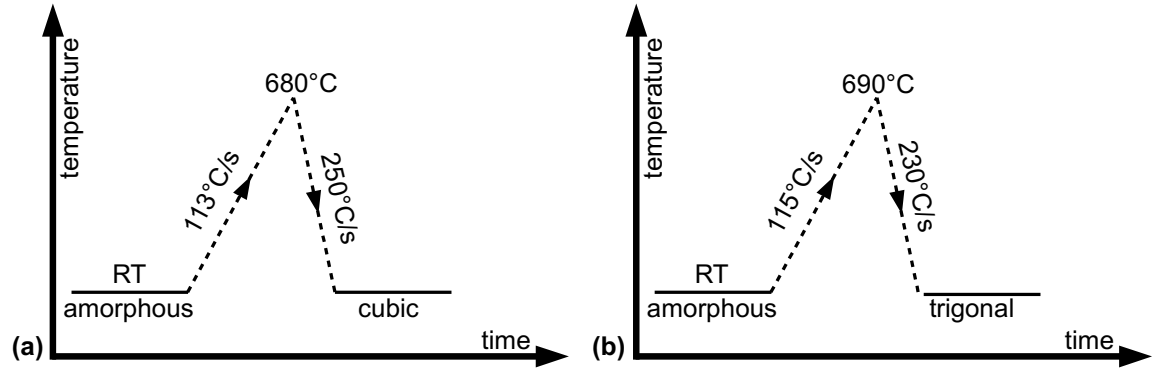

Figure 6.19 Schematic illustration of the experimental procedure for in-situ quenching of an amorphous GST film from RT to almost 700°C and back to RT.

The SAD images of the resulting crystalline films are shown in Fig. 6.20 using an aperture with a diameter of 195 nm. Again, the GST film crystallizes in the cubic as well as the trigonal crystal structure. Figure 6.20(a) displays the SAD image of the cubic film which is recorded along the Si $[1\bar{1}0]$ zone axis. The cubic structure exhibits the same orientation relationship to the substrate as in the previous experiments: (111)Si ∥ (111)GST and $[1\bar{1}0]$Si ∥ $[1\bar{1}0]$GST. Figure 6.20(b) shows the SAD pattern of the trigonal phase. The SAD is recorded close to the GST $[11\bar{2}0]$ zone axis which is about 1° off the Si $[1\bar{1}0]$ zone axis. The GST basal planes $\{000l\}$ are slightly tilted with respect to the Si(111) planes by about 3.5°. The GST lattice spacing corresponds to GST124.

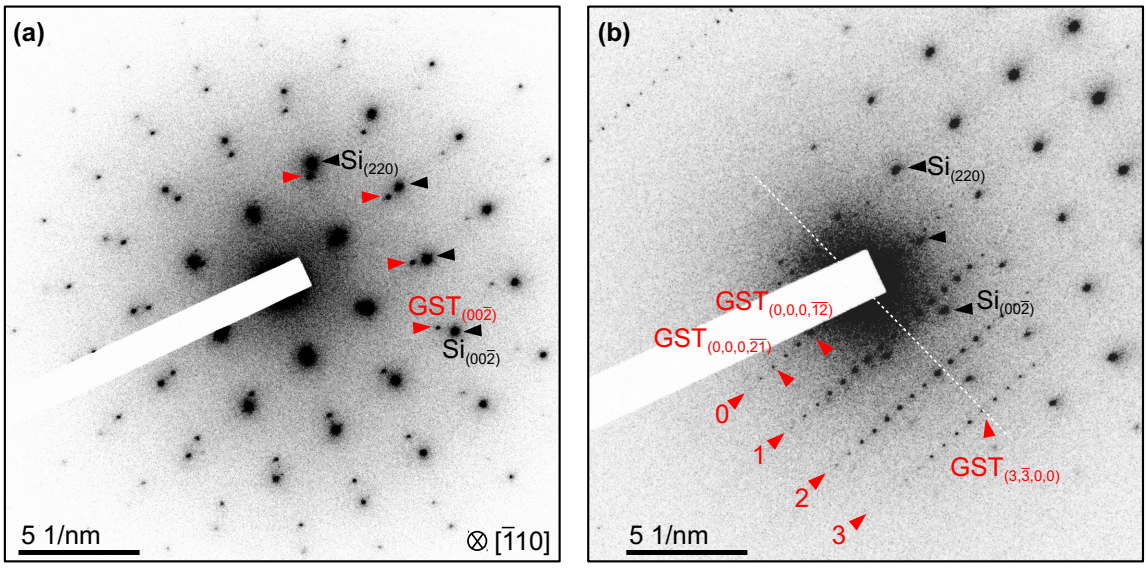

Figure 6.20 SAD image of crystalline film after quenching for (a) cubic GST taken along Si [-110] zone axis and (b) trigonal GST taken close to the GST[11-20] zone axis which is about 1° off the Si [-110] zone axis

6.4.4 Discussion

Both the cubic and the trigonal phase can be found after solidification under several different conditions even though one expects to find only the trigonal phase at temperatures above the cubic-to-trigonal transition temperature. A possible explanation for the formation of the cubic phase at high temperatures would be different thermal expansion behaviors favoring the cubic phase by lowering the lattice mismatch between GST and silicon. However, according to estimations based on the scarce literature data, the thermal expansion of cubic and trigonal GST124 is the same [110] and both are larger compared to Si [217] and therefore the lattice mismatch increases even further eliminating this possibility. (More details of the approximation of thermal expansion can be found in section A.1.) The possible influence of the electron beam on the formation of the cubic crystal structure upon solidification is improbable. During the quenching experiments the formation of the cubic grain occurred within seconds during which the sample is observed at a low magnification minimizing the e^--beam exposure. In addition, cubic grains are observed even outside regions exposed to the e^--beam at high temperatures. Another possible explanation would be a small energy difference between both states leading to their coexistence in fast solidification conditions. And indeed, Sun *et al.* [127] calculated the total energy using *ab initio* calculations both for the trigonal and the cubic phase and the energy difference is only 0.3%. This small energy difference could be the reason that it is possible to form both phases during a quick cool down. Noteworthy is that cubic grains formed after solidification are epitaxially aligned opposed to cubic grains that form from an amorphous film after heating to 140°C and opposed to trigonal grains exhibiting multiple orientation relationships. This indicates that the crystalline interface might play a role in the formation of the cubic phase at high temperatures. In the next chapter the cubic structure is further investigated. However, so far the formation mechanism remains unclear.

6.5 In-situ study of surface energy

In this section, the interfacial energies between Si and GST are estimated based on contact angle measurements, and surface energies for different low-index $\{hkl\}$ planes are estimated based on the Wulff-Kaishev construction.

6.5.1 Interfacial energy measurements based on contact angle

There are two components to the interfacial energy:

$$\gamma_{\text{interface}} = \gamma_{\text{chem}} + \gamma_{\text{struc}} \tag{6.2}$$

(1) the chemical contribution, γ_{chem}, because of the bonding between atoms of different phases and (2) the structural (strain) contribution, γ_{struc}, resulting from the misfit of lattices.

There is no data on interfacial energies for the GST-Si system available. The measurement of the contact angle of a GST melt droplet on the Si substrate is therefore used to roughly estimate the interfacial energies between GST melt and Si as well as trigonal structured GST and Si. Using the wetting behavior of a liquid droplet on a solid surface, the surface energy

can be calculated using Young's equation [218, 219] which is based on the force balance at the contact line where the three phases (liquid (l), solid (s), vapor (v)) meet:

$$\gamma_{lv} \cos(\theta) = \gamma_{sv} - \gamma_{sl} \tag{6.3}$$

Thereby, γ_{lv} is the surface energy of the liquid-vapor, γ_{sv} of the solid-vapor and γ_{sl} of the liquid-solid interface.

Figure 6.21(a) shows a TEM image of an exemplary GST melt droplet on the Si substrate used to measure the contact angle. The formation of the melt droplet is discussed in section 6.4.2. The contact angle measurement is done using an ImageJ plugin for droplet shape analysis based on B-spine snakes [220]. The used droplet shape is shown as a blue line and yields a contact angle of $\theta_{\text{melt, Si}}$=(60±5)°. Note that the same result is gained by applying the alternative $\theta/2$ method. There, the contact angle can be geometrically calculated by measuring the drop diameter and height of the apex [216].

Applying eq. (6.3) leads to eq. (6.4) which can then be used to calculate the interfacial energy between Si(111) and GST melt:

$$\gamma_{\text{melt, Si}} = \gamma_{\text{Si(111), vac}} - \gamma_{\text{melt, vac}} \cos(\theta_{\text{melt, Si}}) \tag{6.4}$$

For the determination of $\gamma_{\text{melt, Si}}$, the reported surface energy of Si(111) is used, $\gamma_{\text{Si(111), vac}} = 1.23$ J/m^2 [221]. For the surface energy of molten GST $\gamma_{\text{melt, vac}}$ no value is reported. Bai *et al.* used thermodynamic calculations based on size-dependent melting temperatures to determine the surface energy for amorphous GST225 to be $\gamma_{\text{a, vac}} = 0.094$ J/m^2 [222]. Because of the similar structure and bonding conditions in the amorphous and the molten state (cf. section 5.2.4), it is assumed in a first approximation that the surface energy of molten GST is equal to the amorphous phase: $\gamma_{\text{melt, vac}} \approx \gamma_{\text{a, vac}} = 0.094$ J/m^2. Using those surface energies, the interfacial energy between Si(111) and GST melt is estimated with eq. (6.4) to be $\gamma_{\text{melt, Si}} = (1.18 \pm 0.01)$ J/m^2.

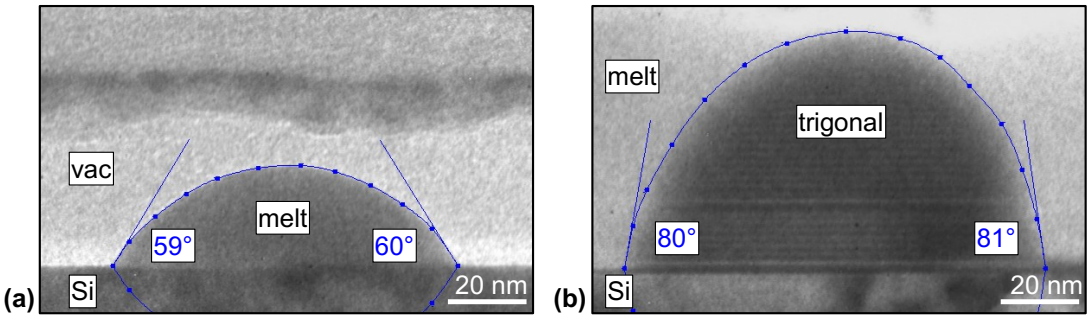

Figure 6.21 Analyzing the contact angle using TEM images of (a) a melt droplet in vacuum (inside an empty capillary) and (b) trigonal GST surrounded by melt both on the Si(111) substrate

Figure 6.21(b) shows a TEM image of a trigonal GST particle surrounded by its melt which is taken from the final melting sequence (cf. Fig. 6.11). Upon melting, the surface energy of crystal grain becomes isotropic resulting in a round shape and loss of faceting. Because of this isotropic surface energy, the Young's equation is used to estimate the interfacial energy between Si and trigonal structured GST even though it was developed for

liquid-solid systems. The contact angle measurement yields $\theta_{\text{trig, Si}}$=(80±5)°. Equation (6.3) can then be used to calculate the interfacial energy:

$$\gamma_{\text{trig,Si}} = \gamma_{\text{melt, Si}} - \gamma_{\text{trig, melt}} \cos(\theta_{\text{trig, Si}}) \tag{6.5}$$

For the determination of the interfacial energy between trigonal structured GST and Si(111), $\gamma_{\text{trig,Si}}$, the above estimated interfacial energy between Si(111) and GST melt ($\gamma_{\text{melt, Si}} = 1.18$ J/m^2) is used. Kalb *et al.* calculated the interfacial energy between trigonal structured GST225 and its melt from the measured nucleation temperature: $\gamma_{\text{trig, melt}} = 0.04$ J/m^2 for GST225 [167, 223]. Inserting those values for the interfacial energies in eq. (6.5), the interfacial energy between trigonal structured GST and Si(111) can be estimate to be $\gamma_{\text{trig,Si}} = (1.17 \pm 0.01)$ J/m^2.

The estimation of the interfacial energy based on the contact angle analysis can only be a very rough estimation because some assumptions used in Young's equation are not fulfilled. First, the silicon surface is not flat and surface inhomogeneities are known to influence the contact angle [216, 219]. The TEM images of the interface region show that the silicon surface exhibits surface steps. In addition, when the melt moves inside the capillary the melt front (vac-melt interface) exhibits a changing receding contact angle which ranges between 35° and 55° which indicates a rough interface [216]. The same is true for the growing (advancing contact angle) and shrinking (receding contact angle) of the trigonal structured crystal surrounded by melt where the contact angle varies around 90° (cf. Fig. 6.16). Additional inhomogeneities can result from impurities (e.g. glue residue, capillary). Secondly, the Si surface is not entirely inert to the GST film as silicon diffusion into the GST film is observed and discussed in the next chapter. Finally, for nanoscale droplets Young's equation needs to be modified to include an unknown term to take the line tension effect into account [216]. Nonetheless, the good wetting behavior (<90°) of the melt and the intermediate wetting behavior of trigonal structured GST (~90°) can be used to conclude:

$$\gamma_{\text{Si(111)}} > \gamma_{\text{Si,melt}} \approx \gamma_{\text{Si,tri}} \tag{6.6}$$

The solid-liquid interface lacks the strain contribution to the interfacial energy due to flexible atomic arrangement of the liquid. The conclusion that the interfacial energy is similar between melt and Si and between trigonal structured GST and Si ($\gamma_{\text{Si,melt}} \approx \gamma_{\text{Si,trigonal-GST}}$) indicates that the strain contribution to the interface between Si and trigonal structure GST is low. Finally, note that interfacial energies are temperature dependent, and therefore the statement can only be made for T=600°C.

6.5.2 Surface energy measurements based on Wulff-Kaishev construction

Figure 6.22(a) shows an exemplary melt droplet (cf. section 6.4.2). Figure 6.22(b) shows the same droplet after crystallization at 600°C exhibiting clear crystal facets.

Faceting of surfaces is generally driven by the anisotropy in surface energy, γ_{hkl}, as a function of the crystallographic orientation {hkl}. In case of a crystal grown on a substrate (cf. illustration in Fig. 6.23), the shape is determined by the Wulff-Kaishev construction

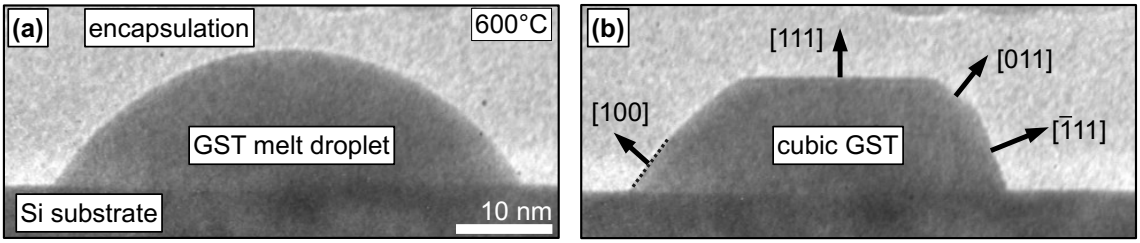

Figure 6.22 (a) TEM image of melt droplet at 600°C. (b) TEM image of the same droplet after solidification at 600°C exhibiting {100}, {110} and {111} facets.

given by eq. (6.7) [224]

$$\frac{\gamma_{\text{hkl}}}{h_{\text{hkl}}} = \frac{\gamma_{\text{sub}} - \gamma_{\text{int}}}{h_{\text{int}}} = \text{constant} \tag{6.7}$$

which takes into account the interfacial energy γ_{int} between substrate and crystal.

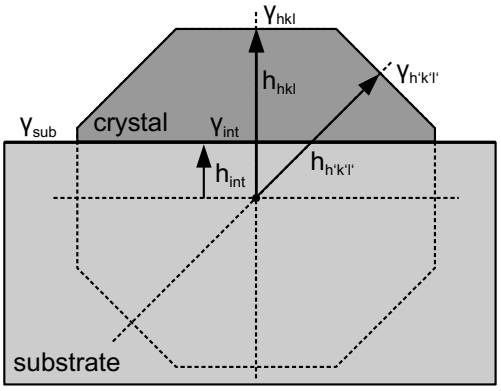

Figure 6.23 Schematic drawing of a faceted crystalline particle on a substrate illustrates the terms used in the Wulff-Kaishev construction.

Figure 6.24 shows a schematic drawing displaying the involved facets of the GST crystal shown in Fig. 6.22(b). It illustrates that the projected crystal edges observed in Fig. 6.22(b) indeed correspond to crystal facets. During the solidification, the three low-index facets {100}, {110} and {111} are developed. With the help of the Wulff-Kaishev construction, the surface energies for the four visible facets ((111), $(\bar{1}11)$, (011) and (100)) are measured. Because the facets slightly change over time after solidification of the melt droplet, the measurement is done for three different points in time after crystallization. Figure 6.25 displays three TEM images of the same crystal as shown in Fig. 6.22(b) at three different points in time. The median lines for the (111) and (011) facets are used to find the origin of the Wulff-Kaishev construction. From there, the heights h_{hkl} and h_{int} defined in the schematic shown in Fig. 6.23) are measured. Applying eq. (6.7) leads to eq. (6.8) which is then used to calculate the surface energies for the different facets in multiple of $\Delta\gamma = \gamma_{\text{Si(111)}} - \gamma_{\text{cub,Si}}$.

$$\gamma_{\text{hkl}} = \underbrace{\left(\gamma_{\text{Si(111)}} - \gamma_{\text{cub,Si}}\right)}_{\Delta\gamma} \frac{h_{\text{hkl}}}{h_{\text{int}}} \tag{6.8}$$

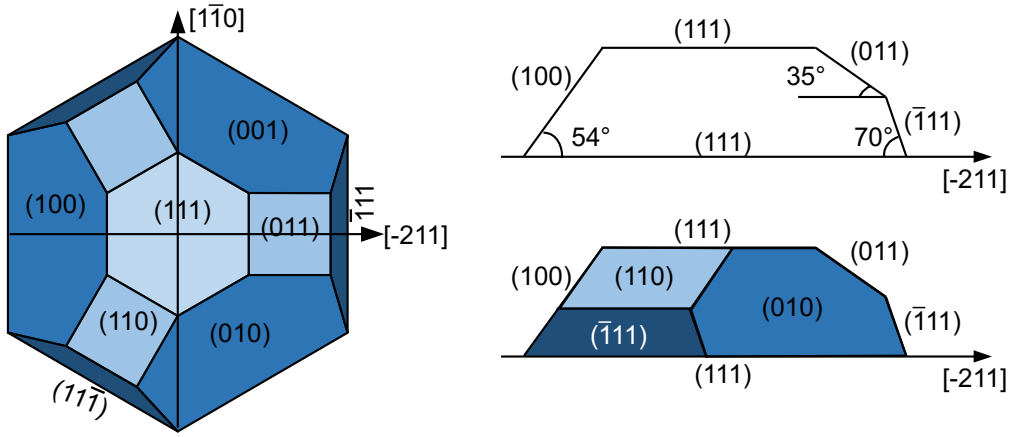

Figure 6.24 Schematic drawing illustrating the {100}, {110} and {111} facets of the crystal developed during solidification displayed in top and side-view.

The resulting surface energies are summarized in table 6.2.

time [sec]	$\gamma_{(111)}$ [$\Delta\gamma$]	$\gamma_{(\bar{1}11)}$ [$\Delta\gamma$]	$\gamma_{(011)}$ [$\Delta\gamma$]	$\gamma_{(100)}$ [$\Delta\gamma$]
1	3.2	3.2	3.6	3.7
2	3.0	3.0	3.6	3.3
3	2.6	2.6	2.9	3.0
ø	2.9 ± 0.3	2.9 ± 0.3	3.4 ± 0.4	3.3 ± 0.4

Table 6.2 Relative surface energies (in terms of $\Delta\gamma$) for the (111), ($\bar{1}$11), (011) and (100) facets of cubic structured GST for different points in time after solidification of the crystal.

The analysis shows that the {111} facet has the lowest surface energy followed by {110} and {100}:

$$\gamma_{111} < \gamma_{110} \approx \gamma_{100} \tag{6.9}$$

The deviations over time are attributed to the uncertainty of the measurement.

A first approximation for the surface energy can be made by applying the simplified broken-bond model [219, 225] on a rock-salt crystal structure and including the surface density of atoms. This model yields that the {100} surface should have the lowest energy followed by the {110} and {111} surface, respectively: $\gamma_{100} < \gamma_{110} < \gamma_{111}$. (Detailed information can be found in the appendix A.4). Consequently, a small particle in equilibrium shape consists primarily of those facet types. And indeed, the cubic grain formed after crystallization from the melt droplet exhibiting only {100}, {110} and {111} facets. The difference in ranking from lowest to highest surface energy between model and experiment can be traced back to the assumptions of the model. It does not take into account effects like surface reconstruction or relaxation which can lower the energetic state of the surface.

For the calculation of the absolute value of the surface energy of cubic GST, the interfacial energy γ_{int} between Si(111) substrate and cubic GST is needed. Since no values have been reported in the literature so far, in a first approximation it is assumed to be equal to the above determined interfacial energy between trigonal structured GST and Si(111), $\gamma_{\text{cub,Si}} \approx$

$\gamma_{\text{trig,Si}} = (1.17 \pm 0.01)$ J/m^2. The surface energy of the Si(111) substrate is reported to be $\gamma_{\text{Si,111}} = 1.23$ J/m^2 (determined by cleavage experiments) [221]. Using eq. (6.8) the absolute values for the surface energy are determined and summarized in table 6.3.

$\gamma_{(111)}$ [J/m^2]	$\gamma_{(\bar{1}11)}$ [J/m^2]	$\gamma_{(011)}$ [J/m^2]	$\gamma_{(100)}$ [J/m^2]
0.16 ± 0.04	0.16 ± 0.04	0.19 ± 0.05	0.18 ± 0.05

Table 6.3 Absolute values of surface energies for the (111), $(\bar{1}11)$, (011) and (100) facets of cubic structured GST.

So far, the surface energy for GST used as parameter in several thermodynamic calculations in the literature to describe the nucleation behavior of amorphous GST is in the range of 0.092 to 0.15 J/m^2 [169, 222, 226–228]. The surface energies for the three different facets determined in this thesis (based on the Wulff-Kaishev construction) lay in the same order of magnitude.

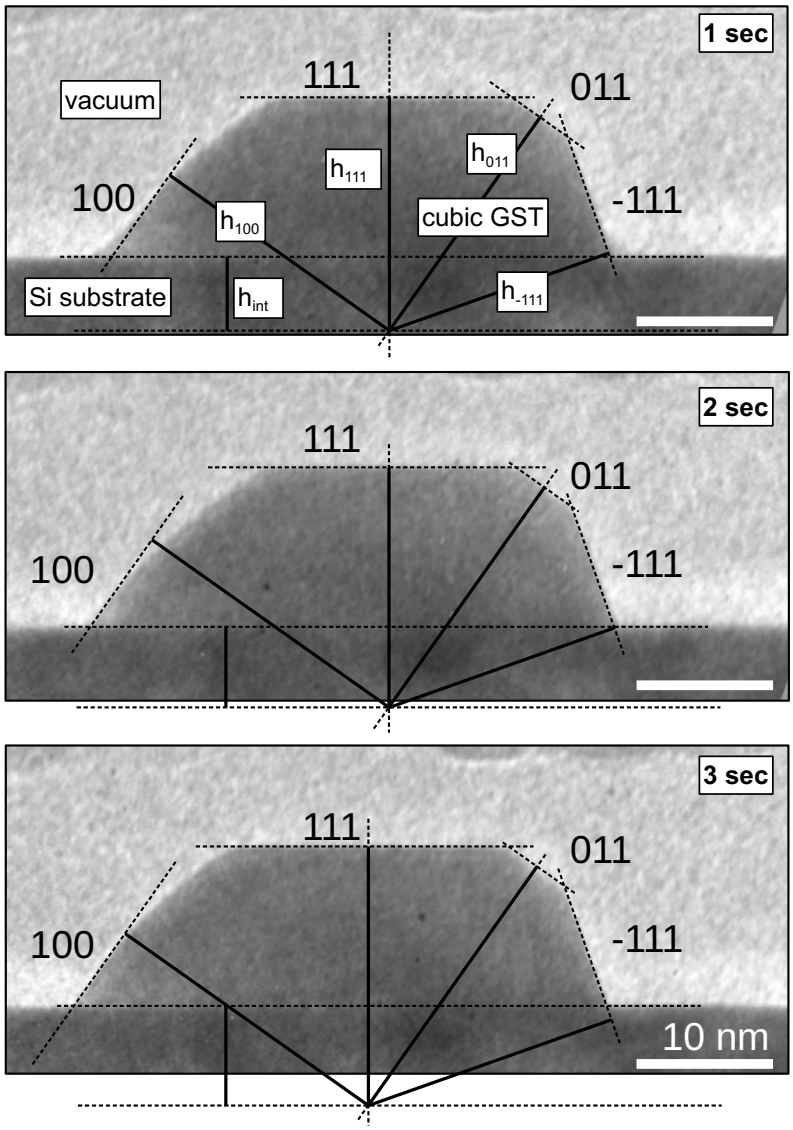

Figure 6.25 Wulff-Kaishev construction of a cubic structured GST crystal on a Si substrate for three different points in time after the solidification of the melt droplet.

6.6 Summary

The high-temperature phase transitions such as melting and crystallization from the melt of the GST124 thin film deposited on a Si(111) substrate is studied inside a TEM with high spatial resolution and in real time. The starting point of this phase transition study is an ordered trigonal GST124 film. The chemical composition and the ordered trigonal crystal structure are experimentally verified by EELS and TEM. Melting instead of sublimation is observed in spite of high vapor pressures due to a full encapsulation of the thin film. The liquid-vacuum as well as the solid-liquid interface movements are tracked. The molten GST describes an oscillatory motion independent of the melting and crystallization of the crystalline GST. During melting the solid-liquid interface exhibits a broad and diffuse transition zone characterized by a vacancy induced disordered state that can be linked to a premelting mechanism. The melting as well as the solidification process exhibit similar velocities in the nanometer per second scale. While the melting occurred linearly, crystallization showed a clear time-dependent growth superimposed with a distinct start-stop motion. The influence of the interface on the crystallization is discussed, but the underlying mechanism of the start-stop behavior is yet unclear. After solidification both crystalline phases, trigonal and cubic, are found independent of the investigated solidification processes. The influences on the unexpected growth of cubic GST are discussed and the small energy difference between both phases emphasized. The interfacial energy of the GST-Si system is estimated based on the contact angle measurements. Furthermore, the surface energies for different low-index facets is calculated based on the Wulff-Kaishev construction and it is concluded that the {111} facets have the lowest surface energy.

7 Sublimation

In the previous chapter, in-situ TEM is used to analyze the molten state and the solid-liquid transitions of GST. The present chapter is dedicated to another high-temperature transition of crystalline GST, the solid-to-gas transformation. The local and dynamic observation of the process is made possible by in-situ TEM and provides insights to the atomistic processes involved in the solid-to-gas transformation.

First, section 7.1 introduces the terrace-step-kink model and discusses the process of stepwise sublimation and surface roughening based on that model. Section 7.2 addresses the in-situ experiments of sublimation of the cubic phase of GST124 starting with the discussion of the experimental details. The main focus are the experimental results, where the structure and thermal stability of the cubic phase are investigated initially, and then, the anisotropic dynamics of sublimation involving kink nucleation and step motion are analyzed. Afterwards, section 7.3 provides insights in the sublimation of trigonal structured GST. Finally, the chapter ends with concluding remarks in section 7.4. (Parts of the work presented in this chapter are submitted to be published.)

7.1 Terrace-step-kink model

For the description of the atomistic processes involved in sublimation the nearest-neighbor broken-bond model, describing how atoms are bound to the surface, and the terrace-step-kink (TSK) model of surfaces are used. The models are based on ideas by Volmer [229], Kossel [230] and Stranski [231], and further developed by Burton *et al.* [232] and Hirth and Pound [233]. In this section, the general ideas are reproduced based on the explanations in Ref. [14, 219, 225, 234] and on recent experiments in the field of in-situ TEM.

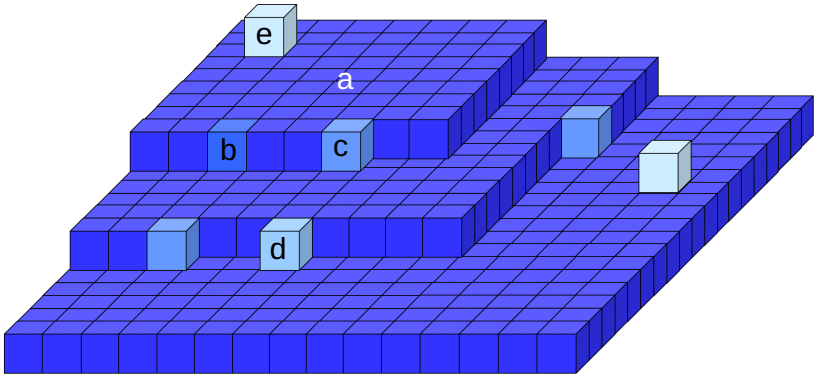

Figure 7.1 Schematic model of a vicinal surface displaying different atomic positions: a) terrace atom, b) step atom, c) kink atom, d) step adatom and e) terrace adatom

Surface atoms experience a different environment compared to atoms in the bulk of a

crystal. Atoms in the surface layer have fewer nearest-neighbors and therefore possess an excess energy due to broken bonds. Figure 7.1 displays several possible atomic positions on a vicinal surface in a schematic drawing. For simplicity, a monoatomic simple cubic crystal is displayed. Vicinal surfaces consist of large flat areas called terraces and atomic steps (sometimes also referred to as ledges). Atoms can sit at different position on those surfaces as marked in Fig. 7.1: a) terrace atom, b) step atom, c) kink atom, d) step adatom and e) terrace adatom. The atoms in the positions a) - e) have a decreasing number of nearest-neighbors in the crystal. The broken-bond model can then also be used to estimate the energy needed to remove an atom from the different positions on a given surface. According to this model, if an atom in one position (e.g. a kink site) possesses more broken bonds (fewer nearest-neighbors) than in another position (e.g. terrace or step site) this atom is bound weaker to the crystal surface and therefore its removal requires less energy.

7.1.1 Stepwise sublimation

Sublimation (as well as the reverse process of crystal growth for which the TSK model was originally developed) is argued to involve a multi-step process [14, 15, 232]. According to the TSK model, the desorption during the solid-to-gas transition is expected to be faster from a position with low coordination (high number of broken bonds) than from a position with high coordination (few number of broken bonds). Therefore, the multi-step process first involves atom movement from a terrace position into a step position. From there movement into a kink position, then surface diffusion and finally desorption to the gas phase from a terrace surface. There is strong experimental evidence for stepwise sublimation from macroscopic ([15] and references therein) more recently from microscopy studies [12, 16, 18–21, 50, 235, 236].

Most studies however only indirectly confirm the applicability of TSK model for sublimation processes. For instance, Hellebusch *et al.* [16] reported the sublimation of dispersed CdSe nanorods by in-situ BF-TEM in the temperature range of 370-450°C. The sublimation is reported as continuous at high temperatures and punctuated at lower temperatures. They argued that this can be explained with having fluctuations between kink-free and highly kink populated facets at low temperatures, and only kinks sites (or easy generation of kinks) at high temperatures. Because the sublimation from kink sites is expected to be faster than from terrace sites, this leads to a start-stop motion in the former and a continuous dynamic with a rounded shaped tip in the latter case. Others also reported anisotropic sublimation in agreement with the TSK model, where facets with a lower packing density and hence a larger free surface energy sublime prior to other facets [20, 21] or where defects and crystal edges enhance the sublimation rate [12, 18, 235, 236] as predicted by Hirth and Pound [14] using the TSK model to describe the stepwise sublimation mechanism that crystal edges act readily as kink sources.

The few studies where sublimation is shown with atomic resolution are done for dispersed nanoparticles [19, 20] or 2D crystalline materials like graphene [235, 236] and black phosphorus [50].

An open question is however, how a complex system such as the quasi-binary GST alloy and a heterostructure configuration, influence the sublimation process and whether it can be viewed as the reverse growth process where the theoretically described TSK model is

applicable. In this study, in-situ HRTEM is therefore applied to the GST-Si system in order to study the intermediate steps leading to the formation of terraces at atomic resolution and to directly observe the kink-step-terrace formation mechanism for a heterostructure.

7.1.2 Surface roughening

Defects like adatoms and surface vacancies can be created due to thermal fluctuations because of the entropy gain in the surface energy at finite temperatures [237]. At nonzero temperatures a surface is therefore rough at a microscopic scale whereas macroscopically the surface remains flat. At temperatures above a critical value, called the roughening temperature T_R, the surface becomes macroscopically rough meaning the fluctuation of the height diverges [238]. Burton *et al.* and then Mullins and Hirth ([219] and references therein) used the TSK model together with the nearest-neighbor bond model to consider the creation of terrace and step vacancies and adatoms and thereby predicated that a surface becomes appreciably rough at a temperature of about 0.5 T_M. They also pointed out, that the roughening temperature depends on the bond strength and is higher for materials with stronger bonds. Since then, it was experimentally observed for various metal surfaces, e.g. for fcc (110) surfaces around $\frac{T_R}{T_m} = 0.75$ [237, 238]. As a roughening transition would have implications for the crystal growth process, it is worthwhile to investigate whether or not such a transition can be observed for GST.

7.2 Sublimation of cubic phase

This section is dedicated to the sublimation behavior of the cubic crystalline phase of GST which is the crystalline phase of interest in applications [24, 47, 98]. First, the experimental details of this study are addressed. Next, the structural and compositional stability of the GST film are analyzed. The epitaxial alignment of the cubic grain enables then the study of the dynamics of the anisotropic sublimation process with atomic resolution.

7.2.1 Experimental details

The experimental details of this study are addressed by discussing the experimental conditions inside the TEM, the setting up of the initial state of the specimen and the possible influence of the experimental set-up on the observed dynamics.

Experimental conditions inside the microscope

The vacuum inside the microscope is in the range of 10^{-5}–10^{-6} Pa. Considering a typical temperature-pressure phase diagram in the low pressure regime of a material with a negative thermal expansion such as GST [30] (cf. Fig. 2.1(b)), the solid state has a smaller Gibbs free energy at temperatures below the sublimation temperature T_{sub} compared to the gas phase and is therefore the thermodynamically stable phase. Above the sublimation temperature however, the Gibbs free energy for the gas phase is lower and the difference in Gibbs energy, ΔG, is the thermodynamic driving force for the expected solid-to-gas transformation (sublimation).

There is a lack of data on low-pressure phase transitions of GST and the pressure dependence of the sublimation temperature is unknown. But in-situ heating of GST at temperatures above the melting temperature (T_M=615°C for GST124) is expected to lead to sublimation without encapsulation of the thin film when taking into account that the partial pressures of Te ($\sim 10^3$ Pa) and Sb ($\sim 10^1$ Pa) [95] at this temperature are well above the low base pressure of the microscope. Even though the partial pressure for Ge is lower ($\sim 10^{-10}$ Pa [95]) than the base pressure in the TEM, GST does not point to any Ge excess compared to the composition before annealing as will be shown in the next section.

Setting up the initial state

Figure 7.2 summarizes the setting up of the initial state for the sublimation study of the cubic crystalline GST. The temperature treatment of a GST thin film inside the TEM (JEOL 2100F) is displayed in a schematic temperature-versus-time plot in Fig. 7.2(a). The heat treatment was performed with the DENSsolutions heating holder. In order to generate epitaxially aligned GST the amorphous film was heated in a first step to 625°C followed by a fast cool down to 400°C within 3 sec. The sample is then heated in a second step to 640°C, in order to observe the sublimation of the cubic GST grain at atomic resolution. A BF-STEM overview image of the as-deposited amorphous GST film prepared in lamella geometry is shown in Fig. 7.2(b). The film is continuous and exhibits a sharp interface to the crystalline Si substrate. On top of the GST film the carbon protective layer is visible. At 625°C, sublimation instead of melting is observed as the film is not encapsulated as discussed in the previous chapter. The BF-STEM image taken at 625°C in Fig. 7.2(c) shows that the GST thin film decomposes leading to an overall thinning of the sample leaving faceted grains and holes behind. Simultaneously, crystal grains with cubic structure are formed which are epitaxially aligned to the crystalline silicon (111) substrate. An example of an epitaxially aligned cubic GST is shown in the HRTEM image of a similarly treated sample in Fig. 7.2(d). The cubic grains produced in this way serve as initial state in this sublimation study.

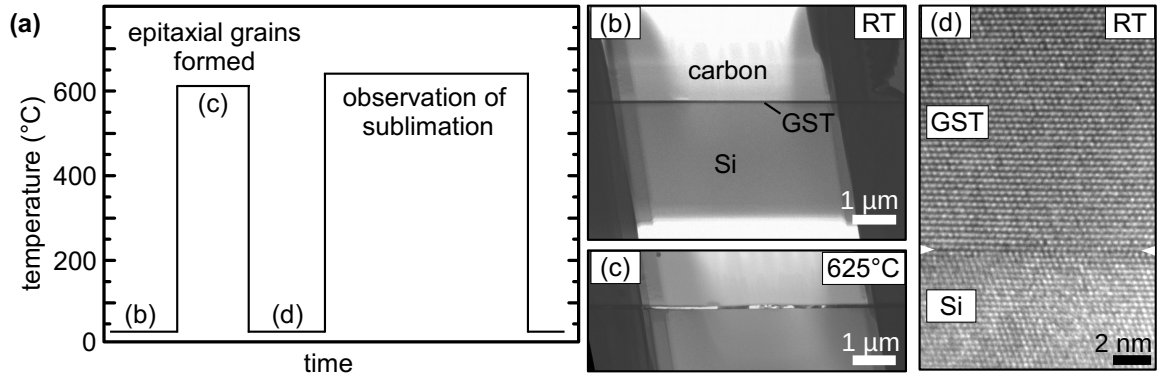

Figure 7.2 (a) Schematic experimental procedure for in-situ heating of GST thin film first from RT to 625°C to generate epitaxial aligned cubic grains and secondly to 640°C for in-situ observation of sublimation of cubic grains. (b) BF-TEM image of a FIB-lamella on a DENSsolutions chip with GST thin film in initial amorphous state featuring the Si substrate and carbon protective layer, (c) same lamella at 625°C showing the thinned areas and voids left by first heat treatment and (d) HRTEM image of cubic epitaxially aligned grain (image taken from similarly treated sample).

Influence of experimental set-up

The possible influences of the experimental set-up on the described sublimation mechanism need to be discussed. The observed sublimation could be influenced by the electron beam, contamination of the sample, and temperature fluctuations of the holder.

Electron beam. As previously mentioned in section 4.2.3, the interaction of high-energy electrons with the sample can lead to the decomposition of the structure and an increase in temperature. There is no indication for a decomposed structure caused by the electron beam when considering the stable composition and the stable crystallographic orientation of the investigated grain. Concerning the possible effect of an increase in temperature through the electron beam: When the experiment is done at higher temperatures, the same formation of stable facets is found which only occurs faster. Therefore, an increase in temperature caused by the electron beam would only increase the observed formation speeds. On the other hand, the measured speeds are independent of the observed time and magnification used. This implies that the temperature applied by the sample holder is more important than the heating effects of the electron beam.

Contamination. The inevitable amorphous layer on the specimen could act as contamination and influence the kink motion. Fortunately, the amorphous film is not continuous and there are regions without coverage of the amorphous film. There is no difference in the kink motion between covered and uncovered areas making the influence of the amorphous film improbable.

Temperature. The sublimation mechanism could be influenced by temperature fluctuations of the TEM holder. According to the measured average temperature of the holder, the fluctuations are less than $0.01\,^{\circ}\mathrm{C}$ over the time period of the entire experiment. Nonetheless, the local temperature might fluctuate stronger. A possible indicator that even the local temperature is stable, are the constant step velocities measured over several minutes. Recently Lian *et al.* [239] studied the sublimation and wetting behavior of Ag nanowires for temperatures up to $750\,^{\circ}\mathrm{C}$ using in-situ BF-TEM. The observed sublimation velocities are also in the nm/s range, but showed a dependence on the heating time. The sublimation speeds are cut in half after a few minutes. They explained that the sublimation slowed down with time because of the decrease in thermal contact between the nanowire and the holder. In this study, the thermal contact between substrate and thin film does not decrease. Therefore, the fact that the step velocities stay in the same order of magnitude for all observed steps indicates that the local temperature is stable.

7.2.2 Structure and composition stability

Before the dynamics of the sublimation process can be discussed, the stability of the cubic structure and the GST124 composition need to be addressed.

Stability of structure

The initial state of a GST grain used to investigate the dynamics of the sublimation process is shown in Fig. 7.3(a). The TEM micrograph is taken at room temperature along the $[1\bar{1}0]$ zone axis of Si and displays an overview of the grain with a projected size of about 130 nm $\times$ 50 nm. The high-resolution image reveals a crystallographic alignment of the GST grain

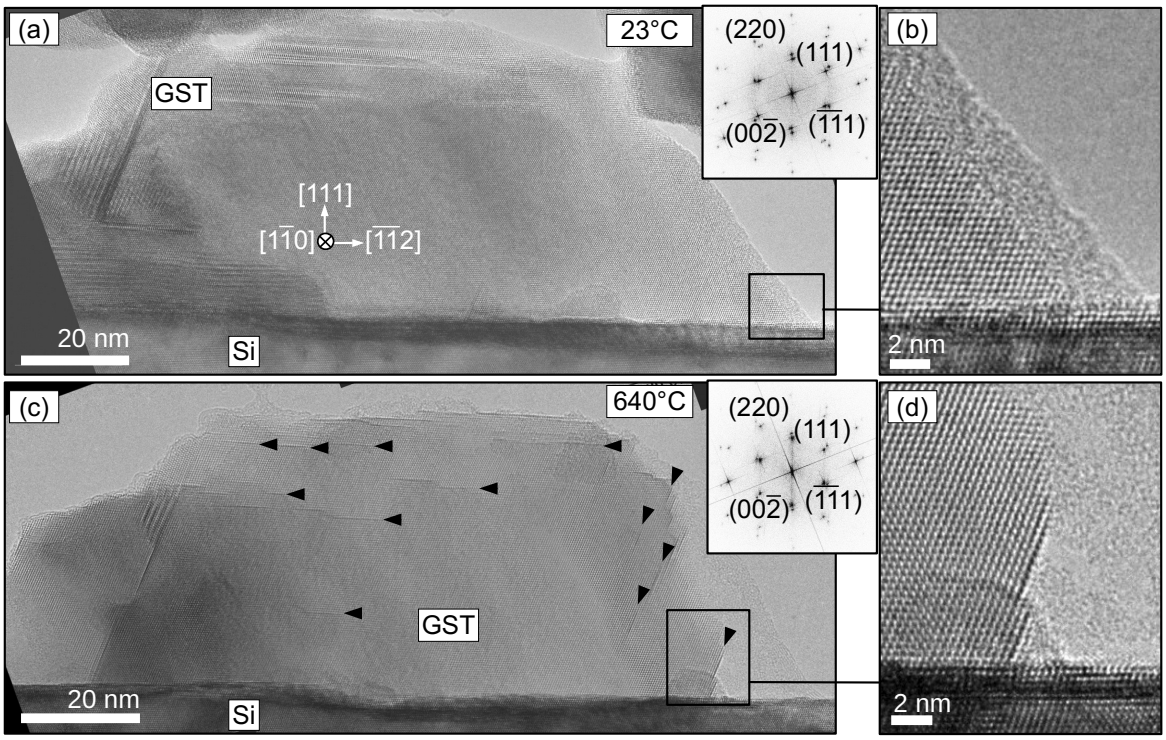

Figure 7.3 HRTEM image of cubic GST grain at (a) 23°C (initial state) and (c) 640°C (onset of sublimation) stitched together from several micrographs. Black arrows in (c) mark some of the edges along [112] that form during sublimation. Insets showing FFT of central region of the image containing Si and GST. Close-up views in (b) and (d) show corresponding magnifications of the grain at the Si-GST interface region.

with the Si substrate as verified by the matching of the $\{111\}$ planes between cubic GST and Si across the interface (see magnified image of the edge of the grain in Fig. 7.3(b)). The Fourier transformed (FFT) image (shown as inset in Fig. 7.3(a)) can be used to differentiate between trigonal and cubic phase. In this case, the cubic phase is identified by ratios of the principal spot spacings and angles between the principal plane normals. Based on the plane matching combined with the results of the Fourier analysis, the following orientation relationship is deduced: (111)GST $\parallel$ (111)Si and [1$\bar{1}$0]GST $\parallel$ [1$\bar{1}$0]Si.

The lattice parameter, $a_{\text{cub-GST}}$, of the GST grain is determined from measured d-values of the FFT image by applying eq. (7.1) which takes into account the cubic symmetry [181]:

$$a_{\text{cub-GST}} = \sqrt{h^2 + k^2 + l^2}\, d_{hkl} \tag{7.1}$$

Therefore, the FFT image is first calibrated using the known distance of the reflection corresponding to the Si $(11\bar{1})$ plane ($d_{\text{Si},11\bar{1}} = 0.3136\,\text{nm}$ at $T = 23°\text{C}$ [217]). In order to estimate the accuracy of the measurement, the measured d-values for the 111, 002 and 220 reflections of the Si substrate are compared to the tabulated values ($d_{\text{Si},111} = 0.3136\,\text{nm}$, $d_{\text{Si},002} = 0.2716\,\text{nm}$, $d_{\text{Si},220} = 0.1920\,\text{nm}$) for several micrographs leading to an accuracy of $\Delta d/d = 1.5\%$. The average lattice parameter of GST is then calculated from the measured d-values for the 111, 11$\bar{1}$, 002 and 220 GST planes and yields $\langle a_{\text{cub-GST}} \rangle = (0.61 \pm 0.01)\,\text{nm}$. This is in good agreement with the reported lattice parameter of 0.60440 nm for bulk cubic

structured GST124 [110, 118].

Such a well-oriented grain is required for the in-situ heating study in order to be able to observe the time-dependent variations in shape and surface morphology with respect to crystallographic planes and directions with highest spatial resolution. Accordingly, the HRTEM image in Fig. 7.3(c) shows the very same GST grain after heating up to 640°C. The micrograph is stitched together from several images of a video sequence which is recorded a few seconds after reaching the target temperature. Compared to the initial status, which is described by a shapeless grain morphology, the short-time heated grain has already visibly modified its shape without changing the overall crystallographic orientation (cf. HRTEM in Fig. 7.3(d)). The initial surface roughness is remarkably flattened, in particular in the thin areas of the grain on the top and at the right side, accompanied with the formation of straight-lined $\{111\}$ oriented steps as indicated by black arrows in Fig. 7.3(c).

Again, the lattice parameter of GST is determined using the FFT image. Within the accuracy of the measurement there is no difference measured in the GST lattice parameter compared to room temperature. During calibration, the known thermal expansion of silicon (a_{Si}(T=640°C)=0.5443 nm [217]) is taken into account. Even though the difference in lattice parameter for Si at room temperature and 640°C is smaller than the accuracy of our measurement.

Stability of composition

The change in volume and shape is a result of surface and volume diffusion and atom evaporation processes at this high temperature. Since those processes can potentially alter the composition of the grain, it is important to analyze the chemical composition after sublimation. For example, the partial pressures of the three individual components of the GST alloy, Te ($\sim 10^3$ Pa), Sb ($\sim 10^1$ Pa) and Ge ($\sim 10^{-10}$ Pa) [95], differ by orders of magnitude which could lead to a Ge excess compared to the composition before annealing. Note that the observed constant lattice parameter alone does not suffice to differentiate whether the composition has changed. The lattice parameter cannot be used to distinguish between different chemical compositions of stable GST alloys due to our limited measurement accuracy and also the uncertainty in reported lattice parameters for different GST alloys.

EELS analysis performed on similarly treated samples has proven that there is no change in the ratio of the three GST components after partial sublimation. Figure 7.4 summarizes the results of the EELS analysis. The TEM micrograph in Fig. 7.4(a) shows a sample at room temperature after heating and partial sublimation. It was therefore treated similar to the grain described in Fig. 7.3. If a change in composition during partial sublimation does occur, it should be most notable in areas neighboring voids. Therefore, for the EELS analysis, a grain which is neighbored by a void is selected. The area where the EEL spectra are taken is marked in red in Fig. 7.4(a). Figure 7.4(b) shows one EEL spectrum taken at room temperature with the corresponding modeled background signal. It shows the edges related to oxygen (O-K), antimony (Sb-M) and tellurium (Te-M) in the first part of the spectrum in the energy-loss range of 500-800 eV. At higher energy-losses (1100-1500 eV) the edges related to gallium (Ga-L) and germanium (Ge-L) are visible. In case of FIB prepared TEM lamellae, a contamination with Ga^+ ions is observed as discussed in section 4.3.2. The (Ga-L) core-loss edge ($\sim$ 1115 eV [45]) with its delayed maximum overlaps with the Ge-L edge

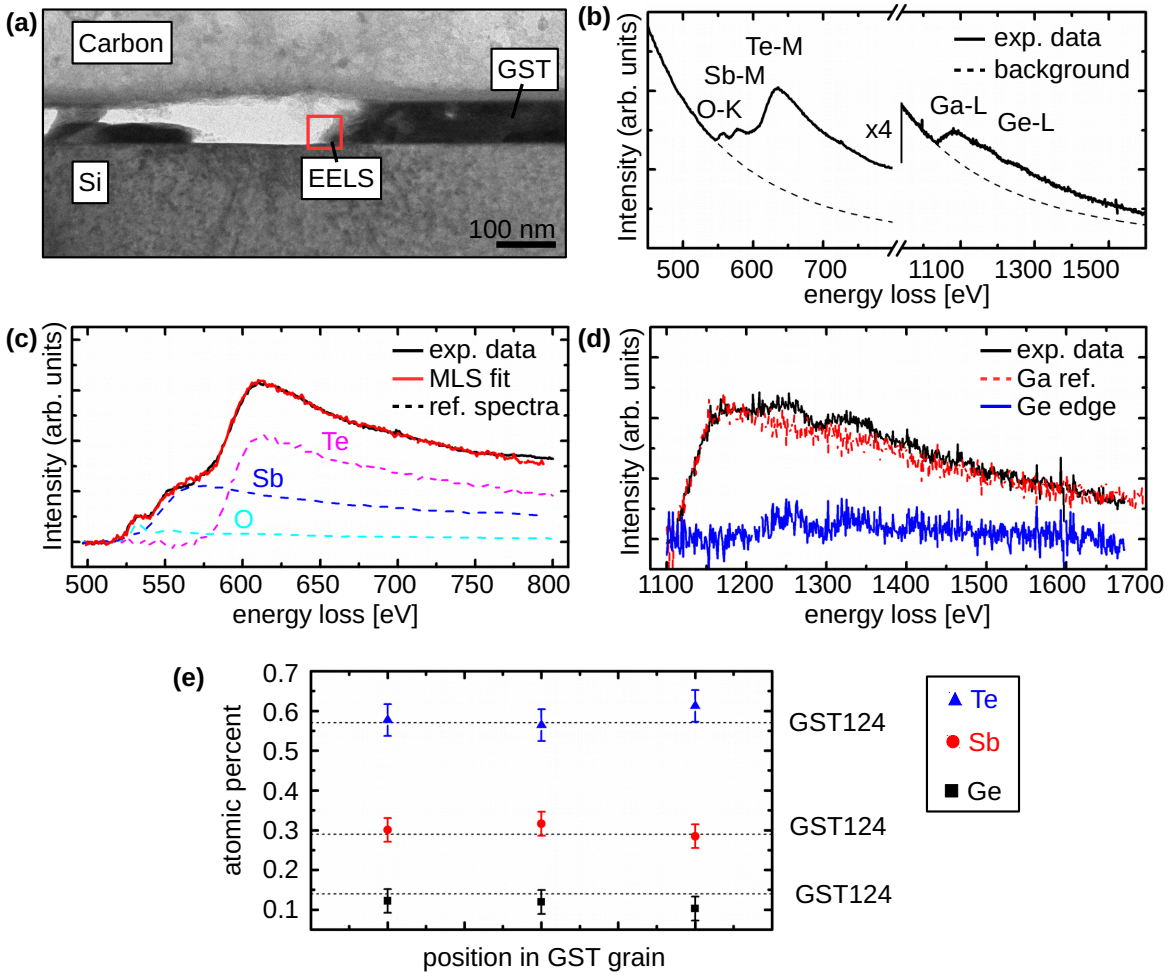

Figure 7.4 EELS analysis after partial sublimation: (a) HRTEM image of GST film after partial sublimation. The region of interest where the EEL spectra are taken from is marked in red. (b) Typical EEL spectrum of GST film after partial sublimation with modeled background signal. (c) Exemplary MLS fit of background subtracted EEL spectrum and corresponding reference spectra of O, Sb and Te. (d) Exemplary background subtracted EEL spectrum in high energy-loss range containing the data of the GST film (black), a Ga reference spectrum (red) and the Ge signal obtained after Ga reference subtraction and (e) Graph of chemical composition of the GST film after partial sublimation at three different positions.

($\sim$ 1217 eV[45]). In order to quantify the GST alloy, the assumption is made that Ga does not interact with GST. Then, a Ga-reference spectrum can simply be subtracted in order to quantify the ratios of the three GST components. The Ga reference spectrum is taken from a Ga droplet in the carbon protective layer. The method for quantification of overlapping edges using MLS fitting is described in section 3.3. The result of the fitting is shown in Fig. 7.4(c) and (d) for both energy ranges of the spectrum, 500-800 eV and 1100-1500 eV. As shown, the MLS fit (red) is in good agreement with the experimental data (black) in both cases. Figure 7.4(e) compares the result of the quantification for three different positions (within the area marked in red in Fig. 7.4(a)) with the initial composition of GST124 (black dotted line). It shows that the composition is stable upon partial sublimation and the average mounts to Ge(12$\pm$2)%:Sb(30$\pm$3)%:Te(58$\pm$4)%. Because the ratios of the three components do not

change, the assumption that Ga only accumulates and does not interact with GST seems reasonable.

Discussion

As stated in previous reports [129, 132] and described in section 5.4, annealing of cubic structured GST should first lead to the formation of vacancy ordering on $\{111\}$ planes, followed by the transition into the trigonal phase above 300°C [89, 149]. Interestingly here, the aligned GST grain retains the cubic structure without the transition into the trigonal phase even up to the sublimation point. In addition, the formation of a highly-vacancy-ordered phase is not observed because no additional periodicity along $\{111\}$ planes is found.

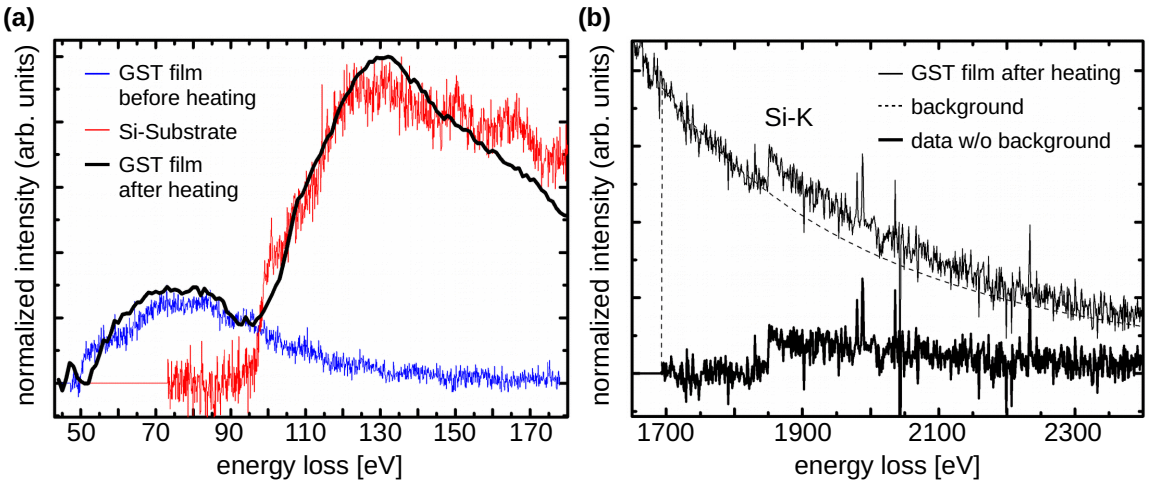

Figure 7.5 (a) EEL spectrum in the low energy range (50-170 eV) after background subtraction taken from the silicon substrate (red), and from the GST film before (blue) and after (black) heating, (b) EEL spectrum in high energy range (1700-2300 eV) taken from the GST film after heating featuring the data with and without background subtraction.

Qiao *et al.* found that adding Si to a GST film can suppress the transition from cubic to trigonal phase [117]. Therefore, a diffusion of silicon in the GST film could be responsible for stabilizing the cubic grain even up to the sublimation point. Indeed, Fig. 7.3(a) and (c) show that the GST-Si interface roughens at higher temperatures indicating that Si diffusion takes place. EELS analysis confirms that Si is found in the GST film after heating above the sublimation temperature. Si content can be verified both in the low energy-loss range where it gives rise to Si-L edges exhibiting a delayed maximum with a threshold at 100 eV and in the high energy-loss range featuring a Si-K edge with an abrupt onset at 1839 eV [240]. Both energy ranges can therefore be used to confirm Si diffusion into the GST film after heating. The result of the EELS analysis is summarized in Fig. 7.5. Figure 7.5(a) displays the low energy range between 50 and 170 eV. Three different spectra with normalized intensities for easy comparison are shown. The first spectrum is taken from the Si substrate (red) featuring the Si-L edges and used as reference for detecting Si content. The second spectrum is taken from the GST film before heating (blue) featuring Sb-N (threshold 31 eV [240]) and Te-N (threshold 40 eV [240]) edges. Since there is no Si-L edge visible, the GST film did not

contain Si before the heat treatment. The last spectrum is taken from the GST film after heating (black). This spectrum is a superposition of the first two spectra featuring all three edges from Sb, Te and Si. Additionally, Fig. 7.5(b) shows the spectrum of the GST film after heating in the high energy-loss range between 1700 and 2300 eV where the Si-K edge is visible. The advantage of the higher energy range is that the Si edge is isolated with no overlapping Ge, Sb or Te edges, but on the other hand the signal-to-ratio is inferior. Taking both energy ranges together, the EELS analysis confirms that Si is found within the GST film.

Although the suppression of the cubic-to-trigonal phase transition was measured for others dopants including nitrogen [241] and titanium [163, 164], a comprehensive understanding of the stabilization mechanism is still unclear. As discussed in section 5.4.2 vacancies in the GST structure play a vital role in forming the stable trigonal phase. There are two possibilities to suppress the cubic-to-trigonal transition, either by reducing the mobility of vacancies or by reducing the number of vacancies. Qiao *et al.* mention the possible role of stronger covalent bonds which Si can form [117]. Stronger bonds reduce the atomic mobility and could therefore hinder the movement of vacancies which is needed to form the trigonal phase. The other possibility for the stabilization of the cubic phase is the reduction of the number of vacancies in GST by filling them with diffused Si atoms. Intrinsic vacancies are only found in the Ge/Sb/vac sublattice and not in the Te sublattice. Therefore, the formation of (*dopant*)-Ge/Sb bonds and with that the insertion of the dopants in the Te sublattice should not reduce the numbers of intrinsic vacancies. The formation of (*dopant*)-Te bonds however could lead to the insertion of dopants in the Ge/Sb/vac sublattice and thereby fill the intrinsic vacancies in this sublattice hindering the transition to the trigonal phase. Indeed, for dopants which suppress the cubic-to-trigonal transition and thereby stabilize the cubic phase, (*dopant*)-Te bonds are preferentially formed. In Ti-doped GST where the transition to the trigonal phase is suppressed the preferential formation of Ti-Te bonds is found [163, 164]. In N-doped GST the doping increases the phase transition temperature and the authors speculate that nitrogen exists in the vacancies [241]. Caravati *et al.* [242] calculated that the incorporation of atomic nitrogen in Te-position is energetically favorable compared to other positions. But the incorporation still requires a large amount of energy of 1.7 eV, whereas molecular nitrogen can easily be inserted into Ge/Sb-vacancies [242]. In contrast to those examples, in Se-doped GST the preferred formation of Ge-Se bonds is reported [243]. And there, no cubic phase is formed at all and the film directly crystallizes in the trigonal phase [243].

There is no data about the preferential bonds of Si dopants in GST, but Saito *et al.* [156] found that the formation of Si-Te bonds is preferred during Si-doping of the related phase change material GeTe. Therefore, it is reasonable to assume that Si-Te bonds are also preferred in Si-doped GST. Thus Si dopants fill the vacancies in GST and thereby stabilize the cubic phase. Regardless of those indications, the stabilization mechanism remains under investigation.

7.2.3 Dynamic anisotropic sublimation

An overview of the subsequent stages of the sublimation process is shown in Fig. 7.6. The HRTEM image series is taken from a video recording at 640°C which starts approximately

14.5 minutes after the target temperature has been reached. The series shows the sublimation of the investigated cubic grain (cf. Fig. 7.3) over a time period of 234.6 sec at a fixed time interval between two images. It is evident that the grain shrinks in a self-similar manner retaining the rhomboidal shape in projection. Thereby, the sublimation occurs via the kink-step-terrace formation mechanism.

In this section, the octahedron-like morphology which develops during sublimation is characterized initially and subsequently the sublimation dynamics involving kink nucleation and step propagation are presented and discussed.

Octahedron-like sample morphology

The in-situ observation demonstrates that sublimation of the cubic GST grain is distinctly anisotropic. In order to describe the dynamics with the help of the involved crystallographic directions, the sample morphology needs to be addressed first. Figure 7.7 depicts a HRTEM image and a schematic model illustrating the octahedron-like sample morphology.

Figure 7.7(a) shows the tested grain after 17 min of overall sublimation time in a HRTEM image recorded along the $[1\bar{1}0]$ zone axis. The grain is significantly reduced in size compared to the situation displayed in Fig. 7.3(c) (onset of sublimation) leading to a thin crystal. There are several indications visible in Fig. 7.7(a) that the cubic grain consists of $\{111\}$ facets: (i) the projected rhomboidal shape, (ii) the edge projections along $\langle 112 \rangle$ directions and (iii) the contrast modulations along the grain.

The observations can be explained with an octahedral crystal shape that is formed by $\{111\}$ facets. Figure 7.7(b) displays a 3D atomic model of cubic GST consisting of only $\{111\}$ facets. A $\{111\}$ octahedron is the simplest shape to fulfill the cubic symmetry and the observed rhomboidal shape in the projection along $[1\bar{1}0]$ direction (cf. atomic model projected along $[1\bar{1}0]$ in Fig. 7.7(b)). The $\{111\}$ facets are plausible low-index candidates to form stable surfaces since they have the lowest surface energy as determined in section 6.5.2. In Figure A.3 the atomic model for three configurations of plausible low-index facets is displayed and only a crystal consisting of only $\{111\}$ facets produces a rhomboidal shape in the projection along $[1\bar{1}0]$ direction. Additionally, the octahedron features crystal edges along $\langle 110 \rangle$ directions which lead to observable edges along $\langle 112 \rangle$ directions in a $[1\bar{1}0]$ projection (cf. crystal structure projected along $[1\bar{1}0]$ in Fig. 7.7(b)). Furthermore, the observed contrast modulations indicate changes in local thickness (cf. thickness-defocus map in Fig. 3.6). A change in local thickness is consistent with sloping $\{111\}$ facets.

On the other hand, abrupt transitions along crystallographic directions are visible in the HRTEM micrograph (Fig. 7.7(a)). Because of the slightly off-zone axis imaging condition, the surface structure contributes more strongly to the HRTEM contrast, and thus surface steps became clearly visible [244] indicating that the real shape of the crystal in Fig. 7.7(a) is more complex than a perfect equilateral $\{111\}$ octahedron and might be composed of steps along $\langle 110 \rangle$.

Mostly $\{111\}$ facets form steadily during the sublimation process indicating that they are the most stable facets during the sublimation. This is surprising because during the crystal growth from melt all three low-index facets $\{100\}$, $\{110\}$ and $\{111\}$ are developed (cf. section 6.5.2). The discrepancy can be ascribed to the influence of the particular GST structure and the different partial pressure for the different atomic species: The $\{111\}$ surfaces consist

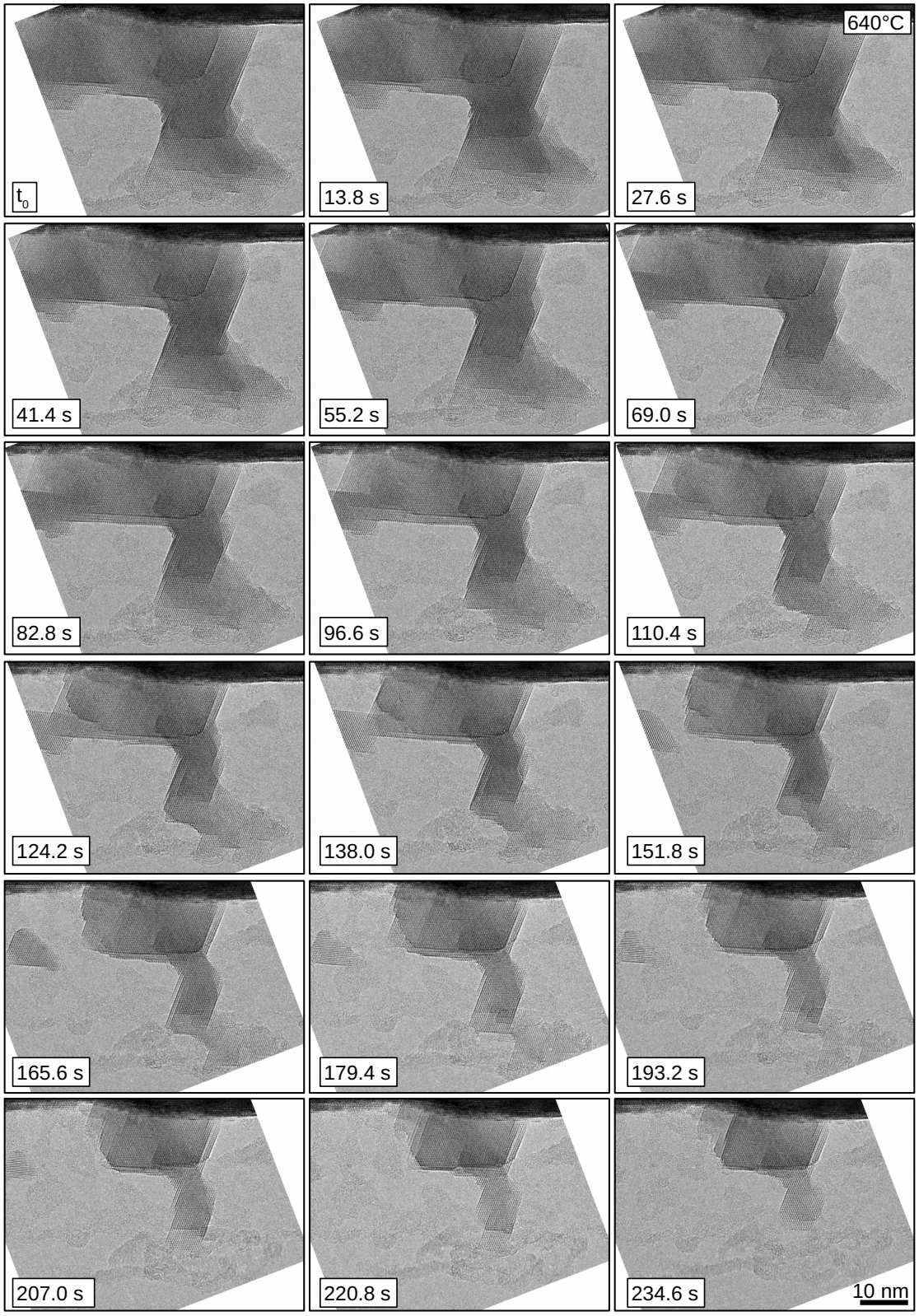

Figure 7.6 HRTEM image series showing an overview of the sublimation process.

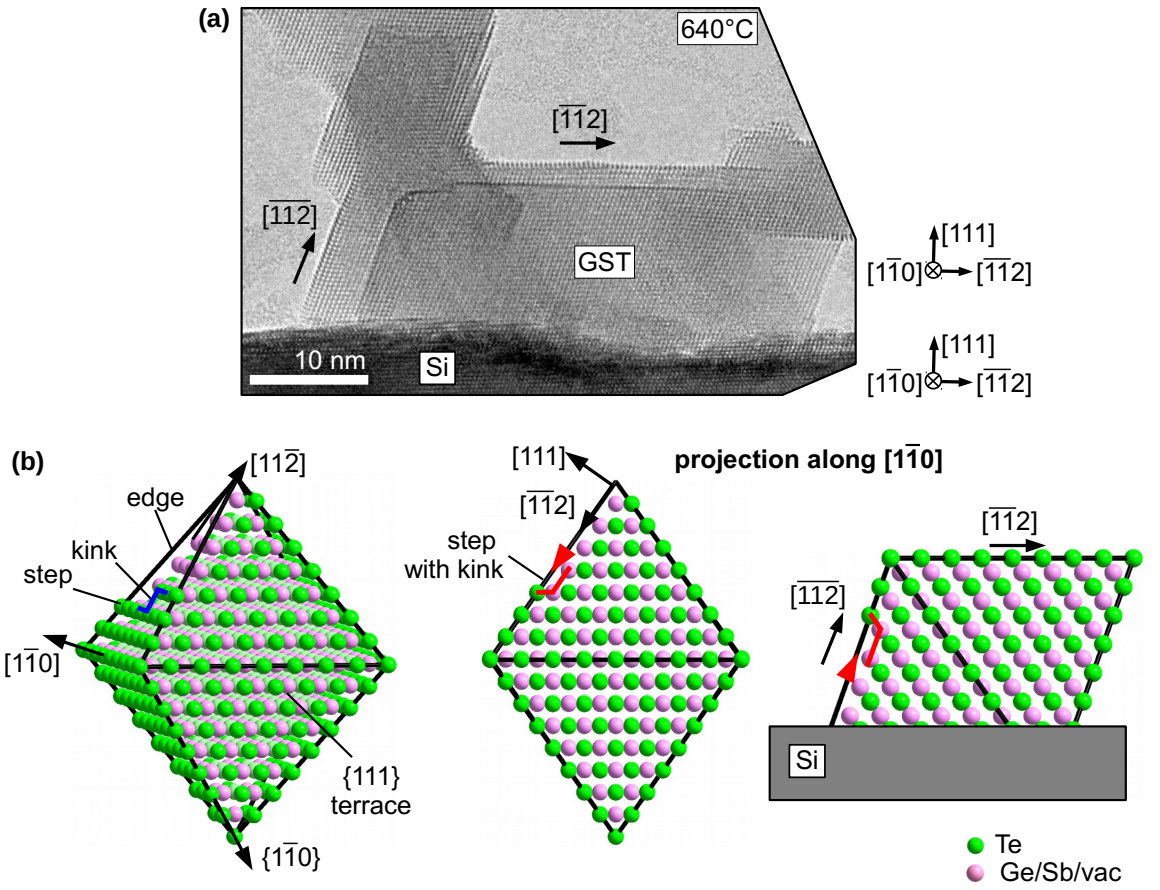

Figure 7.7 Illustration of sample geometry (a) HRTEM image of cubic GST grain at 640°C recorded 17 min after the start of sublimation and displayed close to the Si-[1$\bar{1}$0] zone axis. (b) Schematic 3D model of cubic GST with {111} facets forming an octahedron and projections of the GST structure along [1$\bar{1}$0] with and without a Si substrate. The Te atoms (green) make up the {111} surfaces and the Ge and Sb atoms as well as vacancies (magenta) form the second layer.

of atoms from only one sublattice, either Te or Ge/Sb. Due to the low vapor pressure of Ge, one can imagine that there is a preference for the Ge/Sb sublattice to form stable surfaces during sublimation. For the formation of {111} surfaces during the growth of trigonal GST grain, Kooi *et al.* [25] also discussed the lowering of the surface energy by a preference of Sb atoms to be at the surface. A different approach is to consider vacancies aiding the sublimation process by lowering the energies of bonds that need to be broken. Then, the plane where most vacancies are exposed to the surface is the stable facet. This would lead to the formation of {111} facets because vacancies are allocated on the Ge/Sb sublattice and are possibly already ordered to a certain degree which cannot be observed yet in HRTEM phase contrast.

For the description of the sublimation dynamics in this section, terms like "kink", "step" and "terrace" are used. The terms describe different positions in the GST grain and the atomic model in Fig. 7.7(b) is used to illustrate them. Kinks are atomic sites that are also known as half-crystal sites and were already schematically illustrated in Fig. 7.1(c). Kink sites in the sample morphology of the investigated grain are marked in blue in Fig. 7.7(b).

Note that kink sites are not directly visible in the $[1\bar{1}0]$ projection. It is assumed that after being nucleated, kinks propagate along $\langle 110 \rangle$ directions creating a step on $\{111\}$ facets. One example of such a step is marked in red in Fig. 7.7(b). The movement of the step along $\langle 112 \rangle$ direction is then visible in the projection and is a direct result of the nucleation and propagation of kink sites. After the step moved across the whole $\{111\}$ surface it leaves behind a flat $\{111\}$ facet, also known as a terrace.

TEM sample geometry

In in-situ TEM experiments, the thin specimen geometry can influence the observed mechanism. For a quantitative estimation of the grain thickness on the thinner side ($(\bar{1}\bar{1}1)$ facet), the kink velocity along the projection direction parallel to the electron beam is assumed to be equal to the observed step velocity in the [112] direction ($\sim$11 nm/s). Taking into account that the step movement is mostly faster than our temporal resolution (1.15 sec), the thickness has an upper limit of 13 nm. The significant reduction from the initial lamella thickness which is about 200 nm to the final state makes an influence on the observed sample morphology by the geometric confinement of TEM sample preparation improbable.

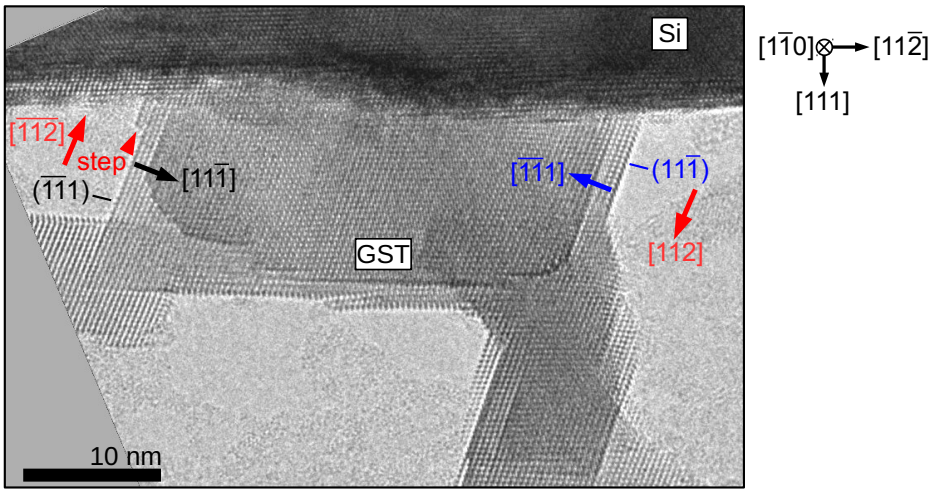

Figure 7.8 HRTEM image of the cubic GST grain during the sublimation process at 640°C labeled with relevant crystallographic directions: red for the direction of step movement, and blue and black for the sublimation on two opposing facets, $(\bar{1}\bar{1}1)$ and $(11\bar{1})$, which are used to describe the mechanism in more detail. A visible step on the $(\bar{1}\bar{1}1)$ facet is marked with a short red arrow.

Figure 7.8 displays one HRTEM image which is taken out of the sublimation sequence shown in Fig. 7.6 to label the relevant crystallographic directions. The sublimation takes place via the predominant formation of kinks at $\{111\}$ facets, which subsequently move along the $\langle 110 \rangle$ direction and thus lead to an observable step motion along the $\langle 112 \rangle$ direction. One of those steps is exemplary marked with a red arrow in Fig. 7.8. The kink formation is initiated at edge corners or at triple points to the substrate, which are energetically preferential starting points. The anisotropic and fast kink movement results in a reduction of the surface roughness through the development of straight-lined steps and finally terraces provided that the process is nucleation-limited.

In the following, the sublimation process is discussed using the examples of the dynamics on the $(\bar{1}\bar{1}1)$ facet along the $[11\bar{1}]$ direction (black arrow in Fig. 7.8) and on the opposite $(11\bar{1})$ facet along the $[\bar{1}\bar{1}1]$ direction (blue arrow in Fig. 7.8).

Kink nucleation and step movement on $(\bar{1}\bar{1}1)$ facet

The $\{111\}$ stable terraces are left behind by the predominate formation of kinks at crystal edges forming steps that subsequently move along the $\langle 112\rangle$ direction. This happens all over the grain on all terraces, but can be examined best at the thinnest part at the edge of the sample where the $(\bar{1}\bar{1}1)$ terrace finally disappears.

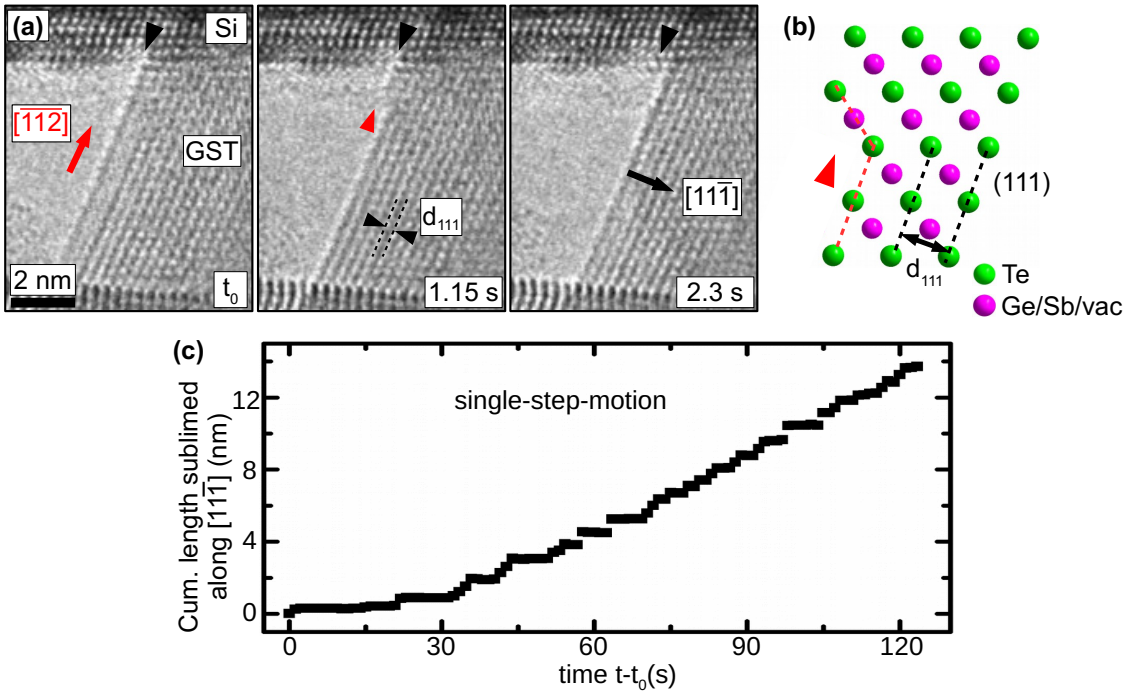

Figure 7.9 Sublimation at the $(\bar{1}\bar{1}1)$ facet via kink nucleation and single-step movements along $[\bar{1}\bar{1}\bar{2}]$ direction: (a) Series of HRTEM images taken from a video of the cubic GST grain at 640°C showing the nucleation and movement along $[\bar{1}\bar{1}\bar{2}]$ (red arrow) of one step in three consecutive images. (b) Atomic arrangement on a (110) plane where one set of atomic sites on (111) planes is occupied by Te, while the other is occupied by Ge, Sb and vacancies. A schematic single-step is shown with a red dotted line and marked with a red short arrow. (c) The cumulative sublimed length is measured as a function of time along $[11\bar{1}]$ direction (black arrow in (a)) featuring mostly single-steps.

Figure 7.9 extensively illustrates the dynamics of step motion during sublimation at the atomic scale. The figure in (a) presents three consecutive HRTEM snapshots of the border of the crystal. The images clearly resolve the $\{111\}$ planes of cubic GST which terminate the edges of the grain forming an atomically sharp and straight facet.

Figure 7.9(b) displays a model of the atomic arrangement of cubic GST in projection along our viewing direction. The measured lateral step height of 0.35 nm corresponds to the distance of the $\{111\}$ lattice planes, $d_{111} = 0.3489\,\mathrm{nm}$. One set of visible $\{111\}$ planes is composed of a pair of planes belonging to both sublattices, the Te atoms on the one hand and

randomly distributed Ge and Sb atoms on the other hand [110]. For this reason, a step with a lateral expansion (step height) of one $\{111\}$ plane ("single-step") involves the sublimation of all three atomic species within our spatial and temporal resolution.

The kink nucleates at the edge corner where two facets form a "convex" crystal edge and propagates along the $[1\bar{1}0]$ direction until the entire row is removed. The kink thereby forms a single-step or occasionally a double-step edge along the viewing direction which is easily recognizable in the HRTEM images (cf. red arrow in the central image of Fig. 7.9(a)). Most commonly, steps move across the entire length of the grain edge (about 13 nm) within one consecutive frame, i.e. within 1.15 sec. The kink/step velocity can be therefore estimated to be equal or faster than 11 nm/s.

To follow up on the time dependent process more comprehensively, the cumulative sublimed length along the $[11\bar{1}]$ direction is plotted as a function of time in Fig. 7.9(c). Thereby, the time measurement starts when the $(\bar{1}\bar{1}1)$ facet entered the field of view around 17 min after reaching 640°C. The curve progression resembles an irregular step-function representing the continuous shrinkage of the grain over a period of two minutes. Each step in the graph corresponds to the fast kink/step motion, the step height corresponds to the lateral expansion of the crystal step and the plateau area between two steps measures the time between two nucleation events. In total 33 events can be identified. In Figure 7.10 the number of events as a function of time between two events is displayed showing that the time between two nucleation events ranges mostly between 1.15 sec (two consecutive images) and 3.45 sec.

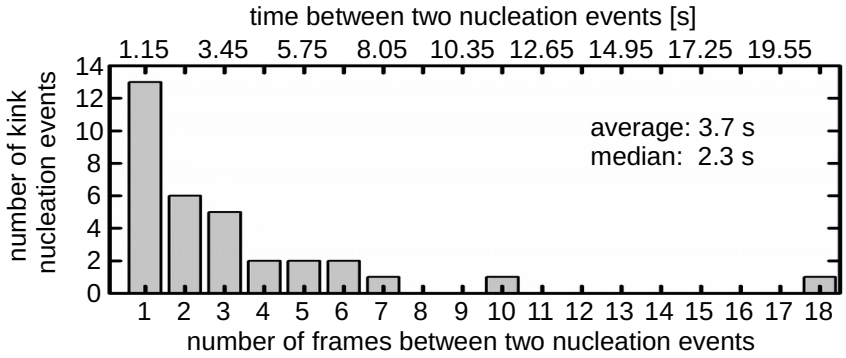

Figure 7.10 Frequency of kink nucleation events displayed as number of events versus time between two nucleation events for the stable step at $[11\bar{1}]$.

Regardless of the low time resolution of the measurement, it must be concluded that the sublimation process is kink nucleation-limited as furthermore evidenced by the fact that straight facets develop and, accordingly, no step roughening is observed at this high temperature.

Kink nucleation and step movement on $(11\bar{1})$ facet

The result of a kink nucleation-limited sublimation is further supported by the observation of the sublimation along the $[\bar{1}\bar{1}1]$ direction observed at the opposite side of the grain, namely the $(11\bar{1})$ facet which is labeled in blue in the overview HRTEM image of Fig. 7.8. Figure 7.11(a) presents the corresponding cumulative sublimed distance-versus-time plot. Note

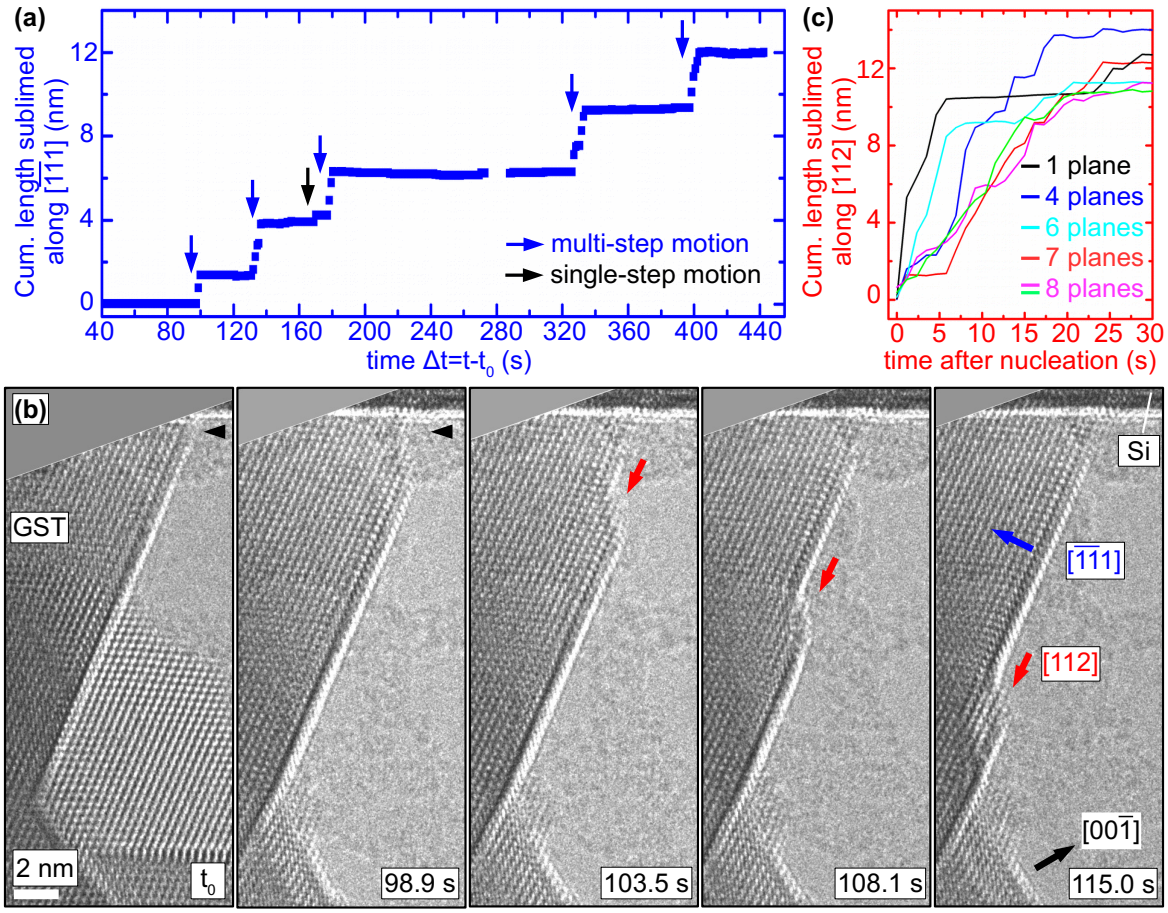

Figure 7.11 Sublimation at the $(11\bar{1})$ facet via nucleation and multi-step motion along [112]: (a) The cumulative sublimed length is measured as a function of time along the $[\bar{1}\bar{1}1]$ direction (blue arrow in (b)) featuring six steps. (b) Series of HRTEM images of the cubic GST grain at 640°C taken from a video sequence showing the nucleation of the first kink after 98.9 sec (black short arrow) followed by mass desorption from the kink site seen as step movement along [112] (red arrow). (c) Graph of step movement along $[112]$ (red arrow in (b)) showing the cumulative sublimed length of each step starting after they nucleated at the Si-GST interface. Each step is labeled with its corresponding step height measured in number of involved d_{111} planes.

that the measurement is interrupted around 280 sec when the observed facet leaves the field of view. In spite of the large time frame of 7.5 min in total, only six nucleation events are observed (indicated by arrows). The time between two nucleation events ranges from 8 sec to 150 sec according to the plateau widths. The height of the jumps in the step-function reflects the lateral step expansion (step height), which is - in this case - mostly larger than the distance between two $\{111\}$-planes indicating a multi-kink nucleation behavior.

Indeed, the HRTEM image series in Fig. 7.11(b) reveals the presence and structure of a multi-step construction. The exemplary step ensemble covers four $\{111\}$ planes with a staggered arrangement along the viewing direction and also perpendicular to the $\{111\}$ plane. Figure 7.11(b) covers a time period of 115 sec. After a stationary period of 98.9 sec at the stable $(11\bar{1})$ facet, a kink nucleates at the Si-GST interface as marked by the black arrow. The nucleation happens within two consecutive image frames (1.15 sec) and involves

multiple kinks as evidenced by the occurrence of a multi-step. The subsequent propagation of the multi-step ensemble proceeds along the $[112]$ direction until it crosses the transversely running $\{001\}$ facet. All six recorded nucleation events occur at the Si-GST interface and the HRTEM image series for all six events, including the subsequent step motion, can be found in the appendix in Fig. A.1 and A.2.

The velocity of the multi-step ensemble depends on the number of step units involved, as shown in Fig. 7.11(c), where the sublimed length along the step propagation direction is plotted over time starting after each nucleation occurred. The step movement can be approximated as a linear motion until it reaches the transversely running $\{001\}$ facet. Therefore, the step velocity is estimated using linear fits for the data points up until the first time the step stopped. Table 7.1 summarizes the results for all six steps sorted by increasing step height. The estimated velocities of the multi-steps in the linear sectors range from 0.5 to 1.8 nm/s where smaller velocities are observed for wider multi-step arrangements, i.e. $v_{\text{4-steps}} > v_{\text{7-steps}} > v_{\text{8-steps}}$. This demonstrates the influence of the number of kinks involved in the correlative ensemble motion. Compared to the velocity of the single-step configuration, these values are about one order of magnitude smaller. (Note that the step with a height of 6 $\{111\}$ layers is one exception to the rule.)

height [d_{111}]	step-ID	pause between events [s]	velocity [nm/s]
1	3	46.0	4.6 ± 0.4
4	1	$\geq$98.9	0.78 ± 0.05
6	4	8.05	1.44 ± 0.08
7	2	29.9	0.57 ± 0.03
8	5	149.5	0.48 ± 0.01
8	6	71.3	0.59 ± 0.02

Table 7.1 Summary for step motion along [112] direction including step height, the time between nucleation events and the step velocity along $[112]$.

Discussion of kink nucleation site and step propagation

According to the TSK model [14], the sublimation of solid surfaces starts from sites with the lowest activation energy required to remove an atom from the surface. These preferential sites are discussed in terms of nearest neighbor bonds which must be broken [14]. Figure 7.12 shows a schematic drawing of the cubic grain to illustrate the four different possible kink nucleation start points, two for each opposing crystal edge. There are homogenous sites where only the GST crystal is involved in the sublimation process and heterogeneous sites where the GST and Si crystal form an interface. Additionally, the potential sites can be differentiated in "convex" and "concave" depending on the crystal facets that meet at the specific site. For two of the possible kink sites an atomic model is added to illustrate the number of broken bonds involved. Invoking the TSK model, the most preferable kink nucleation site is located at the homogenous, "convex" site of the grain (bonds to be broken: 1) compared to the other possible sites marked in Fig. 7.12. There is no "convex" site at

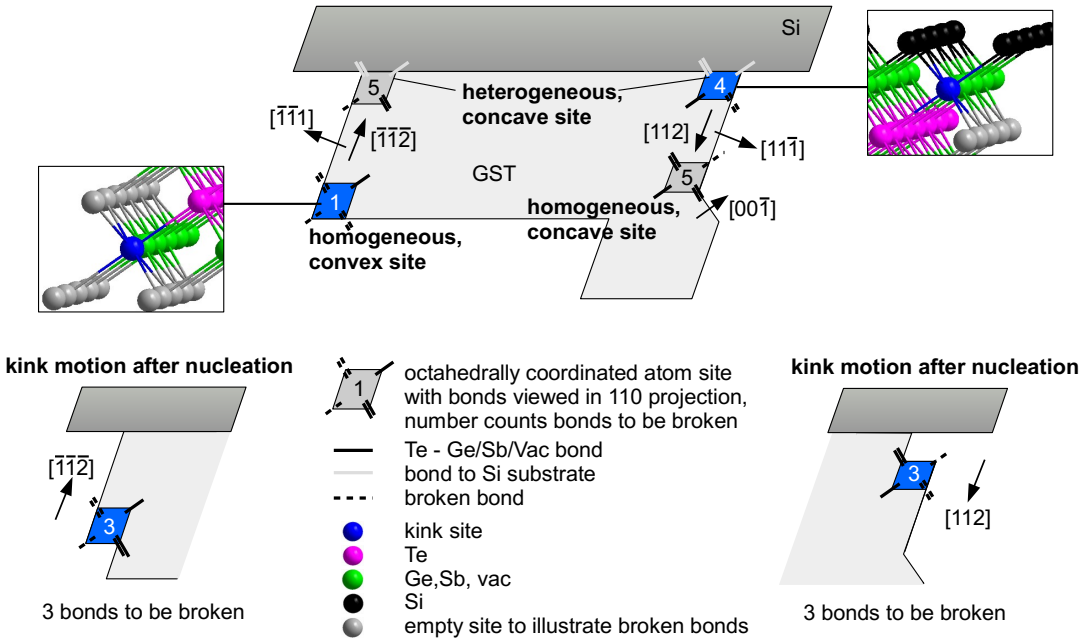

Figure 7.12 Schematic drawing and atomic model to illustrate the different possible kink nucleation sites featuring two heterogeneous, concave sites at the GST-Si interface and two homogeneous sites where one is convex and the other one concave. The kink sites with the most broken bonds at each facet are marked in blue. Additionally, on the lower left and right hand side of the figure, the number of broken bonds after the kink nucleation and during the subsequent step motion along $[112]$ and $[\bar{1}\bar{1}\bar{2}]$ direction, respectively, is illustrated.

the $(11\bar{1})$ facet due to a stable facet with a projected edge in $[00\bar{1}]$ direction crossing it. The second most favorable kink nucleation site considering the number of bonds is the heterogeneous, "concave" site on the $[11\bar{1}]$ facet (bonds to be broken: 4). The discussed preferred nucleation site at each facet are marked in blue in Fig. 7.12 and are those that are observed during sublimation. The rate with which the kinks are formed (and consequently steps are observed) is 30 times faster for the $(\bar{1}11)$ facet compared to the opposing facet. As expected from the TSK model, the kink nucleation rate is much faster for the most preferable kink nucleation site.

Besides the preferential starting points for kink formation, the subsequent kink propagation along $[1\bar{1}0]$ direction should be identical on both crystal sites because of the same number of bonds which must be broken. Indeed, step velocities along $[112]$ and $[\bar{1}\bar{1}\bar{2}]$ direction of about 11 nm/s and 5 nm/s, respectively, are estimated for the single step-motion. The apparent discrepancy is attributed to the fact that the step width along e-beam direction (local thickness) is different at both sides of the grain. The grain is thinner at the $(\bar{1}\bar{1}1)$ facet: The amorphous background features there are in focus at the same time as the GST crystal and the contrast is lighter (the average intensity is 10% less) compared to the opposing facet. Therefore less material would have to sublime for the same amount of step movement along $\{112\}$.

Furthermore, the dynamic behavior of the GST sublimation is nucleation-limited. Once a kink has nucleated, GST units sublime fast from this kink site forming a step and then a

flat terrace. The kink itself is only one (111)-layer wide since the nucleation of a second kink is slower than the kink movement. On the other hand, the much slower nucleation process at the Si-GST interface on the $(11\bar{1})$ facet give rise to the nucleation of multi-steps whose formation mechanism is still unclear. A possible approach is to study the influence of interfacial defects which form due to a high lattice mismatch between Si and GST on the sublimation mechanism. One multi-step is mostly made up of six to eight (111)-layers (step height). The lattice mismatch of GST and Si amounts to 11.3%. That means that an additional Si (111) plane is required every nine GST (111) planes which is in the same order of magnitude as the height of the multi-steps indicating that the strain state of the interface plays a role in the formation of multi-steps.

Faceting

At 640°C, the grain develops straight-lined facets (cf. TEM images in Fig. 7.8). Because the grain remains clearly faceted and no roughening of the facets up to the sublimation point is detected, the surface roughening transition temperature, T_R (cf. section 7.1.2), of GST $\{111\}$ planes must be above the sublimation temperature.

Another interesting point to note is that the initial grain surface at room temperature (cf. HRTEM image in Fig. 7.3) is non-faceted and roundly shaped as opposed to the clear facets at 640°C. This effect is reversible: The faceted grain at high temperature regains a round shape after cooling down to room temperature as shown in Fig. 7.13. A possible explanation for this change in surface morphology is the absorption of contaminants during cooling down which changes the surface energies from anisotropic at high temperatures (without contaminants) to more isotropic at room temperature. The minimization of isotropic surface energies lead to a round shape since a sphere has the lowest surface-to-volume ratio whereas anisotropic surface energies lead to clear crystal facets.

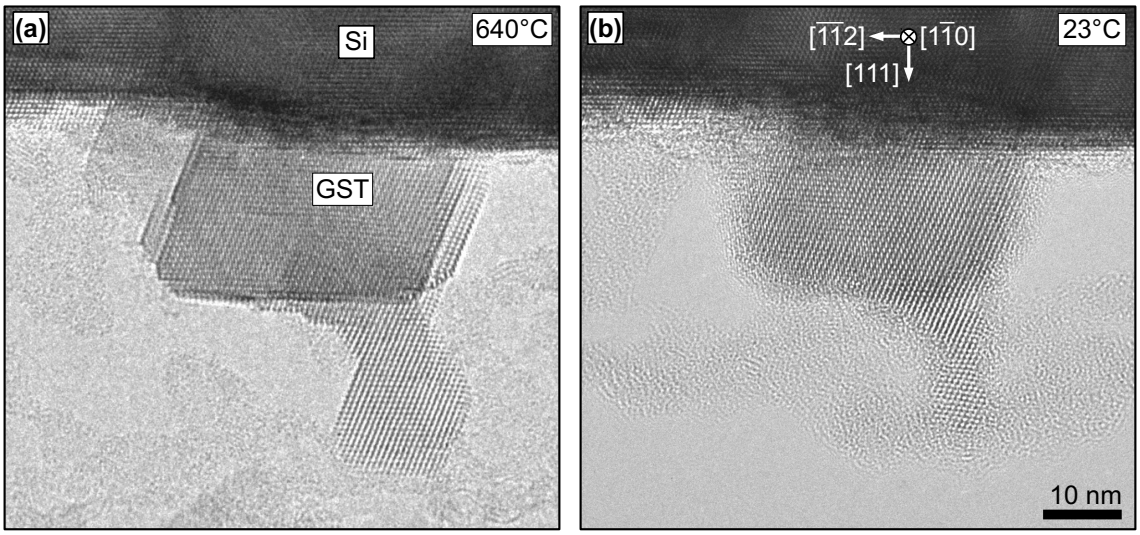

Figure 7.13 Reversible change in surface morphology of a cubic GST grain: TEM images showing the cubic grain at (a) 640°C with straight-lined facets and at (b) room temperature with resumed roundly shaped morphology.

7.3 Sublimation of trigonal phase

In this section, the sublimation of the trigonal phase of GST is discussed and compared to the results obtained for the cubic phase.

Initial state

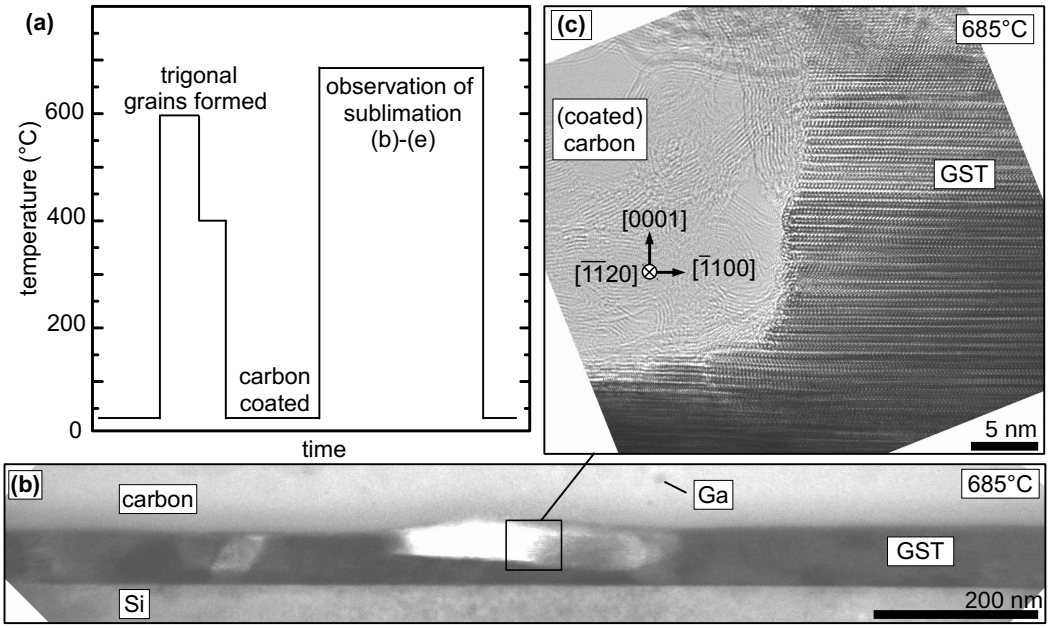

Figure 7.14 (a) Schematic experimental procedure for in-situ heating of GST thin film first from RT to 600°C and back to 400°C to generate GST grains with trigonal structure and then to 685°C for in-situ observation of sublimation of trigonal grains, (b) TEM micrograph of GST thin film with a void featuring the Si substrate and carbon protective layer with Ga droplets and (c) magnified HRTEM image of trigonal aligned grain displayed in (b).

Figure 7.14 summarizes the setting up of the initial state for the sublimation study of the trigonal crystalline GST. The temperature treatment of a GST thin film inside the TEM is displayed in a schematic temperature-versus-time plot in Fig. 7.14(a). The amorphous film is heated in a first step to 600°C followed by a quick cool down to 400°C where trigonal structured GST grains are generate. The grains are aligned with the GST basal planes being parallel to the Si(111) planes. The sample is then heated in a second step to 685°C for the in-situ observation of the sublimation of trigonal GST. Figure 7.14(b) shows a TEM overview image of the heat treated sample at 685°C. The cross-section shows the Si substrate, the GST thin film and the carbon protective layer including Ga droplets visible as faint contrast features. The GST thin film features a hole caused by partial sublimation during the generation of trigonal GST. The trigonal structure of the grain is visible in the magnified HRTEM image displayed in Fig. 7.14(c). The trigonal grain is aligned with respect to the Si substrate with the basal planes of GST being parallel to the (111) planes of Si as discussed in section 5.4.2. The trigonal structure is not well ordered and exhibits an irregular stacking sequence. Furthermore, a partially graphitized film is visible inside the hole in Fig. 7.14(c)

which stems from a prior treatment with a carbon coater. In this way produced trigonal grains serve as the initial state for the first sublimation experiments for trigonal GST.

Terrace-like morphology formed during sublimation

The experiment indicates that the GST grain develops a stepped morphology parallel to the viewing direction with terraces of different local thicknesses. Figure 7.15 displays a BF- and a HAADF-STEM image which is recorded at 400°C after the in-situ observation of the sublimation. Both images show the same position of the trigonal structured GST grain with two areas of different constant average intensity on the left and right hand side. The difference in average intensity stems from local thickness variation because the average atomic number of the trigonal GST grain stays the same.

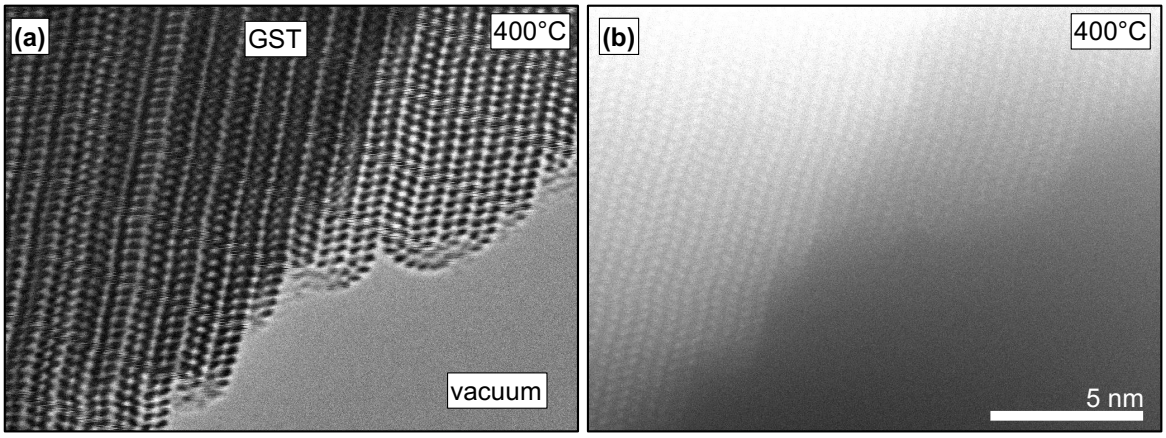

Figure 7.15 Stepped morphology with terraces of different thicknesses: (a) BF-STEM and (b) HAADF-STEM image of the same sample area featuring areas of different local thickness recorded at 400°C after in-situ observation of sublimation at 685°C.

Figure 7.16 shows a HRTEM image series displaying the sublimation process that is observed at 685°C. Because of the slightly off-zone axis imaging condition, the surface structure contributes more strongly to the HRTEM contrast, and thus surface steps became clearly visible [244]. Examples of which are marked by blue arrows in Fig. 7.16(a). The terraces-like features sublime independently of one another as is shown in an image sequence in Fig. 7.16(b). The process speeds are also in the nm/s regime as in the case of sublimation of the cubic grain.

Carbon contamination

Because of the carbon coating treatment prior to the in-situ observation of sublimation there is a lot of carbon on the sample. This carbon film is mobile under heat treatment and e-beam irradiation and forms graphite like structures with interlayer spacing of 0.34 nm as shown in Fig. 7.14(c).

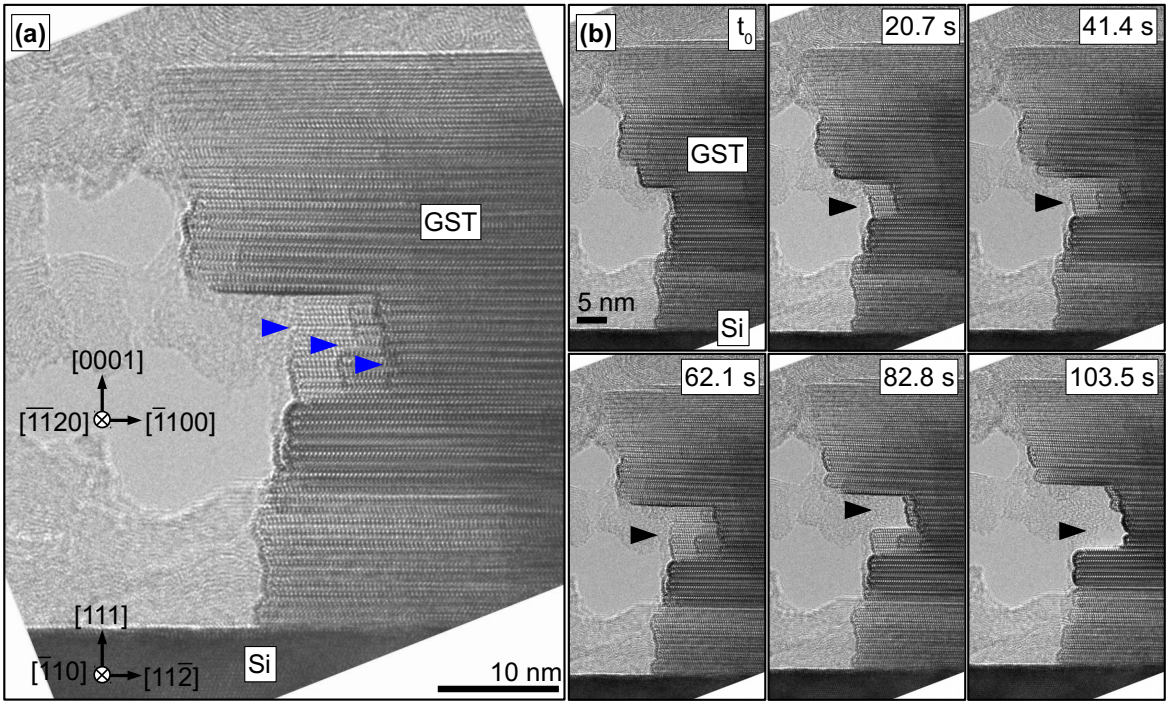

Figure 7.16 Sublimation of trigonal structured GST: (a) HRTEM image of GST on Si featuring terraces of different heights (blue arrow) and (b) HRTEM image series showing the independent sublimation of the terraces at 685°C over a time period of about 100 sec. All images are taken from a video sequence.

Faceting

During the high temperature treatment at 685°C, GST exhibits atomically smooth, round shaped surfaces which are formed repeatedly during the sublimation process (cf. HRTEM image series in Fig. 7.16). The round shape crystal edges are stable when cooled down to 400°C (cf. BF-STEM image in Fig. 7.15(a)). But when cooling down to room temperature, the atomically flat surface is roughened which is comparable to the loss of faceting for the cubic structured GST grain.

Figure 7.17 shows that the rounded GST surface is reproducible formed. The HRTEM image series shows the same sample position of the GST grain at different temperatures. The first image in Figure 7.17 displays the GST grain at room temperature several days after the in-situ observation of the sublimation process shown in Fig. 7.16 where the grain exhibited a rounded surface. The atomically smooth surface at high temperature is lost at room temperature and becomes microscopically rough. This rough surface is maintained even during heating up to 400°C. The smooth rounded surface is reproduced after reaching 600°C. Once the rounded surface is formed it stays stable during cooling down to 400°C. The roughening transition temperature, T_R, of trigonal GST is therefore also above the sublimation temperature at this low pressure since no roughening up to the sublimation point is observed.

The rounded crystal edges are clearly visible in the BF-STEM image shown in Fig. 7.15(a), but vanish under HAADF Z-contrast imaging conditions as shown in Fig. 7.15(b) indicating that the atomic number of the edge structure is lower than the average atomic number

of remaining structure. This fact together with the fact that carbon is readily available and mobile leads to the assumption that carbon acts as surface contaminant making the surface energy more isotropic and therefore facilitating the round shape. An open question remains how the round shape (and therefore the carbon contamination) is steadily reproduced during the sublimation process where GST units and possible contaminates break away from the surface.

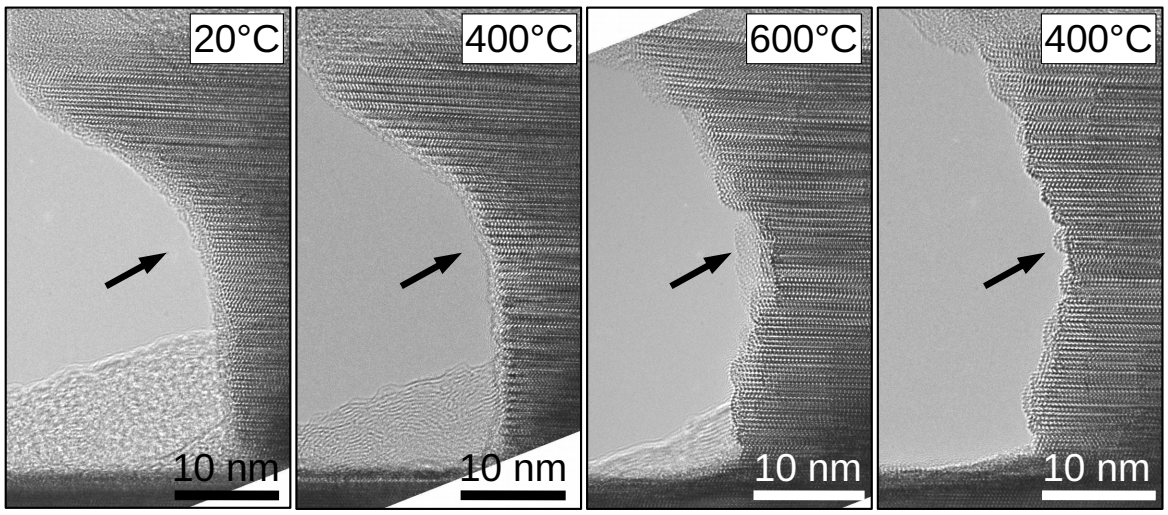

Figure 7.17 HRTEM micrograph of GST on Si several days after first sublimation study at (a) 20°C , (b) 400°C , (c) 600°C and (d) again 400°C showing the reproducibility of the formation of round GST surface.

Discussion

The sublimation process shown here is influenced by carbon contamination and the many defects in the structure. Therefore, the process is not only driven by the crystallography of the trigonal structure making a deeper analysis and comparison to the cubic structure difficult. In order to analyze the influence of the trigonal structure on the sublimation process some measures need to be taken in future experiments. First, the trigonal structure should be well ordered and defect-free. Therefore, the GST thin film needs to be annealed at higher temperature for a longer period of time as described in previous experiments. Secondly, the carbon contamination needs to be minimized by abstaining from carbon coating prior to the sublimation study and cleaning the sample with the plasma cleaner prior to the in-situ observation. In a second step then, the influence of defects and deliberate surface contamination can be investigated as well to gain interesting insights into the sublimation process.

7.4 Concluding remarks

The sublimation behavior of cubic structured GST is investigated in this study. The cubic phase once formed, remains stable even up to the sublimation point and no ordering phenomena or transition to the trigonal phase is observed. This behavior is related to Si diffusion into GST at high temperatures indicating that Si doping helps to improve the thermal

stability of cubic $Ge_1Sb_2Te_4$. The suppression of the cubic-to-trigonal transition at higher temperatures is relevant in applications where the fast reversible transition between amorphous and cubic is used. On the other hand, Si diffusion needs to be taken into account when considering multi-level data storage which is based on different degree of vacancy ordering in GST [132].

In-situ TEM made the direct observation of the nucleation-limited sublimation process with atomic resolution possible even for a heterostructure consisting of a ternary thin film on a crystalline substrate. Thereby, the kink-step-terrace sublimation mechanism can be directly observed. In addition, the formation of stable facets during thermal treatment can be investigated. In the case of GST, the sublimation is anisotropic leading to the formation of $\{111\}$ facets which is attributed to vacancies playing a role in the sublimation process. The stable facets are different than expected and observed during crystal growth indicating that sublimation may not be an exact inverse process of crystal growth. The observed dynamics, on the other hand, are in accordance with the TSK-model for nucleation-limited dynamics: The sublimation happens via kink nucleation on stable steps and subsequent sublimation from those kink sites. The dynamics are identical for crystallography equivalent terrace. Slow and fast kink nucleation in accordance with the broken-bond model and subsequent step movement with similar velocities are identified on opposing facets. Open questions include the formation process of the observed multi-steps. A possible approach is to study the influence of interfacial defects on the sublimation mechanism which form due to a high lattice mismatch between Si substrate and GST thin film. In addition, the results of the sublimation of trigonal GST also indicates processes according to the TSK model. Finally, the transition temperature for GST $\{111\}$ facets must be above the sublimation temperature since surface smoothing with straight steps and no roughening of the facets was observed.

The in-situ TEM investigations can be expanded to directly observe the sublimation mechanism at atomic resolution for various crystalline materials and correlate the mechanism directly to the investigated structure (e.g. differences in sublimation rates from different atomic sites or dependencies on defect structure and crystalline phases).

8 Conclusion and outlook

The expansion of the possibilities for materials analysis with nanometer scale resolution motivated the introduction of in-situ transmission electron microscopy (TEM) at the Paul-Drude-Institute in the context of the presented work. The capability to investigate the thermal stability and degradation of material phases and interfaces especially for heterostructures at high spatial resolution and in real time assists in accelerating the solution of various scientific and technological problems. Thermally activated processes such as diffusion, dislocation motion or vacancy clustering influence the growth of such heterostructures as well as their functionality in devices. Therefore, the understanding of those processes is crucial in advancing the control during growth and application. The intermediate stages and dynamics of the involved atomistic processes are otherwise not experimentally accessible with the same temporal and high spatial resolution.

In this work, in-situ TEM is applied to investigate high-temperature phase transitions of heterostructures. In detail, the solid-liquid and solid-vapor phase transitions of $Ge_1Sb_2Te_4$ (GST) on a crystalline Si substrate are investigated.

The in-situ study involves two major experimental challenges: The appropriate sample preparation and the determination of experimental boundary conditions. First, the preparation of the bulk sample must ensure that the intended in-situ processes are observable. For the investigation of the solid-vapor phase transition a clean surface is necessary whereas the solid-liquid transition needs an encapsulation to ensure a high local partial pressure. Here, the encapsulation is achieved by oxidation of the damaged surface layer formed during conventional preparation or by the purposeful deposition of carbon coating. The clean surface is obtained by preparing the TEM foil in the vacuum of the focused ion beam (FIB) chamber and afterwards inserting it directly into the microscope. However, the use of focused ion beams lead to Ga^+ ions contamination. An effective way to suppress the interference of forming Ga droplets during in-situ observation is identified. A sufficiently thick protective carbon layer allows the Ga droplet to form away from the region of interest. Additionally, the direct observation of the phase transition on the atomic scale requires the sample to be orientated in a low zone axis. In this work, this is simplified by the alignment of the investigated film to the substrate during in-situ solid-state epitaxy prior to the investigation.

Secondly, the spectroscopic capability of the TEM is applied to address the question of compositional stability of the investigated samples because diffusion processes are enhanced at high temperatures. With the use of reference spectra, it is shown that the chemical composition of GST thin films is stable during the solid-vapor transformation. After the liquid-to-solid transition however, grains with different compositions are found which is linked to the spraying out of the molten state through ruptures in the encapsulation. Additionally, electron energy-loss spectroscopy is used to identify the oxidation of the GST thin film as the origin of the encapsulation during conventional sample preparation.

By applying in-situ TEM on the solid-liquid phase transition of trigonal structured GST crystal, the processes in both directions - melting and solidification - are analyzed and compared. The alignment of the GST basal planes parallel to the Si(111) planes allows the direct differentiation between the crystalline and molten phase via the vacancy ordered superlattice structure of the trigonal phase. A transition zone at the solid-liquid interface of 5 nm is found during melting but not during solidification. It is characterized by the disordering of the vacancy ordered superlattice. The existence of an intermediate interface state in a liquid-solid system is therefore observed experimentally and linked to a premelting mechanism. In addition, the interface dynamic of the solid-liquid phase transitions is observed. The process of melting is linear whereas crystallization is non-linear with a square-root time dependence due to long-range diffusion and a superimposed start-stop behavior linked to the influence of the crystalline interface. The two thermodynamic reversible processes of melting and crystallization are therefore not inverse during the growth process implying that different atomic processes are involved. Crystallization of the molten state leads to both crystal structures of GST - cubic and trigonal - independent of the temperature profile. This observation substantiates the theoretically calculated small energy difference between both crystalline states. Additionally, the interfacial and surface energies in the GST and Si heterostructure are determined. Surface energies are generally very difficult to measure and only very little data is available in particular for many component systems. On the other hand they are extremely useful for technological applications. The analysis yields that the {111} facets are the energetically favorable facets at high temperatures in GST and thereby demonstrating the capability of in-situ TEM for advancing material characterization with respect to temperature dependent surface energy determination.

The application of high-resolution in-situ TEM on the sublimation process is made possible by the prior in-situ epitaxial alignment of the cubic structure to the substrate. Opposed to dispersed nanoparticles of known morphology (used in most TEM sublimation studies in literature), here the developing sample morphology of thin film heterostructure needs to be addressed in order to understand the observed processes. It is determined that the GST crystal forms stable {111} facets leading to an octahedron-like morphology which is linked to the role of vacancies aiding the sublimation process. Moreover, the development of flat facets indicates that the transition temperature of surface roughing for cubic GST must lie above its sublimation temperature. Active nucleation sites and the anisotropic formation of kinks, steps and subsequently stable terraces during sublimation is directly observed and shown to be independent of the GST crystal structure (cubic and trigonal). This observation experimentally substantiates the applicability of the theoretically described terrace-step-kink (TSK) model even for multi-component system with a complex crystal structure. Furthermore, the observed preferential and faster nucleation of kinks on lower bonded lattice sites corroborates the broken-bond model which the TSK model is based on. The surprising formation of multi-kinks is observed and associated with interfacial defects formed due to the high lattice mismatch between Si substrate and GST thin film. This is thus indicative of the influence of the GST-Si heterogeneous interface on the phase transition process. A further influence of the substrate on the high-temperature behavior of GST is identified. The cubic phase of GST is stable until the sublimation temperature, even though the transition into an ordered cubic and subsequently into a trigonal structure is expected. The stability is linked to Si diffusion into the GST alloy during thermal annealing. The gained knowledge can be

used for applications as phase change material as it provides instructive insights into the thermal stability of the technological important cubic structure as well as having implications for multi-level storage concepts which are based on ordering of the cubic phase.

Future investigation can build directly on the results and techniques presented in this thesis. For example, successful encapsulation of the GST sample opens the possibility to investigate the molten state locally if the spraying out of the capillary can be prevented to hinder the oscillatory motion of the melt. The local melt structure can be analyzed and compared to the melt-quenched amorphous state in order to confirm the similarities between them.

Throughout the thesis further studies are implicitly suggested: The influence of the crystal structure on the transitional layer can be investigated. For example by using simpler material systems such as binary phase change materials like GeTe. Additionally, the described start-stop behavior during various atomic dynamics warrants further investigations. On the one hand, the investigation on the influence of the substrate should be continued. Crystallization can thereby be studied in dependence on the substrate material thereby varying the interface chemistry and strain induced through differences in lattice mismatch. The influence on the substrate symmetry can be analyzed by using different oriented substrates of the same material. On the other hand, the observation of similar start-stop behaviors under different experimental conditions for GST in this thesis (grain-boundary growth, crystal growth from melt, crystal growth from amorphous phase [189]) and for different materials reported in literature (such as Si [73, 76], Ni-GaAs [73], Al-Cu-Mg-Ag [49] or Fe-Ni-Mn [245]) could also point to a more general cooperative motion during structural phase transitions and would be interesting to explore further.

In case of the solid-to-gas phase transition, it might by worthwhile to revisit the sublimation of {111} facets with higher temporal resolution to confirm the suggested role of vacancies in aiding the sublimation process since up to now atoms from both sublattices in GST seem to desorb at the same time. Additionally, open questions in the sublimation process of GST include the formation process of the observed multi-steps. The suggested influence of interfacial defects due to the high lattice mismatch between Si substrate and GST thin film can be studied further by changing the substrate material. Furthermore, the origin of the surface reconstruction during the sublimation of trigonal structured GST leading to rounded edge features and their influence on the sublimation mechanism remains an open question.

Finally, the in-situ TEM investigations can be expanded to study different dynamical phenomena. Figure 8.1 shows an example of a dislocation in GST that moves towards an approaching surface of the GST crystal as it shrinks during melting. The study of dislocation dynamics in general and in particular in complex multi component materials such as GST is interesting as dislocations strongly affect the properties of materials. Thus, understanding dislocation dynamics furthers the ability in controlling them. In addition, the influence of defects on phase transitions advances the understanding of phase transitions in real structures.

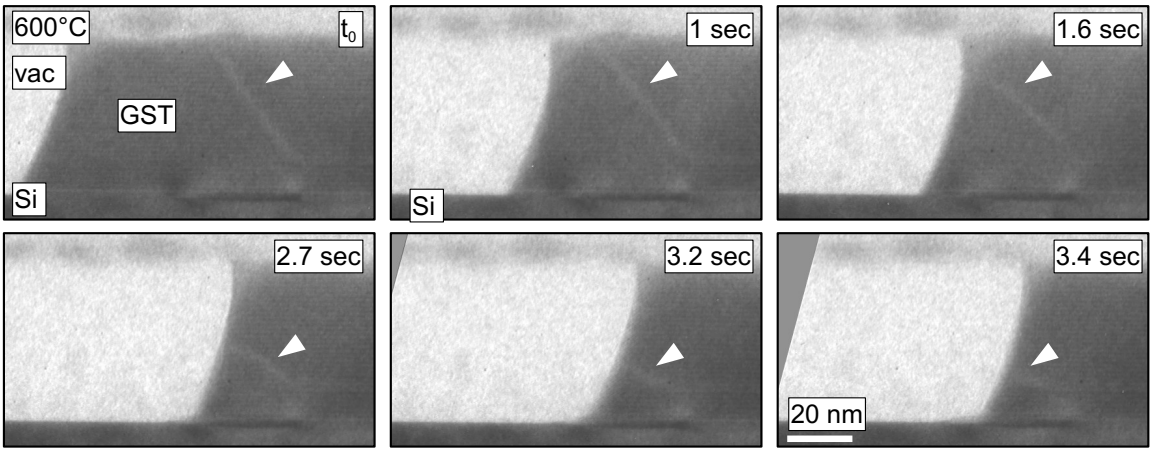

Figure 8.1 Dislocation movement in GST during the shrinking of the GST crystal caused by melting, recorded at 600°C.

A Appendix

A.1 Thermal expansion of Si and GST

The description of thermal expansion follows [217]: Linear thermal expansion of solids is measured in terms of the change in length, da, with respect to the length, a_0, at some temperature T_0. The linear thermal expansion coefficient, $\alpha(T)$, is given by eq. (A.1).

$$\alpha(T) = \frac{1}{a_0}\frac{\mathrm{d}a}{\mathrm{d}T} \tag{A.1}$$

The total length change and therefore the lattice parameter at temperature T can be calculated with eq. (A.2):

$$a(T) = a_0 \left(\int_{T_0}^{T} \alpha(T)\,\mathrm{d}T + 1 \right) \tag{A.2}$$

In practice, α at temperature $T = (T_1 + T_2)/2$ is determined by eq. (A.3):

$$\alpha(T) = \frac{1}{a_0}\frac{(a_1 - a_2)}{(T_1 - T_2)} \tag{A.3}$$

where a_1 and a_2 are lengths at temperatures T_1 and T_2.

To fit the data of the temperature dependent thermal coefficient, an empirical formula is used:

$$\alpha(T) = [C_1(1 - \exp[-C_2(T - C_3)]) + C_4 T]\,10^{-6}\,\mathrm{K}^{-1} \tag{A.4}$$

Linear and volume thermal coefficient. Assuming a material is isotropic in the thermal expansion behavior, the linear thermal expansion (α_L) can be calculated from the volume expansion (α_V) as follows. The cubic unit cell volume is given by $V_{\text{cubic}} = L^3$. Therefore at higher temperature the new volume will be

$$V + \Delta V = (L + \Delta L)^3 = L^3 + 3L^2\Delta L + 3L\Delta L^2 + \Delta L^3 \approx L^3 + 3L^2\Delta L = V + 3V\frac{\Delta L}{L}$$

with $\Delta V = \alpha_V L^3 \Delta T$ and $\Delta L = \alpha_L L \Delta T$. With that, the relationship between volume and linear thermal coefficient can be derived:

$$V + \alpha_V L^3 \Delta T = V + \Delta V = V + 3V\frac{\Delta L}{L} = V + 3L^3\frac{\alpha_L L \Delta T}{L}$$

$$\rightarrow \alpha_V = 3\alpha_L$$

$$\Rightarrow \alpha_L = 1/3 \cdot \alpha_V$$

Silicon. For silicon the thermal coefficient is reported as [217]:

$$\alpha(T) = \left[3.725 \cdot (1 - \exp\left[-5.88 \cdot 10^{-3}(T - 124)\right]) + 5.548 \cdot 10^{-4} \cdot T\right] 10^{-6}\,\mathrm{K}^{-1} \quad \text{(A.5)}$$

with $a_0 = 0.5430741\,\mathrm{nm}$ at $T_0 = 273.2\,\mathrm{K}$.

GeSbTe. Several authors [31, 246–248] mention the thermal expansion of GST, but some give a wrong value. For clarification the reported values are listed in table A.1.

thermal coefficient (α)	linear or volume	Reference	material	comment
$6.24 \cdot 10^{-5}$/K	volume	[31] p.159ff	GST225	book, where authors reproduce a figures of an extended abstract (E\PCOS 2003)
$6.24 \cdot 10^{5}$/K	volume	[246]	GST225	authors reference said extended abstract (E\PCOS 2003), but are probably missing a minus sign in the exponent
$1.8 \cdot 10^{-5}$/K	linear	[247]	GST225	authors give [246] as reference
$1.8 \cdot 10^{-6}$/K	linear	[248]	GST225	authors give [247] as reference
$1.65 \cdot 10^{-5}$/K	linear	[110]	GST124	
$5.02 \cdot 10^{-5}$/K	volume	[110]	GST124	

Table A.1 Summary of reported values for the volume and linear thermal expansion of Ge-Sb-Te.

It is assumed that the value for the volume thermal expansion referenced in [246] and [31] is correct and that GST225 behaves isotropic in its thermal expansion. Then, the linear thermal expansion of GST225 is $\alpha_{L,\,\mathrm{GST}} = 1/3 \cdot \alpha_{Volume} = 2.08 \cdot 10^{-5}\,\mathrm{K}^{-1}$. Interestingly, the value referenced in Ref. [247] is equal to $\sqrt[3]{6.24} \cdot 10^{-5} = 1.8 \cdot 10^{-5}$ which would not be the correct way to calculate α_L from a given α_V.

Comparison of thermal expansion for Si and GST. There is a large lattice mismatch between silicon and cubic GST of 11.3%. When heated to higher temperatures, cubic epitaxially aligned GST is formed. A possible explanation of the formation and/or stabilization of the cubic phase at high temperatures is that through different thermal expansion the lattice mismatch is reduced and therefore the formation of aligned cubic GST is favorable to the formation of the trigonal phase.

The lattice parameter for Si can be calculated using eq. (A.5):

- $400^{\circ}\mathrm{C}: \frac{\Delta a}{a_0} = 0.135\%,\ a = 0.543\,81\,\mathrm{nm}$
- $640^{\circ}\mathrm{C}: \frac{\Delta a}{a_0} = 0.233\%,\ a = 0.544\,34\,\mathrm{nm}$

Due to the lack of available data for GST124, it is assumed that $\alpha_{L,\,\mathrm{GST124}}$ is constant over the entire temperature range up to $600^{\circ}\mathrm{C}$. Then, the lattice parameter at the melting temperature

can be calculated using eq. (A.6):

$$\frac{\Delta a}{a_0} = \alpha_L \cdot \Delta T \tag{A.6}$$

where $\alpha_{L,\,\mathrm{GST124}} = 1.65 \cdot 10^{-5}\,\mathrm{K}^{-1}$ and $a_0 = a(23°\mathrm{C}\,) = 0.60440\,\mathrm{nm}$ [110, 118].

- 400°C : $\frac{\Delta a}{a_0} = 0.62\%$, $a = 0.6082\,\mathrm{nm}$
- 640°C : $\frac{\Delta a}{a_0} = 1.02\%$, $a = 0.6106\,\mathrm{nm}$

Comparing the calculated thermal expansion for GST124 with experimental values for GST(8,2,11) of $\frac{\Delta a}{a_0} = 0.676\%$ at 400°C and $\frac{\Delta a}{a_0} = 1.17\%$ at 650°C [109], the values are not unreasonable even with the rough estimation of a constant thermal expansion over this temperature range. Also, the calculated values are in good agreement with the experimentally determined lattice parameter of GST124 of (0.61 ± 0.01) nm at 400°C and 640°C using FFT analysis (cf. section 7.2.2).

Finally, comparing the lattice parameter at high temperature of Si and GST, it is evident that the lattice mismatch increases even further because the GST expansion is larger than the Si expansion and is not suitable to explain the formation and stabilization of the cubic GST phase at high temperatures.

A.2 Kink nucleation and movement

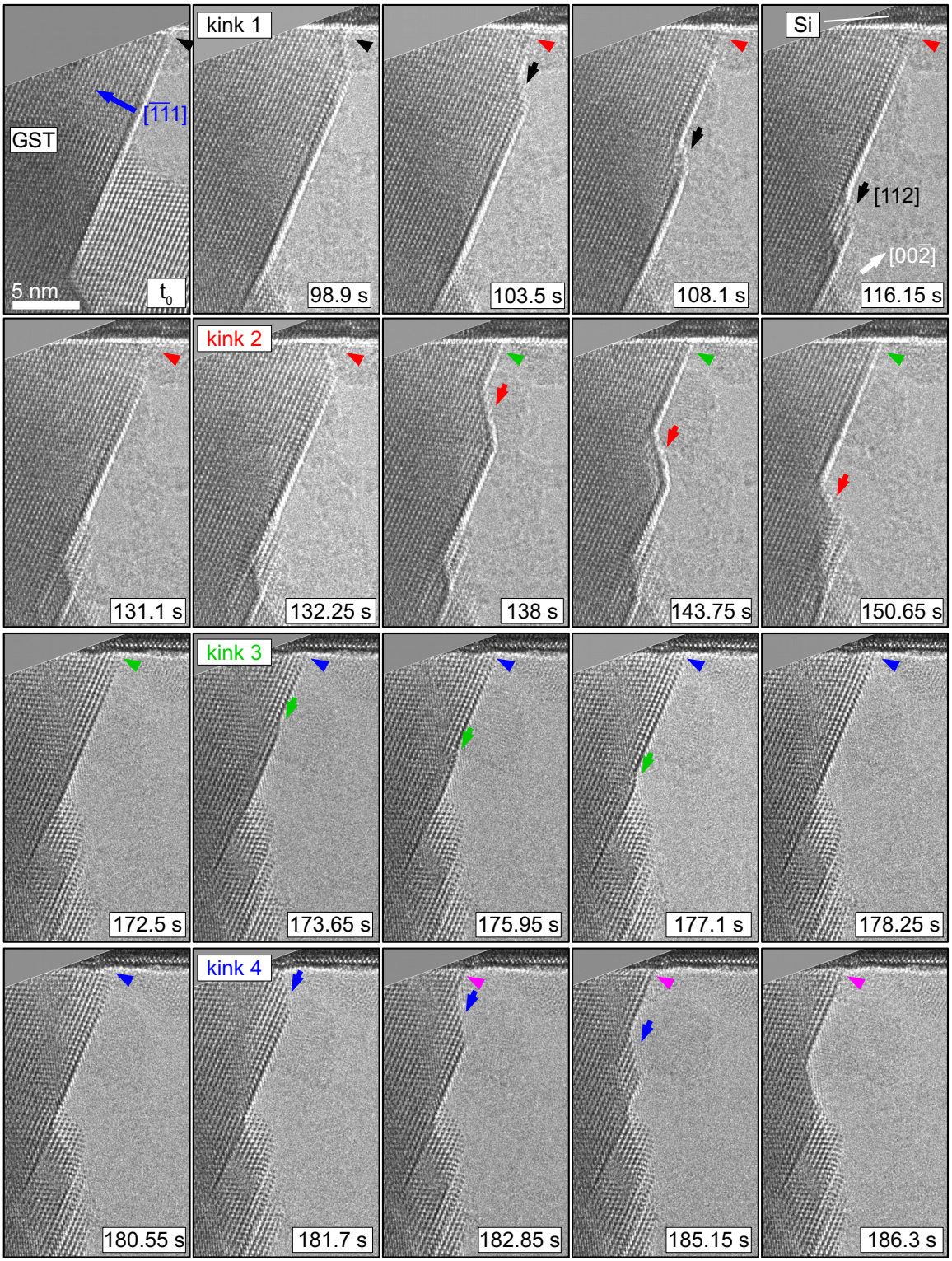

Figure A.1 Series of HRTEM images of the cubic GST grain at 640°C showing the sublimation at the $[\bar{1}\bar{1}1]$ step via kink nucleation and movements along [112]

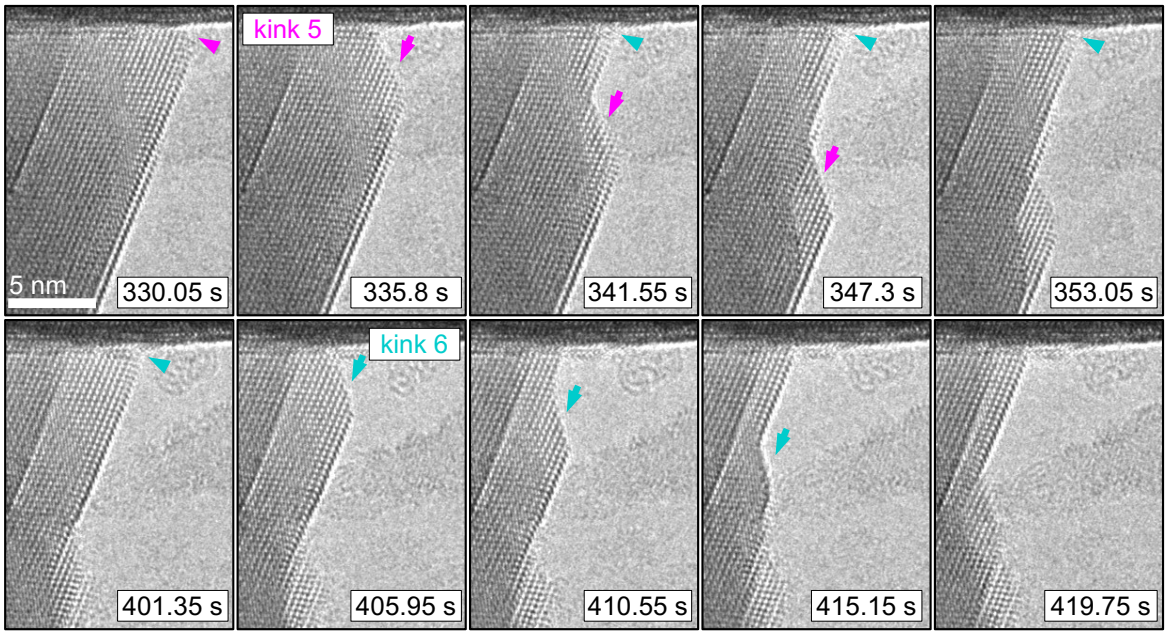

Figure A.2 (Part 2) Series of HRTEM images of the cubic GST grain at 640°C showing the sublimation at the $[\bar{1}\bar{1}1]$ step via kink nucleation and movements along [112], time reference point t_0 is found in Fig. A.1

A.3 Models of stable facets during sublimation

Faceting of surfaces is generally driven by the anisotropy in surface energy γ_{hkl} as a function of the crystallographic orientation {hkl}. As discussed in section A.4, applying the broken-bond model on the rock salt crystal structure of GST yields that the {100} surface has the lowest energy followed by the {110} and {111} surface. Therefore, the minimizing of the total surface energy should lead to the formation of all three facets {100}, {110} and {111}. Figure A.3 shows a 3D atomic model of the crystal shape and its projection along $[1\bar{1}0]$ direction for three different configurations of stable facets: (a) {100}, {110} and {111} facets where the facet with the lowest surface energy ({100}) is the most stable and is therefore the largest facet, (b) {100}, {110} and {111} facets where the {111} form the largest surface and (c) only {111} facets. As seen by the projections, only an octahedron of {111} facets has a rhomboidal shape in the projection along $[1\bar{1}0]$ as is observed for the cubic grain during sublimation.

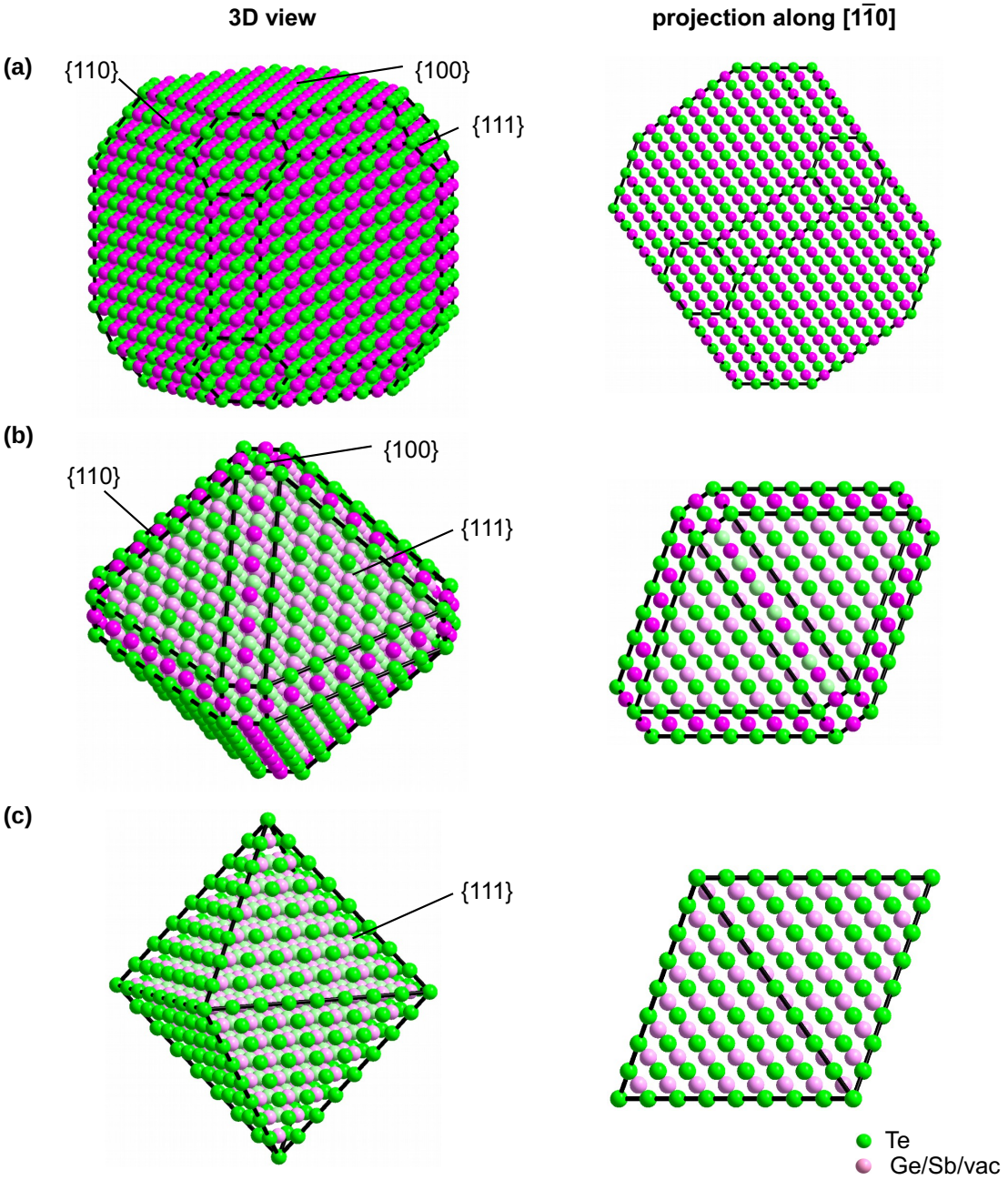

Figure A.3 3D Atomic model of crystal shape and its projection along [[1$\bar{1}$0] direction for three different configurations of stable GST facets: (a) {100}, {110} and {111} facets where {100} has the largest surface, (b) {100}, {110} and {111} facets where {111} has the largest surface and (c) only {111} facets.

A.4 Surface energy calculated by nearest-neighbor broken-bond model

Due to the lack of data on specific surface energies for GST, a first approximation can be made by applying the simplified broken-bond model [219]. Surface atoms experience a different environment compared to atoms in the bulk of a crystal. Atoms in the surface layer have fewer nearest-neighbors and therefore possess an excess energy due to broken bonds. The surface energy of a newly formed crystal surface can be calculated in a first approximation using the nearest-neighbor broken-bond model. Thereby, it is assumed that each atom is bounded by an equal bond energy of ϵ_b to Z nearest neighbors. Z is then also known as the coordination number. Other interactions like higher order neighbors are ignored. The surface energy, γ, is then equal to the number of broken bonds per atom, N_b, multiplied by half the bond strength, ϵ_b, and the density of surface atoms, ρ_s:

$$\gamma = \frac{1}{2} N_b \epsilon_b \rho_s \tag{A.7}$$

Even though real surfaces can lower their energetic state by surface relaxation, surface reconstruction, surface adsorption or compositional segregation, the relationship in eq. (A.7) will provide a rough estimation for the surface energy of various crystal facets. Faceting of surfaces is generally driven by the anisotropy in surface energy γ_{hkl} as a function of the crystallographic orientation {hkl}. As stable systems always try to minimize their total energy, the comparison of surface energies of different crystal facets allows finding the most likely stable crystal facets.

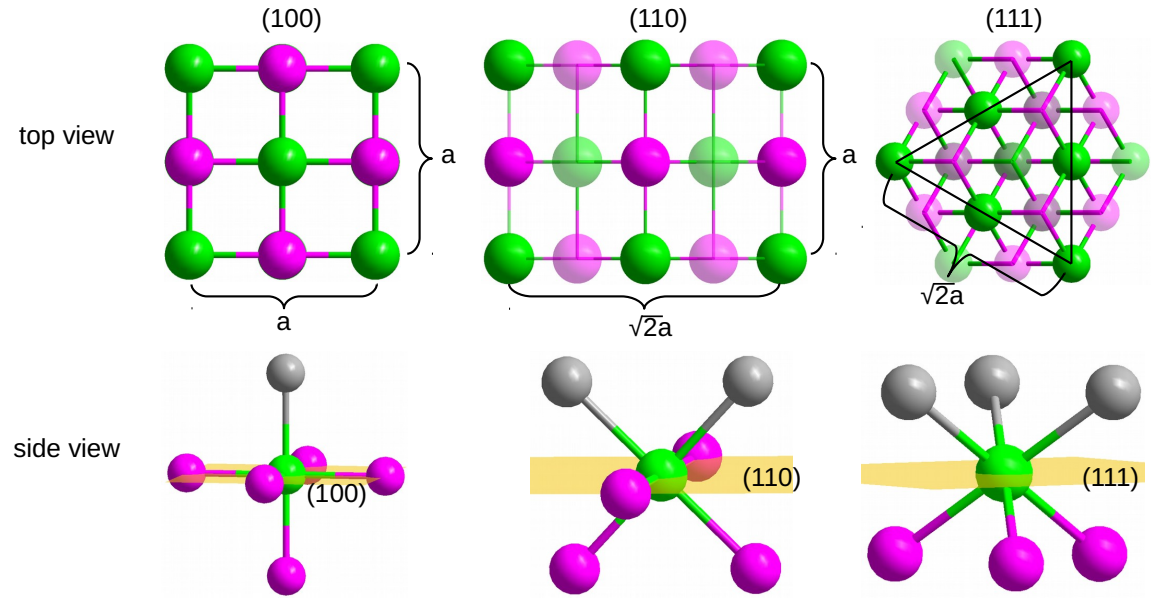

Figure A.4 Schematic model showing the (100), (110) and (111) surfaces of the GST cubic structure in top and side view illustrating the atomic density and number of broken bonds for each surface. Atoms that do not lie in the surface layer are shown as transparent in the top view.

Figure A.4 shows a schematic atomic model of three low-index surfaces {100}, {110}

and $\{111\}$ of the cubic GST phase in projection (top view) and in side view. From the top view illustration the surface area, A_s, and the number of surface atoms, N_s, within this area can be found easily. Using both the density of surface atoms, $\rho_s = \frac{N_s}{A_s}$, can be calculated. The side view illustrates the number of broken bonds, N_b, per surface atom for each of the three crystal surfaces. Using eq. (A.7) an approximation for the surface energy of the $\{100\}$, $\{110\}$ and $\{111\}$ facets of a NaCl-structured crystal can be calculated. A summary of the calculations are shown in table A.2 and yield that the $\{100\}$ surface has the lowest energy followed by the $\{110\}$ and $\{111\}$ surface: $\gamma_{100} < \gamma_{110} < \gamma_{111}$. Higher indexed planes will have a higher surface atom density and therefore higher surface energies. The equilibrium shape of a small particle therefore primarily consists of those facets. And indeed, GST grains that form after the crystallization from melt droplets on a Si(111) substrate exhibit $\{100\}$, $\{110\}$ and $\{111\}$ facets as shown in chapter 6.

	$\{100\}$	$\{110\}$	$\{111\}$
surface area A_s	a^2	$\sqrt{2}a^2$	$\sqrt{3}/2a^2$
number of atoms in surface area N_s	$4\ (=4{\cdot}\frac{1}{4}+4{\cdot}\frac{1}{2}+1)$	$4\ (=4{\cdot}\frac{1}{4}+4{\cdot}\frac{1}{2}+1)$	$2\ (=3{\cdot}\frac{1}{6}+3{\cdot}\frac{1}{2})$
density of surface atoms ρ_s	$\frac{4}{a^2}$	$\frac{2\sqrt{2}}{a^2}$	$\frac{4}{\sqrt{3}a^2}$
number of broken bonds N_b	1	2	3
surface energy γ_{hkl}	$\frac{2}{a^2}\epsilon_b$	$\frac{2\sqrt{2}}{a^2}\epsilon_b$	$\frac{2\sqrt{3}}{a^2}\epsilon_b$

Table A.2 Summary of relative surface energy of low-index planes for the NaCl-structure.

A.5 Literature summary of reported transition temperatures

Table A.3 lists the melting temperatures and table A.4 the first and second solid-to-solid phase transitions temperatures for different GST compositions reported in several references. Thereby, the method to measure the temperature, information about the samples and the method to determine the composition if applicable are listed as well.

Reference	Material	T_m[°C]	Method	Sample	Composition
Seo2000 [157]	GST225	610.8	DSC	100 nm film	ICP
Yamada1991 [89]	GST225	616	DSC	powder	ICP
Kalb2003 [153]	GST225	621	DSC	7 µm film	ICPES, EDX
Ryu2008 [159]	GST225	622	DSC	1.5 µm film	RBS, XFS
Bordas1986 [152]	GST225	630			
Qiao2006 [117]	GST225	640.7	DSC	230 nm on SiO_2	XPS
Qiao2006 [117]	Si(4.1%)-225	589.9 / 635.6*[1]	DSC	230 nm on SiO_2	XPS
Qiao2006 [117]	Si(7.2%)-225	591.5 / 622.6*[1]	DSC	230 nm on SiO_2	XPS
Qiao2006 [117]	Si(11.8%)-225	590.3 / 618.4*[1]	DSC	230 nm on SiO_2	XPS
Kalkan2011 [30]	GST124	607	XRD		
Yamada1991 [89]	GST124	614	DSC	powder	ICP
Shelimova01 [136]	GST124	615			
Bordas1986 [152]	GST124	616			
Matsunaga04 [110]	GST124	700*[2]	XRD	powder	ICP
Bordas1986 [152]	GST147	606			
Yamada1991 [89]	GST147	607	DSC	powder	ICP
Shelimova2001 [136]	GST147	607			

Table A.3 Reported melting temperatures T_m of different GST compositions including the experimental methods used to determine $T_m$and the composition. This should not be considered to be an exhaustive list.
*[1]peak separation in DSC observed
*[2] increased temperature is attributed to pressure rise in sealed capillary [110]

Reference	Material	T_{c1}[°C]	T_{c2}[°C]	Method	Sample	Composition
Privitera2003 [135]	GST225	130		resistivity	50 nm on SiO2	Auger, EDXS
Kooi2004 [25]	GST225	130	340	in-situ TEM	10-70 nm thin film	EDXS
Morales2005 [118]	GST225	138	225	resistivity	100 nm films	EDS in SEM
Friedrich2000 [119]	GST225	140	310	resistivity	80 nm film	
Yamada1991 [89]	GST225	142	183	DSC	powder	ICP
Park1999 [249]	GST225*[1]	143.8*[3]		DSC	powder	
Park1999 [249]	GST225*[2]	149.7*[4]		DSC	powder	
Kalb2003 [153]	GST225	155.1		DSC	7 µm film	ICPES, EDX
Seo2000 [157]	GST225	162		DSC	100 nm film	ICP
Qiao2006 [117]	GST225	162.8		DSC	230 nm on SiO_2	XPS
Sun2009 [250]	GST225		200	ex situ TEM	200 nm film	target 225
Qiao2006 [117]	Si(4.1%)-225	193.8		DSC	230 nm on SiO_2	XPS
Qiao2006 [117]	Si(7.2%)-225	234.7		DSC	230 nm on SiO_2	XPS
Qiao2006 [117]	Si(11.8%)-225	274.3		DSC	230 nm on SiO_2	XPS
Seo2000 [157]	N(11.8%)-225	239		DSC	100 nm film	ICP
Subramaniam09 [151]	GST124	120	216		STM	Auger
Tomforde2011 [90]	GST124	127(2)	220	XRD	1 µm film	EDX
Morales2005 [118]	GST124	130	200	resistivity	100 nm film	EDS in SEM
Yamada1991 [89]	GST124	131	217	DSC	powder	ICP
Blachowicz2007 [149]	GST124	140	300	XRD	176 nm on Si111	
Matsunaga2004 [110]	GST124		227	XRD	powder	ICP
Kalkan2011 [30]	GST124		>150	XRD		
Morales2005 [118]	GST147	110	187	resistivity	100 nm films	EDS in SEM
Yamada1991 [89]	GST147	123	239	DSC	powder	ICP
Morales2005 [118]	GST415	152	no trigonal	resistivity	100 nm films	EDS in SEM
Kalb2003 [153]	GST415	190.2		DSC	7 µm film	ICPES, EDX
Tomforde2011 [90]	GST224	150	265	XRD	1 µm film	EDX

Table A.4 Reported transition temperatures T_{c1} and T_{c2} of different GST compositions including the experimental methods used to determine T_{c1}, T_{c2} and the composition. This should not be considered to be an exhaustive list.
*[1] laser-amorphized; *[2]as-deposited amorphous state; *[3]depends on heating rates: 5°C /min: 143.8°C , 10°C /min: 148.3°C , 20°C /min: 154.0°C ; *[4]depends on heating rates: 5°C /min:149.7°C , 10°C /min: 154.0°C , 20°C /min: 158.7°C

A.6 Temperature-thermoelectric voltage conversion

Table A.5 lists the coefficients a_i, b_i and c_i used in eq. (4.2) and (4.1) for the conversion of temperature and thermoelectric voltage. Figure A.5 displays the conversion graph for easy reference.

Table A.5 Coefficients for converting a temperature T [°C] to a corresponding thermoelectric voltage U [μV] (a_i) and for converting U [μV] to T [°C] (b_i, c_i) [82].

i	a_i	b_i	c_i
0	-	-	$1,334584505 \cdot 10^{1}$
1	$5,28961729765$	$1,8891380 \cdot 10^{-1}$	$1,472644573 \cdot 10^{-1}$
2	$1,39166589782 \cdot 10^{-2}$	$-9,3835290 \cdot 10^{-5}$	$-1,844024844 \cdot 10^{-5}$
3	$-2,3885693017 \cdot 10^{-5}$	$1,3068619 \cdot 10^{-7}$	$4,031129726 \cdot 10^{-9}$
4	$3,56916001063 \cdot 10^{-8}$	$-2,2703580 \cdot 10^{-10}$	$-6,249428360 \cdot 10^{-13}$
5	$-4,62347666298 \cdot 10^{-11}$	$3,5145659 \cdot 10^{-13}$	$6,468412046 \cdot 10^{-17}$
6	$5,00777441034 \cdot 10^{-14}$	$-3,8953900 \cdot 10^{-16}$	$-4,458750426 \cdot 10^{-21}$
7	$-3,73105886191 \cdot 10^{-17}$	$2,8239471 \cdot 10^{-19}$	$1,994710149 \cdot 10^{-25}$
8	$1,57716482367 \cdot 10^{-20}$	$-1,2607281 \cdot 10^{-22}$	$-5,313401790 \cdot 10^{-30}$
9	$-2,81038625251 \cdot 10^{-24}$	$3,1353611 \cdot 10^{-26}$	$6,481976217 \cdot 10^{-35}$
10	-	$-3,3187769 \cdot 10^{-30}$	-

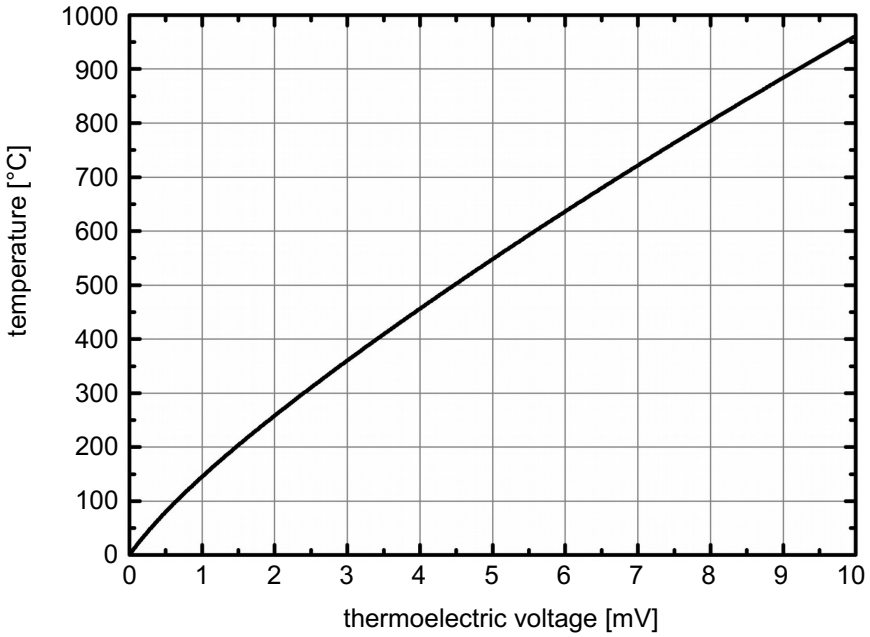

Figure A.5 Conversion graph of thermoelectric voltage and temperature for a type R thermocouple calculated with eq. (4.1).

A.7 Bragg condition

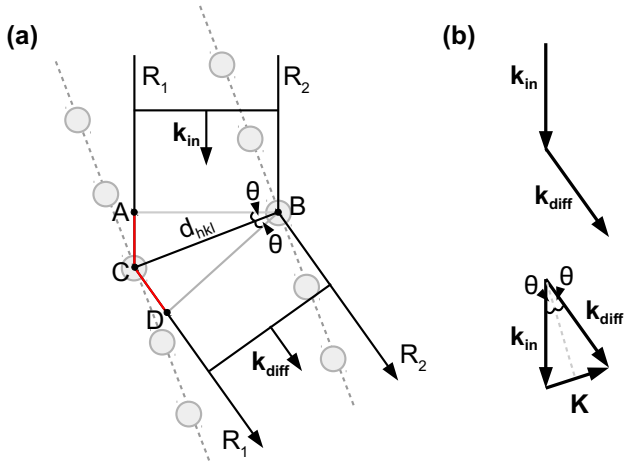

Figure A.6 Illustration of electron scattering geometry in a crystalline sample: (a) diffraction of electron wave on two parallel atomic planes and (b) involved electron wave vectors of incident and diffracted beam; based on illustrations in Ref. [35].

Using the Bragg condition the position of diffraction spots in a diffraction pattern can be explained. For thin specimens and small scattering angles, scattering is approximated to involve single elastic scattering events (kinematical approximation). The involved scattering geometry for crystalline specimens is illustrated in Fig. A.6 and can be described as follows: When the incident plane electron wave with wave vector $\boldsymbol{k}_{\text{in}}$ strikes two atomic lattice planes with a distance of d_{hkl}, the electron wave will be diffracted and can be described by a wave vector $\boldsymbol{k}_{\text{Diff}}$. Note that for the characterization of the atomic lattice planes the Miller indices (h, k, l) are used. For elastic scattering, there is no energy change between the incident and the diffracted electron beam. The absolute value of both beams is therefore given by the wavelength of the electrons, λ:

$$|\boldsymbol{k}_{\text{in}}| = |\boldsymbol{k}_{\text{diff}}| = \frac{1}{\lambda} \tag{A.8}$$

Using geometrical considerations (cf. Fig. A.6(b)) and using eq. (A.8) the difference between the incident and diffracted beam is given by

$$|\Delta\boldsymbol{k}| = |\boldsymbol{k}_{\text{diff}} - \boldsymbol{k}_{\text{in}}| = \frac{2\sin(\theta)}{\lambda} \tag{A.9}$$

where θ is the diffraction angle. Additionally, the path difference between ray 1 and ray 2 shown in Fig. A.6(a) is given by

$$\text{AC} + \text{CD} = 2d_{hkl}\sin(\theta) \tag{A.10}$$

Constructive interference occurs when the path difference is equal to a multiple of the wave-

length. The diffraction angle is then called Bragg angle, θ_B, and eq. (A.10) becomes:

$$\begin{aligned} n\lambda &= 2d_{hkl}\sin(\theta_B) \\ \frac{n}{d_{hkl}} &= \frac{2\sin(\theta_B)}{\lambda} \\ |\boldsymbol{g}| \equiv \frac{n}{d_{hkl}} &= |\Delta \boldsymbol{k}_B| \end{aligned} \tag{A.11}$$

Equation A.11 is called the Bragg condition. When the difference between incident and diffracted beam is equal to a reciprocal lattice vector, $\boldsymbol{g}$, there is constructive interference which leads to the formation of a diffraction spot. Therefore, each diffraction spot in a diffraction pattern corresponds to a set of parallel atomic planes.

Bibliography

[1] R. Sinclair. In situ high-resolution transmission electron microscopy of material reactions. *Materials Research Society Bulletin*, 38:1065–1071, 2013.

[2] E. P. Butler and K. F. Hale. *Dynamic Experiments in the Electron Microscope*, volume 9 of *Practical methods in electron microscopy*. North-Holland Publishing Company, 1981.

[3] F. M. Ross. In Situ Transmission Electron Microscopy. In P. W. Hawkes and J. C. H. Spence, editors, *Science of Microscopy*, pages 445–534. Springer US, New York, 2007.

[4] J. W. M. Frenken and J. F. van der Veen. Observation of surface melting. *Physical Review Letters*, 54(2):134–137, 1985.

[5] R. W. Cahn. Melting from within. *Nature*, 413:582–583, 2001.

[6] Y. Li, L. Zang, D. L. Jacobs, J. Zhao, X. Yue, and C. Wang. In situ study on atomic mechanism of melting and freezing of single bismuth nanoparticles. *Nature Communications*, 8:14462, 2017.

[7] A. R. Ubbelodhde. *The molten state of matter: melting and crystal structure*. John Wiley & Sons Ltd, Chichester, 1978.

[8] Z. Sun, J. Zhou, and R. Ahuja. Unique melting behavior in phase-change materials for rewritable data storage. *Physical Review Letters*, 98(5):055505, 2007.

[9] R. Kofman, P. Cheyssac, R. Garrigos, Y. Lereah, and G. Deutscher. Solid-liquid transition of metallic clusters. Occurrence of surface melting. *Physica A*, 157(1):631–638, 1989.

[10] R. Rosenberg. Why Is Ice Slippery? *Physics Today*, 58(12):50–54, 2005.

[11] Y. Li and G. A. Somorjai. Surface Premelting of Ice. *The Journal of Physical Chemistry C*, 111(27):9631–9637, 2007.

[12] J. W. L. Yim, B. Xiang, and J. Wu. Sublimation of GeTe nanowires and evidence of its size effect studied by in situ TEM. *Journal of the American Chemical Society*, 131(40):14525–14530, 2009.

[13] Y. Yang, M. Asta, and B. B. Laird. Solid-liquid interfacial premelting. *Physical Review Letters*, 110(9):096102, 2013.

[14] J. P. Hirth and G. M. Pound. *Condensation and Evaporation: Nucleation and Growth Kinetics*, volume 11 of *Progress in Materials Science*. Pergamon, Oxford, 1963.

[15] G. A. Somorjai and J. E. Lester. Evaporation mechanism of solids. *Progress in Solid State Chemistry*, 4:1–52, 1967.

[16] D. J. Hellebusch, K. Manthiram, B. J. Beberwyck, and A. P. Alivisatos. In Situ Transmission Electron Microscopy of Cadmium Selenide Nanorod Sublimation. *The Journal of Physical Chemistry Letters*, 6(4):605–611, 2015.

[17] M. A. Asoro, D. Kovar, and P. J. Ferreira. In-situ Transmission Electron Microscopy Observations of Sublimation in Silver Nanoparticles. *ACS Nano*, 7(9):7844–7852, 2013.

[18] Q. Yu, M.-M. Mao, Q.-J. Li, X.-Q. Fu, H. Tian, J.-X. Li, S. X. Mao, and Z. Zhang. In Situ Observation on Dislocation-Controlled Sublimation of Mg Nanoparticles. *Nano Letters*, 16:1156–1160, 2016.

[19] M. A. van Huis, N. P. Young, G. Pandraud, J. F. Creemer, D. Vanmaekelbergh, A. I. Kirkland, and H. W. Zandbergen. Atomic imaging of phase transitions and morphology transformations in nanocrystals. *Advanced Materials*, 21(48):4992–4995, 2009.

[20] C.-L. Hsin, C.-W. Huang, J.-Y. Chen, K.-C. Liao, P.-L. Liu, W.-W. Wu, and L.-J. Chen. Direct Observation of Sublimation Behaviors in One-Dimensional In_2Se_3/In_2O_3 Nanoheterostructures. *Analytical Chemistry*, 87(11):5584–5588, 2015.

[21] J. Buha, R. Gaspari, A. E. Del Rio Castillo, F. Bonaccorso, and L. Manna. Thermal Stability and Anisotropic Sublimation of Two-Dimensional Colloidal Bi_2Te_3 and Bi_2Se_3 Nanocrystals. *Nano Letters*, 16(7):4217–4223, 2016.

[22] J.-G. Lee, J. Lee, T. Tanaka, and H. Mori. In Situ HREM Observation of Crystalline-to-Gas Transition in Nanometer-Sized Ag Particles. *Physical Review Letters*, 96(7):075504, 2006.

[23] C. Chen, Z. Hu, Y. Li, L. Liu, H. Mori, and Z. Wang. In-Situ High-Resolution Transmission Electron Microscopy Investigation of Overheating of Cu Nanoparticles. *Scientific Reports*, 6(2015):19545, 2016.

[24] M. Wuttig and N. Yamada. Phase-change materials for rewriteable data storage. *Nature Materials*, 6(11):824–832, 2007.

[25] B. J. Kooi, W. M. G. Groot, and J. T. M. De Hosson. In situ transmission electron microscopy study of the crystallization of $Ge_2Sb_2Te_5$. *Journal of Applied Physics*, 95:924–932, 2004.

[26] J. C. Baker and J. W. Cahn. Thermodynamics of Solidification. In *The Selected Works of John W. Cahn*. John Wiley & Sons, Inc., Hoboken, NJ, USA, 1998.

[27] G. Gottstein. *Physical Foundations of Material Science*. Springer, Berlin, Heidelberg, 2004.

[28] W. Nolting. *Grundkurs Theoretische Physik 4*. Springer, Berlin, Heidelberg, 2005.

[29] D. A. Young. Phase diagrams of the elements. Technical report, Lawrence Livermore Laboratory, University of California, 1975.

[30] B. Kalkan, S. Sen, B. G. Aitken, S. V. Raju, and S. M. Clark. Negative P-T slopes characterize phase change processes: Case of the $Ge_1Sb_2Te_4$ phase change alloy. *Physical Review B*, 84(1):014202, 2011.

[31] A. V. Kolobov and J. Tominaga. *Chalcogenides - Metastability and Phase Change Phenomena*. Springer, Berlin, Heidelberg, 2012.

[32] R. J. Kirkpatrick. Crystal Growth from the Melt: A Review. *American Mineralogist*, 60:798–814, 1975.

[33] J. A. Kalb. Crystallization Kinetics. In S. Raoux and M. Wuttig, editors, *Phase Change Materials - Science and Applications*, pages 125–148. Springer US, New York, 2009.

[34] G. A. Somorjai. Mechanism of Sublimation. *Science*, 162(3855):755–760, 1968.

[35] D. B. Williams and C. B. Carter. *Transmission Electron Microscopy - A Textbook for Materials Science*. Springer US, New York, 2nd edition, 2009.

[36] L. Reimer. *Transmission Electron Microscopy: Physics of Image Formation and Microanalysis*. Springer, Berlin, Heidelberg, 1984.

[37] A. I. Kirkland, S. L.-Y. Chang, and J. L. Hutchison. Atomic Resolution Transmission Electron Microscopy. In P. W. Hawkes and J. C. H. Spence, editors, *Science of Microscopy*, pages 3–64. Springer US, New York, 2007.

[38] P. A. Stadelmann. EMS - a software package for electron diffraction analysis and HREM image simulation in materials science. *Ultramicroscopy*, 21(2):131–145, 1987.

[39] S. J. Pennycook. Structure determination through Z-contrast microscopy. *Advances in Imaging and Electron Physics*, 123:173–206, 2002.

[40] P. Hartel, H. Rose, and C. Dinges. Conditions and reasons for incoherent imaging in STEM. *Ultramicroscopy*, 63(2):93–114, 1996.

[41] L. Krusin-Elbaum, C. Cabral, K. N. Chen, M. Copel, D. W. Abraham, K. B. Reuter, S. M. Rossnagel, J. Bruley, and V. R. Deline. Evidence for segregation of Te in $Ge_2Sb_2Te_5$ films: Effect on the "phase-change" stress. *Applied Physics Letters*, 90(14):141902, 2007.

[42] T. Matsunaga, R. Kojima, N. Yamada, K. Kifune, Y. Kubota, Y. Tabata, and M. Takata. Single structure widely distributed in a GeTe-Sb_2Te_3 pseudobinary system: a rock salt structure is retained by intrinsically containing an enormous number of vacancies within its crystal. *Inorganic Chemistry*, 45(5):2235–2241, 2006.

[43] Z. Zhang, J. Pan, L. W.-W. Fang, Y.-C. Yeo, Y. L. Foo, R. Zhao, L. Shi, and E. S. Tok. Temperature-dependent phase separation during annealing of $Ge_2Sb_2Te_5$ thin films in vacuum. *Applied Surface Science*, 258(16):6075–6079, 2012.

[44] S. A. Song, W. Zhang, H. Sik Jeong, J.-G. Kim, and Y.-J. Kim. In situ dynamic HR-TEM and EELS study on phase transitions of $Ge_2Sb_2Te_5$ chalcogenides. *Ultramicroscopy*, 108(11):1408–1419, 2008.

[45] R. F. Egerton. *Electron energy-loss spectroscopy in the electron microscope*. Plenum Press, New York, 2nd edition, 1996.

[46] K. Perumal. *Epitaxial growth of Ge-Sb-Te based phase change materials*. Dissertation, Humboldt-Universität zu Berlin, Mathematisch-Naturwissenschaftliche Fakultät I, 2013.

[47] A. V. Kolobov, P. Fons, A. I. Frenkel, A. L. Ankudinov, J. Tominaga, and T. Uruga. Understanding the phase-change mechanism of rewritable optical media. *Nature Materials*, 3(10):703–708, 2004.

[48] R. Sinclair, T. Itoh, and R. Chin. In Situ TEM Studies of Metal-Carbon Reactions. *Microscopy and Microanalysis*, 8(4):288–304, 2002.

[49] W. E. Benson and J. M. Howe. An in-situ high-resolution transmission electron microscopy study of the growth and dissolution of $\theta\{111\}$ precipitate plates in an Al-Cu-Mg-Ag alloy. *Philosophical Magazine A*, 75(6):1641–1663, 1997.

[50] X. Liu, J. D. Wood, K. S. Chen, E. Cho, and M. C. Hersam. In situ thermal decomposition of exfoliated two-dimensional black phosphorus. *Journal of Physical Chemistry Letters*, 6(5):773–778, 2015.

[51] T. Kamino, T. Yaguchi, M. Tomita, and H. Saka. In-situ high-resolution electron microscopy study on a surface reconstruction of Au-deposited Si at very high temperatures. *Philosophical Magazine A*, 75(1):105–114, 1997.

[52] E. T. Kim, J. Y. Lee, and Y. T. Kim. In situ transmission electron microscopy study on the crystallization of GeTe binary alloy. *Applied Physics Letters*, 92(19):191915, 2008.

[53] Y. J. Park, J. Y. Lee, and Y. T. Kim. In situ transmission electron microscopy study of the nucleation and grain growth of $Ge_2Sb_2Te_5$ thin films. *Applied Surface Science*, 252(23):8102–8106, 2006.

[54] E. A. Lewis, T. J. A. Slater, E. Prestat, A. Macedo, P. O'Brien, P. H. C. Camargo, and S. J. Haigh. Real-time imaging and elemental mapping of AgAu nanoparticle transformations. *Nanoscale*, 6(22):13598–13605, 2014.

[55] A. M. Minor, J. W. Morris, and E. A. Stach. Quantitative in situ nanoindentation in an electron microscope. *Applied Physics Letters*, 79(11):1625–1627, 2001.

[56] L. Wang, D. Kong, T. Xin, X. Shu, K. Zheng, L. Xiao, X. Sha, Y. Lu, Z. Zhang, X. Han, and J. Zou. Deformation mechanisms of bent Si nanowires governed by the sign and magnitude of strain. *Applied Physics Letters*, 108(15):151903, 2016.

[57] Y. Yue, Q. Gong, and Q. Zhang. In Situ Atomistic Deformation Mechanisms Study of Nanowires. *Journal of Nanomaterials*, 2016:8497242, 2016.

[58] S. Meister, S. B. Kim, J. J. Cha, H.-S. P. Wong, and Y. Cui. In situ transmission electron microscopy observation of nanostructural changes in phase-change memory. *ACS Nano*, 5(4):2742–2748, 2011.

[59] Q. Jeangros, M. Duchamp, J. Werner, M. Kruth, R. E. Dunin-Borkowski, B. Niesen, C. Ballif, and A. Hessler-Wyser. In Situ TEM Analysis of Organic-Inorganic Metal-Halide Perovskite Solar Cells under Electrical Bias. *Nano Letters*, 16(11):7013–7018, 2016.

[60] C. R. Winkler, A. R. Damodaran, J. Karthik, L. W. Martin, and M. L. Taheri. Direct observation of ferroelectric domain switching in varying electric field regimes using in situ TEM. *Micron*, 43(11):1121–1126, 2012.

[61] M. R. Armstrong, K. Boyden, N. D. Browning, G. H. Campbell, J. D. Colvin, W. J. DeHope, A. M. Frank, D. J. Gibson, F. Hartemann, J. S. Kim, W. E. King, T. B. LaGrange, B. J. Pyke, B. W. Reed, R. M. Shuttlesworth, B. C. Stuart, and B. R. Torralva. Practical considerations for high spatial and temporal resolution dynamic transmission electron microscopy. *Ultramicroscopy*, 107(4-5):356–367, 2007.

[62] M. K. Santala, B. W. Reed, T. Topuria, S. Raoux, S. Meister, Y. Cui, T. LaGrange, G. H. Campbell, and N. D. Browning. Nanosecond in situ transmission electron microscope studies of the reversible $Ge_2Sb_2Te_5$ crystalline $\Leftrightarrow$ amorphous phase transformation. *Journal of Applied Physics*, 111(2):024309, 2012.

[63] F. M. Ross. Electrochemical nucleation, growth and dendrite formation in liquid cell TEM. *Microscopy and Microanalysis*, 16(S2):326–327, 2010.

[64] N. de Jonge and F. M. Ross. Electron microscopy of specimens in liquid. *Nature Nanotechnology*, 6(11):695–704, 2011.

[65] P. L. Hansen. Atom-Resolved Imaging of Dynamic Shape Changes in Supported Copper Nanocrystals. *Science*, 295(5562):2053–2055, 2002.

[66] H. Saka, K. Sasaki, S. Tsukimoto, and S. Arai. In situ Observation of Solid-liquid Interfaces by Transmission Electron Microscopy. *Journal of Materials Research*, 20(7):1629–1640, 2005.

[67] J. M. Yuk, J. Park, P. Ercius, K. Kim, D. J. Hellebusch, M. F. Crommie, J. Y. Lee, A. Zettl, and A. P. Alivisatos. High-Resolution EM of Colloidal Nanocrystal Growth Using Graphene Liquid Cells. *Science*, 336(6077):61–64, 2012.

[68] B. L. Mehdi, J. Qian, E. Nasybulin, C. Park, D. A. Welch, R. Faller, H. Mehta, W. A. Henderson, W. Xu, C. M. Wang, J. E. Evans, J. Liu, J. G. Zhang, K. T. Mueller, and N. D. Browning. Observation and Quantification of Nanoscale Processes in Lithium Batteries by Operando Electrochemical (S)TEM. *Nano Letters*, 15(3):2168–2173, 2015.

[69] A. L. Koh, E. Gidcumb, O. Zhou, and R. Sinclair. Oxidation of Carbon Nanotubes in an Ionizing Environment. *Nano Letters*, 16(2):856–863, 2016.

[70] N. de Jonge. Membrane protein stoichiometry studied in intact mammalian cells using liquid-phase electron microscopy. *Journal of Microscopy*, 0:1–9, 2017 (online preview).

[71] J. Hermannsdoerfer and N. de Jonge. Studying Dynamic Processes of Nano-sized Objects in Liquid using Scanning Transmission Electron Microscopy. *Jove-Journal of Visualized Experiments*, (120):e54943, 2017.

[72] R. Sharma. Experimental set up for in situ transmission electron microscopy observations of chemical processes. *Micron*, 43(11):1147–1155, 2012.

[73] R. Sinclair, M. A. Parker, and K. B. Kim. In situ high-resolution electron microscopy reactions in semiconductors. *Ultramicroscopy*, 23(3-4):383–396, 1987.

[74] S. Privitera, C Bongiomo, E. Rimini, R. Zonca, A. Pirovano, and R. Bez. Amorphous-to-polycrystal transition in GeSbTe thin films. *Materials Research Society Proceedings*, 803:HH1.4, 2011.

[75] R. Sinclair, T. Yamashita, and F. A. Ponce. Atomic Motion on the Surface of a Cadmium Telluride Single-Crystal. *Nature*, 290(5805):386–388, 1981.

[76] R. Sinclair and M. A. Parker. High-resolution transmission electron microscopy of silicon re-growth at controlled elevated temperatures. *Nature*, 322(6079):531–533, 1986.

[77] Z. C. Kang and L. Eyring. Analysis of time-resolved, in-situ change in high-resolution electron microscopy. *Ultramicroscopy*, 52(3-4):377–382, 1993.

[78] B. Kabius, N. Browing, T. Thevuthasan, and E. Stach. Dynamic processes in biology, chemistry, and material science: Opportunities for ultrafast transmission electron microscopy. EMSL Workshop Report, 2011. http://www.pnnl.gov/main/publications/external/technical_reports/PNNL-21407.pdf.

[79] A. H. Zewail. Four-dimensional electron microscopy. *Science*, 328(5975):187–193, 2010.

[80] A. Feist, N. Bach, N. Rubiano da Silva, T. Danz, M. Möller, K. E. Priebe, T. Domröse, J. G. Gatzmann, S. Rost, J. Schauss, S. Strauch, R. Bormann, M. Sivis, S. Schäfer, and C. Ropers. Ultrafast transmission electron microscopy using a laser-driven field emitter: Femtosecond resolution with a high coherence electron beam. *Ultramicroscopy*, 176:63–73, 2017.

[81] C. A. Schneider, W. S. Rasband, and K. W. Eliceiri. NIH Image to ImageJ: 25 years of image analysis. *Nature Methods*, 9(7):671–675, 2012.

[82] G. W. Burns, G. F. Strouse, B. W. Mangum, M. C. Croarkin, W. F. Guthrie, and M. Chattle. New reference functions for platinum-13% rhodium versus platinum (type R) and platinum-30% rhodium versus platinum-6% rhodium (type B) thermocouples based on the ITS-90. In J. F. Schooley, editor, *Temperature: Its Measurement and Control in Science and Industry*, volume 6, pages 559–564. American Institute of Physics, 1992.

[83] E. A. Stach, R. Hull, J. C. Bean, K. S. Jones, and A. Nejim. In Situ Studies of the Interaction of Dislocations with Point Defects during Annealing of Ion Implanted Si/SiGe/Si (001) Heterostructures. *Microscopy and Microanalysis*, 4(3):294–307, 1998.

[84] D. D. L. Chung. Graphite-halogens as temperature calibration standards for transmission electron microscopy. *Review of Scientific Instruments*, 51(7):932–934, 1980.

[85] R. F. Egerton, P. Li, and M. Malac. Radiation damage in the TEM and SEM. *Micron*, 35(6):399–409, 2004.

[86] L. W. Hobbs. Radiation effects in analysis of inorganic specimen by TEM. In J. J. Hren, J. I. Goldstein, and D. C. Joy, editors, *Introduction to Analytical Electron Microscopy*, chapter 17, pages 437–480. Plenum Press, New York, 1979.

[87] A. Lotnyk, S. Bernütz, X. Sun, U. Ross, M. Ehrhardt, and B. Rauschenbach. Real-space imaging of atomic arrangement and vacancy layers ordering in laser crystallised $Ge_2Sb_2Te_5$ phase change thin films. *Acta Materialia*, 105:1–8, 2016.

[88] I. Jenčič, M. W. Bench, I. M. Robertson, and M. A. Kirk. Electron-beam-induced crystallization of isolated amorphous regions in Si, Ge, GaP, and GaAs. *Journal of Applied Physics*, 78(2):974–982, 1995.

[89] N. Yamada, E. Ohno, K. Nishiuchi, N. Akahira, and M. Takao. Rapid-phase transitions of GeTe-Sb_2Te_3 pseudobinary amorphous thin films for an optical disk memory. *Journal of Applied Physics*, 69(5):2849–2856, 1991.

[90] J. Tomforde, W. Bensch, L. Kienle, V. Duppel, P. Merkelbach, and M. Wuttig. Thin Films of Ge-Sb-Te-Based Phase Change Materials: Microstructure and in Situ Transformation. *Chemistry of Materials*, 23(17):3871–3878, 2011.

[91] J. Bravman and R. Sinclair. The preparation of cross-section specimens for transmission electron microscopy. *Journal of Electron Microscopy Technique*, 1(1):53–61, 1984.

[92] A. Romano, J. Vanhellemont, H. Bender, and J.R. Morante. A fast preparation technique for high-quality plan view and cross-section TEM specimens of semiconducting materials. *Ultramicroscopy*, 31(2):183–192, 1989.

[93] L. A. Giannuzzi and F. A. Stevie, editors. *Introduction to Focused Ion Beams*. Springer US, New York, 2005.

[94] T. Kamino, T. Yaguchi, T. Hasimoto, T. Ohnishi, and K. Umemura. A FIB microsampling technique and a site specific TEM specimen preparation method. In L. A. Giannuzzi and F. A. Stevie, editors, *Introduction to Focused Ion Beams*, chapter 11, pages 229–234. Springer US, New York, 2005.

[95] W. F. Gale and T. C. Totemeier, editors. *Smithells Metals Reference Book*. Butterworth-Heinemann, 8th edition, 2003.

[96] S. Raoux and M. Wuttig. *Phase Change Materials*. Springer US, New York, 2009.

[97] T. Siegrist, P. Merkelbach, and M. Wuttig. Phase Change Materials: Challenges on the Path to a Universal Storage Device. *Annual Review of Condensed Matter Physics*, 3(1):215–237, 2012.

[98] S. Raoux. Phase Change Materials. *Annual Review of Materials Research*, 39(1):25–48, 2009.

[99] S. Raoux, R. M. Shelby, J. Jordan-Sweet, B. Munoz, M. Salinga, Y. C. Chen, Y. H. Shih, E. K. Lai, and M. H. Lee. Phase change materials and their application to random access memory technology. *Microelectronic Engineering*, 85(12):2330–2333, 2008.

[100] I.-M. Park, J.-K. Jung, S.-O. Ryu, K.-J. Choi, B.-G. Yu, Y.-B. Park, S. M. Han, and Y.-C. Joo. Thermomechanical properties and mechanical stresses of $Ge_2Sb_2Te_5$ films in phase-change random access memory. *Thin Solid Films*, 517(2):848–852, 2008.

[101] T. Matsunaga, J. Akola, S. Kohara, T. Honma, K. Kobayashi, E. Ikenaga, R. O. Jones, N. Yamada, M. Takata, and R. Kojima. From local structure to nanosecond recrystallization dynamics in AgInSbTe phase-change materials. *Nature Materials*, 10(2):129–134, 2011.

[102] M. H. R. Lankhorst, B. W. S. M. M. Ketelaars, and R. A. M. Wolters. Low-cost and nanoscale non-volatile memory concept for future silicon chips. *Nature Materials*, 4(4):347–352, 2005.

[103] T.-Y. Lee, C. Kim, D.-S. Kang, Y.and Suh, K. H. P. Kim, and Y. Khang. Rapid crystallization of GeTe-Bi_2Te_3 mixed layer. *Applied Physics Letters*, 92(10):101908, 2008.

[104] G.-F. Zhou. Materials aspects in phase change optical recording. *Materials Science and Engineering: A*, 304-306:73–80, 2001.

[105] G. Bruns, P. Merkelbach, C. Schlockermann, M. Salinga, M. Wuttig, T. D. Happ, J. B. Philipp, and M. Kund. Nanosecond switching in GeTe phase change memory cells. *Applied Physics Letters*, 95(4):043108, 2009.

[106] R. E. Simpson, P. Fons, A. V. Kolobov, T. Fukaya, M. Krbal, T. Yagi, and J. Tominaga. Interfacial phase-change memory. *Nature Nanotechnology*, 6(8):501–505, 2011.

[107] W. Zhang, I. Ronneberger, P. Zalden, M. Xu, M. Salinga, M. Wuttig, and R. Mazzarello. How fragility makes phase-change data storage robust: insights from ab initio simulations. *Scientific Reports*, 4:6529, 2014.

[108] S.-H. Lee, Y. Jung, and R. Agarwal. Highly scalable non-volatile and ultra-low-power phase-change nanowire memory. *Nature Nanotechnology*, 2(10):626–630, 2007.

[109] T. Matsunaga, H. Morita, R. Kojima, N. Yamada, K. Kifune, Y. Kubota, Y. Tabata, J.-J. Kim, M. Kobata, E. Ikenaga, and K. Kobayashi. Structural characteristics of GeTe-rich GeTe-Sb_2Te_3 pseudobinary metastable crystals. *Journal of Applied Physics*, 103(9):093511, 2008.

[110] T. Matsunaga and N. Yamada. Structural investigation of $GeSb_2Te_4$: A high-speed phase-change material. *Physical Review B*, 69(10):104111, 2004.

[111] B. Zhang, W. Zhang, Z. Shen, Y. Chen, J. Li, S. Zhang, Z. Zhang, M. Wuttig, R. Mazzarello, E. Ma, and X. Han. Element-resolved atomic structure imaging of rocksalt $Ge_2Sb_2Te_5$ phase-change material. *Applied Physics Letters*, 108(19):191902, 2016.

[112] E. Rotunno, L. Lazzarini, M. Longo, and V. Grillo. Crystal structure assessment of Ge-Sb-Te phase change nanowires. *Nanoscale*, 5(4):1557–1563, 2013.

[113] N. Yamada and T. Matsunaga. Structure of laser-crystallized $Ge_2Sb_{2+x}Te_5$ sputtered thin films for use in optical memory. *Journal of Applied Physics*, 88(12):7020–7028, 2000.

[114] T. Nonaka, G. Ohbayashi, Y. Toriumi, Y. Mori, and H. Hashimoto. Crystal structure of GeTe and $Ge_2Sb_2Te_5$ meta-stable phase. *Thin Solid Films*, 370(1-2):258–261, 2000.

[115] W. Wełnic, A. Pamungkas, R. Detemple, C. Steimer, S. Blügel, and M. Wuttig. Unravelling the interplay of local structure and physical properties in phase-change materials. *Nature Materials*, 5(1):56–62, 2005.

[116] M. Wuttig, D. Lüsebrink, D. Wamwangi, W. Wełnic, M. Gillessen, and R. Dronskowski. The role of vacancies and local distortions in the design of new phase-change materials. *Nature Materials*, 6(2):122–128, 2007.

[117] B. Qiao, J. Feng, Y. Lai, Y. Ling, Y. Lin, T. Tang, B. Cai, and B. Chen. Effects of Si doping on the structural and electrical properties of $Ge_2Sb_2Te_5$ films for phase change random access memory. *Applied Surface Science*, 252(24):8404–8409, 2006.

[118] E. Morales-Sánchez, E. F. Prokhorov, J. González-Hernández, and A. Mendoza-Galván. Structural, electric and kinetic parameters of ternary alloys of GeSbTe. *Thin Solid Films*, 471(1-2):243–247, 2005.

[119] I. Friedrich, V. Weidenhof, W. Njoroge, P. Franz, and M. Wuttig. Structural transformations of $Ge_2Sb_2Te_5$ films studied by electrical resistance measurements. *Journal of Applied Physics*, 87(9):4130–4134, 2000.

[120] Y. J. Park, J. Y. Lee, M. S. Youm, Y. T. Kim, and H. S. Lee. Crystal structure and atomic arrangement of the metastable $Ge_2Sb_2Te_5$ thin films deposited on SiO_2\Si substrates by sputtering method. *Journal of Applied Physics*, 97(9):093506, 2005.

[121] I. I. Petrov, R. M. Imamov, and Z. G. Pinsker. Electron-diffraction determination of the structures of $Ge_2Sb_2Te_5$ and $GeSb_4Te_7$. *Kristallografiya*, 13(3):417–421, 1968.

[122] B. J. Kooi and J. Th. M. De Hosson. Electron diffraction and high-resolution transmission electron microscopy of the high temperature crystal structures of $Ge_xSb_2Te_{3+x}$ (x=1,2,3) phase change material. *Journal of Applied Physics*, 92(7):3584–3590, 2002.

[123] T. Matsunaga, N. Yamada, and Y. Kubota. Structures of stable and metastable $Ge_2Sb_2Te_5$, an intermetallic compound in GeTe-Sb_2Te_3 pseudobinary systems. *Acta Crystallographica Section B*, 60(6):685–691, 2004.

[124] P. Urban, M. N. Schneider, L. Erra, S. Welzmiller, F. Fahrnbauer, and O. Oeckler. Temperature dependent resonant X-ray diffraction of single-crystalline $Ge_2Sb_2Te_5$. *CrystEngComm*, 15(24):4823–4829, 2013.

[125] K. A. Agaev and A.G. Talybov. Electron-Diffraction Analysis of the Structure of $GeSb_2Te_4$. *Kristallografiya*, 11(3):454–456, 1966.

[126] L. E. Shelimova, O. G. Karpinsku, V. S. Zemskov, and P. P. Konstantinov. Structural and Electrical Properties of Layered Tetradymite-like Compounds in the GeTe-Bi2Te3 and GeTe–Sb_2Te_3 Systems. *Inorganic Materials*, 36(3):235–242, 2000.

[127] Z. Sun, J. Zhou, and R. Ahuja. Structure of Phase Change Materials for Data Storage. *Physical Review Letters*, 96(5):055507, 2006.

[128] J. Da Silva, A. Walsh, and H. Lee. Insights into the structure of the stable and metastable $(GeTe)_m(Sb_2Te_3)_n$ compounds. *Physical Review B*, 78(22):224111, 2008.

[129] U. Ross, A. Lotnyk, E. Thelander, and B. Rauschenbach. Direct imaging of crystal structure and defects in metastable $Ge_2Sb_2Te_5$ by quantitative aberration-corrected scanning transmission electron microscopy. *Applied Physics Letters*, 104(12):121904, 2014.

[130] T. Siegrist, P. Jost, H. Volker, M. Woda, P. Merkelbach, C. Schlockermann, and M. Wuttig. Disorder-induced localization in crystalline phase-change materials. *Nature Materials*, 10(3):202–208, 2011.

[131] P. Zalden, K. Simon Siegert, S. Rols, H. E. Fischer, F. Schlich, T. Hu, and M. Wuttig. Specific Heat of $(GeTe)_x(Sb_2Te_3)_{1-x}$ Phase-Change Materials: The Impact of Disorder and Anharmonicity. *Chemistry of Materials*, 26(7):2307–2312, 2014.

[132] B. Zhang, X.-P. Wang, Z.-J. Shen, X.-B. Li, C.-S. Wang, Y.-J. Chen, J.-X. Li, J.-X. Zhang, Z. Zhang, S.-B. Zhang, and X.-D. Han. Vacancy Structures and Melting Behavior in Rock-Salt GeSbTe. *Scientific Reports*, 6:25453, 2016.

[133] B. Kalkan, S. Sen, and S. M. Clark. Nature of phase transitions in crystalline and amorphous GeTe-Sb_2Te_3 phase change materials. *The Journal of Chemical Physics*, 135(12):124510, 2011.

[134] M. Xu, Y. Q. Cheng, H. W. Sheng, and E. Ma. Nature of Atomic Bonding and Atomic Structure in the Phase-Change $Ge_2Sb_2Te_5$ Glass. *Physical Review Letters*, 103(19):195502, 2009.

[135] S. Privitera, E. Rimini, C. Bongiorno, R. Zonca, A. Pirovano, and R. Bez. Crystallization and phase separation in $Ge_{2+x}Sb_2Te_5$ thin films. *Journal of Applied Physics*, 94(7):4409–4413, 2003.

[136] L. E. Shelimova and O. G. Karpinskii. Composition and Properties of Layered Compounds in the GeTe-Sb_2Te_3 System. *Inorganic Materials*, 37(4):421–427, 2001.

[137] U. Schürmann, V. Duppel, S. Buller, W. Bensch, and L. Kienle. Precession Electron Diffraction - a versatile tool for the characterization of Phase Change Materials. *Crystal Research and Technology*, 46(6):561–568, 2011.

[138] D. J. H. Cockayne. The Study of Nanovolumes of Amorphous Materials Using Electron Scattering. *Annual Review of Materials Research*, 37(1):159–187, 2007.

[139] D. R. G. Mitchell and T. C. Petersen. RDFTools: a software tool for quantifying short-range ordering in amorphous materials. *Microscopy Research and Technique*, 75(2):153–163, 2012.

[140] P. Jóvári, I. Kaban, J. Steiner, B. Beuneu, A. Schöps, and M. A. Webb. Local order in amorphous $Ge_2Sb_2Te_5$ and $GeSb_2Te_4$. *Physical Review B*, 77(3):035202, 2008.

[141] R. T. Sanderson. Electronegativity and Bond Energy. *Journal of the American Chemical Society*, 105(8):2259–2261, 1983.

[142] A. V. Kolobov, P. Fons, M. Krbal, R. E. Simpson, S. Hosokawa, T. Uruga, H. Tanida, and J. Tominaga. Liquid $Ge_2Sb_2Te_5$ studied by extended x-ray absorption. *Applied Physics Letters*, 95(24):241902, 2009.

[143] R. Endo, S. Maeda, Y. Jinnai, R. Lan, Ma. Kuwahara, Y. Kobayashi, and M. Susa. Electric Resistivity Measurements of Sb_2Te_3 and $Ge_2Sb_2Te_5$ Melts Using Four-Terminal Method. *Japanese Journal of Applied Physics*, 49(6):065802, 2010.

[144] P. K. Khulbe, E. M. Wright, and M. Mansuripur. Crystallization behavior of as-deposited, melt quenched, and primed amorphous states of $Ge_2Sb_{2.3}Te_5$ films. *Journal of Applied Physics*, 88(7):3926–3933, 2000.

[145] J. Akola, J. Larrucea, and R. O. Jones. Polymorphism in phase-change materials: Melt-quenched and as-deposited amorphous structures in $Ge_2Sb_2Te_5$ from density functional calculations. *Physical Review B*, 83(9):094113, 2011.

[146] A. V. Kolobov, J. Haines, A. Pradel, M. Ribes, P. Fons, J. Tominaga, C. Steimer, G. Aquilanti, and S. Pascarelli. Pressure-induced amorphization of quasibinary GeTe-Sb_2Te_3: The role of vacancies. *Applied Physics Letters*, 91(2):10–13, 2007.

[147] N. K. Abrikosov and G.T. Danilova-Dobryakova. Study of the ternary system Ge-Sb-Te. *Izvestiya Akademii Nauk, Neorganicheskie Materialy*, 1:204, 1965.

[148] B. Legendre and C. Hancheng. Phase diagram of the ternary system Ge-Sb-Te. I. The subternary GeTe-Sb_2Te_3-Te. *Thermochimica Acta*, 78(1):141–157, 1984.

[149] T. Blachowicz, M. G. Beghi, G. Güntherodt, B. Beschoten, H. Dieker, and M. Wuttig. Crystalline phases in the $GeSb_2Te_4$ alloy system: Phase transitions and elastic properties. *Journal of Applied Physics*, 102(9):093519, 2007.

[150] W. K. Njoroge, H.-W. Woöltgens, and M. Wuttig. Density changes upon crystallization of $Ge_2Sb_{2.04}Te_4.74$ films. *Journal of Vacuum Science & Technology A*, 20(1):230–233, 2002.

[151] D. Subramaniam, C. Pauly, M. Liebmann, M. Woda, P. Rausch, P. Merkelbach, M. Wuttig, and M. Morgenstern. Scanning tunneling microscopy and spectroscopy of the phase change alloy $Ge_1Sb_2Te_4$. *Applied Physics Letters*, 95(10):103110, 2009.

[152] S. Bordas and M. T. Clavaguer-Mora. Phase Diagram of the Ternary System Ge-Sb-Te: II. The Subternary Ge-GeTe-Sb_2Te_3-Sb. *Thermochimica Acta*, 107:239–265, 1986.

[153] J. Kalb, F. Spaepen, and M. Wuttig. Calorimetric measurements of phase transformations in thin films of amorphous Te alloys used for optical data storage. *Journal of Applied Physics*, 93(5):2389–2393, 2003.

[154] J. Feng, Y. Zhang, B. W. Qiao, Y. F. Lai, Y. Y. Lin, B. C. Cai, T. A. Tang, and B. Chen. Si doping in $Ge_2Sb_2Te_5$ film to reduce the writing current of phase change memory. *Applied Physics A*, 87(1):57–62, 2007.

[155] L. Tong, L. Xu, Y. Jiang, F. Yang, L. Geng, J. Xu, W. Su, Z. Ma, and K. Chen. Improved phase-change characteristics of Si doped GeSbTe thin films used for phase change memory. *Journal of Non-Crystalline Solids*, 358(17):2402–2404, 2012.

[156] Y. Saito, Y. Sutou, and J. Koike. Effects of Si addition on the crystallization behaviour of GeTe phase change materials. *Journal of Physics D*, 45(40):405302, 2012.

[157] H. Seo, T. H. Jeong, J. Park, C. Yeon, S. J. Kim, and S. Y. Kim. Investigation of Crystallization Behavior of Sputter-Deposited Nitrogen-Doped Amorphous $Ge_2Sb_2Te_5$ Thin Films. *Japanese Journal of Applied Physics*, 39(2):745–751, 2000.

[158] Y. K. Kim, S. A. Park, J. H. Baeck, M. K. Noh, K. Jeong, M.-H. Cho, H. M. Park, M. K. Lee, E. J. Jeong, D.-H. Ko, and H. J. Shin. Phase separation of a $Ge_2Sb_2Te_5$ alloy in the transition from an amorphous structure to crystalline structures. *Journal of Vacuum Science & Technology A*, 24(4):929–933, 2006.

[159] S. W. Ryu, J. H. Oh, J. H. Lee, B. J. Choi, W. Kim, S. K. Hong, C. S. Hwang, and H. J. Kim. Phase transformation behaviors of SiO_2 doped $Ge_2Sb_2Te_5$ films for application in phase change random access memory. *Applied Physics Letters*, 92(14):142110, 2008.

[160] K. Ding, K. Ren, F. Rao, Z. Song, L. Wu, B. Liu, and S. Feng. Study on the Cu-doped $Ge_2Sb_2Te_5$ for low-power phase change memory. *Materials Letters*, 125(17):143–146, 2014.

[161] S. Raoux, M. Salinga, J. L. Jordan-Sweet, and A. Kellock. Effect of Al and Cu doping on the crystallization properties of the phase change materials SbTe and GeSb. *Journal of Applied Physics*, 101(4):044909, 2007.

[162] K. Wang, C. Steimer, D. Wamwangi, S. Ziegler, M. Wuttig, J. Tomforde, and W. Bensch. Influence of doping upon the phase change characteristics of $Ge_2Sb_2Te_5$. *Microsystem Technologies*, 13(2):203–206, 2007.

[163] S. J. Wei, H. F. Zhu, K. Chen, D. Xu, J. Li, F. X. Gan, X. Zhang, Y. J. Xia, and G. H. Li. Phase change behavior in titanium-doped $Ge_2Sb_2Te_5$ films. *Applied Physics Letters*, 98(23):231910, 2011.

[164] J. Park and J. Bae. Effect of Ti diffusion on the microstructure of $Ge_2Sb_2Te_5$ in phase-change memory cell. *Microscopy*, 64(6):381–386, 2015.

[165] J. Orava, A. L. Greer, B. Gholipour, D. W. Hewak, and C. E. Smith. Characterization of supercooled liquid $Ge_2Sb_2Te_5$ and its crystallization by ultrafast-heating calorimetry. *Nature Materials*, 11(4):279–283, 2012.

[166] M. Salinga, J. Kalb, M. Klein, T. Sontheimer, F. Spaepen, and M. Wuttig. Glass Transition and Crystallization in Phase Change Materials. *Proceedings of the 2007 EPCOS Meeting*, 2007.

[167] J. A. Kalb. *Crystallization kinetics in antimony and tellurium alloys used for phase change recording*. Dissertation, RWTH Aachen University, 2001.

[168] J. Akola and R. O. Jones. Structural Patterns in Ge/Sb/Te Phase-Change Materials. In G. Münster, D. Wolf, and M. Kremer, editors, *NIC Series*, volume 39, pages 169–176. John von Neumann Institute for Computing, Jülich, 2008.

[169] S. Senkader and C. D. Wright. Models for phase-change of $Ge_2Sb_2Te_5$ in optical and electrical memory devices. *Journal of Applied Physics*, 95(2):504–511, 2004.

[170] P. Zalden, A. von Hoegen, P. Landreman, M. Wuttig, and A. M. Lindenberg. How Supercooled Liquid Phase-Change Materials Crystallize: Snapshots after Femtosecond Optical Excitation. *Chemistry of Materials*, 27(16):5641–5646, 2015.

[171] G. Eising, T. Van Damme, and B. J. Kooi. Unraveling crystal growth in GeSb phase-change films in between the glass-transition and melting temperatures. *Crystal Growth and Design*, 14(7):3392–3397, 2014.

[172] M. K. Santala, S. Raoux, and G. H. Campbell. Kinetics of liquid-mediated crystallization of amorphous Ge from multi-frame dynamic transmission electron microscopy. *Applied Physics Letters*, 107(25):252106, 2015.

[173] J. Hegedüs and S. R. Elliott. Microscopic origin of the fast crystallization ability of Ge-Sb-Te phase-change memory materials. *Nature Materials*, 7(5):399–405, 2008.

[174] I. Friedrich, V. Weidenhof, S. Lenk, and M. Wuttig. Morphology and structure of laser-modified $Ge_2Sb_2Te_5$ films studied by transmission electron microscopy. *Thin Solid Films*, 389(1-2):239–244, 2001.

[175] T. H. Jeong, M. R. Kim, H. Seo, S. J. Kim, and S. Y. Kim. Crystallization behavior of sputter-deposited amorphous $Ge_2Sb_2Te_5$ thin films. *Journal of Applied Physics*, 86(2):774–778, 1999.

[176] G. Ruitenberg, A. K. Petford-Long, and R. C. Doole. Determination of the isothermal nucleation and growth parameters for the crystallization of thin $Ge_2Sb_2Te_5$ films. *Journal of Applied Physics*, 92(6):3116–3123, 2002.

[177] P. Noé, C. Sabbione, N. Bernier, N. Castellani, F. Fillot, and F. Hippert. Impact of interfaces on scenario of crystallization of phase change materials. *Acta Materialia*, 110:142–148, 2016.

[178] T. Matsunaga and N. Yamada. A Study of Highly Symmetrical Crystal Structures, Commonly Seen in High-Speed Phase-Change Materials, Using Synchrotron Radiation. *Japanese Journal of Applied Physics*, 41(3):1674–1678, 2002.

[179] F. Katmis, R. Calarco, K. Perumal, P. Rodenbach, A. Giussani, M. Hanke, A. Proessdorf, A. Trampert, F. Grosse, R. Shayduk, R. Campion, W. Braun, and H. Riechert. Insight into the Growth and Control of Single-Crystal Layers of Ge-Sb-Te Phase-Change Material. *Crystal Growth & Design*, 11(10):4606–4610, 2011.

[180] P. Rodenbach, R. Calarco, K. Perumal, F. Katmis, M. Hanke, A. Proessdorf, W. Braun, A. Giussani, A. Trampert, H. Riechert, P. Fons, and A. V. Kolobov. Epitaxial phase-change materials. *Physica Status Solidi - Rapid Research Letters*, 6(11):415–417, 2012.

[181] W. Kleber. *Einführung in die Kristallographie*. VEB Verlag Technik Berlin, Berlin, 9th edition, 1965.

[182] J. A. Kalb, C. Y. Wen, F. Spaepen, H. Dieker, and M. Wuttig. Crystal morphology and nucleation in thin films of amorphous Te alloys used for phase change recording. *Journal of Applied Physics*, 98(5):054902, 2005.

[183] J. Kalb, F. Spaepen, and M. Wuttig. Atomic force microscopy measurements of crystal nucleation and growth rates in thin films of amorphous Te alloys. *Applied Physics Letters*, 84(25):5240–5242, 2004.

[184] S. Privitera, C. Bongiorno, E. Rimini, and R. Zonca. Crystal nucleation and growth processes in $Ge_2Sb_2Te_5$. *Applied Physics Letters*, 84(22):4448–4450, 2004.

[185] S. Raoux, J. L. Jordan-Sweet, and Andrew J. Kellock. Crystallization properties of ultrathin phase change films. *Journal of Applied Physics*, 103(11):114310, 2008.

[186] M. Salinga, E. Carria, A. Kaldenbach, M. Bornhöfft, J. Benke, J. Mayer, and M. Wuttig. Measurement of crystal growth velocity in a melt-quenched phase-change material. *Nature Communications*, 4:3371, 2013.

[187] L. van Pieterson. Experimental Methods for Material Selection in Phase-change Recording. In S. Raoux and M. Wuttig, editors, *Phase Change Materials - Science and Applications*, chapter 5. Springer US, New York, 2009.

[188] J. H. Coombs, A. P. J. M. Jongenelis, W. Van Es-Spiekman, and B. A. J. Jacobs. Laser-induced crystallization phenomena in GeTe-based alloys. II. Composition dependence of nucleation and growth. *Journal of Applied Physics*, 78(8):4918–4928, 1995.

[189] Experiments done by the author of this thesis and described in her master thesis "Investigation of crystallization of $(GeTe)_{1-x}(Sb_2Te_3)_x$ based phase change materials using in-situ transmission electron microscopy", unpublished.

[190] Y. J. Park, J. Y. Lee, and Y. T. Kim. A transmission electron microscopy study on the atomic arrangement and grain growth of hexagonal structured $Ge_2Sb_2Te_5$. *Applied Surface Science*, 253(2):714–719, 2006.

[191] J. Narayan and B. C. Larson. Domain epitaxy: A unified paradigm for thin film growth. *Journal of Applied Physics*, 93(1):278–285, 2003.

[192] S. Mukhopadhyay, J. Sun, A. Subedi, T. Siegrist, and D. J. Singh. Competing covalent and ionic bonding in Ge-Sb-Te phase change materials. *Scientific Reports*, 6:25981, 2016.

[193] K. S. Siegert, F. R. L. Lange, E. R. Sittner, H. Volker, C. Schlockermann, T. Siegrist, and M. Wuttig. Impact of vacancy ordering on thermal transport in crystalline phase-change materials. *Reports on Progress in Physics*, 78(1):013001, 2014.

[194] K. Berlin and A. Trampert. Liquid-solid phase transition of Ge-Sb-Te alloy observed by in-situ transmission electron microscopy. *Ultramicroscopy*, 178:27–32, 2017.

[195] F. A. Lindemann. The calculation of molecular vibration frequencies. *Physikalische Zeitschrift*, 11:609–612, 1910.

[196] M. Born. Thermodynamics of Crystals and Melting. *The Journal of Chemical Physics*, 7(8):591–603, 1939.

[197] Z. H. Jin, P. Gumbsch, K. Lu, and E. Ma. Melting mechanisms at the limit of superheating. *Physical Review Letters*, 87(5):055703, 2001.

[198] H. Saka, S. Arai, S. Tsukimoto, and K. Sasaki. In Situ HRTEM Observation of Solid-Liquid Interfaces. *Materials Science Forum*, 294-296:617–620, 1999.

[199] P. R. Couchman and W. A. Jesser. Thermodynamic theory of size dependence of melting temperature in metals. *Nature*, 269(5628):481–483, 1977.

[200] M. Takagi. Electron-Diffraction Study of Liquid-Solid Transition of Thin Metal Films. *Journal of the Physical Society of Japan*, 9(3):359–363, 1954.

[201] K. K. Nanda, S. N. Sahu, and S. N. Behera. Liquid-drop model for the size-dependent melting of low-dimensional systems. *Physical Review A*, 66(1):013208, 2002.

[202] W. H. Qi, M. P. Wang, M. Zhou, and W. Y. Hu. Surface-area-difference model for thermodynamic properties of metallic nanocrystals. *Journal of Physics D*, 38(9):1429–1436, 2005.

[203] B.-G. Kim. A large thermal hysteresis between melting and solidification temperature on nanoscale Pb particles embedded in amorphous SiO_2 matrix prepared by sputtering. *Metals and Materials*, 5(3):309–316, 1999.

[204] Y. Wang, M. Rafailovich, J. Sokolov, D. Gersappe, T. Araki, Y. Zou, A. D. L. Kilcoyne, H. Ade, G. Marom, and A. Lustiger. Substrate effect on the melting temperature of thin polyethylene films. *Physical Review Letters*, 96(2):028303, 2006.

[205] C. R. M. Wronski. The size dependence of the melting point of small particles of tin. *British Journal of Applied Physics*, 18(12):1731–1737, 1967.

[206] G. L. Allen, R. A. Bayles, W. W. Gile, and W. A. Jesser. Small particle melting of pure metals. *Thin Solid Films*, 144(2):297–308, 1986.

[207] A. N. Goldstein, C. M. Echer, and A. P. Alivisatos. Melting in semiconductor nanocrystals. *Science*, 256(5062):1425–1427, 1992.

[208] M. Asoro, J. Damiano, and P. J. Ferreira. Size Effects on the Melting Temperature of Silver Nanoparticles: In-Situ TEM Observations. *Microscopy and Microanalysis*, 15(S2):706–707, 2009.

[209] S. H. Lee, Y. Jung, H. S. Chung, An. T. Jennings, and R. Agarwal. Comparative study of memory-switching phenomena in phase change GeTe and $Ge_2Sb_2Te_5$ nanowire devices. *Physica E*, 40(7):2474–2480, 2008.

[210] X. Sun, B. Yu, G. Ng, and M. Meyyappan. One-dimensional phase-change nanostructure: Germanium telluride nanowire. *Journal of Physical Chemistry C*, 111(6):2421–2425, 2007.

[211] H. Gabrisch, L. Kjeldgaard, E. Johnson, and U. Dahmen. Equilibrium shape and interface roughening of small liquid Pb inclusions in solid Al. *Acta Materialia*, 49(20):4259–4269, 2001.

[212] S. E. Donnelly. Ordering in a Fluid Inert Gas Confined by Flat Surfaces. *Science*, 296(5567):507–510, 2002.

[213] F. M. Ross, J. Tersoff, and M. C. Reuter. Sawtooth faceting in silicon nanowires. *Physical Review Letters*, 95(14):146104, 2005.

[214] Z. Zhang, J. Pan, Y. Lim, L. W.-W. Fang, Y.-C. Yeo, R. Zhao, L. Shi, and T.-C. Chong. Applied Surface Science Effective method for preparation of oxide-free $Ge_2Sb_2Te_5$ surface: An X-ray photoelectron spectroscopy study. *Applied Surface Science*, 256(24):7696–7699, 2010.

[215] Y. Wu and P. Yang. Melting and welding semiconductor nanowires in nanotubes. *Advanced Materials*, 13(7):520–523, 2001.

[216] Y. Yuan and T. R. Lee. Contact Angle and Wetting Properties. In *Surface Science Techniques*, chapter 1, pages 3–34. Springer, Berlin, Heidelberg, 2013.

[217] Y. Okada and Y. Tokumaru. Precise determination of lattice parameter and thermal expansion coefficient of silicon between 300 and 1500 K. *Journal of Applied Physics*, 56(2):314–320, 1984.

[218] T. Young. An Essay on the Cohesion of Fluids. *Philosophical Transactions of the Royal Society of London*, 95:65–87, 1805.

[219] J. M. Howe. *Interfaces in Materials*. John Wiley & Sons, Inc., New York, 1997.

[220] A. F. Stalder, G. Kulik, D. Sage, L. Barbieri, and P. Hoffmann. A snake-based approach to accurate determination of both contact points and contact angles. *Colloids and Surfaces A*, 286(1-3):92–103, 2006.

[221] R. J. Jaccodine. Surface Energy of Germanium and Silicon. *Journal of The Electrochemical Society*, 110(6):524–527, 1963.

[222] G. Bai, Z. Liu, R. Li, Y. Xia, and J. Yin. Phase change behavior and critical size of $Ge_2Sb_2Te_5$ nanowires and nanotubes. *Physica B*, 411:68–71, 2013.

[223] J. A. Kalb, F. Spaepen, and M. Wuttig. Kinetics of crystal nucleation in undercooled droplets of Sb- and Te-based alloys used for phase change recording. *Journal of Applied Physics*, 98(5):054910, 2005.

[224] C. R. Henry. Morphology of supported nanoparticles. *Progress in Surface Science*, 80(3-4):92–116, 2005.

[225] G. Cao. *Nanostructures&Nanomaterials: Synthesis, Properties & Applications*. Imperial College Press, London, 2004.

[226] S.-W. Nam, T.-Y. Lee, J.-S. Wi, D. Lee, H.-S. Lee, K.-B. Jin, M.-H. Lee, H.-M. Kim, and K.-B. Kim. Electron-Beam Lithography Patterning of $Ge_2Sb_2Te_5$ Nanostructures Using Hydrogen Silsesquioxane and Amorphous Si Intermediate Layer. *Journal of the Electrochemical Society*, 154(9):H844, 2007.

[227] K. B. Blyuss, P. Ashwin, A. P. Bassom, and C. D. Wright. Master-equation approach to the study of phase-change processes in data storage media. *Physical Review E*, 72(1):011607, 2005.

[228] B. Hyot, V. Gehanno, B. Rolland, A. Fargeix, C. Vannufel, F. Charlet, B. Béchevet, J. M. Bruneau, and P. J. Desre. Amorphization and Crystallization mechanisms in GeSbTe-based Phase Change Optical Disks. *Journal of the Magnetics Society of Japan*, 25(3_2):414–419, 2001.

[229] M. Volmer. *Kinetik der Phasenbildung*. Theodor Steinkopff, Dresden, 1939.

[230] W. Kossel. Zur Theorie des Kristallwachstums. *Nachrichten von der Gesellschaft der Wissenschaften zu Göttingen*, pages 135–143, 1927.

[231] I. N. Stranski. Zur Theorie des Kristallwachstums. *Zeitschrift für Physikalische Chemie*, 136:259–278, 1928.

[232] W. K. Burton, N. Cabrera, and F. C. Frank. The Growth of Crystals and the Equilibrium Structure of their Surfaces. *Philosophical Transactions of the Royal Society A*, 243(866):299–358, 1951.

[233] J. P. Hirth and G. M. Pound. Evaporation of Metal Crystals. *The Journal of Chemical Physics*, 26(5):1216–1224, 1957.

[234] J. P. Hirth and G. M. Pound. Coefficients of evaporation and condensation. *The Journal of Physical Chemistry*, 64(5):619–626, 1960.

[235] J. Y. Huang, F. Ding, B. I. Yakobson, P. Lu, L. Qi, and J. Li. In situ observation of graphene sublimation and multi-layer edge reconstructions. *Proceedings of the National Academy of Sciences of the United States of America*, 106(25):10103–10108, 2009.

[236] J. Y. Huang, L. Qi, and J. Li. In situ imaging of layer-by-layer sublimation of suspended graphene. *Nano Research*, 3(1):43–50, 2010.

[237] E. H. Conrad and T. Engel. The equilibrium crystal shape and the roughening transition on metal surfaces. *Surface Science*, 299-300:391–404, 1994.

[238] K. Kern. Thermal Roughening of Surfaces: Experimental Aspects. In D.A. King and D.P. Woodruff, editors, *The Chemical Physics of Solid Surfaces. Phase Transitions and Adsorbate Restructuring at Metal Surfaces*, chapter 9, pages 291–340. Elsevier, 1994.

[239] R. Lian, H. Yu, L. He, L. Zhang, Y. Zhou, X. Bu, T. Xu, and L. Sun. Sublimation of Ag nanocrystals and their wetting behaviors with graphene and carbon nanotubes. *Carbon*, 101:368–376, 2016.

[240] R. F. Egerton. Electron energy-loss spectroscopy in the TEM. *Reports on Progress in Physics*, 72(1):016502, 2009.

[241] Y. Lai, B. Qiao, J. Feng, Y. Ling, L. Lai, Y. Lin, T. Tang, B. Cai, and B. Chen. Nitrogen-doped $Ge_2Sb_2Te_5$ films for nonvolatile memory. *Journal of Electronic Materials*, 34(2):176–181, 2005.

[242] S. Caravati, D. Colleoni, R. Mazzarello, T. D. Kühne, M. Krack, M. Bernasconi, and M. Parrinello. First-principles study of nitrogen doping in cubic and amorphous $Ge_2Sb_2Te_5$. *Journal of Physics: Condensed Matter*, 23(26):265801, 2011.

[243] E. M. Vinod, K. Ramesh, R. Ganesan, and K. S. Sangunni. Direct hexagonal transition of amorphous $(Ge_2Sb_2Te_5)_{0.9}Se_{0.1}$ thin films. *Applied Physics Letters*, 104(6):063505, 2014.

[244] P. Xu, D. Dunn, J. P. Zhang, and L. D. Marks. Atomic imaging of surfaces in plan view. *Surface Science*, 285(1-2):479–485, 1993.

[245] J. Wu, J. M. Howe, and W.-Z. Zhang. An in situ transmission electron microscopy study of interface growth during martensitic transformation in an Fe-Ni-Mn alloy. *Acta Materialia*, 59(8):3297–3303, 2011.

[246] A. V. Kolobov, J. Haines, A. Pradel, M. Ribes, P. Fons, J. Tominaga, Y. Katayama, T. Hammouda, and T. Uruga. Pressure-induced site-selective disordering of $Ge_2Sb_2Te_5$: A new insight into phase-change optical recording. *Physical Review Letters*, 97(3):035701, 2006.

[247] M. H. Jang, S. J. Park, D. H. Lim, M.-H. Cho, Y. K. Kim, H.-J. Yi, and H. S. Kim. Structural Stability and Phase-Change Characteristics of $Ge_2Sb_2Te_5/SiO_2$ Nano-Multilayered Films. *Electrochemical and Solid-State Letters*, 12(4):H151–H154, 2009.

[248] L. Zheng, X. Gu, L. Ma, X. Wu, X. Zhu, and Y. Sui. Investigation of $Ge_2Sb_2Te_5$/Si nano-multilayered films for phase-change memory applications. *Journal of Applied Physics*, 119(4):044901, 2016.

[249] J. Park, M. R. Kim, W. S. Choi, H. Seo, and C. Yeon. Characterization of Amorphous Phases of $Ge_2Sb_2Te_5$ Phase-Change Optical Recording Material on Their Crystallization Behavior. *Japanese Journal of Applied Physics*, 38(8):4775–4779, 1999.

[250] C. Sun, J. Lee, and Y. Kim. TEM study of the structural similarity between NaCl and rhombohedral phase of Te-based ternary chalcogenide materials. *Physica Status Solidi (a)*, 206(1):50–53, 2009.

Selbständigkeitserklärung

Ich erkläre, dass ich die Dissertation selbständig und nur unter Verwendung der von mir gemäß §7 Abs. 3 der Promotionsordnung der Mathematisch-Naturwissenschaftlichen Fakultät, veröffentlicht im Amtlichen Mitteilungsblatt der Humboldt-Universität zu Berlin Nr. 126/2014 am 18.11.2014, angegebenen Hilfsmittel angefertigt habe.

Berlin,